Tin-doped Indium Oxide (ITO) Nanocrystal Superlattices

(Surface Chemistry, Charge Transport, and Sensing Applications)

Dissertation
der Mathematisch-Naturwissenschaftlichen Fakultät
der Eberhard Karls Universität Tübingen
zur Erlangung des Grades eines
Doktors der Naturwissenschaften
(Dr. rer. nat.)

vorgelegt von

Mahdi Samadi Khoshkhoo

aus Tabriz/Iran

Tübingen
December 2017

Gedruckt mit Genehmigung der Mathematisch-Naturwissenschaftlichen Fakultät der Eberhard Karls Universität Tübingen.

Tag der mündlichen Qualifikation:	20.03.2018
Dekan:	Prof. Dr. Wolfgang Rosenstiel
1. Berichterstatter:	Dr. Marcus Scheele
2. Berichterstatter:	Prof. Dr. Thomas Chassé

Preface

The majority of experimental work in this dissertation has been carried out between July 2014 and August 2017 in the Institute of Physical and Theoretical Chemistry at the University of Tübingen in the group of Dr. Marcus Scheele and Prof. Dr. Thomas Chassé. The X-ray scattering measurements have been performed in the Institute of Applied Physics at the University of Tübingen in the group of Prof. Dr. Frank Schreiber and vapor sensing measurements have been carried out in the Institute of Electronic and Sensor Materials at Freiberg University of Mining and Technology in the group of Prof. Dr. Yvonne Joseph.

The theoretical section in this dissertation is mainly excerpted from:

(i) Boris I. Shklovskii and Alexei L. Efros, "Electronic Properties of Doped Semiconductors", Springer-Verlag Berlin Heidelberg, **1984**.
(ii) Simon Min Sze, Kwok K. Ng, "Physics of Semiconductor Devices", John Wiley & Sons, Inc., Hoboken, New Jersey, **2006**.
(iii) Leonid I. Glazman and Michael Pustilnik, "Nanophysics: Coherence and Transport", Vol 81, 1st Ed., Elsevier Science, San Diego, CA, **2005**.
(iv) Paul van der Heide, "X-ray Photoelectron Spectroscopy: An Introduction to Principles and Practices", John Wiley & Sons, Inc., Hoboken, New Jersey, **2011**.
(v) Winfried Mönch, "Semiconductor Surfaces and Interfaces", Springer-Verlag Berlin Heidelberg, New York, **1993**.

as well as from the following research and review articles:

(i) Beloborodov, I. S.; Lopatin, A. V.; Vinokur, V. M.; Efetov, K. B. Granular Electronic Systems. *Rev Mod Phys* **2007**, 79, 469-518.
(ii) Tran, T. B.; Beloborodov, I. S.; Hu, J. S.; Lin, X. M.; Rosenbaum, T. F.; Jaeger, H. M. Sequential Tunneling and Inelastic Cotunneling in Nanoparticle Arrays. *Phys Rev B* **2008**, 78, 075437.
(iii) Skinner, B.; Chen, T. R.; Shklovskii, B. I. Theory of Hopping Conduction in Arrays of Doped Semiconductor Nanocrystals. *Phys Rev B* **2012**, 85, 205316.
(iv) Ishii, H.; Sugiyama, K.; Ito, E.; Seki, K. Energy Level Alignment and Interfacial Electronic Structures at Organic/Metal and Organic/Organic Interfaces. *Adv Mater* **1999**, 11, 605-625.
(v) Braun, S.; Salaneck, W. R.; Fahlman, M. Energy-Level Alignment at Organic/Metal and Organic/Organic Interfaces. *Adv Mater* **2009**, 21, 1450-1472.
(vi) Hwang, J.; Wan, A.; Kahn, A. Energetics of Metal-Organic Interfaces: New Experiments and Assessment of the Field. *Mat Sci Eng R* **2009**, 64, 1-31.

Funding has been provided partly by a scholarship from German Research Foundation (DFG) and by PhD grants of DFG under SCHE1905/3, SCHE1905/4 and SCHR700/25.

This work is organized in five chapters as follows:

In Chapter 1, an introduction to the subject, the theoretical background of the observed physical processes, and the relevant proposed theoretical models are introduced and described. This chapter is kept as short as possible in order to provide the necessary fundamental information.

Chapter 2 is a copy of a manuscript by Mahdi Samadi Khoshkhoo, Santanu Maiti, Frank Schreiber, Thomas Chassé, and Marcus Scheele titled "Surface Functionalization with Copper Tetraaminophthalocyanine Enables Efficient Charge Transport in Indium Tin Oxide Nanocrystal Thin Films" published in *ACS Applied Materials & Interfaces*, **2017**, 9, 14197-14206. doi: 10.1021/acsami.7b00555.

Chapter 3 is a copy of an under-review manuscript by Mahdi Samadi Khoshkhoo, Santanu Maiti, Frank Schreiber, Thomas Chassé, and Marcus Scheele titled "Tunable Charge Transport in ITO Nanocrystal Superlattices – Towards Sensing Applications", *submitted*, **2017**.

Chapter 4 is a copy of manuscript by Mahdi Samadi Khoshkhoo, Heiko Peisert, Thomas Chassé, Marcus Scheele titled "The Role of the Density of Interface States in Interfacial Energy Level Alignment of PTCDA" published in *Organic Electronics*, **2017**, 49, 249-254. doi: 10.1016/j.orgel.2017.06.065.

Finally Chapter 5 describes a summary of the contribution of the author to the following papers:

- "Toward Conductive Mesocrystalline Assemblies: PbS Nanocrystals Cross-Linked with Tetrathiafulvalene Dicarboxylate" by Alexander André, Danylo Zherebetskyy, David Hanifi, Bo He, Mahdi Samadi Khoshkhoo, Maciej Jankowski, Thomas Chassé, Lin-Wang Wang, Frank Schreiber, Alberto Salleo, Yi Liu, Marcus Scheele published in *Chemistry of Materials*, **2015**, 27, 8105–8115. doi: 10.1021/acs.chemmater.5b03821
- "Solution-Processed Two-Dimensional Ultrathin InSe Nanosheets" by Jannika Lauth, Friederieke E. S. Gorris, Mahdi Samadi Khoshkhoo, Thomas Chassé, Wiebke Friedrich, Vera Lebedeva, Andreas Meyer, Christian Klinke, Andreas Kornowski, Marcus Scheele, Horst Weller published in *Chemistry of Materials*, **2016**, 28, 1728-1736. doi: 10.1021/acs.chemmater.5b04646
- "Towards Photo-Switchable Transport in Quantum Dot Solids" by Christine Schedel, Robert Thalwitzer, Mahdi Samadi Khoshkhoo, Marcus Scheele published in *Zeitschrift für Physikalische Chemie*, **2017**, 231, 1, 135-146. doi: 10.1515/zpch-2016-0863
- "Structure, transport and photoconductance of PbS quantum dot monolayers functionalized with a Copper Phthalocyanine derivative" by Alexander André, Christoph Theurer, Jannika Lauth, Santanu Maiti, Martin Hodas, Mahdi Samadi Khoshkhoo, Sachin Kinge, Alfred J. Meixner, Frank Schreiber, Laurens Siebbeles, Kai Braun and Marcus Scheele published in *Chemical Communications*, **2017**, 53, 1700-1703. doi: 10.1039/C6CC07878H

Abstract

This cumulative dissertation is based on three publications. It investigates the surface chemistry of nanocrystals (NC), charge transport in NC superlattices, and energy level alignment at organic/inorganic interfaces. The materials of choice are tin-doped indium oxide (ITO) NCs as well as the organic semiconductors metal-4,4',4″,4‴-tetraaminophthalocyanine (M4APc) and perylene-3,4,9,10-tetracarboxylic dianhydride (PTCDA). A wet chemical approach is used to synthesize the NCs and to control the doping concentration.

Macroscopic superlattices of ITO NCs are prepared by a Langmuir-type self-assembly at the air/liquid interface followed by simultaneous ligand exchange with Cu4APc. X-ray photoelectron spectroscopy (XPS), grazing-incidence small-angle X-ray scattering (GISAXS), and ultraviolet-visible-near-infrared (UV-vis-NIR) spectroscopy are used to track the chemical changes on the nanocrystals' surface before and after ligand exchange and develop a detailed picture of the various components which dominate the surface chemistry of this material. It is demonstrated that the semiconductor molecules largely replace the native surfactant from the ITO NC surface and act as cross-linkers between neighboring particles. Transport measurements reveal a significant increase in electrical conductance, suggesting that Cu4APc provides efficient electronic coupling for neighboring ITO NCs. This material provides the opportunity to study charge and spin transport through phthalocyanine monolayers.

Next, the choice of the metal center of M4APc is expanded to Cu, Co, Fe, Ni, and Zn. These ligands are incorporated into the array of ITO NCs, and the charge carrier transport and resistance-mediated vapor sensing are investigated. Varying the metal center provides the opportunity to systematically study the sole effect of the tunneling barrier height on charge transport through the nanocrystal array, while all other parameters are kept constant. Transport measurements, focusing on the effect of the metal center of the ligand, reveal a ligand-dependent increase in electrical conductance. The resulting I–V characteristics as well as the temperature dependence of the zero-voltage conductance indicates that at low temperatures, transport across the arrays occurs via a sequence of inelastic cotunneling events. At higher temperatures, a crossover to 3D Mott variable range hopping (VRH) mechanism is observed. The vapor sensitivity of chemiresistors made from ITO NCs arrays is investigated by dosing the sensors with four different analytes and concentrations as low as 100 ppm. By testing different classes of analytes, different selectivities of the materials is also registered, depending on whether the analytes behave more vapor- or more gas-like.

Finally, a wide range of substrates (unreactive, reactive or passivated metals and polymers) with different work functions and coupling interactions are used to investigate the electronic structure at the substrate/PTCDA interface by XPS, ultraviolet photoelectron spectroscopy (UPS), and electrostatic calculations. For thick layers of PTCDA, nearly unchanged electron and hole injection barriers on all substrates are observed without any dependence on the type of substrate. For few monolayers of PTCDA, this seemingly universal Fermi level pinning is perturbed depending on the nature of the substrate and the thickness. This behavior is explained with a large induced density of interface states. Using standard electrostatic calculation models as well as introducing extensions to previously reported approaches, the origin of universal Fermi level pinning and its underlying mechanism is investigated. The simulation results demonstrate how the shape of the DOS near the interface has long-range influence on key parameters (e.g. the barrier to charge injection) of the entire organic film.

Zusammenfassung

Die vorliegende kumulative Dissertation basiert auf drei Publikationen. Sie behandelt die Oberflächenchemie von Nanokristallen (NC), Ladungstransport in NC Übergittern und die Energieniveauausrichtung an organisch/anorganischen Grenzflächen. Bei den untersuchten Materialien handelt es sich um Indiumzinnoxid (ITO) NCs und organische Halbleiter der Metall-4,4',4″,4‴-tetraaminophthalocyanine (M4APc) und Perylen-3,4,9,10-tetracarbonsäuredianhydrid (PTCDA). Eine nasschemische Herangehensweise wird für die Synthese der NCs und die Kontrolle ihrer Dotierungskonzentration gewählt.

Durch eine Langmuir-artige selbst-Assemblierung an der Flüssig-Gas-Grenzfläche mit parallel ablaufendem Ligandenaustausch mit Cu4APc werden makroskopische Übergitter aus ITO-NCs hergestellt. Röntgenphotoelektronenspektroskopie (XPS), Röntgenkleinwinkelstreuung unter streifendem Einfall (GISAXS) und UV/Vis/NIR-Spektroskopie werden verwendet, um die chemischen Veränderungen der Oberfläche der Nanokristalle vor und nach Ligandenaustausch zu verfolgen und um ein detailliertes Bild der unterschiedlichen Komponenten zu erhalten, die die Oberflächenchemie dieses Materials dominieren. Es wird gezeigt, dass die halbleitenden Moleküle die ursprünglichen Liganden von der ITO Oberfläche größtenteils ersetzen und als Vernetzer zwischen benachbarten Partikeln fungieren. Transportmessungen weisen eine signifikante Erhöhung der elektrischen Leitfähigkeit auf und legen damit nahe, dass Cu4APc zu einer effizienten elektronischen Kopplung benachbarter ITO NCs führt. Dieses Material bietet die Möglichkeit, Ladungs- und Spintransport durch Phthalocyaninmonolagen zu untersuchen.

Im nächsten Schritt wird die Wahl des Metallzentrums von M4APc auf Cu, Co, Fe, Ni und Zn ausgedehnt. Diese Liganden sind in die Anordnung der ITO NCs integriert, und es werden Ladungsträgertransport sowie die Widerstands-abhängige Detektion von Dampf dieser hybriden Materialien untersucht. Die Variation des Metallzentrums ermöglicht es, systematisch den alleinigen Effekt der Höhe der Tunnelbarriere auf den Ladungstransport durch die Nanokristallanordnung zu untersuchen, während alle anderen Parameter konstant gehalten werden. Transportmessungen, die sich auf den Effekt des Metallzentrums des Liganden fokussieren, zeigen eine Liganden-abhängige Erhöhung der elektrischen Leitfähigkeit. Die resultierende I-V-Kennlinie und die Temperaturabhängigkeit Leitfähigkeit im Niedrigfeld deuten darauf hin, dass bei niedrigen Temperaturen Ladungstransport durch das Gitter durch eine Sequenz von inelastischen Ko-Tunnelereignissen erfolgt. Bei höheren

Temperaturen wird ein Übergang zum 3D Mott-VRH Mechanismus beobachtet. Die Empfindlichkeit der Chemosensoren, die aus ITO NCs Anordnungen bestehen, wird gegenüber Dämpfen untersucht, indem die Sensoren mit vier unterschiedlichen Analyten und Konzentrationen – bis hinab zu 100 ppm – beladen werden. Es zeigt sich durch Untersuchung verschiedener Analytenarten, dass das Material unterschiedliche Selektivitäten aufweist, die davon abhängen, ob sich die Analyten eher dampf- oder gasartig verhalten.

Zuletzt wird eine Vielzahl an Substraten (inerte, reaktive oder passivierte Metalle und Polymere) mit unterschiedlichen Austrittsarbeiten und Kopplungswechselwirkungen eingesetzt, um die elektronische Struktur der Substrat/PTCDA Grenzfläche mittels XPS, Ultraviolettphotoelektronenspektroskopie (UPS) und elektrostatischen Berechnungen zu untersuchen. Bei dicken PTCDA-Schichten werden, ohne eine Abhängigkeit von der Art des Substrates ausmachen zu können, nahezu unveränderte Elektronen- und Lochinjektionsbarrieren auf allen Substraten beobachtet. Für wenige Monolagen an PTCDA wird diese scheinbare universelle Fixierung des Ferminiveaus abhängig von der Natur des Substrats und der Filmdicke gestört. Dieses Verhalten wird mit einer großen induzierten Grenzflächenzustandsdichte erklärt. Durch Verwendung von standardmäßigen elektrostatischen Kalkulationsmodellen und durch Einführung von Erweiterungen zu bereits berichteten Herangehensweisen wird der Ursprung der universellen Fixierung des Ferminiveaus und dessen zugrundeliegender Mechanismus untersucht. Die Simulationsergebnisse demonstrieren, wie die Form der Zustandsdichte in der Nähe der Oberfläche einen Einfluss langer Reichweite auf Schlüsselparameter (z. Bsp. die Barriere der Ladungsträgerinjektion) des gesamten organischen Films hat.

Contents

Preface ... 3

Abstract ... 5

Zusammenfassung ... 7

Register of Symbols and Abbreviations ... 11

List of Publications and Conferences ... 16

Chapter 1 ... 18

Theory ... 18

1. Introduction ... 19

2. Charge Transport in Arrays of Metallic Nanoparticles ... 27

2.1. Coulomb Blockade ... 29

2.2. Metallic Regime ... 30

2.3. Insulating Regime ... 32

2.4. Coulomb Charging Energy ... 38

3. Charge Transport in Arrays of Semiconductors Nanocrystals ... 42

4. Photoelectron Spectroscopy (PES) ... 46

4.1. Electronic Structure at the Interface ... 47

4.2. Models for Interfaces Free of Gap states ... 50

4.2.1. Schottky-Mott Model ... 50

4.2.2. “Pillow” or “Push-Back” Effect ... 51

4.2.3. Integer charge transfer (ICT) Model ... 51

4.3. Models for Interfaces Dominated by Gap states ... 54

4.3.1. Interfaces Containing Chemisorption ... 54

4.3.2. Induced Density of Interface States ... 56

5. Summary of the Results ... 62

Chapter 2 ... 66

Surface Functionalization with Copper Tetraaminophthalocyanine Enables Efficient Charge Transport in Indium Tin Oxide Nanocrystal Thin Films ... 66

Chapter 3 ... 84

Tunable Charge Transport in ITO Nanocrystal Superlattices – Towards Sensing Applications ... 84

Chapter 4 ... 109

The Role of the Density of Interface States in Interfacial Energy Level Alignment of PTCDA ... 109

Chapter 5 ... 121

Collaborated Manuscripts ... 121

5.1. Collaborated Manuscript 1: Toward Conductive Mesocrystalline Assemblies: PbS Nanocrystals Cross-Linked with Tetrathiafulvalene Dicarboxylate ... 122

5.2. Collaborated Manuscript 2: Solution-Processed Two-Dimensional Ultrathin InSe Nanosheets ... 125

5.3. Collaborated Manuscript 3: Towards Photo-Switchable Transport in Quantum Dot Solids ... 128

5.4. Collaborated Manuscript 4: Structure, transport and photoconductance of PbS quantum dot monolayers functionalized with a copper phthalocyanine derivative ... 130

Appendix A 133
Appendix B 137
Appendix C 153
Acknowledgements 176
References 178

Register of Symbols and Abbreviations

$r_{cluster}$	Radius of cluster
γ	Surface energy per unit area
$\|\Delta G_V\|$	Gibbs free energy per unit volume
r_c	Critical radius
C_S	Supersaturation concentration of monomers
C_{min}	Minimum saturation concentration
G	Tunneling conductance
R_T	Resistance of a tunnel junction connecting two neighboring nanoparticle
α_N	Numerical constant
E_C	Coulomb charging energy
k_B	Boltzman constant
T	Temperature
g	Dimensionless inter-grain tunneling conductance
g_q	Quantum conductance
e	Elementary charge
h	Planck constant
g_{intra}	Intra-grain tunneling conductance
σ_0	Global sample conductivity
σ_D	Drude high-temperature conductivity
a	Particle radius
d_S	Dimensionality of the sample
τ_0	Time that the electron spends inside a nanoparticle
Γ	Characteristic energy / life time broadening
δ	Mean energy-level spacing
V	Volume of the grain
ν_F	Density of states at the Fermi energy
D_{eff}	Effective diffusion coefficient
g_c	Critical conductance
Δ_M	Gap in the electron excitation spectrum
ϵ_0	Vacuum permittivity
ϵ	Dielectric constant
V_t	Global Coulomb threshold voltage
β	Prefactor (0.2-0.5 depends on dimensionality and array geometry)
N	Number of nanoparticles spanning the gap between the electrodes
U	Activation energy
T_0	Characteristic temperature
T_{cross}	Crossover temperature

$\bar{c}$	Numerical coefficient ≈ 0.1
$P(r)$	Hopping probability
ξ	Localization length
r^*	Typical hopping length
r	Hopping length
d	Center-to-center interparticle distance
j	Number of tunnel junctions involved in cotunneling process
E	Electrostatic energy related to the electron-hole pair
C	Numerical constant ($C \sim 2.8$ for three-dimension)
g_0	Conductivity pre-exponential factor
N_{cot}	Optimal number of cotunneling events
V_{jct}	Voltage drop over a single tunneling junction connecting two neighboring nanocrystals
V^*	Characteristic voltage
α	Power law exponent
C_{NP}	Capacity of the nanoparticle
C_0	Self-capacitance of an isolated nanoparticle
s	Length of the tunnel barrier / edge-to-edge interparticle spacing
C_Σ	Total capacitance
C_{inter}	Inter-nanocrystal capacitance arising from nearest-neighbor interactions
C_{nn}	Pairwise capacitance between two neighboring nanocrystals
σ	Resistivity
ΔE	Energy difference
D	Diameter of nanoparticles
ε_{NC}	Internal dielectric constant
a_B	Effective electron Bohr radius
m	Effective electron mass
N_i	Number of donors
$E_i^{(f)}$	Highest filled electron level
$E_i^{(e)}$	Lowest empty electron level
$E_Q(n)$	Energy of n^{th} lowest electron
κ	Effective dielectric constant of the NCs array
κ_{NC}	Internal dielectric constant of the NC
κ_i	External dielectric constant of the insulator in which NC is embedded
f	Volume fraction occupied by the NCs
E_A	Activation energy
ν	Average number of electrons per NC
λ	Inelastic mean free path of the electrons
$h\nu$	Photon energy of the excitation source
E_b	Binding energy of the electron referenced to the vacuum level
E_k	Kinetic energy of the electron

E_F	Fermi level
E_{vac}	Vacuum level
$E_{cut\text{-}off}$	Secondary electron cut-off
Φ_M	Electrode work function
IP	Ionization potential
IE	Ionization energy
EA	Electron affinity
Δ	Interface dipole
Φ_{HIB}	Hole injection barriers
Φ_{EIB}	Electron injection barriers
D_{is}	Density of interface gap states
E_{CNL}	Charge neutrality level
S	Interface parameter
$\delta_{org/metal}$	Effective organic semiconductor/metal distance
E_{ICT+}	Energy of a positive integer charge-transfer state
E_{ICT-}	Energy of a negative integer charge-transfer state
Φ_{sub}	Substrate work function
μ	Chemical potential
μ_{sub}	Chemical potential of a metal
μ_{org}	Chemical potential of an organic molecule
ΔN	Amount of electronic charge transfer
η	Absolute hardness
Γ_i	Energy broadening for each molecular orbital
E_i	Energy for each molecular orbital
Δ^T	Total dipole at the metal/organic interface
Δ^p	Contribution to the dipole due to the "pillow" effect
Δ^{mol}	Dipole generated due to the molecule's permanent dipolar moment
A	Interface area of the molecule
$d_{metal/mol}$	Distance between the molecule and the metal substrate
$\Delta_{OO}{}^T$	Total dipole at the organic/organicinterface
S_{OO}	Screening parameter for organic heterojunction
x	Distance from the substrate
Δx	Distance between organic monolayers / distance between stacking planes
$\rho(x)$	Charge density
n	Number of molecules per unit area and per discretization interval Δx
$f_H(E)$	Fermi functions for HOMO energy level
$f_L(E)$	Fermi functions for LUMO energy level
$V(x)$	Electrostatic potential at the position x from the substrate
$D_H[E+eV(x)]$	Energy distributions of HOMO-derived levels
$D_L[E+eV(x)]$	Energy distributions of LUMO-derived levels

E_H	HOMO peak maximum
E_L	LUMO peak maximum
σ_H	Standard deviation of HOMO peak
σ_L	Standard deviation of LUMO peak
ε_0	Vacuum permittivity
R	Resistance
R_s	Sheet resistance
L	Length of the channel
w	Width of the channel
R_0	Baseline Resistance
α_c	Material-/temperature-specific coefficient
K_b	Binding Constant
C_i	Concentration of the photoelectron emitting atom/ion *i*
J_i	X-ray flux striking the analyzed area
F_i	Sensitivity factor of element *i*
$\alpha_{pc(i)}$	Photoelectron cross section of *i*
k_f	Combined instrument factor
λ_{SiO2}	Photoelectron effective attenuation length in the oxide film
α_A	Photoelectron take-off angle
I_{SiO2}	Si 2p core level intensity of the oxidized silicon film
I_{ox}	Al 2p core level intensity of the aluminum oxide layer
I_{Al}	Al 2p core level intensity of the aluminum sublayer
n_i	Volume density of electron-emitting atom *i*
θ	Electron off-axis angle with respect to the surface normal
NCs	Nanocrystals
QDs	Quantum Dots
SPR	Surface Plasmon Resonance
FET	Field-Effect Transistor
LED	Light- Emitting Diode
PVCs	Photovoltaic Cells
2D	Two-Dimensional
3D	Three-Dimensional
VRH	Variable-Range Hopping
ES-VRH	Efros-Shklovskii Variable-Range Hopping
NNN	Nearest-Neighbor-Number
DOGS	Density of Ground States
CG	Coulomb Gap
PES	Photoelectron Spectroscopy
XPS	X-ray Photoelectron Spectroscopy
UPS	Ultraviolet Photoelectron Spectroscopy

HOMO	Highest Occupied Molecular Orbital
LUMO	Lowest Unoccupied Molecular Orbital
ICT	Integer Charge Transfer
DFT	Density Functional Theory
MIGS	Metal-Induced Gap States
IDIS	Induced-Density of Interface States
FWHM	Full Width at Half Maximum
IPES	Inverse Photoemission Spectroscopy
ITO	Indium Tin Oxide
M4APc	Metal 4,4′,4″,4‴-tetraaminophthalocyanine
GISAXS	Grazing-Incidence Small-Angle Scattering
UV–vis–NIR	Ultraviolet–Visible–Near Infrared
ODE	Octadecene
MA	Myristic Acid
ODA	Octadecylamine
STEM	Scanning Transmission Electron Microscopy
DMSO	Dimethyl Sulfoxide
XRD	X-ray Diffraction
OPE	Oligo(phenylene ethylene)
4M2P	4-methyl-2-pentanone
IC	Inelastic Cotunneling
TLM	Transmission Line Method
LSPR	Localized Surface Plasmon Resonance
Pc	Phthalocyanine
OSC	Organic Semiconductor
DOS	Density of States
TTFDA	Tetrathiafulvalene Dicarboxylate
COIN	Coupled Organic-Inorganic Nanostructure
GIXD	Grazing Incidence X-ray Diffraction
P3HT	Poly(3-hexylthiophene)
AFM	Atomic Force Microscopy
ED	Electron Diffraction
IMFP	Inelastic Mean Free Path
DTCP	1,2-Bis(5′-carboxy-2′-methylthien-3′-yl)-cyclopentene
UHV	Ultra-High Vacuum

List of Publications and Conferences

Journal Papers

1- **Mahdi Samadi Khoshkhoo**, Yvonne Joseph, Santanu Maiti, Frank Schreiber, Thomas Chassé, and Marcus Scheele, "Tunable Charge Transport in ITO Nanocrystal Superlattices – Towards Sensing Applications", *Advanced Materials Interfaces*, **2018**, *116*, 1701623. doi: 10.1002/admi.201701623.

2- **Mahdi Samadi Khoshkhoo**, Heiko Peisert, Thomas Chassé, Marcus Scheele, "The Role of the Density of Interface States in Interfacial Energy Level Alignment of PTCDA", *Organic Electronics*, **2017**, 49, 249-254. doi: 10.1016/j.orgel.2017.06.065

3- **Mahdi Samadi Khoshkhoo**, Santanu Maiti, Frank Schreiber, Thomas Chassé, and Marcus Scheele, "Surface Functionalization with Copper Tetraaminophthalocyanine Enables Efficient Charge Transport in Indium Tin Oxide Nanocrystal Thin Films", *ACS Applied Materials & Interfaces*, **2017**, 9, 14197-14206. doi: 10.1021/acsami.7b00555

4- Alexander André, Christoph Theurer, Jannika Lauth, Santanu Maiti, Martin Hodas, Mahdi **Samadi Khoshkhoo**, Sachin Kinge, Alfred J. Meixner, Frank Schreiber, Laurens Siebbeles, Kai Braun and Marcus Scheele, "Structure, transport and photoconductance of PbS quantum dot monolayers functionalized with a Copper Phthalocyanine derivative", *Chemical Communications*, **2017**, 53, 1700-1703. doi: 10.1039/C6CC07878H

5- Christine Schedel, Robert Thalwitzer, **Mahdi Samadi Khoshkhoo**, Marcus Scheele, "Towards Photo-Switchable Transport in Quantum Dot Solids", *Zeitschrift für Physikalische Chemie*, **2017**, 231, 1, 135-146. doi: 10.1515/zpch-2016-0863

6- Jannika Lauth, Friederieke E. S. Gorris, **Mahdi Samadi Khoshkhoo**, Thomas Chassé, Wiebke Friedrich, Vera Lebedeva, Andreas Meyer, Christian Klinke, Andreas Kornowski, Marcus Scheele, Horst Weller, "Solution-Processed Two-Dimensional Ultrathin InSe Nanosheets", *Chemistry of Materials*, **2016**, 28, 1728-1736. doi: 10.1021/acs.chemmater.5b04646

7- Alexander André, Danylo Zherebetskyy, David Hanifi, Bo He, **Mahdi Samadi Khoshkhoo**, Maciej Jankowski, Thomas Chassé, Lin-Wang Wang, Frank Schreiber, Alberto Salleo, Yi Liu, Marcus Scheele, "Toward Conductive Mesocrystalline Assemblies: PbS Nanocrystals Cross-Linked with Tetrathiafulvalene Dicarboxylate", *Chemistry of Materials*, **2015**, 27, 8105–8115. doi: 10.1021/acs.chemmater.5b03821

Conference Papers

1- **Mahdi Samadi Khoshkhoo**, Santanu Maiti, Frank Schreiber, Thomas Chassé, and Marcus Scheele, "Tunable Charge Transport by Multiple Inelastic Cotunneling in ITO Nanocrystal Superlattices", *nanoGe September Meeting 2017*, Barcelona, Spain, 4-8th September, **2017**.

2- **Mahdi Samadi Khoshkhoo**, Santanu Maiti, Frank Schreiber, Thomas Chassé, and Marcus Scheele, "Efficient Charge Transport by Multiple Inelastic Cotunneling in Indium Tin Oxide Nanocrystal Thin-Films Functionalized with M-Tetraaminophthalocyanine (M = Cu, Co, Fe, Ni, Zn)", *NaNaX8 – Nanoscience with Nanocrystals*, Braga, Portugal, 3-7th July, **2017**.

3- **Mahdi Samadi Khoshkhoo**, Santanu Maiti, Frank Schreiber, Thomas Chassé, and Marcus Scheele, "Quasi- 2 D Monolayers of Plasmonic Nanocrystals Cross-Linked by Phthalocyanines – A New Playing Field for Molecular Electronics", *2017 MRS Spring Meeting & Exhibit*, Phoenix, Arizona, United States, 17th – 21st April, **2017**.

4- **Mahdi Samadi Khoshkhoo**, Marcus Scheele "Indium Tin Oxide Nanocrystals Cross-Linked with Organic Semiconductors as a Solution-Processable Transparent Electrode", *Gordon Research Conference (GRC) and Gordon Research Seminar (GRS) on Colloidal Semiconductor Nanocrystals*, Mount Snow, West Dover, VT, United States, 30th July – 5th August **2016**.

5- Alexander André, **Mahdi Samadi Khoshkhoo**, Marcus Scheele "Coupled Organic-Inorganic Nanostructures: Toward Conductive Mesocrystalline Assemblies", *Gordon Research Conference (GRC) on Colloidal Semiconductor Nanocrystals*, Mount Snow, West Dover, VT, United States, 31st July – 5th August **2016**.

6- Alexander André, **Mahdi Samadi Khoshkhoo**, Michelle Weber, Marcus Scheele, "Conductive PbS Mesocrystals", *2016 MRS Spring Meeting & Exhibit*, Phoenix, Arizona, United States, 28th March – 1st April, 2016.

7- **Mahdi Samadi Khoshkhoo**, Heiko Peisert, Thomas Chassé, Marcus Scheele, "The role of Induced Density of Interface States in the Interfacial Energy Level Alignment of PTCDA", *80th Annual Meeting of the DPG and DPG Spring Meeting*, Regensburg, Germany, 6-11 March **2016**.

8- Jannika Lauth, Friederieke E. S. Gorris, **Mahdi Samadi Khoshkhoo**, Thomas Chasse, Wiebke Friedrich, Vera Paulava, Andreas Meyer, Andreas Kornowski, Christian Klinke, Marcus Scheele, Horst Weller, "Tailoring 2D Materials by Colloidal Means: Ultrathin InSe Nanosheets", *2015 MRS Spring Meeting & Exhibit*, San Francisco, California, United States, 6-10 April, **2015**.

9- Alexander André, **Mahdi Samadi Khoshkhoo**, David Hanifi, Zheng Liu, Yi Liu, Marcus Scheele, "Structural, Optical and Size-Dependent Transport Properties of PbS Quantum Dot Solids Coupled to Small Molecular Organic Semiconductors", *2015 MRS Spring Meeting & Exhibit*, San Francisco, California, United States, 6-10 April, **2015**.

10- Alexander André, **Mahdi Samadi Khoshkhoo**, Marcus Scheele, "Coupled organic-inorganic nanostructures: Size dependent carrier transport in tetrathiafulvalenedicarboxylate capped PbS nanocrystals", *79th Annual Meeting of the DPG and DPG Spring Meeting*, Berlin, Germany, 15-20 March **2015**.

Chapter 1

Theory

1. Introduction

Colloidal semiconductor nanocrystals (NCs) have recently gained substantial attention as promising building blocks for advanced materials and devices. [1-6] They are usually constituted of hundreds to thousands of atoms and exhibit unique properties due to their shape-/size-tunable electronic, magnetic, and optical properties, ease of fabrication and solution processability. The unique optoelectronic properties of NCs are a result of the electron confinement [7] in their small nanostructures that was discovered over 30 years ago. [8-11] They also contain a high concentration of surface atoms which leads to properties greatly different from their bulk counterparts due to the dominant role of the interface. For instance, dangling bonds can introduce new electronic states and modify the electronic structure of NC, or the energy and reactivity of the crystal surface can be substantially altered by changing the surfactant or ligand molecules.

Quantum dots (QDs), which are NCs composed of semiconducting materials, are a well-known example of the systems that show a strong size-dependence optical and electronic properties. [1-6] For instance, the fundamental gap between valance and conduction band in these NCs is strongly affected by changing the size of QDs which leads to different fluorescent wavelengths. [12-14] The properties of NCs can be also strongly affected by their shape. This is due to the confinement of the motion of electrons, holes and plasmons in a certain direction. Two examples are: (i) the shape-dependence of the catalytic activity and selectivity of metal nanoparticles, [15-18] as well as (ii) the strong dependence of the energy and position of the surface plasmon resonance (SPR) peak in Au NCs. [19] Currently, NCs with different geometries such as nanorods, nanoplatelets, and various core-shell structures (e.g. dot-in-dots, dot-in-rods, rod-in-rods, and dot-in-plates) can be easily obtained using different techniques. [13-14, 20-26] NCs already play an important role in field-effect transistors (FETs), lasers, light- emitting diodes (LEDs), catalysis, photodiodes and photovoltaic cells (PVCs), photodetectors, as well as in biological sensing and imaging applications, [1-6, 27-34] and important perspectives in future nano-electronic and nano-optoelectronic devices are expected.

Different approaches have been investigated to synthesized two-dimensional (2D) nanostructures which can be classified into two categories: [1] (i) the top-bottom approaches which include chemical or mechanical exfoliation and the Scotch-type method [35-40] and (ii) bottom-up techniques that comprise lithography, physical deposition methods, and wet chemical approaches. [1, 41-44] Among these various techniques, the wet chemical methods (that has been also used in Chapter 2 and 3) have always attracted a great deal of researches due to advantages such as easy and straightforward implementation with relatively low costs as well as the flexibility of the method in order to scale-up for mass production. However, the wet chemical growth approaches have also some drawbacks e.g. the difficulty to precisely control the size and shape of the NCs. The first synthesis of nearly monodisperse semiconductor NCs by a hot injection method was reported in 1993. [45] In General, synthesizing of the NCs using wet chemical approaches needs the following three main constituents: [1] (i) precursors that play the role of atom providers in the crystal growth process, (ii) ligand or surfactant molecules which form a capping layer, stabilize the grown NCs in the solution medium (by screening the crystals from the environment via steric and/or electrostatic stabilization), and has a crucial role in controlling the size and shape of the NCs, and (iii) a solvent medium which can both dissolve the precursors and stabilize the synthesized NCs in order to provide a reaction medium. These three parameters as well as the synthetic parameters (e.g. reaction time or temperature) provide ample degrees of freedom to explore the effect of each on size and shape of NCs, and hence, on the final optoelectronic properties. Good control over the mentioned factors gives us the possibility to synthetize high-quality crystalline monodisperse particles with well-defined size and shape. [46]

The synthesis of NCs using solution-based techniques includes two important steps which are playing significant roles: nucleation and growth. In the nucleation phase, decomposition or rearrangement of precursors provides monomers, and thus, forms nuclei. At this stage, the factors such as temperature and interfacial tension as well as the degree of supersaturation in solution are significantly determinative. [47] The fresh nuclei, then, start to grow and form bigger NCs by (i) addition of the monomers supplied by decomposition of precursors, (ii) coalescence of individual nuclei, and/or (iii) diffusion of monomeric precursor from smaller to larger NCs as a consequence of a difference in chemical potential which is known as Ostwald ripening. [48-49] It is worth pointing out that according to the diffusion-controlled growth model, [50] the NC growth rate is inversely proportional to its radius. This means that smaller NCs tend to grow faster than larger NCs which acts in the opposite direction to Ostwald ripening. In fact these two phenomena are competing effects during the growth process. The first effect is known as focusing effect while the latter one is called defocusing effect. Thus, one can deduce that in order to produce monodisperse colloidal NCs, a rapid nucleation is required in the first stage as well as a diffusion-limited growth in the following. [45, 51-52] There exists a critical radius, depending on the degree of supersaturation, above which the formed particle become stable. When the average radius of the NCs is below the critical radius, the focusing effect is prevailing, which narrows the size distribution of the system; however, exceeding of the average NC radius over the critical radius leads to a dominating defocusing effect, which broadens the size distribution of the NCs.

In the colloidal approach towards the synthesis of NCs, two kinds of nucleation processes can be distinguished: (i) A homogeneous nucleation which occurs spontaneously and randomly in the liquid phase of the dissolved, supersaturated precursor and (ii) A heterogeneous nucleation that happens at an already existing nucleation site at the phase boundaries between the solid-state nucleus and the liquid phase. The process of nucleation and growth can be theoretically described using the LaMer model which provides worthwhile insights. [53] LaMer proposed this model based on theoretical works by Becker and Döring. [54] The central idea in this model is based on a minimization of the Gibbs free energy in a thermodynamic system. In the case of colloidal solutions and for spherical particles the Gibbs free energy can be expressed as follows: [53]

Equation 1

$$\Delta G = -\frac{4}{3}\pi {r_{cluster}}^3|\Delta G_V| + 4\pi {r_{cluster}}^2\gamma.$$

Here $r_{cluster}$ is the radius of the cluster, γ is the surface energy per unit area, and $|\Delta G_V|$ is the Gibbs free energy per unit volume. The parameter γ can be also considered as the energy needed to create a surface of unit area. In the above equation, the first term corresponds to the volume energy and the second term relates to the change in surface energy. Accordingly, on the one hand, the formation of a bond between a decomposed precursor and the cluster, tends to decrease the Gibbs energy by decreasing the volume energy (negative term), which is a favorable event. On the other hand, this invokes an increase of the Gibbs free energy by increasing the surface energy (positive term), which is an unfavorable event. Therefore, the final change in the Gibbs energy is the outcome of competition between these two events. By setting the derivative of Equation 1 to zero, Polte [55] calculate a critical radius, $r_c = 2\gamma|\Delta G_V|$, above which the absolute value of the first negative term is higher than the second, and thus, the growth process is favored as the Gibbs free energy is decreasing. Below the critical radius, the contribution of the first positive term is higher which pushes the system toward dissolution in order to minimize the Gibbs free energy. The evolution of the Gibbs free energy for a cluster versus its size is schematically indicated in Figure 1. The blue curve is the contribution of the first term of Equation 1 and corresponds to the bulk free energy that is decreased by increasing the radius of the cluster. The contribution of the second term, the red curve, to the free energy is related to the surface energy and continuously increases by increasing the radius of the cluster. The black curve, which is the result of the competition between these two contributions, illustrates that by increasing the cluster size, the Gibbs free energy is increasing up to a critical radius and then starts to decrease (so the stable clusters can be formed; the nuclei).

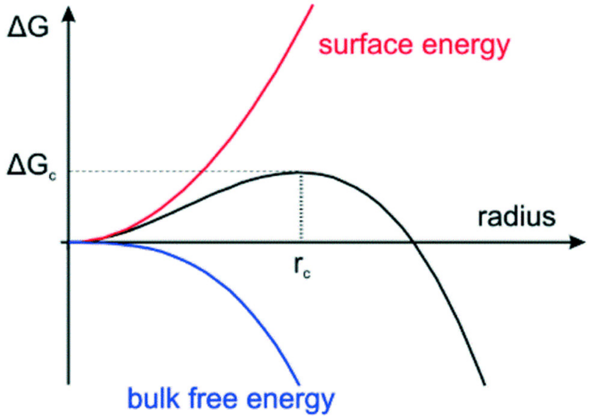

Figure 1. The evolution of bulk free energy, surface energy, and Gibbs free energy for a cluster versus its size adapted with permission from ref. [55] (Copyright 2017 The Royal Society of Chemistry).

Nucleation at phase boundaries is, in fact, easier than homogenous nucleation because the required surface energy is lower for the first kind of nucleation. Therefore, once stable clusters are formed in the solution, subsequent nucleation will preferentially take place at phase boundaries; however, homogeneous nucleation can still happen in the same time. In a conventional synthesis procedure, first the concentration of the monomers is increased either by increasing the temperature of the reaction (in order to decompose and activate the precursors) or by fast injection of precursors into the reaction medium (see Figure 2). This increase continues up to the point where it reaches to the supersaturation concentration of monomers, C_S. At this point, the system is potentially capable to start homogeneous nucleation; however, there still exists an energy barrier, which needs to be overcome. In the second phase, by further increasing the saturation, the system reaches a minimum saturation concentration, C_{min}, at which the system can overcome the energy barrier and homogeneous nucleation can happen. In this phase, the nucleation process is very fast and sometimes referred to as “burst nucleation”. Here, the idea is to separate the nucleation and growth steps, so that all the nuclei form simultaneously at the same time and then let them grow later preferably without any further nucleation. In an ideal case, this leads to the formation of high-quality, monodisperse NCs. In the final phase of the synthesis, homogeneous self-nucleation rapidly consumes the monomers and the concentration drops below the minimum saturation concentration. Hence, further homogeneous nucleation stops and the remaining monomers are consumed by heterogeneous nucleation at the phase boundaries leading to the growth of clusters.

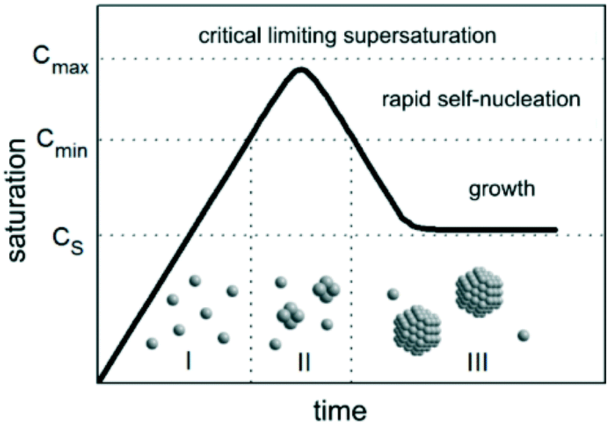

Figure 2. The evolution of monomer concentration versus time in a conventional colloidal synthesis procedure adapted with permission from ref. [55] (Copyright 2017 The Royal Society of Chemistry).

In order to make use of colloidal NCs in practical devices, preparation of a high-quality thin-film of NCs with device relevant thickness is necessary. Among various techniques reported in the literature, self-assembly methods are very promising in order to prepare long-range-ordered nanocrystals superlattices. [3, 6, 56-63] In this context, the superlattice is defined as an array of inorganic nanocrystals which are separated by organic or inorganic surface ligands. Several methods can be used in order to encourage an ensemble of colloidal NCs to form ordered superlattices within the framework of self-assembly. In general, they can be obtained either by the evaporation of solvent, destabilization of NC solution, or gravitational sedimentation. [3]

NC superlattices prepared by evaporation-based techniques can be obtained by: (i) drop casting of a colloidal solution on a solid support, [64-65] (ii) evaporation of the solvent from NCs solution in a tilted vial, [66] (iii) evaporation of the solvent from a colloidal solution of NCs over a polar liquid in a Teflon chamber, [67] and (iv) evaporation of the solvent from a solution of NCs over polar liquid sessile droplet. The first method is based on drop casting a small volume of dilute NC solution on a solid substrate. Over time, the solvent starts to dry and the droplet becomes more and more concentrated over a couple of minutes. This method can finally lead to the formation of a thin-film superlattice, the thickness of which is governed by the concentration of the primary solution. The second approach is principally analogous to the first method but the inclined sample position prevents solvent trapping under the thin-film superlattice and greatly improves the drying procedure of the deposited film. In the third method, the evaporation of the solvent of the NC solution occurs when the colloidal solution is placed over an immiscible liquid phase. Here, two-dimensional superlattice thin-film with the thickness from one monolayer to several unit cell thick film with a typical grain size of hundreds of micrometer can be formed. [68] The factors which determine the thickness of the superlattices include the concentration of the solution as well as the area of the liquid subphase. This method has been used in Chapter 2 and 3 to prepare macroscopic superlattices of ITO NCs. The mechanism in the fourth method is in essence very similar to the previous one except for the geometry of the system.

Destabilization-based techniques are usually used to prepare three-dimensional closed-packed superlattices. This method is based on inducing slow clustering of NCs using their attractive interactions, which occur when the interaction between solvent and the NC capping layer become less favorable than ligand-ligand interaction between neighboring NCs. In practice, it can be accomplished by: (i) controlled transfer of a layer of nonsolvent on top of a NC colloidal solution, [69-70] (ii) slow heating of a solvent/nonsolvent mixture to evaporate the low-boiling solvent and enrich the mixture with higher-boiling nonsolvent [71] and/or (iii) inducing solvophobic interactions by disrupting a surfactant bilayer. [72-73]

Similar to the synthesis of NCs, NC superlattice formation also includes two important steps: nucleation and growth. [3] Along the same lines, two kinds of nucleation can exist in this process, which are homogeneous and heterogeneous nucleation. The former one takes place in the solution phase, it is a slow process and needs to overcome an energy barrier, while the latter is significantly faster than homogeneous nucleation and occurs near an interface. Reducing the energy barrier in homogeneous nucleation can be accomplished by [3] (i) reducing the quality of the solvent by slow addition of nonsolvent, and/or (ii) increasing the volume fraction of NCs by slow evaporation of the solvent; both of them increases the nucleation rate. Following the nucleation stage, growth proceeds by addition of NCs from solution, thus, the speed of this stage is determined by the availability of NCs in the solution as well as the energetics of surface defect formation. In destabilization-based techniques, multiple nucleation happens in the bulk solution, leading to the formation of many crystal domains. [74] The formed superlattice domains move more slowly in solution in comparison to free individual NCs or smaller domains, and hence, cannot completely coalesce. At some point, they start to sediment in the bottom of the container and densify. On the other hand, in evaporation-based self-assembly approaches, nucleation occurs under 2D confinement, leading to polycrystalline thin-films at the air-liquid interface. [64] The structure might be improved and finally turn into a single crystal thin-film by self-healing and defect repair under slow-enough evaporation rate of the solvent as well as having sufficient time. [75]

Among different classes of structures, arrays of few monolayers of NCs connected via organic ligands have recently attracted significant attention due to their numerous novel emerging applications. [76-77] The architecture of these devices include inorganic NCs connected to each other through organic bridges. These nanostructures have demonstrated variable sensitivity and selectivity utilizing different linker molecules which make them promising for developing artificial noses and multivariable sensors. [78-81] The first utilization of organic-capped nanoparticles for gas sensing purposes was reported around twenty years ago. [82] The attractiveness of functionalized NCs in sensing applications arises from the affinity of these nanostructures to different classes of gas and vapor analytes as well as the ability to produce NCs with different functional groups. Currently, the biggest limitation of NCs, prohibiting them to be advanced in practical uses in sensing applications, is the stability problem. Their operational temperature range as well as the range of detectable compounds by such nanostructures also need to be further improved. Arrays of metallic nanoparticles have been the most common systems, which are explored for sensing purposes among which Au, Ag, Pt, Pd, and Ni nanoparticles are the well-studied cases. [82-86] The choice of different metal compounds allows us to engineer the surface of nanoparticles and functionalize them with various and desired functional groups.

The mechanism of vapor sensing in arrays of nanoparticles involves the variation of the interparticle distance and the dimension of the capping layer upon analyte absorption as well as the change in dielectric constant of the nanoparticles' environment. [87-89] In arrays where soft ligands separate nanoparticles from each other, the adsorption of analyte can considerably affect the interparticle distance by changing the dimension length and geometry of capping organic molecules. In contrast, for the arrays of nanoparticles functionalized with rigid ligands, the interparticle spacing is not so sensitive to analyte adsorption; however, the charge transport can be still highly affected by a change in the dielectric constant of the environment. [90] In order to understand the sensing mechanism in such these nanostructures in more detail, a fundamental understanding of charge transport in NCs arrays containing hybrid molecule-nanoparticle junctions is of particular relevance. Moreover, due to the extreme importance of the surface and interface in systems containing NCs, a detailed understanding of the surface chemistry as well as the energy level alignment at the interface is necessary. Two important and fundamental techniques to investigate these properties are temperature-dependent transport measurements and photoelectron spectroscopy, the theory of which will be the subject of discussion in the next sections. At the end of this chapter, short summaries of the results of the present dissertation are also given while detailed discussions and experimental procedures can be found in the following respective chapters.

2. Charge Transport in Arrays of Metallic Nanoparticles

Arrays of metallic nanoparticles are artificial solids that consist of metallic nanoparticles of a size ranging from a few to hundreds of nanometers embedded in a dielectric matrix. They are often viewed as artificial atoms as they possess a distinct electronic structure. Using different organic or inorganic capping ligands provides the possibility to connect and regulate the coupling between the nanoparticle building blocks, while altering their size and shape makes it possible to regulate the quantum confinement effects. Depending on the strength of electron coupling between neighboring metallic nanoparticles, the transport behavior of the array represented by the tunneling conductance G, can be tuned to exhibit the full range from insulating (strong exponential) to a metallic (weak non-exponential) temperature dependence of the conductance which makes them ideal systems for studying metal-insulator transitions. Within the approach of perturbation theory for the conductance of granular systems, the lowest order contribution to the overall conductance of the array arises from tunneling between neighboring particles. At high temperatures, this contribution scales with the junction resistance as $G \propto 1/R_T$ (R_T is the resistance of a tunnel junction connecting two neighboring nanoparticle). In the low temperature regime, the sequential contribution to the conductance decreases exponentially as $G \propto exp(-\alpha_N E_C/k_B T)/R_T$ (where α_N is a numerical constant depending on the structure of the network, E_C is the Coulomb charging energy, k_B stands for Boltzman constant, and T is the Temperature). Here, a dimensionless conductance corresponding to one spin component, g, is introduced which is measured in the unit of quantum conductance ($g_q = e^2/h$, where e is the elementary charge and h is Planck's constant) to make future discussions more convenient: $g = G/(2e^2/h)$. A material is termed "granular" if inter-grain tunneling conductance, g, is much smaller than the intra-grain tunneling conductance, g_{intra} (which is caused by scattering by impurities or grain boundaries). In the regime of strong coupling where $g > 1$, electrons tunnel easily from nanoparticle to nanoparticle and the arrays behave metallic, while in the weak coupling regime, $g < 1$, the arrays mimic the behavior of an insulator. In the latter regime, Coulomb correlation and quantum interference effects may play significant roles in low-conducting samples.

In the following, a summary of theoretical results on the conductivity of granular materials is presented which mainly follows a review by Beloborodov *et al.* [91] as well as theoretical textbooks. [92-94] This section is kept as short as possible in order to provide the necessary background information. Furthermore, in order to provide a brief outlook to the theoretical sections, the most important equations are categorized and summarized in Table 1.

Table 1. A brief outlook to the theoretical part summarizing the most important equations.

			Conductivity/Conductance	Description	Section
Arrays of Metallic Nanoparticles	**Metallic Regime**		$\sigma_0 = 2e^2 v_F D_{eff}$	The classical conductivity for a periodic cubic granular array in the regime of strong coupling and at high enough temperatures.	Sec. 2.2 Page 31
			$\sigma_0^C = \sigma_0 \left(1 + \frac{\delta\sigma_1}{\sigma_0} + \frac{\delta\sigma_2}{\sigma_0}\right)$	The conductivity corrected based on the electron-electron interactions and the quantum interference effects.	Sec. 2.2 Page 31
	Insulating Regime	*Arrhenius behavior characteristic*	$g(T) = g_0 exp[-E_c/k_B T]$	The exponential suppression of the conductance for nanoparticle arrays in the semi-classical Coulomb blockade regime in the zero-bias limit.	Sec. 2.3 Page 33
			$g(T) = g_0 exp[-U/k_B T]$ $(U \approx 0.2E_C)$	The exponential suppression of the conductance for 2D close-packed arrays in which the optimal path can avoid high charging energy costs by branching.	Sec. 2.3 Page 34
		Multiple Inelastic Cotunneling (IC)	$g(T) = g_0 \exp(-\sqrt{T_0/T})$	Cooperative multi-electron process can transport charges over distances of several grains in the case of closely packed nanoparticles array.	Sec. 2.3 Page 36
Arrays of Semiconductors Nanocrystals		*Arrhenius behavior*	$g(T) = g_0 \exp(-E_c/k_B T)$	In an ideal case where all NCs are neutral, the density of ground states of NCs, has a width of $2E_C$ centered at the electron Fermi level and, thus, the resistivity follows the Arrhenius law.	Sec. 3 Page 42
		Variable-range hopping (VRH)	$g(T) = g_0 \exp(-(T_0/T)^{1/2})$	For Efros-Shklovskii (ES) or Coulomb Gap (CG) variable-range hopping (VRH) due to the presence of strong disorder in NCs array. It is observed when the long-range Coulomb potential is not screened in the system.	Sec. 3 Page 42
			$g(T) = g_0 \exp(-(T_0/T)^{1/3})$	For two-dimensional (2D) Mott variable-range hopping (VRH) due to the presence of strong disorder in NCs array. It is observed when the density of ground states of the system is constant near the Fermi Level.	Sec. 3 Page 42
			$g(T) = g_0 \exp(-(T_0/T)^{1/4})$	For three-dimensional (3D) Mott variable-range hopping (VRH) due to the presence of strong disorder in NCs array. It is observed when the density of ground states of the system is constant near the Fermi Level.	Sec. 3 Page 42

2.1. Coulomb Blockade

The single-particle Coulomb charging energy, E_C, is one of the most important parameters in systems consisting of arrays of nanoparticles and plays a vital role for the transport properties of arrays in the insulating regime. The energy E_C can lead to a hard gap in the density of states at the chemical potential, which can hinder charge transport. This energy is defined as the energy needed to add/remove an electron onto/from a neutral grain and plays a central role in the theory. Consider a single grain in contact with a metallic reservoir. In the regime of weak coupling, the electrons cannot freely move and exchange between the grain and the metallic reservoir, and thus, the charge on the grain is almost quantized. However, in the regime of strong coupling, the effect of charge quantization is negligible. This behavior is well-known as the Coulomb blockade phenomenon and extensively discussed in the literature. [95-97] The transport properties of arrays of nanoparticles are strongly affected by Coulomb interactions. Analogously, in arrays of inter-connected metallic nanoparticles, when the grains are strongly coupled, the Coulomb interaction is screened and charges can propagate easily; however, in the regime of weak coupling, charges on each grain become quantized and the electrons have to overcome an electrostatic barrier on the order of E_C in order to hop onto a neighboring nanoparticle. [98] Figure 3 schematically represents the spherical NCs with diameter D, core-to-core interparticle distance d, radius a, and edge-to-edge interparticle spacing s which are covered by organic ligands and arranged in a crystalline lattice. The black arrow shows an electron hopping from one NC to its neighbor leaving a hole behind. The simplified circuit diagram between two NCs is also represented in Figure 3. The charging energy, E_C, related to the capacity of the nanoparticle C_{NP} and the resistance of a tunnel junction connecting two neighboring NCs, R_T. If the thermal energy is lower than the charging energy, the Coulomb energy barrier prohibits the sequential tunneling process (Coulomb blockade). [99] When the Coulomb blockade regime dominates, charge transfer can still occur via “cotunneling”, [100] which will be discussed in detail in the next sections.

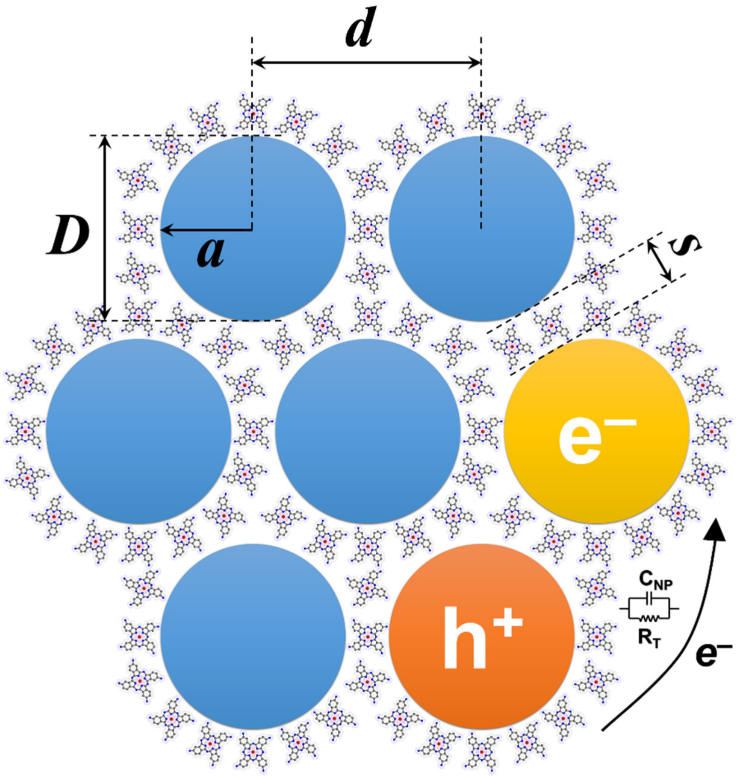

Figure 3. Schematic representation of the spherical NCs with diameter D, core-to-core interparticle distance d, radius a, and edge-to-edge interparticle spacing s which are covered by organic ligands and arranged in a crystalline lattice. The charging energy, E_C, related to the capacity of the nanoparticle C_{NP} and the resistance of a tunnel junction connecting two neighboring NCs, R_T.

2.2. Metallic Regime

As mentioned earlier, the tunneling conductance, g, is the key parameter that determines the transport properties in arrays of metallic nanoparticles. For a periodic cubic granular array in the regime of strong coupling and at high enough temperatures, the global sample conductivity, σ_0, is described by the classical Drude formula:

Equation 2 $$\sigma_0 = 2e^2 g a^{2-d_S},$$

where a is the size of the nanoparticles and d_S is the dimensionality of the sample. This equation is valid for the grains in which the electron motion is chaotic. Upon hopping from one nanoparticle to another one, the momentum of the electron is not conserved and thus leads to the finite conductivity given in Equation 2.

In the metallic regime, the time τ_0 that the electron spends inside a nanoparticle as well as the corresponding characteristic energy, $\Gamma = \tau_0^{-1}$, play significant roles. The latter parameter, Γ, denotes the life-time broadening of the energy levels at the chemical potential inside a grain and is related to the mean energy-level spacing and the tunneling conductance as follows:

Equation 3 $$\Gamma = g\delta.$$

In fact, quantum confinement for a metallic grain imposes a discrete energy level scheme and thus the mean energy-level spacing (δ) in a single nanoparticle is inversely proportional to the volume of the grain (V) and the density of states at the Fermi energy (ν_F) as follows:

Equation 4 $$\delta = (\nu_F V)^{-1}.$$

In the strong coupling regime, the electrons tunnel quite easily from nanoparticle to nanoparticle and the lifetime broadening Γ clearly exceeds the mean energy-level spacing, and thus, the discreteness of the levels within a single nanoparticle vanishes. Apparently, the conductivity on scales larger than the grain size is diffusive, and thus, the electron motion on the time scales exceeding τ_0 is described by the effective diffusion coefficient (D_{eff}), related to Γ as:

Equation 5 $$D_{eff} = \Gamma a^2.$$

Then, based on the Einstein relation, the conductivity of the granular sample is obtained as:

Equation 6 $$\sigma_0 = 2e^2 \nu_F D_{eff}.$$

This equation is equivalent to the classical Drude formula (Equation 2) for periodic arrays as can be seen from Equation 3, Equation 4, and Equation 5. At the same time, it is more general as it can be applied to arrays with arbitrary grain arrangement if the diffusion constant D_{eff} is defined properly. Based on the above discussion, one can simply notice the importance of the energy scale Γ because, depending on whether the physical quantities of the system are dominated by energies higher or lower than Γ, they can have qualitatively different behaviors. Two major reasons that might reportedly lead to an alteration of the classical conductivity σ_0 (Equation 2) are the electron-electron interactions and the quantum interference effects. Accordingly, one can expect two corresponding distinct corrections to σ_0 which leads to: [91, 101-103]

Equation 7 $$\sigma_0^C = \sigma_0 \left(1 + \frac{\delta\sigma_1}{\sigma_0} + \frac{\delta\sigma_2}{\sigma_0}\right)$$

Equation 8 $$\frac{\delta\sigma_1}{\sigma_0} = -\frac{1}{6\pi g} ln\left[\frac{gE_C}{\max(k_B T, \Gamma)}\right]$$

Equation 9 $$\frac{\delta\sigma_2}{\sigma_0} \approx \frac{1.83}{12\pi^2 g}\sqrt{k_B T/\Gamma}$$

The details on these corrections can be found in the literature as it is out of the scope of this study. Within the model of the three-dimensional periodic granular array (cubic lattice) and in the limit of $T \to 0$, there is a critical conductance:

Equation 10 $$g_c = (1/2\pi d)\ln(E_C/\delta),$$

such that samples with $g > g_c$ are metals while those with $g < g_c$ are insulators. This critical conductance is the result of an analysis of both, the metallic and insulating regime, neglecting dispersion of the tunneling conductance. In the case of 1D and 2D granular samples, the Mott transition cannot be formulated due to several difficulties; however, the critical conductance g_c still has the meaning of the boundary between weak insulating behavior ($g > g_c$) and hard-gap insulating behavior ($g < g_c$).

2.3. Insulating Regime

In the weak coupling regime, the array is an example for a Mott insulator at low temperatures. Considering the electron transport via hopping from nanoparticle to nanoparticle, transport can be blocked at low temperatures due to a significant electrostatic energy cost. At very small tunneling conductance, the gap in the electron excitation spectrum Δ_M is simply equal to the Coulomb charging energy of the nanoparticle ($\Delta_M = E_C$). The activation dependence (Arrhenius law) of the conductivity on temperature is observed when a hard gap is present in the excitation spectrum ($T \ll \Delta_M$) as follows:

Equation 11 $$\sigma \sim e^{-\Delta_M/T}.$$

Indeed, the density of electrons and holes, which are present in the system as real excitations, follows the Boltzmann distribution (also called Gibbs distribution), which leads to an exponential dependence of the conductivity as can be seen in Equation 11. For a periodic granular array with a small intergranular coupling, if only short-range Coulomb interactions are taken into account, straightforward calculations by Efetov and Tschersich resulted in [101]

Equation 12 $$\sigma = 2\sigma_D \exp(-E_C/T),$$

where σ_D is the Drude high-temperature conductivity and E_C is the single grain charging energy. The physical meaning of this results is that the conductivity of an insulating nanoparticle array is arbitrated to electrons and holes that are present in the system as real excitations and the factor 2 appears in the equation because of the presence of both electrons and holes. This result demonstrates that the activation exponent is determined by the energy cost to add/remove an electron from the system (*i.e.* Mott gap). The semiclassical theory of the Coulomb blockade regime predicts the exponential suppression of the conductance at low temperatures, [93] which leads to

Equation 13 $$g(T) = g_0 exp[-E_c/k_BT]$$

in the zero-bias limit. The charging energy, E_C, for a weakly coupled particle in the simplest form can be approximated by: [104]

Equation 14 $$E_C = \frac{e^2}{4\pi\epsilon\epsilon_0 a},$$

where ϵ_0 is the vacuum permittivity, ϵ is the dielectric constant and a is the particle radius. In systems containing nanoparticles, a is small, implying large Coulomb charging energies and a significant suppression of sequential tunneling at low temperatures. However, depending on the voltage, conduction can still occur: (i) at voltages larger than the global Coulomb threshold voltage, $V > V_t$, sequential tunneling can commence again by overcoming the Coulomb blockade, (ii) at voltages lower than V_t, cotunneling can be a viable conduction channel. The latter mechanism will be discussed in detail in the following parts. The global threshold voltage, V_t, is defined as $V_t = \beta N E_C$, where β is a prefactor (0.2-0.5 depending on the dimensionality and array geometry) and N is the number of nanoparticles spanning the gap between the electrodes. In the semiclassical picture, for a large array of nanoparticles at $T = 0$ K, no conductance is predicted for $V < V_t$ as shown by Middleton and Wingreen. [105] In this model, conduction only occurs beyond the global threshold voltage (at $T = 0$ K) by percolation of electrons through the array via a multitude of branching paths that optimize the total charging energy cost. As a consequence of this branching, the non-linear *I–V* characteristics with a power-law dependence appears. [105] The semiclassical model for transport at $T = 0$ K can be extended to finite temperatures. [106] Due to large Coulomb charging energies in nanoparticle arrays, the charge disorder is sufficiently strong, thus the main effect of temperature is to “erase” the local Coulomb blockade threshold. As a result, by increasing the temperature, the global threshold voltage decreases linearly, which is also supported by a variety of experimental results. [107-109] The model proposed by Middleton and Wingreen [105] does not consider thermally activated charge excitations and, by design, only applies to the large bias limit. In the limit of low bias voltages, the conductance is significantly controlled by the largest threshold along the optimal path. In this situation, the relevant activation energy, U, is approximately $\approx 0.2E_C$ since the optimal path can avoid high charging energy costs by branching which eventually leads to [106, 110]

$$g(T) = g_0 exp[-U/k_B T]. \quad \text{Equation 15}$$

This simplified picture is the Arrhenius behavior characteristic of nearest-neighbor hopping and it is applicable at sufficiently high temperatures. The strictly periodic granular model predicts and explains only the activated conductivity behavior; however, at low temperature, this type of behavior is usually not observed and instead, the experimentally observed resistivity is reported to follow:

$$\sigma(T) \sim \exp(-\sqrt{T_0/T}), \quad \text{Equation 16}$$

which resembles the Efros-Shklovskii variable-range hopping (ES-VRH) conductivity in doped semiconductors and is observed in both metallic and semiconducting granular arrays [94, 111-114] as well as in the experimental data of this work presented in Chapter 3. Here, the characteristic temperature T_0 is a material-dependent constant. The mechanism involved in this model is based on direct single-charge tunneling events between distributed defect sites. The crucial parameter for understanding hopping transport in granular systems is the electrostatic disorder that appears in a realistic system. Electrostatic disorder in the matrix induces potential disorder in nearby grains. As a consequence, the hard energy gap in the density of states at the chemical potential is partially lifted. [115] For variable-range hopping (VRH) type of conductivity to occur, the presence of two ingredients are necessary: (i) a finite density of states at energies close to the Fermi level, and (ii) a finite probability for tunneling to spatially remote states close to the Fermi level. Accordingly, in order to apply this model to arrays of nanocrystals, first, one needs to consider the finite density of states near the Fermi level as well as the role of Coulomb correlation in its formation. Second, the model should be capable of qualitatively describing the mechanism of tunneling over long distances through a dense array of metallic nanoparticles. Electrostatic disorder can lead to fluctuations in the electrostatic energy of nanoparticles that lifts the Coulomb blockade on some of the grains in the sample. This, in its turn, leads to a finite density of states at energies close to the Fermi level, and thus, makes VRH the dominant mechanism of transport. The hopping lengths derived from VRH model spans several grain sizes, which makes the applicability of this model to arrays of metallic nanoparticles questionable. The problem is that an electron has to hop over several nanoparticles, which in the case of closely packed nanoparticles array does not look probable. Thus, an alternative picture with the same temperature dependence has been proposed by Beloborodov *et al.* to explain an identical ½ exponent based on tunneling via virtual electron levels in a sequence of grains. [100, 116-117] This cooperative multi-electron process is known as the multiple cotunneling model and can transport charges over distances of several grains without incurring the full Coulomb charging energy costs (e.g. it counts as a single-quantum event). [91, 93, 117-118] Tunneling via virtual electron levels through a single granule was first described by Averin and Nazarov. [119] They considered two distinct charge transport mechanisms of elastic and inelastic cotunneling inside the Coulomb blockade regime. In the event of elastic cotunneling, the electron coming out of the nanoparticle has the same energy as the entering one. In other words, an electron of the same eigenstate tunnels from the initial to the final nanoparticle. This is the dominant mechanism for the hopping conductivity at low temperatures $T < T_{cross}$. In inelastic cotunneling (at higher temperatures $T > T_{cross}$), the electron that leaves the grain has a different energy than the incoming one. Charge transport in this mechanism is the consequence of the cooperative motion of multiple electrons, tunneling concertedly from one grain to the nearest neighbor. The crossover temperature T_{cross} from elastic to inelastic tunneling is given by

Equation 17
$$T_{cross} = \bar{c}\sqrt{E_C\delta},$$

where $\bar{c} \approx 0.1$ is a numerical coefficient. In the latter mechanism, the energy difference between incoming and outgoing electron is adsorbed by an electron-hole excitation which is created inside that grain in the course of the process. Here, charge transport via virtual states in both mechanisms manifests as electron transport via classically inaccessible intermediate states. The number of junctions involved in the cotunneling process is the outcome of an optimization process between the number of cooperative cotunneling events and the net energy cost. The hopping probability is given by: [100]

Equation 18
$$P(r) = exp\left[-\frac{r}{\xi} - \frac{e^2}{4\pi\epsilon\epsilon_0 k_B r}\right],$$

where ξ is the localization length. The localization length characterizes the overlap of the wave functions between different sites. It is essentially defined as the decay length of an electron in nanoparticle assemblies. The typical distance of cotunneling events is obtained by maximizing the hopping probability (Equation 18) with respect to *r* which gives: [100]

Equation 19 $$r^* = \left(\frac{e^2\xi}{4\pi\epsilon\epsilon_0 k_B T}\right)^{1/2}.$$

By dividing the typical hopping length, r^*, by the center-to-center interparticle distance, *d*, as well as including Equation 14, one can obtain the number of tunnel junctions involved in the cotunneling process as follows: [116]

Equation 20 $$j = \frac{r^*}{d} = \left(\frac{E_C}{k_B T}\frac{\xi a}{d^2}\right)^{1/2}.$$

This equation has been used in Chapter 3, section 3.4.4, in order to calculate the number of ITO nanocrystals involved in transport across the array via a sequence of cotunneling events. The probability to create an electron-hole pair in an initially neutral particle for the low-bias regime is the key quantity to calculate the conductance, which is proportional to $exp[-E/k_BT]$, where E is the electrostatic energy related to the electron-hole pair. In sequential tunneling, this electrostatic energy is simply equal to the Coulomb charging energy E_C as the electron-hole pair is separated by one particle after the tunneling event. In the cotunneling regime, if we consider j as the number of junctions involved in transport, the electron-hole pair is separated by $j+1$ particles and in this case the electrostatic energy is equal to E_C/j. [116] Using the number of junctions derived from Equation 20 for the activated creation of a dipole excitation results in:

Equation 21 $$g(T) = g_0 \exp(-\sqrt{T_0/T}),$$

with the material-dependent characteristic temperature, T_0, given by:

Equation 22 $$T_0 = \frac{CE_C a}{k_B \xi} = \frac{Ce^2}{4\pi\epsilon\epsilon_0 k_B \xi},$$

where C is a numerical constant ($C \sim 2.8$ for three-dimension [94]). The data presented in Chapter 3, section 3.3, provides compelling evidence that the model proposed by Beloborodov *et al.* [100, 116-117] is actually operative here. The conductivity pre-exponential factor, g_0, describe the hopping rate between nanocrystals. It includes tunneling through the barrier created by the environment of the nanoparticles and can be considered as the attempt frequency of electrons trying to escape the granules. The contribution of cotunneling through j junctions to the overall conductance of the array is proportional to $(h/e^2R_T)^j$. Therefore, based on this dependence, by increasing the number of junctions involved in the process, the probability of cotunneling decreases. On the other hand, as an electron and a hole created after a cotunneling event are separated by j junctions, one can easily expect a decrease of the electrostatic potential barrier associated with this process with increasing j: $U \approx E_C / j$. As a consequence, the optimal number of cotunneling events, N_{cot}, is the outcome of a competition between the increasing activation exponent $exp(-U/k_BT)$ and the decreasing factor $(h/e^2R_T)^j$.

As mentioned before, the functional form obtained in Equation 21 resembles the ES-VRH conductivity in doped semiconductors. In doped semiconductors, the conduction happens by direct single charge tunneling between distributed atomic defect sites, but in dense arrays of metal nanoparticles, cooperative multielectron processes are dominant. The similarity of the functional form for these two cases arise from balancing the net tunnel distance and the energy cost. One can also find other similarities between multiple cotunneling mechanisms and the theory of Mott, Efros, and Shklovskii. For instance, in the cotunneling model the tunneling probability decreases exponentially with the number of granules left behind, N. Similarly, in ES-VRH model, the probability of tunneling between states near the Fermi surface decays exponentially. Therefore, up to the specific expression for the localization length, hopping in nanoparticle arrays is similar to that encountered in amorphous doped semiconductors in that, by minimizing the hopping probability, one ends up with the same functional form for conductivity as in Equation 16 and Equation 21 for both transport processes. This description is based on the assumption that the typical hopping length r^* exceeds the size of a single nanoparticle. When the temperature increases, the hopping length decreases and at some characteristic temperature it reaches the grain size. Then the hops occur between neighboring nanoparticles only and the VRH picture no longer applies. In this regime, transport occurs via sequential tunneling between neighboring grains along a set of optimal paths. [105, 110] This optimal path is the result of the presence of an unavoidable charge disorder in the film, which in its turn, arises from variations in the local chemical potentials.

The signatures of the cotunneling process can be found in different regimes depending on the range of temperature and applied bias voltages. [120] The current in the regime of cotunneling, for an ideal system with identical tunnel resistance and charging energy for all nanoparticles, is given by a Tailor series proposed by Tran *et al.*: [116]

Equation 23 $$I \propto V_{jct} \sum_j \left(\frac{h}{e^2R_T}\right)^j \left(\frac{k_B^2T^2+e^2V_{jct}^2}{E_C^2}\right)^{j-1} exp\left(-\frac{\frac{E_C}{j}-jeV_{jct}}{k_BT}\right),$$

where R_T is the resistance of a single junction and V_{jct} is the voltage drop over a single tunneling junction connecting two neighboring nanocrystals. The contribution of the formation of an electron-hole dipole pair separated by j junctions is reflected in the electrostatic barrier, $U = E_C/j - jeV_{jct}$, present in the Arrhenius exponent and V_{jct} is considered as V/N with N being the total number of tunnel barriers along the array. Based on Equation 23, Dayen *et al.* have found that when the thermal energy becomes smaller than the Coulomb charging energy, the electronic behavior during cotunneling can be split into three regimes depending on different voltage ranges between neighboring particles: [120]

Equation 24 $$C1: \quad I \propto V \qquad eV_{jct} < k_B T$$

Equation 25 $$C2: \quad I \propto V^{\propto} \qquad k_B T < eV_{jct} < k_B T ln\left(\frac{e^2}{h} R_T\right)$$

Equation 26 $$C3: \quad I \propto exp\left(\sqrt{\frac{V^*}{V}}\right) \qquad k_B T ln\left(\frac{e^2}{h} R_T\right) < eV_{jct},$$

where V^* is a characteristic voltage and α is the power law exponent which relates to the number of cotunneling events through $\alpha = 2N_{cot} - 1$. Indeed, the cotunnel distance, which is a characteristic length scale, sets the curvature of the non-linear *I–V* characteristics as well as the temperature dependence of the zero-voltage conductance. The three above-mentioned equations describe the behavior of the system in the cotunneling regimes (C1, C2, and C3) while at higher bias voltages $eV_{jct} \approx E_C$, the system enters the sequential tunneling regime, which has been discussed in much detail in literature. [6, 87, 105] The fact that linear and non-linear *I–V* characteristics with a power-law dependence are observed in the results presented in Chapter 3, section 3.3, can be interpreted as a manifestation of the relationship described in Equation 24 and 25.

2.4. Coulomb Charging Energy

The calculation of the nanoparticle charging energy in assemblies is a puzzling point and different models are reported in the literatures. [95] It can be affected by different parameters including: (i) the particle core size, (ii) the inter-particle distance, (iii) the nearest neighbor number, and (iv) the dielectric constant of the ligand molecules. [121] In a general form, charging of the particle by a single electron, e, requires a charging energy equal to:

Equation 27 $$E_C = \frac{e^2}{2C_{NP}},$$

where C_{NP} is the capacity of the nanoparticle. In the simplest from, using the self-capacitance (C_0) of an isolated nanoparticle (see Figure 4):

Equation 28
$$C_0 = 4\pi\epsilon\epsilon_0 a$$

results in the well-known Equation 14 which is introduced in the previous section. The value of Coulomb charging energy obtained from this model is supposed to be overestimated since the model simply considers the self-capacitance of the granule and ignores the interaction between neighboring granules. To more adequately describe the charging energy in nanocrystal arrays, nearest-neighbor interactions should be also considered. In a widely used picture, it is assumed that the nanoparticle is surrounded by a layer of a dielectric material with thickness s and another infinite concentric layer with the same component as the nanoparticle (see Figure 4). This simple electrostatic model developed by Abeles *et al.* describes the capacitance as follows: [122]

Equation 29
$$C_{Abeles} = 4\pi\epsilon\epsilon_0 a(a+s)/s,$$

where s is the length of the tunnel barrier, *i.e.* inter-nanoparticle spacing. Therefore, the Coulomb charging energy is:

Equation 30
$$E_C = \frac{e^2}{8\pi\epsilon\epsilon_0}\left(\frac{1}{a} - \frac{1}{a+s}\right).$$

This model typically over-estimates the contribution of the mutual capacitance between neighboring granules such that the value for the charging energy deduced from Equation 29 is expected to be underestimated. In an alternative classical model by Laikhtman and Wolf [123], the array of metal granules is assumed to be embedded in a dielectric medium (e.g. organic ligands) with the inter-particle distance s (Figure 4). [97] Here, the charging energy is governed by the total capacitance (C_Σ), which is the sum of the nanocrystal self-capacitance (C_0) and the inter nanocrystal capacitance arising from nearest-neighbor interactions (C_{inter}); *i.e.* $C_\Sigma = C_0 + C_{inter}$. The latter capacitance is estimated to be proportion to $2a$□$ln(1+2a/s)$, thus, the pairwise capacitance between two neighboring nanocrystals (C_{nn}) is defined as follows: [123-125]

Equation 31
$$C_{\mathrm{nn}} = 2\pi\epsilon\epsilon_0 a ln(1+\frac{2a}{s}).$$

By decreasing the particle spacing in this model, the mutual capacitance between two neighboring nanoparticles increases, which in its turn, leads to a decrease of the Coulomb charging energy. For a monolayer granular array with a hexagonal close-packed arrangement, the nearest-neighbor-number (NNN) is 6. For a bilayer nanoparticle array, NNN = 9, and for a tri-layer superlattice, NNN is still 9 for top and bottom layer, but 12 for the middle layer. Therefore, the average total capacitance is: [121]

Equation 32
$$C_{\Sigma} = C_0 + 6C_{nn}$$

Equation 33
$$C_{\Sigma} = C_0 + 9C_{nn}$$

Equation 34
$$C_{\Sigma} = C_0 + \frac{2\times 9C_{nn}}{3} + \frac{12C_{nn}}{3}$$

Neglecting the small contribution of self-capacitance to the total capacitance, [124, 126] within a nanoparticle surrounded by NNN neighbors, the charging energy can be written as $E_C \approx e^2/2C_{inter}$. This simple calculation indicates that the Coulomb charging energy decreases very fast for the first few layers and then levels off for more layers. Table 2 summarizes the different models that has been introduced in order to calculate the nanoparticle charging energy in assemblies.

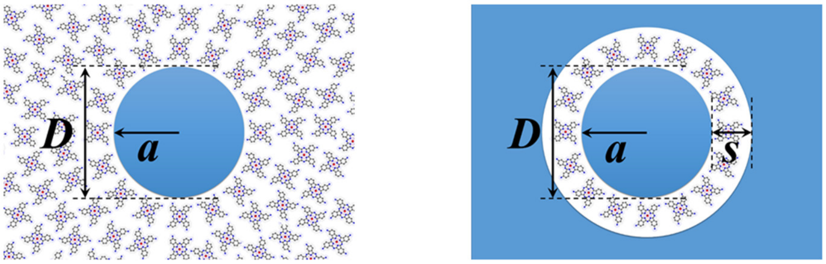

Isolated nanoparticle

Isolated nanoparticle embedded in a dielectric medium surrounded by infinite concentric layer

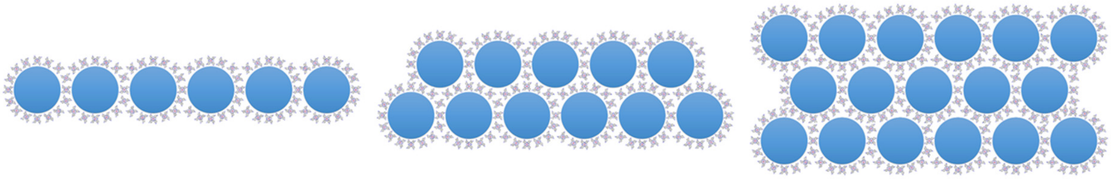

One-monolayer array of metal granules embedded in a dielectric medium

Two-monolayer array of metal granules embedded in a dielectric medium

Three-monolayer array of metal granules embedded in a dielectric medium

Figure 4. Schematic representation of an isolated nanoparticle with diameter *D* surrounded by an organic dielectric medium (self-capacitance model), isolated nanoparticle embedded in a dielectric medium with thickness *s* surrounded by infinite concentric layer (developed by Abeles et al. [122]), and one-, two-, and three-monolayer array of metal granules embedded in a dielectric medium (proposed by Laikhtman and Wolf [123]).

Table 2. The different models that has been introduced in order to calculate the nanoparticle charging energy in assemblies.

	Capacitance	Coulomb Charging Energy	Description	Ref.
Self-capacitance model	$C_0 = 4\pi\epsilon\epsilon_0 a$	$E_C = \frac{e^2}{4\pi\epsilon\epsilon_0 a}$	The value of Coulomb charging energy obtained from this model is supposed to be overestimated since the model simply considers the self-capacitance of the granule and ignores the interaction between neighboring granules	Ref. [121]
Model developed by Abeles et al.	$C_{Abeles} = \frac{4\pi\epsilon\epsilon_0 a(a+s)}{s}$	$E_C = \frac{e^2}{8\pi\epsilon\epsilon_0}\left(\frac{1}{a} - \frac{1}{a+s}\right)$	This model typically over-estimates the contribution of the mutual capacitance between neighboring granules. The value of Coulomb charging energy obtained from this model is expected to be underestimated.	Ref. [122]
Model developed by Laikhtman and Wolf	$C_\Sigma = C_0 + 6C_{nn}$	$E_C = \frac{e^2}{2C_\Sigma}$	For a monolayer granular array with a hexagonal close-packed arrangement	Ref. [123]
	$C_\Sigma = C_0 + 9C_{nn}$	$C_{\mathrm{nn}} = 2\pi\epsilon\epsilon_0 a ln(1 + \frac{2a}{s})$	For a bilayer nanoparticle array with a hexagonal close-packed arrangement	
	$C_\Sigma = C_0 + \frac{2 \times 9C_{nn}}{3} + \frac{12C_{nn}}{3}$		For a tri-layer superlattice with a hexagonal close-packed arrangement	

3. Charge Transport in Arrays of Semiconductors Nanocrystals

In this section, the resistivity of a dense array of semiconductor nanocrystals and its dependence on three important parameters namely (i) doping level, (ii) temperature, and (iii) NC diameter will be described. Here, the semiconductor NCs are doped by donor impurities, covered by a thin layer of insulating ligand, and arranged in an ideal crystalline lattice. The discussions presented in this part mainly follows recent publications by the Shklovskii group on the theory of hopping conduction in arrays of doped semiconductor nanocrystals. [111, 127-130] From a theoretical electronic structure point of view, in an array of semiconductor NCs all electrons from donor impurities reside in the conduction band of the NC. In real cases however, the array cannot be considered as an ideal electroneutral lattice. Due to the presence of fluctuations in the electron energy (i.e. donor number) between different NCs thus, e.g. due to a relatively small amount of disorder, the donor electrons experience Anderson localization, [131] resulting in charged NCs. Conduction in this system occurs only by "hopping" between localized electron states. In this thermally activated process, electron tunneling occurs simultaneously with adsorption or emission of a phonon, thus the process is also known as "phonon-assisted tunneling". The energy of the adsorbed/emitted phonon determines the difference between the initial and final electron states.

In an ideal case where all NCs are neutral, hopping of an electron from one neutral NC to another produces two oppositely charged NCs with a corresponding Coulomb charging energy, E_C. In the global ground state of the system, this barrier plays the role of an activation energy for resistance. In other words, the density of ground states (DOGS) of NCs, has a width of $2E_C$ centered at the electron Fermi level and, thus, the resistivity follows the Arrhenius law: $ln\ \sigma \propto E_C/k_BT$. In experiments, however, charge transport is often reported to follow the variable range hopping (VRH) [94, 111-114] model, $ln\ \sigma \propto (T_0/T)^{\varsigma}$, where $\varsigma = ½$, ⅓, and ¼ for Efros-Shklovskii or Coulomb Gap (CG), two-dimensional (2D), and three-dimensional (3D) transport models, respectively, that is different from simple activation model. Such "stretched exponential" behavior is attributed to the presence of strong disorder in NCs array. Therefore, electrons depart from NCs with a large number of donors and reside instead on nearby NCs with small donor numbers. Thus, in the global ground state, a significant fraction of NCs is spontaneously charged, which in turn, creates a random Coulomb potential landscape that shifts either up or down the electron energy spectra at different NCs. As a consequence, some electron states have energies very close to the Fermi level, and thus, one can find a pair of empty and filled electron states separated by an energy ΔE that is considerably smaller than charging energy, E_C. When the thermal energy becomes smaller than the Coulomb charging energy, $k_BT \ll E_C$, the conduction is dominated by hopping between such pairs that are close in energy between distant NCs. Decreasing the temperature of the system leads to a depletion of available high-energy phonons. As a result, the corresponding energy difference ΔE of electron hops decreases and the typical hopping length increases. This behavior is known as variable range hopping. When the density of ground states of the system is constant near the Fermi Level, charge carrier transport follows the Mott low of VRH: $\ln g \propto T^{-1/4}$. [132] When the long-range Coulomb potential is not screened in the system, electron correlation effects produce a Coulomb gap in the DOGS at the Fermi level, which leads to the ES law of VRH: $\ln g \propto T^{-1/2}$. [133]

In the proposed model by Skinner *et al.*, [111] an array of NCs with random number of dopants is considered as identical spheres of diameter D with large internal dielectric constant $\varepsilon_{NC} \gg \varepsilon$ arranged in a regular, three-dimension cubic lattice. The model has determined the conditions for VRH in an NC array. In their model, the core-to-core interparticle distance, d, is considered to be just barely larger than D, thus, the edge-to-edge interparticle spacing, s, is considerably smaller than the NC diameter, $s \ll D$. The effective electron Bohr radius, a_B, of the semiconductor can be described in terms of the electron charge, e, the effective electron mass, m, and the internal dielectric constant of the nanocrystal as follows:

Equation 35
$$a_B = \frac{\hbar^2 \varepsilon_{NC}}{m e^2}.$$

The radius, a, of the NCs is assumed to be comparable to or smaller than the electron Bohr radius which results in the extension of the wave function of a donor electron across the entire volume of a NC. Under this condition, the energy of the electron is strongly affected by quantum confinement within the NC. In order to produce electron states that are extended across the NC, the diameter D should be less than $6a_B$. [134-135] This has been developed based on perturbation theory as well as confirming numerical calculations (for more details, the reader is referred to the references). This criterion guides us how small the diameter of the NC should be in order for a single donor in the center of the NC has a delocalized electron state.

In the hypothetical case where there is absolutely no disorder in the array and all NCs have the same number of donors, N_i, the ground-state arrangement for electrons means that all donors are uniformly neutralized: $n_i = N_i$. In this situation, every nanocrystal has the same highest filled electron level, $E_i^{(f)} = E_Q(n) - e^2/\kappa D$, and the lowest empty electron level, $E_i^{(e)} = E_Q(n_i) +$

$e^2/\kappa D$, at each NC i, where $E_Q(n)$ is the energy of the n^{th} lowest electron and κ is the effective dielectric constant of the NCs array which are defined as:

Equation 36 $$E_Q(n) = \frac{\hbar^2}{mD^2}\begin{cases} 0, & n = 0 \\ 19.74, & n = 1,2 \\ 40.38, & 3 \le n \le 8 \\ 66.43, & 9 \le n \le 18 \end{cases},$$

Equation 37 $$\kappa \cong \kappa_i \frac{\kappa_{NC}+2\kappa_i+2f(\kappa_{NC}-\kappa_i)}{\kappa_{NC}+2\kappa_i-f(\kappa_{NC}-\kappa_i)}.$$

In Equation 36, the first nonzero energy levels can be labeled as 1S, 1P, and 1D, respectively. In Equation 37, κ_{NC} is the internal dielectric constant of the NC, κ_i is the external dielectric constant of the insulator in which NC is embedded and f is the volume fraction occupied by the NCs defined as:

Equation 38 $$f = \frac{\pi D^3}{6d^3}.$$

It should be noted that Equation 37 also includes the effect of polarization of NCs in response to an applied field, which effectively decreases both the Coulomb self-energy of a single NC and the interaction between neighboring NCs. [136] In this uniformly neutral system, the Fermi level is $\mu = E_Q(n_i)$ and charge carrier transport requires the excitation of a positive/negative NC pair which produces one negative NC containing $n_i + 1$ electrons and one positive NC containing $n_i - 1$. As a consequence, the excitation energy is equal to the sum of twice the Coulomb self-energy, and thus, there is an activation barrier to transport of energy $E_A = e^2/\kappa D$, which leads to activated conductance.

If the randomness in the donor number is taken into account, the ground-state arrangement of electrons is not uniformly neutral. In this situation, NCs with a large number of dopants may become ionized and their electrons can occupy lower energy shells with NCs with a small number of dopants. This is driven by large gaps in quantum energy spectrum, inducing electrons to leave higher shells of one NC and fill the lower shells of the other NC. This results in positively and negatively charged NCs, and the ground-state configuration of the array consists of randomly distributed fixed charges that allows for variable range hopping. The produced random Coulomb potential smears the single electron energy levels, resulting in a finite density of states near the Fermi level. If the created mobile electrons and holes arrange themselves in such a way that the following criteria are met:

Equation 39 $$E_j^{(e)} - E_i^{(f)} - \frac{e^2}{\kappa r_{ij}} > 0,$$

Equation 40 $$E_i^{(e)} - E_j^{(f)} - \frac{e^2}{\kappa r_{ij}} > 0$$

vanishing of the DOGS near the Fermi level will be observed [94, 133] and the conductance is described by Equation 21. In order to identify the conditions which produce VRH, Skinner *et al.* [111] simulated the density of states and the resistivity at various values of the average number of electrons per NC, v, the NC diameter, and the temperature. They have found that VRH appears when the mentioned parameters satisfy the following three conditions: (i) $v \gtrsim 0.6$, (ii) $D \lesssim 34\kappa a_B$, and (iii) $k_B T \lesssim 0.5e^2\xi/\kappa D^2$. Therefore, one can conclude that when the doping level and the quantum confinement energy are sufficiently high and the temperature is sufficiently small, ES-VRH behavior appears, which is driven by the fluctuations in donor numbers from one NC to another.

4. Photoelectron Spectroscopy (PES)

In this section, a short introduction to photoelectron spectroscopy techniques as well as the theoretical approaches in order to model the interface will be introduced. The theoretical background and the discussion presented in this section mainly follows review papers by the Kahn, Koch, and Fahlman research groups [137-139] as well as theoretical textbooks. [140-141] PES is a very powerful nondestructive quantitative spectroscopic technique in surface chemistry and provides valuable information about the electronic structure of materials, the chemical environment of atoms, and compositional changes in the near-surface region due to its extremely surface sensitivity. [142-143] In this technique, the sample is excited with a high energy light source and the energy distribution of emitted electrons is measured. In the photoelectron production process, an electron - initially bound to an atom or ion - is ejected by a photon. Since photons carry neither mass nor charge, a complete energy transfer occurs during photon-electron interactions, resulting in the emission of an electron from the atom or ion. [140] While the conventional excitation sources in PES (X-rays and ultraviolet lights) can excite and ionize atoms down to micrometer depth of the sample, the electrons can only escape from a thin layers near the surface due to scattering. Therefore, 95% of the detected electrons originate within 3λ below the sample surface, where λ is the inelastic mean free path of the electrons. For X-ray photoelectron spectroscopy (XPS), the typical amount of λ are on the order of tens of Angstroms [144] and for ultraviolet photoelectron spectroscopy (UPS), it is less than ten Angstrom. [145] The central equation in photoelectron spectroscopy is given by the Einstein relation in order to describe the kinetic energy of photoelectrons as follows:

Equation 41 $$E_k = h\nu - E_b,$$

where $h\nu$ is the photon energy of the excitation source and E_b is the binding energy of the electron referenced to the vacuum level.

The popularity of XPS stems from the power of this technique in: (i) identifying and quantifying the elemental composition in the near-surface region of any solid with all elements detectable, and (ii) revealing the chemical environment of the respective elements by recognizing small changes in the valence-electron density. [140] Such small changes are reflected as considerable shifts in the core-level binding energies of the atom. As a consequence, the formation of chemical bonds as well as charge transfer can be investigated using XPS. Furthermore, this technique is capable of obtaining the mentioned information with relative ease and minimal sample preparation. Commercially available X-ray sources used in XPS instruments can be categorized as (i) standard sources and (ii) monochromatic sources; which produce X-rays by directing a sufficiently energetic electron beam at some metallic X-ray anode, with the electron source being the cathode. [140] The most commonly used X-ray anode in XPS is Al due to the relatively high energy and intensity of Al Kα X-rays (with excitation energy equal to 1486.6 eV and energy spread of 0.85 eV), heat conductivity, the ease of manufacturing, and its robustness. This kind of excitation source has been used for the XPS measurements presented in Chapter 4 and 5. Standard sources commonly equipped with dual Al and Mg (with excitation energy equal to 1253.6 eV and an energy spread of 0.70 eV) anodes that provide unfocused X-ray beams, which excite the entire sample as well as the surrounding area in close proximity. The advantages of these sources include lower cost and freedom of using any anode material as well as the ease of switching between them. However, in comparison to monochromatic sources, they suffer from some drawbacks such as large energy spread, the presence of additional excitation peaks, lower photon flux per unit area, and greater sample degradation. The conventional monochromatic sources produce a focused X-ray beam with a narrower energy spread, e.g. between 0.2-0.3 eV for Al $K\alpha_1$ emission, and spot sizes from such sources can be as small as ~10 μm. However, these sources are more expensive, limited number of anode metals can be used in such sources, and they have greater potential for sample charging during measuring of insulating surfaces.

The UPS technique, which can be viewed as an extension of the XPS, is used to explore the valence electronic structure of the materials. The higher photoionization cross-section of the electrons in the valence region as well as the higher energy resolution of photon sources make UPS a very powerful and suitable technique for studying the interfacial electronic structure. The most commonly used source of photons in this technique is a gas discharge lamp, operated with He gas through the discharge region, which is formed by applying a potential difference between the anode and cathode regions. In this process, He electrons are excited to higher states and during de-excitation, photons with the energy equal to the energy difference of contributing states are released. This process leads to a primary emission of He I (with excitation energy of 21.21 eV) and a secondary weaker radiation of He II (with excitation energy of 40.8 eV). The former has been applied to explore the organic semiconductor valence band in Chapter 4.

4.1. Electronic Structure at the Interface

The principle of UPS and its application to the determination of the details of the interfacial electronic states are illustrated in Figure 5 (adapted from reference) [142]. Figure 6 represent the electronic structure of a typical organic semiconductor/metal interface. The most important energy levels are the metal Fermi level, E_F, the organic semiconductor highest occupied and lowest unoccupied molecular orbitals (HOMO and LUMO) that are responsible for hole and electron transport, respectively, and the vacuum level, E_{vac}, of each material. The vacuum level of the sample is measured directly with the secondary electron cut-off, $E_{cut\text{-}off}$. The energy difference between vacuum level and Fermi level for metal electrodes is the electrode work function, Φ_M. It determines the minimum energy necessary to remove an electron from the metal.

Equation 42 $$\Phi_M = h\nu - E_{cut-off}$$

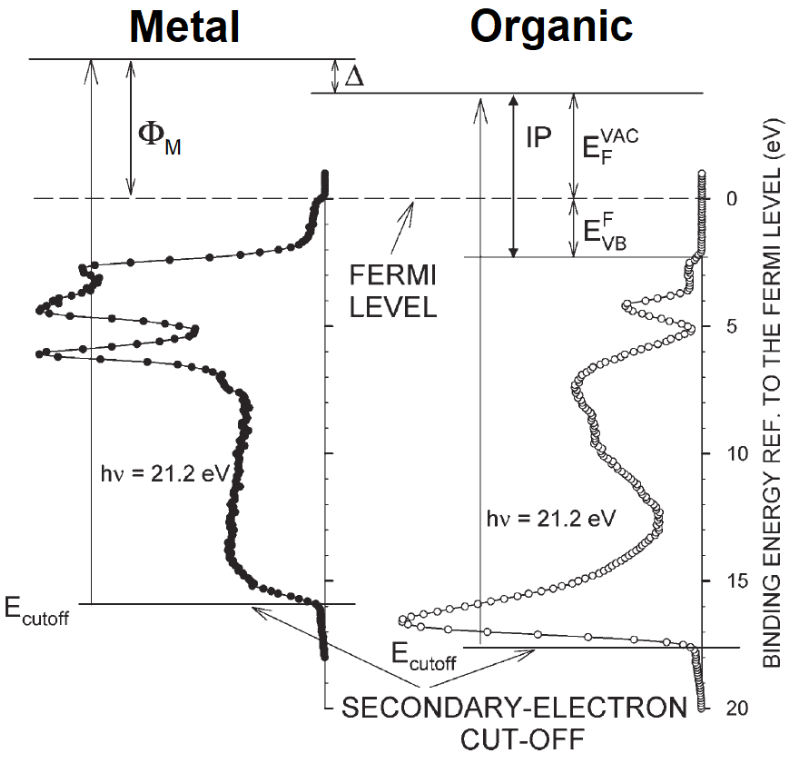

Figure 5. The principle of UPS and its application to the determination of the details of the interfacial electronic states (Reprinted with permission from ref. [142]. Copyright 2017 John Wiley and Sons).

On the organic side, the position of the HOMO is determined by the low binding energy onset of the UPS spectrum, i.e. the intercept between the tangent line of the onset feature and the baseline of the spectrum, is considered. The energy distance between the vacuum level and HOMO edge is known as the organic ionization potential/energy, *IP* or *IE*. The electron affinity, *EA*, of the organic semiconductor is defined as the energy difference between the vacuum level and LUMO. The interface dipole, denoted as Δ, is defined as the shift between the vacuum levels of two materials at the interface. The energy difference between electrode

Fermi level and HOMO or LUMO are hole or electron injection barriers, Φ_{HIB} or Φ_{EIB}, respectively. Finally, the density of interface gap states, D_{is}, as well as charge neutrality level, E_{CNL}, of the interface states are schematically shown in Figure 6 between HOMO and LUMO of the organic semiconductor.

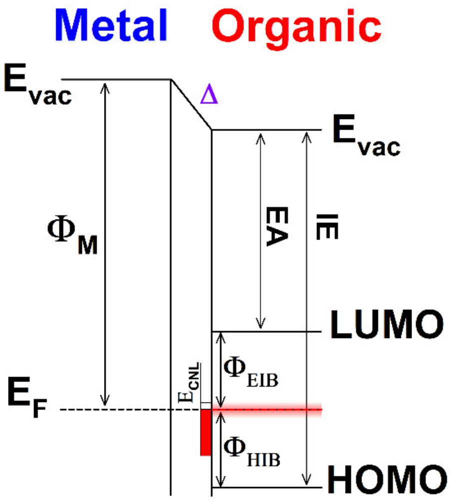

Figure 6. Electronic structure of a typical organic semiconductor/metal interface.

The electron injection barrier using standard organic semiconductor/metal interface methods can be described using the following equations: [92, 141, 146]

Equation 43
$$\Phi_{EIB} = S(\Phi_M - EA) + (1 - S)E_{CNL},$$

Equation 44
$$S = \frac{1}{1+4\pi e^2 D_{is}\delta_{org/metal}},$$

where S is the interface parameter, representing the strength of the interaction. $\delta_{org/metal}$ is the effective organic semiconductor/metal distance that plays an important role in the Fermi level pinning regime. This term refers to the situation when, for multilayer organic semiconductor film, the Fermi level cannot cross the onsets of the HOMO or LUMO level, and hence, regardless of the choice of material for electrode, the charge injection barriers cannot completely be eliminated. This means that the Fermi level is stuck at a specific energy inside the fundamental gap of the organic semiconductor and the injection barriers in such interfaces depend on the nature of the material. If the interface Fermi level is above/below the charge neutrality level, then the net charge at the interface is negative/positive, and thus, a corresponding interfacial dipole develops across the interface. Bringing the organic material in contact with the surface of another material can lead to a wide variety of interaction types at the interface. [143] This range can span from weakly physisorbed molecules on clean inert substrates to strong chemisorbed molecules on clean reactive surfaces. [142] For instance: (i) the adsorption of noble gas atoms or saturated hydrocarbons on clean metal surfaces results in physisorption of molecules without any charge transfer at the interface. [147-148] (ii) At the interfaces between π-conjugated small molecules or polymers and organic or passivated metal surfaces, one can have physisorption as well as a possible integer electron charge transfer through tunneling. [149-150] (iii) For π-conjugated molecules on non-reactive clean metal surfaces, a weak chemisorption can happen as well as partial charge transfer. [151-152] (iv) The interfaces between molecules and reactive clean metal surfaces are characterized by strong chemisorption, covalent bonding between molecules and the metal, and a partial or total charge transfer at the interface. [153] (v) In the case of molecules with intrinsic dipole and anchoring groups on metal surfaces, a strong chemisorption, covalent band at specific sites of the molecules and metal, a partial or total charge transfer as well as a surface dipole may exist. [154-155] In the literature, one can find several models that address the nature of the interface through the density of interface states, which will be discussed in the following sections.

4.2. Models for Interfaces Free of Gap states

4.2.1. Schottky-Mott Model

This model describes non-interactive semiconductor/metal interfaces in the limit of vanishingly small density of interface states. In this model, no dipole is considered at the interface, $\Delta = 0$, and the system is assumed to be in the vacuum level alignment regime. Here, the electron or hole injection barrier is equal to the difference between the electrode work function and the organic electron affinity or ionization energy, respectively: $\Phi_{EIB} = \Phi_M - EA$ and $\Phi_{HIB} = IE - \Phi_M$. The interface parameter, S, is defined as the derivative of the charge injection barriers with respect to the substrate work function: $S = d\Phi_{HIB}/d\Phi_M = d\Phi_{EIB}/d\Phi_M$. This parameter is equal to unity in the Schottky-Mott limit where the electrode Fermi level situated within the gap of the organic semiconductor: $EA < \Phi_M < IE$. [92, 141, 146] If the work function of the electrode decreases/increases to reach and cross the EA/IE of the organic semiconductor, the interface will deviate from the simple Schottky-Mott picture and a significant amount of charges will be transferred from the metal Fermi level to the semiconductor LUMO or from the organic HOMO to the metal. In this situation, the electronic structure of the system enters the Fermi level pinning regime, which is characterized by the alignment of the metal Fermi level with the polaron state of the organic material [150] or penetration of the electrode Fermi level into the density of states tailing into the gap. [156] Based on published papers in literature, interfaces formed by spin-coated polymer films on metal electrodes as well as those formed by evaporation of small molecule organic semiconductors on contaminated metal centers closely follow the vacuum level alignment and approach the Schottky-Mott limit. [157-159] A deviation from vacuum level alignment is reported for the interfaces created by thermal evaporation of metal on polymers as well as those prepared by evaporation of small molecule semiconductors on clean metal surfaces, which will be discussed in the next sections. [153, 160-162]

4.2.2. "Pillow" or "Push-Back" Effect

The "Pillow" or "Push-Back" effect is a phenomenon which systematically reduces the work function of the metal. In order to understand the mechanism of this effect, it is worth noting that the total work function of a metal originates from two main potentials, namely the chemical potential of the bulk metal and the electrostatic potential across the metal surface. [163-164] Physisorption of organic molecules at the interface cannot affect the bulk chemical potential of the metal, however, it can have a substantial effect on the electrostatic potential across the surface by modifying the tail of the electron cloud leaking out into vacuum. Indeed, when a molecule is deposited onto a metal surface, the tail of the electron wave function is locally suppressed due to the Coulomb repulsion between the semiconductor molecule's electron density and that of the surface metal electrons. This phenomenon has been extensively investigated in previous decades, and the amount of reduction by 0.5-1.0 eV upon deposition of organic molecules on clean noble metal surfaces can be found in literature (the origin of which is partially attributed to this effect). It is worth pointing out that the change in the work function by the "Pillow" or "Push-Back" effect should be considered as a result of the modification of the electrostatic potential across the metal surface and not from the charge transfer or formation of an interface dipole at the interface. This effect is observed in action in the data presented in Appendix C.

4.2.3. Integer charge transfer (ICT) Model

The π-conjugated small molecules and polymers are considered as soft materials with a very strong electron-phonon interaction. [142] This is due to the fact that their HOMO and LUMO energy levels are significantly changed upon adding or removing an electron to or from their electronic structure. This substantial change is attributed to a deformation of their structure in order to compensate the added/removed charge. Therefore, the HOMO and LUMO energy levels of the neutral system are not relevant anymore in determining the energy level alignment in such charged system and one should consider the singly occupied molecular orbital of the charged molecule instead (in cationic or anionic form). These charge-carrying states for π-

conjugated polymers are polaronic states (called polarons if they carry a single charge or bipolarons in case of two charges) that reside in the fundamental gap of the organic molecule and differ significantly in energy in comparison to the HOMO and/or LUMO energy level. In π-conjugated polymer films, the mechanism of transport is reported to follow the hopping between these singly charged localized polaron states. [165]

The ICT model is proposed for interfaces with a negligible interaction between π-electronic molecular orbitals and substrate wave functions. [142, 166-169] In this model, it is considered that the presence of surface hydrocarbons and/or native oxides decouples the π-electrons from the substrate's bands, which inhibits the hybridization of electronic states. Consequently, the formation of interface dipoles via partial electron transfer is blocked. However, tunneling implies the transfer of an integer amount of charge into well-defined charged states on the organic molecule. This is possible if the passivating layer is thin enough. For interfaces with negligible interaction, a positive or a negative interface dipole can be found, originating from charge transfer based on differences between the organic *IE* or *EA* and the work function of the substrates. As described previously, any addition and reduction of charge to soft organic materials results in geometric and electronic relaxations and creates self-localized states (polarons and bipolarons) which are separated from the HOMO/LUMO edge of the neutral molecule. Within the framework of this model, two important energy levels, namely the energy of a positive/negative integer charge-transfer state, E_{ICT+}/E_{ICT-}, are defined as the energy required to take away/add an electron from/to the organic molecule to produce a geometrically and electronically fully-relaxed state (including the screening from the substrate as well). Therefore, at this type of weakly interacting interfaces, the HOMO and LUMO energy levels are not the relevant energies to determine the electronic structure.

In such a case, when bringing the organic material in contact with the substrate, if the substrate work function is smaller than the ICT$^-$ energy, $\Phi_{sub} < E_{ICT-}$, electrons will flow spontaneously from the substrate to the organic molecules (see Figure 7). The essential reason for this charge transfer is that the cost in energy gained by organic semiconductor at the interface when accepting an electron is higher than the cost in energy for taking off an electron from the substrate. Therefore, upon this charge transfer, the substrates progressively become positively charged and the organic side becomes negatively charged, which develops a potential at the interface. This leads to Fermi-level pinning to a positive integer charge-transfer state with a substrate-independent resulting work function. Further decreasing the substrate work function increases the magnitude of the interface dipole in a way that the substrate work function becomes equal to the energy of the ICT$^-$ level minus the interface dipole.

If the substrate work function is larger than the ICT$^+$ energy level, $\Phi_{sub} > E_{ICT+}$, electrons will flow in the opposite direction from the organic molecules to the substrate (see Figure 7). The substrate progressively becomes negatively charged and the organic side becomes positively charged which develops an opposite potential at the interface. Consequently, Fermi-level pinning to a negative integer charge-transfer state is observed with a substrate-independent resulting work function as well. In the same manner, further increasing the substrate work function increases the interface dipole in a way that the substrate work function becomes equal to the energy of the ICT$^+$ level plus the interface dipole.

Finally, in the case where the work function of the substrate is larger than the ICT$^-$ and smaller than the ICT$^+$ energy levels, $E_{ICT-} < \Phi_{sub} < E_{ICT+}$, there will be no electron transfer between the substrate and the organic semiconductor (see Figure 7). This is because the cost in energy of removing an electron from the organic part at the interface is greater than the energy gained by the substrate when accepting an electron. Similarly, the energy gained by the organic semiconductor when accepting an electron is less than the energy needed to remove an electron from the substrate Fermi level. Consequently, there will be no vacuum level offset at the substrate/organic interface, i.e. no interface dipole, and hence, the system will be in the vacuum level alignment regime with a substrate-dependent resulting work function.

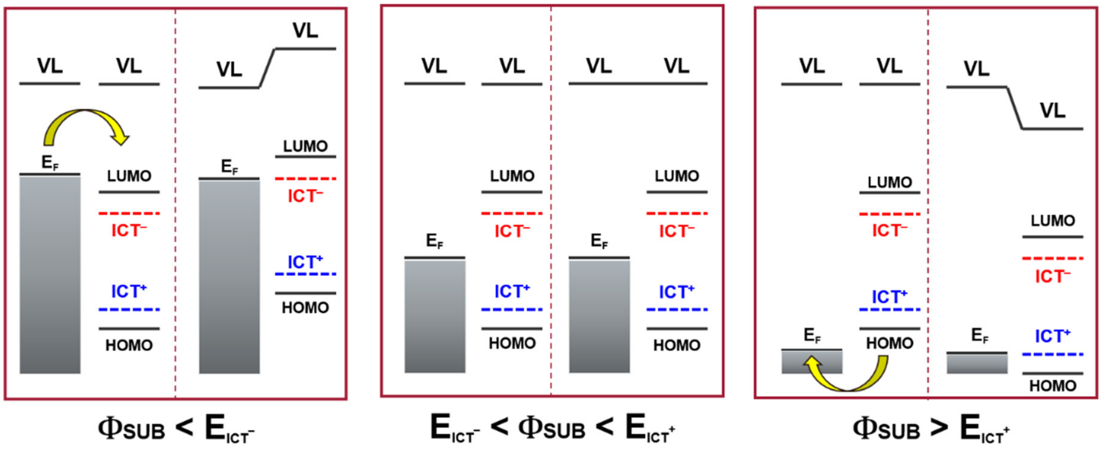

Figure 7. Schematic representation of energy-level alignment at the organic/substrate interface for the cases where: (i) the substrate work function is smaller than the energy of a negative integer charge-transfer state (Fermi level pinning regime). (ii) The substrate work function is located between the energy of a negative and a positive integer charge-transfer state (vacuum level alignment regime). (iii) The substrate work function is larger than the energy of a positive integer charge-transfer state (Fermi level pinning regime)

Accordingly, sweeping the substrate work function over a large-enough range leads to the so-called "z-shape" behavior for Φ_{EIB} and Φ_{HIB}. This behavior is observed in Chapter 4, section 4.3, when the density of states of the organic layers are approximated by Gaussian peaks. Once again, it should be emphasized that the "z-shape" behavior was only observed for electrode-organic interfaces with weak interaction where the organic molecules were electronically decoupled from the substrate by a thin layer of hydrocarbon contaminations or oxide layers. [138-139, 151, 161, 170-173] The ICT model can also be successfully used for the case of heterojunction interfaces between organic semiconductors. Since semiconductor organic heterojunctions mostly create weakly interacting interfaces (by weak van der Waals intermolecular bonding), the energy level alignment at the interface is determined by the relative positions of integer charge-transfer states and, using the pinning values (E_{ICT-} and E_{ICT+}), the ICT model can predict the behavior of organic heterojunctions.

4.3. Models for Interfaces Dominated by Gap states

The models described in the previous sections are related to interfaces free of gap states. In the presence of density of interface states, the degree of freedom for the Fermi level is limited and in the cases where D_{is} is large enough, the system enters the Fermi level pinning regime. As indicated by Equation 44, increasing D_{is} decreases the interface parameter, which weakens the sensitivity of the charge injection barriers towards the electrode work function. In this situation, the position of the Fermi level is defined by the charge neutrality level based on Equation 43. As a rough quantitative estimate, it is worth pointing out that a density of interface states in excess of approximately 5×10^{13} $cm^{-2}eV^{-1}$ [141, 146] within the gap of the organic semiconductor can significantly alter the position of the interface Fermi level.

4.3.1. Interfaces Containing Chemisorption

Interface states can have various origins. Frequently encountered reasons include defect and chemistry-induced gap states, which correspond to the formation of chemical bonds or defects upon vacuum-evaporation of a metal onto a molecular organic film. [174-175] These kinds of interfaces are often characterized by rough interfaces as a consequence of diffusion of the evaporated metal atoms into the organic layer and are usually considered as the most complicated systems to describe. Under this circumstance, filled or empty electronic states are induced inside the fundamental gap of the organic semiconductor due to the formation of an organometallic complex or due to metal-induced defects. [176-177] Defect and chemistry-induced gap states are also observed on interfaces formed by molecular evaporation of organic semiconductors on reactive metals surfaces. [160] However, the interfaces are more abrupt and less reactive in comparison to those prepared by evaporating the metal onto the organic semiconductor. This is due to the much lower heat of adsorption of organic molecules and also the higher stability of metal/inorganic semiconductor surfaces. Some of the interfaces presented in Chapter 4 are of this type.

Several parameters play important roles and can affect the final energy-level alignment as follows: (i) chemical bonding between the metal and the organic molecule usually leads to charge transfer at the interface to the molecule or to the metal. This introduces a dipole-induced potential at the interface and results in a downshift or an upshift of the vacuum level. [143, 153, 178] (ii) As a result of chemisorption, the organic molecules and the metal surface are in close proximity, which gives rise to a pronounced "push-back" or "pillow" effect as described previously, the metal surface dipole is modified and the vacuum level is downshifted. (iii) The intrinsic dipole of the organic material can also play a role and make the system more complex. All these factors affect the metal work function at the interface and the overall shift in the vacuum level will be the sum of these contributions. In the following, a basic model outlined by Crispin et al. in order to describe this type of interface is described. [153]

When there is a significant overlap of the metal continuum states and the resonance of molecular states at the interface as a result of chemisorption, a rearrangement of the electron densities can happen due to formation of chemical bonds. This leads to a partial charge transfer between the metal side and the organic side, the direction of which is dictated by the chemical potential, μ, of the two species. In general, the direction of charge transfer is from the material with the higher chemical potential to the one with lower chemical potential. Based on a fundamental thermodynamics approach, the chemical potential of a metal, μ_{sub}, and an organic molecule, μ_{org}, are defined by the work function, electron affinity, and ionization potential values as follows:

Equation 45 $$\mu_{sub} = -\Phi_{sub},$$

Equation 46 $$\mu_{org} = -(IP + EA)/2.$$

Using the simulation/experimental results for Φ_{sub}, IP, and EA, one can easily predict the direction of charge transfer, and thus, the dipole at the interface as well as the direction of the dipole-induced shift of the vacuum level. In order to determine the magnitude of the chemisorption-induced dipole energy, two more parameters should be known, namely the amount of electronic charge transfer, ΔN, and the distance between the organic molecule and the metal surface. The latter parameter is more complicated to determine and can be obtained experimentally (e.g. by X-ray Standing Wave technique) or by simulation approaches. The first parameter can be estimated using the concept of absolute hardness, η, using the following expression: [179]

Equation 47 $$\Delta N = {}^{1}\!/_{2}\frac{\mu_{sub}-\mu_{org}}{\eta_{sub}-\eta_{org}}.$$

The absolute hardness is inversely proportional to the density of states at the Fermi level and can produce significant differences in the charge transfer, interface dipole, and hence, the final energy level alignment at the interface. According to Equation 47, metals with relatively similar chemical potential but different absolute hardness leads to different amounts of charge transfer, and hence, can produce a significantly different energy level alignment at the interface with a given organic semiconductor. Indeed, a metal atom with larger absolute hardness is expected to accept less charge given the same difference in chemical potential with the organic molecule. Using the approach outlined above, the shift in the resulting work function, the value of $\Phi_{sub/org}$, and the chemisorbed-induced modifications to the molecular orbitals can be successfully modeled. As a final remark, one useful approach to reduce the complexity of the system is to consider the substrate with the first chemisorbed organic molecules as a "new" substrate. In this sense, only the molecular orbitals of the first monolayer of the molecules, which are in direct contact with the substrate, will undergo strong modifications. The rest of the molecules can be considered to be deposited on an organic-passivated substrate with weak physical interactions. Therefore, the ICT model can be applied using the work function of an organic-passivated substrate instead of a bare substrate.

4.3.2. Induced Density of Interface States

Another origin of the presence of gap states at the metal/semiconductor interface is the tailing of the metal electron wave function into the organic semiconductor with a short penetration depth depending on the semiconductor band gap. [180-182] This phenomenon is the result of a broadening of the semiconductor states due to the close proximity of and overlap with the continuum of metal states. It is also known as the metal-induced gap states (MIGS) or induced-density of interface states (IDIS). [139, 151, 171, 183] A combination of DFT, many-body, and Green-functions techniques are used to describe the interface in this model. The main idea is that the resonance of the molecular states with the metal continuum states results in shifting and broadening of molecular levels. Therefore, the HOMO and LUMO of the organic molecule can be hybridized by some interactions between the clean metal surface and the molecular orbitals without the formation of covalent bonds. The calculated energy broadening Γ_i for each molecular orbital energy E_i contributes to the density of states of the organic semiconductor at the interface through the Lorentzian function: [184]

Equation 48 $$\Gamma_i/2\pi[(E-E_i)^2+(\Gamma_i/2)^2].$$

The broadening of states at the interface strongly depends on the distance between the molecule and the metal substrate. Here, the central parameter is the concept of a charge neutrality level, E_{CNL}, originally proposed for inorganic semiconductors [185-186]; however, it is also suggested by Vázquez *et al.* for organic semiconductors within the framework of the IDIS model. [139, 151, 171, 183] The E_{CNL} describes the Fermi level of an organic molecule in the proximity of a metal surface when no charge transfer is considered. It is calculated by filling the induced density of states by the charge of the isolated and neutral molecule. If the Fermi level precisely aligns with the E_{CNL}, the total charge in the IDIS is zero. The E_{CNL} can be considered as a kind of electronegativity marker and defines the direction and magnitude of charge transfer. In this model, the driving mechanism is the alignment of the E_{CNL} with the Fermi level of the metal to reach thermodynamic equilibrium. This driving force is partially screened by the presence of an induced density of interface states. When bringing the organic material in contact with the electrode, if the metal work function is smaller than E_{CNL}, then electrons will flow spontaneously from the metal to the IDIS. Therefore, upon this charge transfer, the electrode progressively becomes positively charged and the organic semiconductor becomes negatively charged which develops a potential at the interface. The result is a dipole barrier shifting the vacuum level of the organic part upward, which reduces the energy difference between E_F and E_{CNL}. If the metal work function is larger than E_{CNL}, electrons will flow in the opposite direction, resulting in a dipole barrier and down-shifting of the organic semiconductor's vacuum level. The important factor, which determines to what extent E_F aligns with, or diverges from, E_{CNL}, is the density of states at or around E_{CNL}.

This model provides an explanation for the magnitude and the sign of the observed interface dipoles based on the partial alignment of the organic E_{CNL} and the Fermi level of the metal. Within the above mentioned description, the total dipole at the metal/organic interface in the IDIS model [139] is given by:

Equation 49 $$\Delta^T = S\left(\Delta^P + \Delta^{mol}\right) + (1-\mathrm{S})(\Phi_M - E_{CNL}),$$

where Δ^p is the contribution to the dipole due to the "pillow" effect, Δ^{mol} is the dipole generated due to the molecule's permanent dipolar moment with a non-zero component perpendicular to the interface. As can be seen, this equation also incorporates the effect of the interface parameter S. It describes the ability of the material to screen the potential difference at the interface and is defined in terms of the density of states at the Fermi level, the interface area of the molecule, A, and the distance, $d_{metal/mol}$, between the molecule and the metal substrate:

Equation 50 $$S = 1/(1 + 4\pi e^2 D_{is} d_{metal/mol}/A).$$

As the initial difference between the work function of the metal and the E_{CNL} of the organic molecules is reduced by the S parameter, the resulting work function for the organic/metal interface is given by the following formulae, which is the central equation in the IDIS model [139] for metal/organic interfaces:

Equation 51 $$E_F - E_{CNL} = \mathrm{S}\left(\Delta^P + \Delta^{mol}\right) + \mathrm{S}(\Phi_M - E_{CNL}).$$

One can clearly conclude from Equation 50 that by increasing the density of interface states, the interface parameter S decreases, and consequently, the position of the interface Fermi level as well as the charge injection barriers become independent of the metal work function. In the limit of a large density of interface states and strong Fermi level pinning regime, $S \approx 0$, the total dipole based on Equation 49 is equal to the energy difference between the metal Fermi level and E_{CNL} of the organic semiconductor, since they tend to align at equilibrium. The final energy level alignment depends on the initial offset between E_F and E_{CNL} as well as the efficiency of the potential difference screening at the interface, S parameter. If no screening happens at all, then the total interface dipole will be $\Delta^T = \Delta^p + \Delta^{mol}$ and the Fermi level is given by the following relation: $E_F = \Phi_M + (\Delta^p + \Delta^{mol})$.

Using the same assumptions of Lorentzian broadening of the molecular orbital energies as well as the concept of charge neutrality level, Vazquez *et al.* tried to formulate and predict the energy-level alignment for organic/organic semiconductor heterojunctions as follows:

Equation 52 $$\left(E_{CNL_1} - E_{CNL_2}\right)_{final} = S_{OO}\left(E_{CNL_1} - E_{CNL_2}\right)_{initial},$$

Equation 53 $$\Delta_{OO}^{T} = S_{OO}\Delta^{mol} + (1 - S_{OO})\left(E_{CNL_1} - E_{CNL_2}\right)_{initial},$$

where Δ_{OO}^{T} is the total dipole, Δ^{mol} is the molecular dipole, E_{CNL1} and E_{CNL2} are the energy of the charge neutrality level for organic semiconductors, and S_{OO} is the screening parameter for organic heterojunction which can be calculated as: [139, 151, 187]

Equation 54 $$S_{OO} = \frac{1}{2}\left(\frac{1}{\varepsilon_1} + \frac{1}{\varepsilon_2}\right),$$

where ε_1 and ε_2 are the static dielectric constants of both media. Analogous to metal/organic interfaces, it is considered that at organic/organic interfaces, the molecular orbitals are hybridized, which results in a broadening of the HOMO and LUMO energy levels at the interface between the two organic media. Therefore, a continuous density of states is developed inside the fundamental gap of organic semiconductors, leading to charge flow from E_{CNL} of one organic side into the empty states of the other organic semiconductor with lower-laying E_{CNL}. As apparent in Equation 52, the final alignment at the organic/organic interface is determined by the offset of charge neutrality levels at the initial state as well as the screening parameter. The total interface dipole at the interface is also determined by the mentioned parameters as well as the molecular dipole (since the size of orbitals in both organic materials are similar, a contribution to the dipole due to the "pillow" effect does not appear). According to Equation 54, the potential drop is considered to take place at the mid-distance between two organic media. It should be emphasized that the concept of the charge neutrality level and the IDIS model is proposed for weakly interacting organic/metal and organic/organic interfaces which do not account for the cases where defect- and/or chemistry-induced gap states are present at the interface. This model was almost successful in correctly predicting the interfacial energy level alignments (qualitatively and in some cases quantitatively); [139, 151, 171, 183] however, it is limited to single molecular layers of organic semiconductors, thus, it fails to see the band-bending across the organic film.

Electrostatic Potential Model: Oehzelt *et al.* [137, 188-192] recently proposed numerical electrostatic potential calculations with the capability to simulate more than one monolayer and also to account for band-bending. It has been used to understand the origin of universal Fermi level pinning of the investigated organic semiconductor molecule, PTCDA, and its underlying mechanism in Chapter 4. This model discretizes the organic deposited film into layers of thickness Δx and distance x from the substrate in order to calculate the amount of transferred charges in each layer, therefore it can see the effect of thickness and the spatial profile of charge distribution (interfacial dipole and/or band bending). The core formula here, which specifies the charge density, $\rho(x)$, in different thicknesses of the deposited organic film is given by:

Equation 55

$$\rho(V(x)) = e \cdot n \cdot \left\{ \int_{-\infty}^{+\infty} dE \cdot f_H(E) \cdot D_H[E + eV(x)] - \int_{-\infty}^{+\infty} dE \cdot f_L(E) \cdot D_L[E + eV(x)] \right\}$$

where *n* is the number of molecules per unit area and per discretization interval Δx, $f_H(E)$ and $f_L(E)$ are the Fermi functions for each individual energy levels, $V(x)$ is the electrostatic potential at the position *x* from the substrate and finally $D_H[E+eV(x)]$ and $D_L[E+eV(x)]$ are the energy distributions of the HOMO- and LUMO-derived levels. This model takes into account a continuous density of states for molecular levels rather than discrete electronic states. In fact, Equation 55 shows the density profile of charge carriers in organic molecules according to Fermi statistics and the first and second integral correspond to the number of holes and electrons in occupied and unoccupied density of states, respectively. For simplicity, they consider one Gaussian peak centered at the HOMO maximum, E_H, with a standard deviation of σ_H (Equation 56) and another peak centered at the LUMO maximum, E_L, with a standard deviation of σ_L (Equation 57):

Equation 56

$$D_H(E + eV(x)) = G_H(E + eV(x)) = \frac{1}{\sigma_H\sqrt{2\pi}} exp\left[-\frac{(E+eV(x)-E_{HOMO})^2}{2\sigma_H^2}\right],$$

Equation 57

$$D_L(E + eV(x)) = G_L(E + eV(x)) = \frac{1}{\sigma_L\sqrt{2\pi}} exp\left[-\frac{(E+eV(x)-E_{LUMO})^2}{2\sigma_L^2}\right].$$

The standard deviation for the organic HOMO and LUMO can be estimated from the full width at half maximum (FWHM) of experimental UPS and inverse photoemission spectroscopy (IPES) measurements. The HOMO and LUMO centers can be found using *IE* and *EA* of the organic molecules. As the position of *IE* was recognized through the position of the intercept between the tangent line of the HOMO onset feature and the baseline of the spectrum, one should put the centers $2\sigma_{H/L}$ away from the onset edges. By considering the layer-by-layer deposition for organic molecules on the substrate, Δx can be chosen equal to the distance between stacking planes, which corresponds to the height of one molecular layer. Assuming a single charging of each organic molecule, the Fermi function for each individual energy level can be obtained through Equation 58 and Equation 59 for the HOMO and LUMO, respectively.

Equation 58 $$f_H(E) = \frac{1}{\frac{1}{g_H}e^{-\beta(E-E_F)}+1}$$

Equation 59 $$f_H(E) = \frac{1}{\frac{1}{g_H}e^{-\beta(E-E_F)}+1}$$

Finally, numerical solving of the generalized one-dimensional Poisson equation (Equation 60) yields the electrostatic potential across the organic deposited film as a function of thickness, $V(x)$.

Equation 60 $$\nabla[\varepsilon(x)\nabla V(x)] = -\frac{\rho(V(x))}{\varepsilon_0},$$

where ε_0 is the vacuum permittivity and $\varepsilon(x)$ is the static dielectric constant for each discretization interval. The latter quantity was considered to be constant over the total thickness. Iterative solving of Equation 55 simultaneously with Equation 60 by considering the electric field equal to zero at the outside surface of the organic provides the charge density and electron potential energy as a function of organic film thickness. The organic film is assumed to be in thermal equilibrium with the substrate; hence, the Fermi level of the organic film is aligned with the Fermi level of the substrate, that is, its substrate work function, Φ_{sub}. The final injection barriers are obtained by the following expression: $\Phi_{EIB} = E_F - EA$ and $\Phi_{EIB} = IE - E_F$. It is worth pointing out that this is the basic version of the proposed model and there are some other parameters, which are currently not taken into account in the above-mentioned formulation. This includes: (i) different line shapes of the DOS for each discretization interval. (ii) The effect of possible polaronic states. (iii) The effect of image-charge screening by the substrate. (iv) The effect of different temperatures on the energy level alignment. (v) Additional molecular states, e.g. due to structural imperfections or defects. (vi) Broadening of the valence levels in response to the photoexcitation. In Chapter 4, extensions to this recently developed numerical model are introduced in order to investigate the electronic structure of PTCDA on a wide range of substrates with different work functions and coupling interactions.

5. Summary of the Results

In this section, summaries of the results of the present dissertation are briefly described. The detailed discussions and experimental procedures can be found in the respective chapters.

In chapter 2, indium oxide nanocrystals, degenerately doped with tin ("ITO") are used as nanoscale electrodes to investigate carrier transport through monolayers of semiconducting phthalocyanine. The native surfactant of tin-doped indium oxide nanocrystals is replaced after synthesis by the organic semiconductor copper 4,4′,4″,4‴-tetraaminophthalocyanine (Cu4APc) to fabricate conductive and optically transparent thin films of ITO nanocrystals cross-linked with monolayers of Cu4APc. It is demonstrated that *in-situ* ligand exchange of ITO nanocrystals at the liquid–air interface yields an electronically coupled network of well-separated nanocrystals. The material - which is a macroscopic, nanostructured thin film - can be viewed as a series circuit of resistors, consisting of repetitive units of two ITO nanocrystals connected by a layer of the semiconducting molecule. It is shown that without the phthalocyanine molecule, charge transport across the ITO network is poor and dominated by occasional hopping events. Upon replacing the native ligand sphere of the ITO nanocrystals by the semiconductor molecule, the conductivity jumps by nine orders of magnitude suggesting that the phthalocyanine derivative acts as an electronic linker. Photoemission spectroscopy is used to track the chemical changes on the nanocrystals' surface before and after ligand exchanges which develops a detailed picture of the various components that dominate the surface chemistry of this material. UV–vis–NIR, grazing-incidence small-angle scattering (GISAXS), and XPS results demonstrate the presence/binding of the semiconductor ligand between/to the ITO nanocrystals.

From a material's perspective, the approach to conductive networks of ITO nanocrystals introduced in Chapter 2 differs from previous studies by other groups in that rather than making "bare" inorganic surfaces (e.g. by thermal desorption of organic surface molecules), molecules are selected which are conductive themselves. In this sense, Chapter 2 is not only an investigation of charge transport through ITO nanocrystal networks, but even more so a study of transport through repetitive units of molecular resistors.

An additional aspect discussed in Chapter 2 are the optical properties of this hybrid material, which feature the visible absorption band of the HOMO-LUMO transition of the molecular conductor as well as the infrared plasmonic band of the quasi-metallic oxide nanocrystals. The presented thin-film preparation method in this chapter is generally suitable for the synthesis of all kinds of hybrid materials where plasmonic nanocrystals are in intimate contact with organic semiconductor molecules, which enables future studies of the antenna effect of the metallic particles onto light absorption by the molecules. The synthetic concept pursued in this chapter enables future testing of theoretical models for the description of transport through granular metal systems as well as investigations of the interplay between organic semiconductor molecules with plasmonic nanocrystals. Typically, such studies are performed with Au nanocrystals, where the carrier concentration is relatively high and fixed. ITO nanocrystals exhibit significantly lower and tunable carrier concentrations (by doping) which allows for an additional degree of freedom.

In Chapter 3, charge carrier transport and resistance-mediated vapor sensing in thin films of ITO nanocrystals cross-linked with semiconducting metal phthalocyanine derivatives of five different metal centers are studied. Here, arrays of ITO NCs cross-linked with different M4APc (M = Cu, Co, Fe, Ni, and Zn) molecules are fabricated and studied to understand the electron transport mechanism as well as the effect of the ligands' dielectric constant, which is strongly affected by the metal center of the molecule. Varying the metal center enables to systematically study the sole effect of the tunneling barrier height on charge transport through the nanocrystal array, while all other parameters are kept constant. Performing these studies in a large temperature window from 7 – 300 K allows to test the applicability of rivaling models for the description of charge transport in granular metals. The results presented in this chapter indicate that the dielectric constant of the semiconductor ligands significantly regulates charge transport, the Coulomb charging energy, and the localization length in particular.

It is found that transport in the presented materials is best described with multiple inelastic cotunneling, a mechanism in which large local charging energies are mitigated by a series of simultaneous tunneling events of several charge carriers. The resulting I–V characteristics as well as the temperature-dependent conductivity measurements indicate that at low temperatures, transport across the arrays occurs via a sequence of cotunneling events, each involving ~ 3–4 ITO NCs. In effect, the total resistance in this mechanism scales exponentially with the number of tunneling junctions, which bears exciting prospects for sensing applications. At higher temperatures, the number of hops decreases to one and cotunneling behavior makes way for sequential tunneling. The potential of this material for vapor sensing applications is investigated by dosing the materials with vapors of 4-methyl-2-pentanone (4M2P), toluene, 1-propanol, and water and concentrations as low as 100 ppm. It is observed that the sensitivities of the vapor sensing devices depend on the type of metal center. By testing different classes of analytes, different selectivities of the materials are identified, depending on whether the analytes behave more vapor- or more gas-like. From this, a general picture emerges, in which resistance changes by the vapor-like analytes are predominantly caused by film swelling, while gas-like analytes bind to the phthalocyanine metal center to induce a permittivity change. The latter leads to saturation at very low analyte concentrations and highlights the potential advantages of such hybrid materials with several binding sites and components for multivariable sensors. The results presented in Chapter 3 are not only of fundamental interest for a better understanding of charge transport in granular metals, but also demonstrate how such knowledge can lead to applications in future sensing devices by exploiting the particular physics of such materials. Along the same lines, the fast response, high sensitivity, robustness under ambient condition, room-temperature operability and optical transparency render phthalocyanine-coupled ITO NC superlattices promising materials for novel sensing applications.

In Chapter 4, the origin of the interface dipole between the important organic semiconductor perylene-3,4,9,10-tetracarboxylic dianhydride (PTCDA) and metals, oxides, and polymeric surfaces are investigated. The research presented in this chapter is motivated by a previously published report on Fermi level pinning of PTCDA on unreactive as well as reactive metal substrates. First the universal Fermi level pinning of PTCDA at the interface with practically every metallic substrate is reinvestigate by UPS and XPS. In the original work by Hill et al., [193] four metal substrates (Mg, In, Sn, Au) were studied in this respect to represent interactions with reactive as well as unreactive metal surfaces, and Fermi level pinning was found for a 64 Å thick PTCDA layer. The results presented in Chapter 4 expands this range of substrates to a total of eleven, including technologically highly relevant materials such as ITO and PEDOT:PSS. Most importantly, while the obtained data confirms the universal Fermi level pinning at 4.5 ± 0.1 eV *vs*. vacuum in excellent agreement with the original work by Hill et al. [193] for thick PTCDA layers, a pronounced deviation for thin PTCDA films is found for lower thicknesses. This thickness-dependence as well as the universal value for the work function of PTCDA on eleven different investigated substrates are explained by electrostatic calculations following a recently developed model by Oehzelt et al. [137] In continuation, extensions to this electrostatic model are introduced to explain the occurrence of universal Fermi level pinning of the organic semiconductor PTCDA at the interface with practically every substrate. While the original version of the model was successful in predicting the injection barriers for pentacene, it had limitations in the applicability for molecules exhibiting a large degree of Fermi level pinning on metals, such as PTCDA.

It is shown in Chapter 4 that the universal Fermi level pinning of PTCDA is realized by either introducing a gradual change in the DOS shape from a Lorentzian or Voigt profile at the interface to a Gaussian distribution far away from the surface of the substrate, mimicking a long-range influence of the substrate far into the organic semiconductor film, or considering a direct gap-state in the DOS shape for the first layers at the interface. This assumption, which predicts injection barriers in excellent agreement with experiment, is corroborated by detailed XPS and UPS measurements demonstrating experimentally such gradually damped Lorentzian peak profiles of the molecular HOMO or gap states. These modifications have the potential to increase the applicability of the model to a much wider range of organic semiconductors. The results presented in this chapter highlight the pivotal role of the induced density of interface states for the interfacial energy level alignment of PTCDA. In addition, it greatly expands the applicability of a powerful electrostatic model to a much wider range of organic semiconductors, allowing for accurate quantitative predictions for molecules with strong Fermi level pinning in general. Moreover, the results should facilitate the application of numerical electrostatic models for the prediction of the interfacial electronic structure of organic semiconductors on metals with strong interactions.

Chapter 2

Surface Functionalization with Copper Tetraaminophthalocyanine Enables Efficient Charge Transport in Indium Tin Oxide Nanocrystal Thin Films

Manuscript 1

Surface Functionalization with Cu Tetraaminophthalocyanine Enables Efficient Charge Transport in Indium Tin Oxide Nanocrystal Thin-Films

Mahdi Samadi Khoshkhoo[†], *Santanu Maiti*[‡], *Frank Schreiber*[‡,§], *Thomas Chassé*[†,§], *and Marcus Scheele*[†,§,*]

[†] Institute of Physical and Theoretical Chemistry, University of Tübingen, Auf der Morgenstelle 18, 72076 Tübingen, Germany.

[‡] Institute of Applied Physics, University of Tübingen, Auf der Morgenstelle 10, 72076 Tübingen, Germany

[§] Center for Light-Matter Interaction, Sensors & Analytics LISA+, University of Tübingen, Auf der Morgenstelle 15, 72076 Tübingen, Germany.

Abstract

Macroscopic superlattices of tin-doped indium oxide (ITO) nanocrystals (NCs) are prepared by self-assembly at the air/liquid interface followed by simultaneous ligand exchange with the organic semiconductor Cu-4,4`,4``,4```-tetraaminophthalocyanine (Cu4APc). By using X-ray photoelectron spectroscopy (XPS), grazing-incidence small-angle X-ray scattering (GISAXS), ultraviolet-visible-near infrared (UV–vis–NIR) spectroscopy, we demonstrate that the semiconductor molecules largely replace the native surfactant from the ITO NC surface and act as cross-linkers between neighboring particles. Transport measurements reveal an increase in electrical conductance by nine orders of magnitude, suggesting that Cu4APc provides efficient electronic coupling for neighboring ITO NCs. This material provides the opportunity to study charge and spin transport through phthalocyanine monolayers.

Keywords: Colloidal Nanocrystals, Self-Assembly, Thin Films, Molecular Electronics, Nanoparticles, Indium Tin Oxide (ITO), Transparent Electrodes, Phthalocyanine.

2.1. Introduction

Exploiting the optoelectronic behavior of molecular monolayers or individual molecules sandwiched in between two electrodes bears exciting opportunities for nanoscale electronic devices. [194-195] Such "molecular electronics" is considered a promising means to continue the increasing miniaturization of memory chips as the length scale of current transistors is approaching the size of individual molecules. [196-197] The physics of molecular electronics is typically characterized by different transport mechanisms compared to conventional bulk crystalline conductors which holds for new possibilities to e.g. tune electronic coupling, design novel thermoelectric materials and sensors. [198-203] In order to study these effects, a key question to address is the choice of the contacts for the molecular junction. [204-206] One possibility in this respect are metal colloidal nanocrystals which are relatively cheap to synthesize, solution-processable and tunable in shape. [207-211] Of particular advantage for molecular optoelectronics are (doped) metal oxide nanocrystals, which combine high optical transparencies in the visible regime with metallic electric conduction. [212-216] Such transparent electrodes are crucial in the design of single-molecular devices for photo-switching and light-emitting diodes, which are currently two very promising target applications of molecular electronics. [217-218]

In this work, we replace the native surfactant of tin-doped indium oxide (ITO) nanocrystals after synthesis by the organic semiconductor Cu 4,4‘,4‘‘,4‘‘‘-tetraaminophthalocyanine (Cu4APc) to fabricate conductive and optically transparent thin films of ITO nanocrystals cross-linked with monolayers of Cu4APc. While previous studies typically applied thermal annealing to replace the surfactant from the surface of the metal oxide nanocrystals and/or induce particle sintering, a deliberate functionalization of these nanocrystals with conductive molecules has not been demonstrated to the best of our knowledge. [219-224] Metal Phthalocyanines with non-zero spin are actively pursued as molecular magnets for single-molecule spintronics. [225-228] As recently suggested, the spin state of Cu phthalocyanine molecules can potentially be manipulated by an external optical stimulus, holding for a promising combination of molecular optoelectronics with spintronics. [229] While the single molecule deposition of unsubstituted phthalocyanines is challenging due to their limited solubility, Cu4APc is easily soluble in common organic solvents. We show here that this allows synthesizing a hybrid material consisting of a network of isolated ITO nanocrystals, which are electronically connected by the molecular conductor.

2.2. Methods

2.2.1. Synthesis of ITO Nanocrystals: ITO NCs were synthesized based on a previously reported method. [214] Briefly, an octadecene (20 mL ODE) solution of indium and tin acetate (0.95 mmol $In(Ac)_3$ and 0.05 mmol $Sn(Ac)_2$, respectively) with myristic acid (3 mmol MA) was degassed at 120 °C for 2 h in a three-neck flask attached to a Schlenk line. A similar preparation was performed with an ODE (10 mL) solution of octadecylamine (3 mmol ODA). The carboxylic solution was heated to 295 °C under nitrogen in order to yield carboxylate precursors. Particle nucleation was initiated by rapid injection of the amine solution. The solution temperature was dropped to 280 °C and was maintained for 1 h. The solution color gradually changed from yellow to dark green within 5 minutes after injection. Afterwards, the temperature was further reduced to 240 °C for 1 h. The NCs were collected by polarity-mediated precipitation using ethanol/chloroform, utilizing a high-speed centrifuge. Finally, the NCs were dispersed in *n*-hexane.

2.2.2. Synthesis of Cu 4,4‘,4‘‘,4‘‘‘-tetraaminophthalocyanine (Cu4APc): Cu4APc was synthesized following a previously reported precedure.[230]

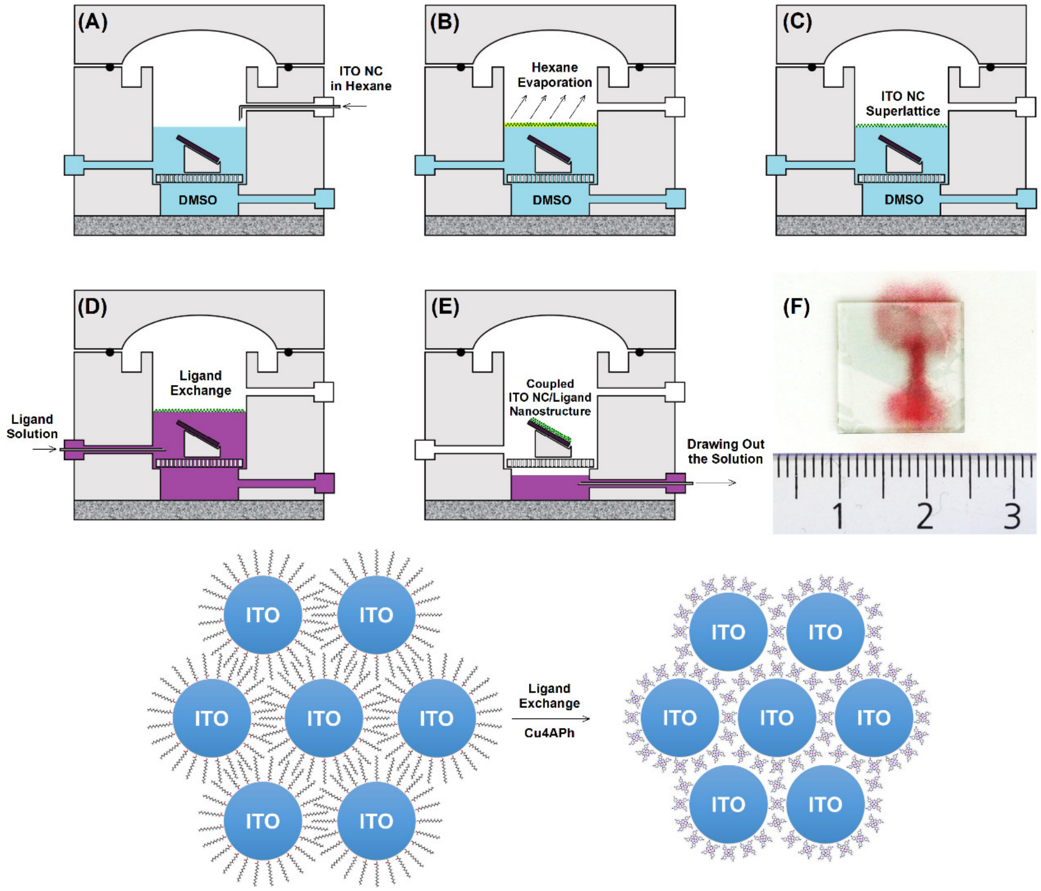

Figure 8. The fabrication process of electronically coupled large-area NC superlattice films. (A) The desired substrate is placed at the bottom of the chamber, and the chamber is filled with DMSO. A controlled amount of MA-capped ITO NCs dispersed in hexane is introduced to the DMSO surface. (B-C) An ultrathin film of NCs is formed upon spreading the NC dispersion on the liquid subphase and evaporation of hexane. (D) A solution of Cu4APc in DMSO is injected into the subphase to start the in-situ ligand exchange process. (E) The free-floating ligand-exchanged NC superlattice is transferred to the substrate by retracting the solution from the bottom of the chamber. (F) Photograph of the macroscopic, transparent, crack-free film of ITO NC / Cu4APc superlattice on a glass substrate.

2.2.3. Self-assembly of NC Superlattice and In-Situ Ligand Exchange at the Liquid-Air Interface: Electronically coupled large-area NC superlattice films were prepared by a

Langmuir-type assembly at the liquid/air interface. [231-234] The fabrication process was carried out in a home-built Teflon chamber which is shown in Figure 8. In the first stage of the preparation, the desired substrate (TEM grid, amorphous glass, Au-patterned Si wafer for conductivity measurements, etc.) is placed at the bottom of the chamber, which is then filled with DMSO as a subphase liquid. 35 µl of MA-capped ITO NCs dispersed in hexane (with the concentration of approximately 1 mg/ml) is introduced to the DMSO surface (~ 200 µl/min) which after ~5 minutes leads to the self-assembly of a 1-2 monolayer thick film after evaporation of hexane (Figure 8A-C). In the second stage of the process, a solution of 0.25 mg/ml Cu4APc in DMSO is slowly injected into the subphase by a syringe in order to start the in-situ ligand exchange (Figure 8D). By adding the solution of Cu4APc to the subphase, simultaneous diffusion of phthalocyanine molecules into the NC superlattice and diffusion of primary organic ligand out of the floating film completes the ligand exchange process overnight. Finally, the free-floating ligand-exchanged NC superlattice is transferred to the substrate by retracting the solution from the bottom of the chamber and lowering the NC superlattice onto the solid substrate (Figure 8E).

2.2.4. Instrumentation: Particle size and shape were verified by Scanning transmission electron microscopy (STEM) on a Hitachi SU 8030 microscope operating at 30 kV. The crystallographic phase of ITO was determined by X-ray diffraction (XRD) with an XRD-7000 X-ray diffractometer, Shimadzu Co., Japan, and Cu Kα radiation with λ=1.5405 Å. In order to evaluate the dopant incorporation and surface characteristics, XPS measurements were carried out using a photoelectron spectrometer which was equipped with a conventional XR50 X-ray source (Al Kα, working at 12.5 kV and 20 mA, 1486.61 eV) and a PHOIBOS 100 MCD analyzer (SPECS). The pressure in the analyzer chamber was maintained below 3×10^{-10} mbar during the measurements. No changes in the core level signals of the as-prepared films and the films under X-ray irradiation were observed that represent the stability of the molecules during the data acquisition time. The resolution in XPS measurements was determined as 0.8 eV (calculated from the width of the Fermi edge on the Au substrate). The binding energies were corrected for electrical charge effects by referencing to Au 4f and adventitious C1s peak, which were assumed to have a binding energy of 84.0 eV and 284.8 eV respectively. The photoelectrons were detected at a takeoff angle of $\Phi = 0°$ with respect to the surface normal (normal emission). Each spectrum was corrected for the satellite peaks ($\Delta = 9.8$ and 11.8 eV from AlKα3 and AlKα4, respectively). Data fitting was performed using Gauss-Lorentz profiles. [235] The background was calculated using the Shirley method. The relative tin content was determined by the ratio of the Sn3d peak area to the total area of the In and Sn3d peaks, scaled by the relative photoionization cross-section for each element. The error introduced by differences in the escape depth of photoemitted electrons is neglected, since the binding energies of $3d_{5/2}$ signals for both In and Sn are close to each other. GISAXS measurements were performed at a laboratory-based Xeuss 2.0 instrument from Xenocs, France, with a wavelength of 1.5405 Å (CuK_α). An incident beam of size 0.5 x 0.5 (V x H) mm^2 was used with a grazing angle of 0.2^o onto the surface of the sample. A two-dimensional Pilatus 300K detector was employed at a distance of 2.5m from the sample center to collect the scattering spectra at low momentum transfer vector (q) value – to resolve the NPs size. Each sample was measured for 1 hour to achieve good statistics. Optical measurements were performed on solid state films on glass substrates as well as dilute dispersions in tetrachloroethylene using an UV–vis–NIR spectrometer (Agilent Technologies, Cary 5000). The electrical measurements on the 2D NC array were performed using a Keithley 2634B dual source-meter unit, controlled by the included test script builder program. The free-floating ligand-exchanged NC superlattices were deposited on a commercially available bottom-gate, bottom-contact transistor substrates (Fraunhofer Institute for Photonic Microsystems, Dresden, Germany) with interdigitated Au electrodes of 10 mm width and varying channel lengths (2.5, 5, 10, and 20 µm, see Figure S3, Appendix A) followed by annealing at 250 °C for 2 h under nitrogen atmosphere for further drying and improving the electrical conductance. Substrates were contacted using a home-built probe station enclosed in a nitrogen glovebox.

2.3. Results

Figure 9A shows STEM images of a 1-2 monolayer thick film of MA-capped ITO NCs self-assembled into 2D close-packed arrays at the air/liquid interface recorded on a TEM grid. In contrast to other approaches, [233, 236] the interface method yields 1-2 monolayer thick, large-area, free of crack interlinked nanoparticle arrays which can be easily transferred to the desired substrate. High-magnification STEM (Figure S1B, Appendix A) reveals that the NCs are well separated from each other by the myristic acid chains. The average particle size is found to be 6.8 nm by evaluating several STEM pictures from the same grid and counting more than 500 particles. The standard deviation with respect to the size is evaluated to be ~ 15%. The histogram for size analysis can be found in Appendix A (Figure S2). Figure 9B displays the XRD patterns for ITO NC films before and after annealing at 250 °C. First, the highly crystalline nature of the synthesized NCs is confirmed. The obtained patterns match very well with those of the standard cubic bixbyite phase of In_2O_3 (JCPDS no. 06-0416) and are in good agreement with those reported for ITO NCs in literature. [214-215, 237] Next, the X-ray diffraction pattern and peak widths remain unchanged after annealing which provides supporting evidence that the crystal size remains fixed and the NCs do not fuse upon annealing.

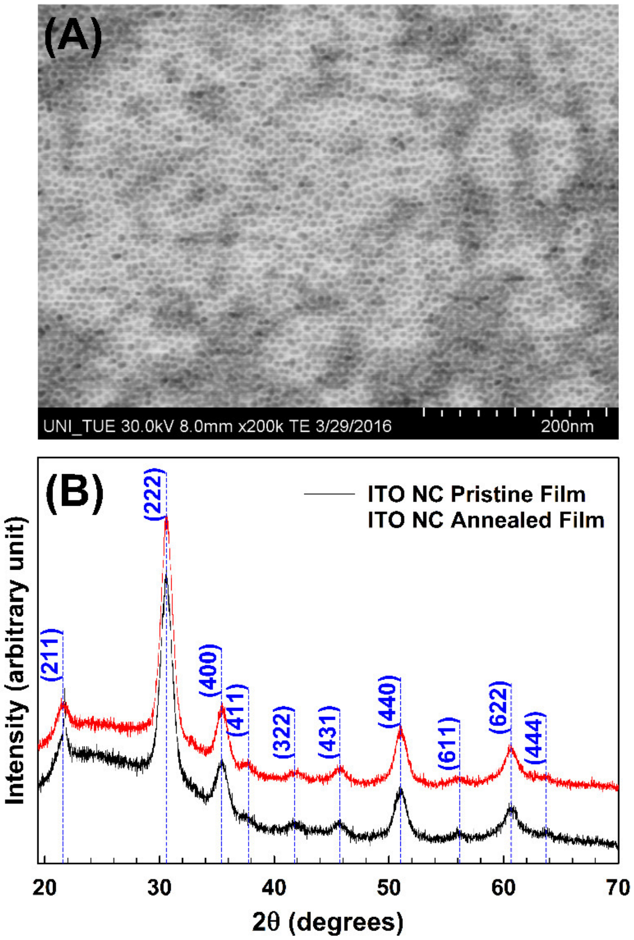

Figure 9. (A) Electron microscopy images of 1-2 monolayer thick film of myristic acid-caped ITO NC prepared at an air/liquid interface. (B) XRD patterns of ITO NC films before and after annealing.

XPS provides valuable information about compositional changes in the near-surface region. Figure 10 shows the XPS spectra of the ITO NC superlattices prepared by the interface method before and after ligand exchange. As expected, one can detect indium, tin, oxygen, carbon (not shown here), and nitrogen. The latter element is only detected after ligand exchange. The individual core level spectra of O1s, In3d, Sn3d, and N1s are presented in Figure 10A, B, C, and D, respectively. The O1s core-level spectra could be fitted with four components of identical peak shape but various intensities labeled O_{I} (530.2 eV), O_{II} (531.5 eV), O_{III} (532.5 eV), and O_{IV} (533.5 eV) (see Figure 10A). After ligand exchange, the intensity of the O_{IV} component is significantly decreased and the O_{III} / (O_{I} + O_{II}) intensity ratio is considerably reduced. No change in the O_{I}/O_{II} intensity ratio is observed. The spin-orbit split In3d and Sn3d signals can be decomposed into two doublet peaks labeled In_I and In_{II} ($In3d_{5/2}$ component centered at 444.6 and 445.8 eV, respectively), and the peaks labeled Sn_I and Sn_{II} ($Sn3d_{5/2}$ component centered at 486.5 and 487.7 eV, respectively). No changes in their relative intensities are detected after ligand exchange (see Figure 10B and C). The relative tin content is calculated to be ~ 4.6 %, by taking the sensitivity factors of 13.32 and 14.8 for $In3d_{5/2}$ and $Sn3d_{5/2}$, respectively; using the ratio of the Sn3d peak area to the total area of the In and Sn3d signals. The observed line widths and positions of the main components of the $In3d_{5/2}$ (BE 444.6 eV) and $Sn3d_{5/2}$ (BE 486.5 eV) are in good accordance with earlier reports on the In^{3+} and the Sn^{4+} oxidation state in ITO. [238-239] The second components centered at 445.8 eV for $In3d_{5/2}$ and 487.7 eV for $Sn3d_{5/2}$ are attributed to surface-bound hydroxide. [240] Figure 10D represents the N1s core-level signal for the ITO NCs superlattice film before and after ligand exchange. Before ligand exchange, no nitrogen signal can be detected in the film, but a strong signal appears after the exchange process. The inset in Figure 10D shows the chemical structure of Cu4APc.

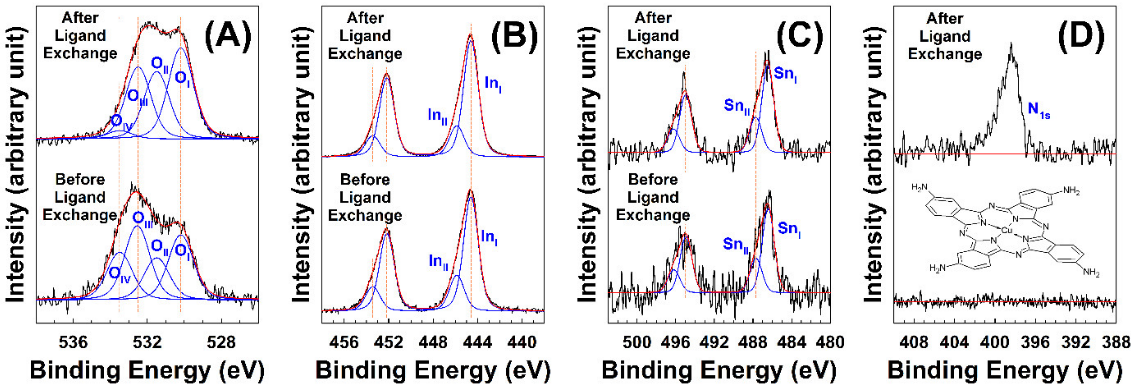

Figure 10. Core level XPS spectra of (A) O1s, (B) In3d, (C) Sn3d, and (D) N1s region of the ITO NCs superlattice films prepared by interface method before and after ligand exchange.

Grazing-incidence small-angle X-ray scattering (GISAXS) is a very powerful tool for characterizing in-plane density correlations (i.e. typical distances etc.) of nanoscale objects at surfaces or in thin films. [241-242] The GISAXS technique is highly surface sensitive as the incidence angle of X-ray is chosen near the critical angle of the film material, thus leading to a limited penetration depth (typically down to a few nanometers, if pushed to the extreme), and therefore reducing the scattering contribution of the substrate. GISAXS can provide information such as in-plane structural correlations or ordering among the assembled objects embedded in thin films and sizes of nano-objects including nanoparticles and islands. [241-245] This technique is used here to probe the ITO NC correlations in the prepared film of hybrid

NCs-organic molecule network and to study the effect of ligand exchange and thermal annealing onto the self-assembled hybrid structure. For self-assembled monolayer films, the GISAXS patterns used to have largely vertical rods spectra whose position along q_y direction indicates the in-plane periodicity between the NCs, whereas the width of these reflections represents the degree of ordering among the NCs in the film. For MA-capped ITO NCs, we find an in-plane correlation ‘arc-like rod’ scattering spectra at $q_y = 0.0715$ Å which corresponds to the in-plane radial average distance of 8.8 nm between the NCs. We attribute the ‘arc-like rod’ shape of the GISAXS signal to the presence few bi(-multi)layer/buckled islands on top of a self-assembled hybrid monolayer of NCs and MA. [245] We note that while the relatively broad scattering patterns and the rather broad size-distribution of the ITO NCs make conclusions on the exact absolute distances difficult, the relative changes upon sample annealing and ligand exchange as discussed in the following should be considered reliable. After thermal annealing of the same film at 250 □C for 2 hours, the overall intensity of the GISAXS pattern is reduced by a factor of 1.4 (Figure 11B), possibly due to coalescence of some of the nanoparticles. More importantly, the in-plane correlation peak shifts towards higher q_y, corresponding to a decrease of the interparticle spacing along the in-plane direction by ~ 0.6 nm. We attribute this contraction to the partial removal of MA. This also supported by the decreased scattering intensity, indicating a partial destruction of the superlattice or reduction of domain sizes. The GISAXS pattern of ITO NCs from the same batch after ligand exchange with Cu4APc is depicted in Figure 11C. The first-order correlation peak is found at $q_y = 0.0785\ \text{Å}^{-1}$, corresponding to an average in-plane correlation distance between the nanoparticles of about 8.0 nm. In contrast to the MA-capped NCs, this distance is observed for the sample before annealing, such that it cannot be explained with thermal desorption or possible particle fusion. We attribute this to the significantly smaller size of Cu4APc (~1.1 nm), acting as a cross-linker between adjacent NCs and establishing the ligand exchange process. We note that there is no further shift along q_y upon annealing the exchanged film at 250□C for 2 hours other than a reduction in scattering intensity (Figure 11D). The absence of significant changes in real-space correlation distances may be due the very strong interaction between ITO NCs and Cu4APc ligands and also the high melting point of the Cu4APc ligand itself.

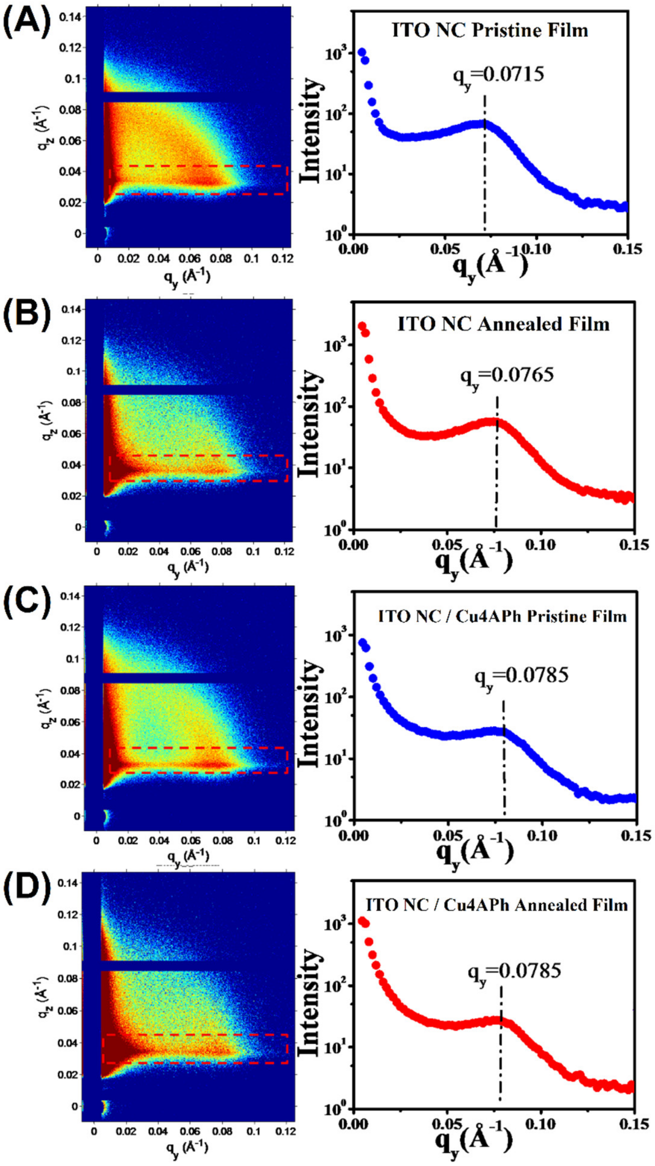

Figure 11. GISAXS of self-assembled ITO NCs arrays (A) capped with MA, (B) capped with MA and annealed at 250 °C for 2 h, (C) after ligand exchange with Cu4APc, and (D) after ligand exchange with Cu4APc and annealed at 250 °C for 2 h. Right Panel: The extracted line profiles from the corresponding GISAXS images as a function of in-plane scattering vector q_y. To improve the statistics of the line profiles, the ROI (red dotted box) was integrated along the q_z direction. The footprint of the incident beam is 0.5 mm × 100 mm.

Figure 12A displays the UV–vis–NIR absorption spectra of as-prepared ITO NC films before and after ligand exchange (red and black curves, respectively) as well as a dilute dispersion of MA-capped ITO NCs in tetrachloroethylene (blue curve). All samples show the interband transition of ITO at around 400 nm and a strong localized surface plasmon resonance (LSPR) peak in the near infrared region indicating a significant density of free electrons. The position of the LSPR peak is red-shifted from 1740 nm for ITO NCs in dilute dispersion to 1984 nm for

ITO NCs in thin films. These values are in good agreement with those reported in the literature.[215, 246] After ligand exchange with Cu4APc, we observe the appearance of a new absorption band at 736 nm which is assigned to Cu4APc. In addition, the LSPR peak is further red-shifted from 1984 nm to 2016 nm. Figure 12B shows the UV–vis–NIR spectra of the same two films (MA- or Cu4APC-capping) after annealing at 250 °C for 2 h under nitrogen atmosphere. Neglecting the small change in the shape of the Cu4APc feature, the maximum remains at 736 nm. In contrast, the LSPR peaks are significantly red-shifted to 2103 nm, but the effect is the same for both films.

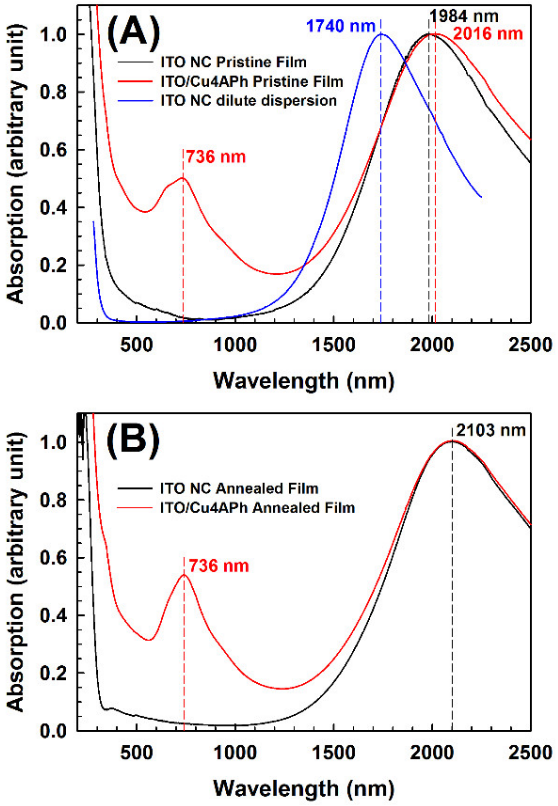

Figure 12. (A) The UV–vis–NIR absorption spectra of ITO NC thin films before and after ligand exchange with Cu4PAc (red and black curves, respectively) as well as a dilute dispersion of ITO NCs in tetrachloroethylene (blue curve) (B) The UV–vis–NIR absorption spectra of the same films after annealing at 250 °C for 2 h under nitrogen atmosphere.

In order to compare the electrical properties of the ITO NC films before and after ligand exchange, we extract the sheet resistance by low-field 2-point current-voltage (I-V) measurements on substrates with pre-patterned Au contacts in Figure 13. The sheet resistance is obtained from $R_s = Rw/l$, where R is the measured resistance of the 2D NC arrays, with *L* and *w* the length and width of the channel between two gold electrodes (2.5 µm and 10 mm, respectively). For the MA-capped ITO NCs, we find $R_s = 3.72\times10^{15}$ Ω/□ (blue circles) for films prepared at room temperature and $R_s = 2.45\times10^{13}$ Ω/□ (dark-blue circles) after annealing. Ligand exchange with Cu4APc reduces the sheet resistance to 5.97×10^{7} Ω/□ for films prepared at room temperature. Annealing further reduces R_s by more than one order of magnitude (dark-red circles, 1.94×10^{6} Ω/□). Thus, a dramatic increase in conductivity of the films by more than nine orders of magnitude is observed after ligand exchange and annealing. A photograph of ITO NC films after exchange with Cu4APc on a pre-patterned substrate for conductivity measurements is shown in the inset of Figure 13. In order to evaluate the contact resistance, we measure the total resistance for varying contact distances (see Appendix A, Figure S3) and apply transmission line method (TLM). [247-248] The *y*-intercept of the fitted line gives the contact resistance and the slop multiply by *w* yields the sheet resistance. The extracted contact resistance is at least two-orders of magnitude lower than the measured total resistance, indicating that its effect on our system is negligible.

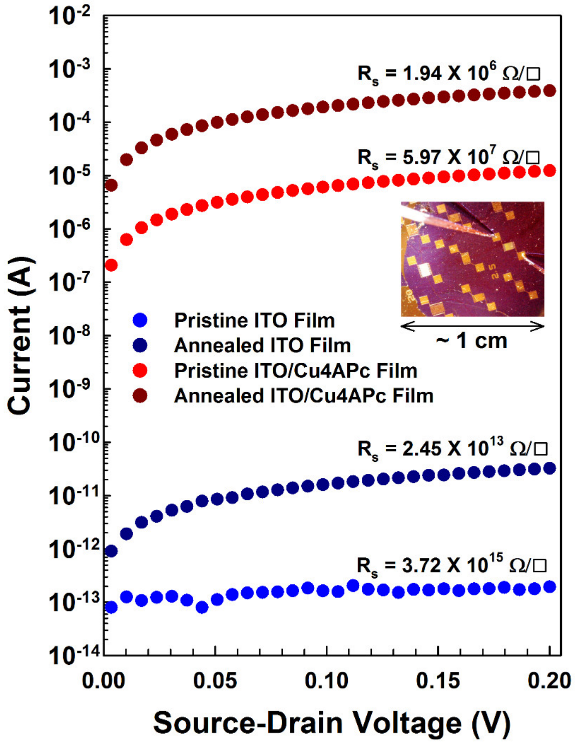

Figure 13. Current–voltage (I–V) characteristics as well as the sheet resistance measured for different processing histories of ITO NC films. Blue circles: MA-capped ITO NC films, dark-blue circles: MA-capped ITO NC films after annealing, red circles: ITO NC films after ligand exchange with Cu4APc, and dark-red circles: ITO NC films after ligand exchange and annealing. The graph is plotted on a logarithmic scale for better comparison. Inset: photograph of a typical ITO NC film after exchange with Cu4APc on a pre-patterned substrate with Au contacts for I-V measurements.

2.4. Discussion

In this section, we first utilize the XPS data in Figure 10 to develop a chemical understanding of the ITO NC surface before and after ligand exchange with Cu4APc. We continue with analyzing the changes in optical (Figure 12) and electrical properties (Figure 13) upon ligand exchange with respect to the changes in the dielectric environment as well as structural changes elucidated by GISAXS in Figure 11. Finally, we comment on the transport properties of ITO-Cu4APc networks in the light of other reports on the electrical properties of metallic NCs.

The chemical nature of the ITO NC surface before and after ligand exchange

To elucidate the reactions involved in the ligand exchange from MA to Cu4APc at the ITO NC surface, we use our XPS results and previously reported XPS studies on macroscopic ITO samples to propose a possible scheme.[238-240, 249-251] With respect to the four different oxygen species found in Figure 10 (O_I to O_{IV}), we make the following assignments: (O_I, BE 530.2 eV) O^{2-} ions bound to In^{3+}-atoms; (O_{II}, BE 531.5 eV) O^{2-} ions next to vacancies in the In_2O_3 lattice;[239-240, 251-252] (O_{III}, BE 532.5 eV) oxygen-atoms in hydroxyl groups;[240, 251] and (O_{IV}, BE 533.5 eV) carboxylic oxygen as part of the CO_2^--groups in MA and/or adventitious contaminations.[253] It is well-known that MA readily chemisorbs to ITO surfaces via its carboxylic acid head group, for instance by protonating the bridging oxides and hydroxyl groups or bounding to oxygen vacancies.[249] Figure 14 shows schematic views of the possible ITO NC surface before ligand exchange (part A) and the more complex surface after ligand exchange (part B). As the film fabrication and the ligand exchange processes are both carried out in direct exposure to ambient air out of the glovebox, the residual water vapor can react with bridging oxygen atoms and also oxygen vacancy sites at the surface to form hydroxyl groups (Figure 14A). [250-251] After ligand exchange, the intensity of the O_{IV} signal is significantly decreased, suggesting that most of the MA molecules have been replaced from the ITO NC surface. Simultaneously, the new N1s core-level signal confirms the presence of a nitrogen-rich species, such as Cu4APc (Figure 10D), in agreement with UV–vis–NIR results. This replacement is facilitated by the rather moderate binding strength of fatty acids to ITO.[240]

With respect to the preferred binding site of Cu4APc at the ITO surface, we suggest a reaction of the primary amino groups of the phthalocyanine and the NC surface hydroxyl groups according to:

$$CuPh(NH_2)_4 + (ITO\ NC)M^+OH^- \longrightarrow (NH_2)_3CuPh(NH){-}M(ITO\ NC) + H_2O$$

where M is the metal atom (In or Sn) at the surface. This is corroborated by our XPS results (Figure 10A), which indicate a substantial reduction of the $O_{III} / (O_I + O_{II})$ intensity ratio upon ligand exchange, that is, a loss of OH-groups. It is worth pointing out that Cu4APc might also bind "side-on" to the ITO surface via its metal center atom (Figure 14B). Although we detected a very weak signal from the metal center of Cu4APc (Cu 2p, data not shown), due to the low concentration of copper atoms (only one atom per ligand molecule) and strong attenuation of this signal by the surrounding atoms the signal strength is too small to derive any meaningful information on the chemical environment of the Cu atom.

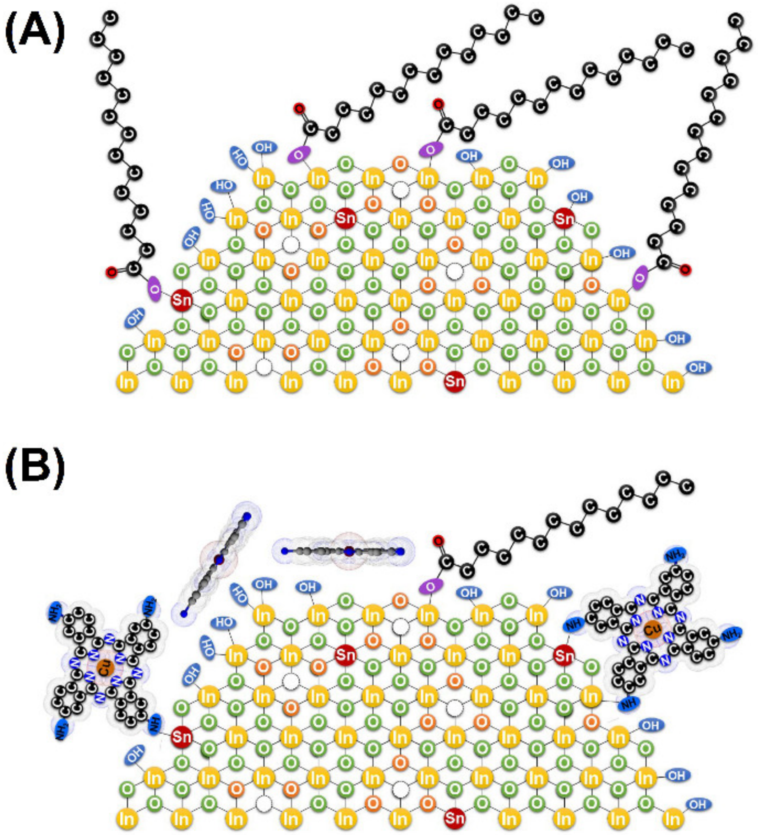

Figure 14. Schematic views of (A) the possible ITO NC surface before ligand exchange and (B) binding of the new incoming ligand molecules and the more complex surface after ligand exchange.

Correlation between structure, dielectric environment and optoelectronic properties

In good accordance with XPS, our GISAXS results also confirm the successful ligand exchange. In the as-prepared NC films, the nanoparticles are separated by MA molecules. The average correlation distance between neighboring NCs (center to center distance) is reduced by about 0.8 nm upon ligand exchange (Figure 11C). This in the inter-particle correlation distances matches with the difference between the molecular lengths of MA (~1.8 nm) and Cu4APc (~1.1 nm).

Decreasing the distance between two metallic NCs typically induces a red-shift of the LSPR due to a growing interaction of the surface electrons of the two NCs. In addition, changes in the dielectric environment of the surface electrons can also alter the LSPR. [254] We therefore attribute the 88 meV bathochromic shift of the LSPR for MA-capped ITO NCs obtained upon drying the NC solution on a substrate (Figure 12) to a mixture of these two effects, as the dielectric medium and the interparticle distance both change drastically in the process. In contrast, annealing of the dried ensemble primarily leads to a decrease in interparticle spacing, such that the additional 35 meV bathochromic shift of the LSPR of the MA-capped ITO NCs upon annealing are mainly attributed to a structural effect (Δd_{SL} = -0.6 nm). A comparison of the LSPRs of the dried NCs before and after ligand exchange indicates that in this case the different dielectric environment provided by Cu4APc supposedly causes a hypsochromic shift which competes with the shift due to the change in structure (Δd_{SL} = -0.8 nm): although the volume contraction is even larger than in the first case, the observed bathochromic shift is only 10 meV. Annealing of this sample does not lead to further volume contractions (see Figure 11), but the LSPR experiences another bathochromic shift by 25 meV which, as one possibility, we attribute to the evaporation of the non-volatile solvent DMSO and the associated change in the dielectric environment. Thus, although the LSPRs of the two annealed samples are practically identical, this is likely to be a coincidence since the dielectric environments are quite different.

Charge transport in arrays of metallic NCs is typically described within the framework of granular metals. [91, 115, 133, 255-256] For transport in the dielectric regime, the resistance (R) follows a temperature-activated behavior according to

$$R \sim exp\left(\frac{e^2}{\varepsilon d} \cdot \frac{1}{T}\right)^{\alpha_c} \qquad (1)$$

with the elemental charge (e), the effective dielectric constant of the material ε, the effective localization length d and the material-/temperature-specific coefficient α_c. Therefore, the sheet resistance in ITO NC networks is expected to be correlated to both, the dielectric environment (represented by ε) and the structure (represented by d). In addition, the effective correlation length depends on the tunneling probability between adjacent NCs, which is again a function of structure (*via* the width of the tunneling barrier) and the chemical environment (e.g. due to a surrounding matrix with a non-zero conductance [257]). Our results in Figure 13 suggest that all investigated samples are in the dielectric regime since even for the most conductive sample (after ligand exchange and annealing), the estimated conductivity is on the order of 0.5 $\mathrm{Scm^{-1}}$ (assuming an average film thickness of 1-2 NC monolayers). This is two orders of magnitude lower than the expected conductivity for a coherently coupled network of metallic NCs with diameter a = 6.8 nm according to [258]

$$\sigma_{Coher} \approx \frac{e^2}{ha} \qquad (2)$$

This observation is in line with our GISAXS results which suggest that even after annealing the NCs remain well-separated, presumably by a monolayer of MA or Cu4APc. The slight decrease in R_s upon annealing MA-capped ITO thin films can be understood in terms of a reduction of the tunneling barrier width (Δd_{SL} = -0.6 nm). However, because of the largely insulating nature of MA, the tunneling probability increases only slightly due to the very large tunneling barrier height. The importance of the electronic structure of the surfactant in this respect is immediately apparent upon comparing the R_s values for ITO NC films before and after ligand exchange: Although the structural properties of the annealed MA-capped sample and the pristine Cu4APc-functionalized material (Figure 11B and C) are quite similar, the difference in conductivity is 5-6 orders of magnitude. Such a large change cannot be explained with an alteration of the dielectric environment alone and points to a dramatically enhanced tunneling probability between adjacent NCs *via* the semiconductor molecule. In contrast, the additional reduction of R_s after annealing of the Cu4APc-capped sample is probably mostly due to removal of the non-volatile solvent DMSO, which is mainly a dielectric effect. On the other hand, annealing could also lead to beneficial geometric relaxation of Cu4APc at the ITO surface. We note that we did not observe any changes in XPS signals of ITO NCs capped with Cu4APc after annealing.

Comparison of the transport properties of Cu4APc-capped ITO NCs with other reports on ITO NC thin films

Despite the parameters discussed in the section above, transport in ITO NC networks also strongly depends on the size of the NCs, the doping concentration, the processing history/annealing temperature as well as the film thickness. [220, 223, 259]

Table 3. Comparison of recently published electrical conductivities for nanocrystalline ITO thin films.

Ref.	σ / Scm^{-1}	NC diameter / nm	Processing history	Film thickness / nm	Sn-doping concentration / %	Surfactant
This work	0.5	6.8	Annealed at 250 °C for 2 h	1-2 ML	5	Cu4APc
Ref. [222]	0.001	10.5	25 °C	350	7	butanoate
Ref. [220]	20	16	Annealed at 500 °C	1100	5	n.a.
Ref. [223]	200	11	Annealed under 5% H_2 at 300 °C for 6 h	146	10	None
Ref. [221]	1.7	9.5	As deposited by spin-coating	200	5	Oleylamine
Ref. [219]	1.0	14.6	350 °C in air for 10 min	165	10	None

Table 3 summarizes some recent results from the literature in terms of these additional parameters and demonstrates the large influence of the surface functionalization on the efficiency of charge transport between ITO NCs. Removing the surface molecules by annealing at $T \geq 300$ °C and/or under reductive conditions can lead to transport approaching the quantum conductance limit. [258] Here, transport is merely inhibited by the charging energy associated with injecting a charge into the confined volume of the NC. In contrast, if the surface functionalization remains intact, transport is predominantly limited by tunneling through the molecular layer and not by the charging energy of the NC. A comparison of the conductivity and lattice spacings measured in this work (0.5 Scm^{-1}; 1.2 nm) with that on similar ITO NC layers capped with butanoate (0.001 Scm^{-1}; 0.4 nm) implies that Cu4APc does not merely act as a molecular spacer but rather as an electronic bridge which greatly facilitates transport between adjacent NCs. In this sense, the material in the present work could also be viewed as an array of ITO contacts, which serve to study transport through molecular layers of Cu4APc. In the same context, it is instructive to compare the Cu4APc-ITO system with the vast literature of noble metal NCs (e.g. Au, Ag) separated by molecular monolayers, [87, 260-261] such as saturated alkanethiols. Although the carrier concentration in such real metal NCs is significantly larger than in degenerately doped ITO, typical conductivities for molecular lengths of 1.2 nm are on the order of 10^{-3} Scm^{-1}. If the molecular layer is a semiconducting polymer, such as thiolated oligo(phenylene ethylene) (OPE) with a molecular length of 2.1 nm, a conductivity on the order of 0.02 Scm^{-1} has been reported.[208-209] These comparisons strongly suggest that carrier migration through the ITO-Cu4Pc network is remarkably efficient.

Conclusion

We have demonstrated that *in-situ* ligand exchange of ITO nanocrystals at the liquid-air interface with semiconducting tetraamino Cu-phthalocyanine yields an electronically coupled network of well-separated nanocrystals. UV–vis–NIR, GISAXS and XPS results demonstrate the presence/binding of the semiconductor ligand between/to the ITO nanocrystals. 2-point probe conductivity measurements reveal a dramatic decrease in sheet resistance by more than nine orders of magnitude after ligand exchange, suggesting that the phthalocyanine derivative acts as an electronic linker. The synthetic concept pursued in this work enables future testing of theoretical models for the description of transport through granular metal systems as well as investigations of the interplay between organic semiconductor molecules with plasmonic nanocrystals.

Acknowledgements

The authors wish to thank Mrs. Nadler for SEM/STEM measurements, Dr. Liang for assistance with XRD experiments and the DFG for support under grant SCHE1905/4 and SCHR700/25.

Corresponding Author:

*email: marcus.scheele@uni.tuebingen.de

Author Contributions:

The manuscript was written through contributions of all authors. All authors have given approval to the final version of the manuscript.

Supplementary Material:

This material is available free of charge *via* the Internet at http://pubs.acs.org.

Scanning transmission electron microscopy images, histogram for size analysis of nanocrystals, and evaluation of contact resistance applying transmission line method (TLM).

Chapter 3

Tunable Charge Transport in ITO Nanocrystal Superlattices – Towards Sensing Applications

Manuscript 2

Tunable Charge Transport in ITO Nanocrystal Superlattices – Towards Sensing Applications

Mahdi Samadi Khoshkhoo[†], *Yvonne Joseph*[⊥], *Santanu Maiti*[‡], *Frank Schreiber*[‡,§], *Thomas Chassé*[†,§], *and Marcus Scheele*[†,§,*]

[†] Institute of Physical and Theoretical Chemistry, University of Tübingen, Auf der Morgenstelle 18, 72076 Tübingen, Germany.

[⊥] Institute of Electronic and Sensor Materials, TU Bergakademie Freiberg, Gustav-Zeuner-Straße 3, 09599 Freiberg, Germany.

[‡] Institute of Applied Physics, University of Tübingen, Auf der Morgenstelle 10, 72076 Tübingen, Germany

[§] Center for Light-Matter Interaction, Sensors & Analytics LISA+, University of Tübingen, Auf der Morgenstelle 15, 72076 Tübingen, Germany.

Abstract

Macroscopic superlattices of tin-doped indium oxide (ITO) nanocrystals (NCs) are prepared by self-assembly at the air/liquid interface followed by simultaneous ligand exchange with the organic semiconductors M-4,4′,4″,4‴-tetraaminophthalocyanine (M4APc, M = Cu, Co, Fe, Ni, Zn). Transport measurements, focusing on the effect of the metal center of the ligand, reveal a ligand-dependent increase in electrical conductance by six to nine orders of magnitude, suggesting that M4APc provides efficient electronic coupling for neighboring ITO NCs. The resulting *I–V* characteristics as well as the temperature dependence (7–300 K) of the zero-voltage conductance indicates that at low temperatures, transport across the arrays occurs via a sequence of inelastic cotunneling events, each involving ≈3 ITO NCs. At higher temperatures, a crossover to 3D Mott-variable range hopping mechanism is observed. Finally, the vapor sensitivity of chemiresistors is investigated made from ITO NCs coupled via Cu- and Zn4APc by dosing the sensors with 4-methyl-2-pentanone (4M2P), toluene, 1-propanol, and water in the concentration range of 100–5000 ppm at 0% relative humidity. The nanocrystal superlattices respond with an increase in resistance to these analytes with the highest sensitivity to 4M2P.

Keywords: colloidal nanocrystals, multiple inelastic co-tunneling, electron localization length, self-assembly, indium tin oxide (ITO), vapor sensors.

3.1. Introduction

Due to their shape/size-tunable electronic and optical properties, ease of fabrication, and solution processability, colloidal semiconductor nanocrystals (NCs) have gained substantial attention as promising building blocks for advanced materials and devices. They already play a relevant role in field-effect transistors (FETs), light-emitting diodes (LEDs), photodiodes and photovoltaic cells (PVCs) as well as in biological applications, and important perspectives in future nanoelectronic and nano-optoelectronic devices are expected. [1-6, 27] Among different classes of structures, arrays of few monolayers of NCs connected via organic ligands have recently attracted significant attention due to their numerous novel emerging applications. [3, 77, 262-263] The architecture of these devices includes inorganic nanocrystals physically and electronically connected to each other through organic semiconductor bridges. These nanostructures have demonstrated variable sensitivity and selectivity utilizing different linker molecules which make them promising for developing artificial noses and multivariable sensors. [80, 264-266] To this end, a fundamental understanding of charge transport in NCs arrays containing hybrid molecule–nanoparticle junctions is of particular relevance.

Charge transport in NC assemblies is often reported to follow the variable range hopping (VRH) model, $g(T) \propto \exp[-(T_0/T)^{\gamma}]$, [112, 267-268] where T_0 is a characteristic temperature and $\gamma = ½, ⅓$, and ¼ for Efros–Shklovskii (ES) or Coulomb Gap (CG), 2D, and 3D transport models, respectively. The similarity of charge transport properties in arrays of NCs versus VRH in doped semiconductors was first noticed by Beverly et al. [269] Since that observation, many experiments on metallic and semiconducting nanocrystal arrays at low temperatures (inside the Coulomb blockade regime) revealed $\gamma = ½$, suggesting that transport in these systems can be satisfactorily described by the ES-VRH model. [113-114, 270] This model is based on direct, single-charge tunnel events between distributed defect sites. However, when applied to NC arrays, the derived hopping lengths are often equivalent to several NC diameters, which questions its applicability to arrays of NCs. Thus, an alternative picture with the same temperature dependence has been proposed by Beloborodov et al. to explain an identical ½ exponent based on cooperative multielectron processes, known as the multiple inelastic cotunneling (IC) model. [116-117, 271] In this process, the electron tunnels from an initial to a final state via virtual intermediate states. [118, 272] Inelastic cotunneling can be visualized as a superposition of electron tunneling events into a nanocrystal and simultaneous escape of another electron from the same nanocrystal, creating electron–hole pairs. [273] Although these synchronized cooperative multielectron hops occur over distances of several nanoparticles, they entail only the Coulomb energy cost of roughly a single-quantum event. [119] On the other hand, the probability for such synchronized hops to occur is quite low, which negatively impacts the hopping rate. Thus, the resulting cotunneling distance is the outcome of an optimization process between the number of electron cooperative cotunneling events and the net energy cost.

The characteristics of the IC regime are affected by the properties and arrangement of the NC arrays, e.g., the diameter of nanocrystals, *D*, the length of the tunnel barrier or edge-to-edge interparticle distance, *s*, the size distribution of NCs, and the dielectric constant of the NCs environment, ε (organic ligand molecules). As two examples, Kang et al. [112] have reported the influence of particle size, *D*, on charge transport in PbSe nanocrystal thin films while keeping *s* constant. Dugay et al. [274] and Moreira et al. [275] have investigated the effect of the length of the ligand molecule, *s*, on the characteristics of the IC regime in metallic cobalt nanoparticles and Au NCs thin films, respectively. These results indicate that investigating the sole effect of the ligand's dielectric constant on charge transport requires a set of samples with precisely the same nanocrystals and the same molecular lengths of the molecules. In this work, we present such a study by fabricating arrays of indium tin oxide (ITO) NCs crosslinked with different M4APc (M = Cu, Co, Fe, Ni, and Zn) molecules to understand the electron transport mechanism as well as the effect of the ligands' dielectric constant, which is strongly affected by the metal center of molecule. Our results indicate that the dielectric constant of the semiconductor ligands significantly regulates charge transport, the Coulomb charging energy, and the localization length in particular. Finally, we investigate the potential of this material for vapor sensing applications. To this end, the sensor response characteristics of ITO NCs coupled via Cu- and Zn4APc are measured by dosing the films with dilute vapors of 4-methyl-2-pentanone (4M2P), toluene, 1-propanol, and water. We suggest that a combination of swelling of the NCs network and permittivity changes dominates the sensing mechanism in the superlattices.

3.2. Methods

3.2.1. Synthesis of ITO Nanocrystals: Myristic acid-capped ITO nanocrystals (ITO/MA) were synthesized according to the method reported in our previous work. [276]

3.2.2. Synthesis of Ligands: Cu- and Zn-4,4‘,4‘‘,4‘‘‘-tetraaminophthalocyanine (Cu- and Zn4APc) were synthesized following previously reported procedures. [230] Co-, Fe-, and Ni4APc were purchased from Abcr and used without further purification.

3.2.3. Thin-Film Preparation and Ligand Exchange: Electronically coupled NC superlattice thin-films were prepared by a Langmuir-type assembly at the liquid/air interface. [231, 234, 276-277] The fabrication process and ligand exchange were carried out in a home-built Teflon chamber according to our previously reported method. [276]

3.2.4. Instrumentation: The quality and the structure of NC thin-films, the thickness, and also the particle size and shape were verified by STEM on a Hitachi SU 8030 microscope operating at 30 kV. The presence of M4APc in the NC-thin films after ligand exchange was confirmed by XPS and UV–vis–NIR spectroscopy. XPS measurements were carried out using a photoelectron spectrometer which was equipped with a conventional XR50 X-ray source (Al K_α, working at 12.5 kV and 20 mA, 1486.61 eV) and a PHOIBOS 100 multi-channel detector analyzer (SPECS). The binding energies were corrected for electrical charge effects by referencing to Au4f and adventitious C1s peak, which were assumed to have a binding energy of 84.0 and 284.8 eV, respectively. The relative tin content was determined by the ratio of the Sn3d peak area to the total area of the In and Sn3d peaks, scaled by the relative photoionization cross-section for each element. Optical measurements were performed on solid state films on glass substrates using an UV–vis–NIR spectrometer (Agilent Technologies, Cary 5000). GISAXS was performed at a laboratory-based Xeuss 2.0 instrument from Xenocs, France, with a wavelength of 1.5405 Å (CuK_α source). A 2D Pilatus 300 K detector was employed at a distance of 2.5 m from the sample to collect the data. An incident beam of size 0.5 × 0.5 ($V \times H$) mm^2 was used at a grazing angle of 0.2° onto the sample surfaces. Electrical measurements on the NC arrays at room temperature were performed using a Keithley 2634B dual source-meter unit, controlled by the included test script builder program. The free-floating ligand-exchanged NC superlattices were deposited on a commercially available bottom-gate, bottom-contact transistor substrates (Fraunhofer Institute for Photonic Microsystems, Dresden, Germany) with interdigitated Au electrodes of 10 mm width and 2.5 μm channel length (distance between Au electrodes) followed by annealing at 250 °C for 2 h under nitrogen atmosphere. Substrates were contacted using a home-built probe station enclosed in a nitrogen glovebox. The temperature-dependent charge transport properties of the NC thin-films were measured by a Lake-Shore CRX-6.5K probe station and a Keithley 2636B dual source-meter unit. The temperature was controlled by a Lake Shore (Model 336) temperature controller. For investigating the vapor sensing properties, NC superlattices were deposited on commercially available glass substrates with interdigitated gold electrode structure (90 finger pairs, 10 μm microelectrode gap, and 10 μm and 150 nm microelectrode width and height, respectively; ED-

IDE1-Au micrux Technologies). The sensitivity of the films was characterized by dosing them with vapors of 4M2P, toluene, isopropanol, and water while monitoring their resistances at 0.1 V. All vapor sensing experiments were carried out at room temperature (ca. 25 °C) with dried purified air as carrier gas using the previously reported commercial instrumentation. [278] Due to the integrated mass flow controllers in the system $\approx 3x$ to $\approx 1000x$ dilution of saturated test vapors is possible. With the vapor pressures of the analytes (21, 29, 20, and 23 mbar at 20 °C, respectively) [279], concentrations between 50 and 5000 ppm are possible. As all the mentioned test vapors have comparable vapor pressures, their interaction with the samples is expected to mainly arise from their chemical nature (polarity and structural features) and not from the differences in vapor pressure.

3.3. Results

The scanning transmission electron microscopy (STEM) images of the ITO NCs thin-films before and after ligand exchange are presented in Figure 15. Figure 15A shows STEM images of a two monolayer thick film of myristic acid (MA)-capped ITO NCs. Figure 15B,F shows STEM images of the same film after ligand exchange with Cu-, Co-, Fe-, Ni-, and Zn4APc, respectively. STEM reveals that the NCs are self-assembled into large-areas and they are well separated from each other by either the myristic acid chains or the M4APc molecules. The results suggest that the films are not subjected to significant cracks after ligand exchange (see the lower magnification STEM images which are shown in Appendix B; Figure S4 to Figure S9). The average particle size is found to be 6.8 nm by evaluating several STEM pictures from the same substrate and counting more than 500 particles. The histogram for size analysis can be found in Appendix B (Figure S10). By using X-ray photoelectron spectroscopy (XPS), grazing-incidence small-angle X-ray scattering (GISAXS), and UV–vis–near infrared (NIR) spectroscopy, we have demonstrated that the semiconductor molecules largely replace the native surfactant from the ITO NC surface and act as crosslinkers between neighboring particles (detailed results can be found in Appendix B).

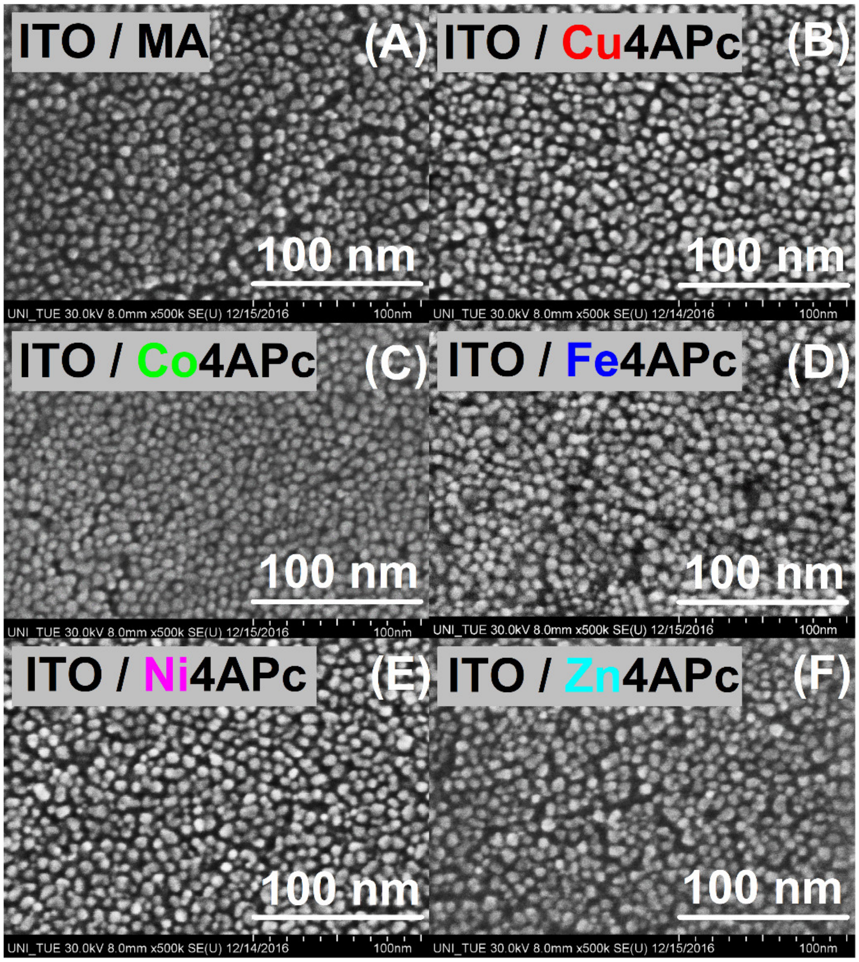

Figure 15. Electron microscopy images of the ITO NCs thin-films A) before and B–F) after ligand exchange with Cu-, Co-, Fe-, Ni-, and Zn4APc, respectively.

An estimate of the carrier concentration (N) in the ITO NCs used in this work is obtained through the following equation:

$$\omega_p = \sqrt{\frac{Ne^2}{m_e \epsilon_0}},$$

where ω_p is the plasma frequency, e is the elementary charge, m_e is the effective mass, and ε_0 is the vacuum permittivity. Applied to the spectroscopic data displayed in Appendix B (Figure S12), we estimate the charge carrier concentration as 9×10^{18} cm^{-3}, which is well placed in the range (10^{18}-10^{22} cm^{-3}) often reported for n-type conductive metal oxides.

The electrical properties of the ITO NC films before and after ligand exchange are investigated by low-field two-point current–voltage (I–V) measurements at room temperature. We used the sheet resistance ($R_s = Rw/l$, where R is the measured resistance of the 2D NC arrays, with L and w the length and width of the channel between two gold electrodes) in order to compare the results. Figure 16 shows the *I–V* characteristics measured for ITO NCs arrays before and after ligand exchange. For the MA-capped ITO NCs, we find $R_s = 7.0 \times 10^{14}$ Ω □$^{-1}$ for the annealed film. Ligand exchange followed by annealing at 250 °C for 2 h reduces the sheet resistances to 2.0×10^6, 1.6×10^7, 3.7×10^7, 1.0×10^8, and 5.9×10^8 Ω □$^{-1}$ for thin-films exchanged to Cu-, Co-, Fe-, Ni-, and Zn4APc, respectively. Therefore, ligand exchange followed by annealing leads to a ligand-dependent increase in conductivity of the films by several orders of magnitude. It is worth pointing out that the lowest sheet resistance of the sample (observed for ITO/Cu4APc thin-film) is on the order of MΩ which is larger than any expected contact resistance. Furthermore, previously we have shown using the transmission line method that the effect of contact resistance in our system is negligible, thus, a two-point measurement is appropriate in this experiment. [247-248]

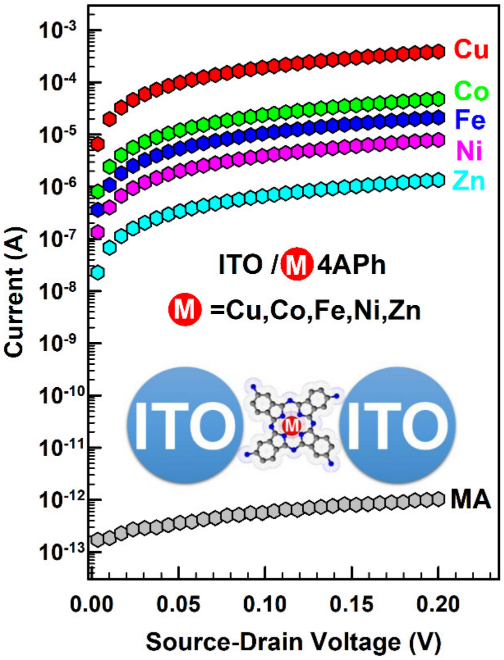

Figure 16. The *I–V* characteristics measured at room temperature for ITO NCs arrays before (gray circles) and after ligand exchange to Cu- (red), Co- (green), Fe- (blue), Ni- (pink), and Zn4APc (cyan).

The charge carrier transport mechanism in ITO NC thin-films is investigated by analyzing the temperature-dependent *I–V* characteristics as well as the zero-voltage conductance. Figure 17 illustrates the power law behavior of the NC films crosslinked with Cu- and Zn4APc. The results for the films connected via ligand molecules with Co, Fe, and Ni metal centers as well as primary myristic acid ligand can be found in Appendix B (Figure S15 and Figure S16). For all samples, the conductance experiences a strong decrease of two to four orders of magnitude upon decreasing the temperature, which is typical for Coulomb blockade-dominated transport in NCs arrays. All samples exhibit a characteristic crossover voltage, indicating the transition point from ohmic ($I \propto V$) to power-law ($I \propto V^{\alpha}$, α = power-law exponent) behavior. At small bias voltages, the *I*–*V* characteristics obey ohmic behavior in the whole temperature range for all samples, while at large bias, the *I*–*V* characteristics follow power-law behavior with a temperature-dependent exponent. Figure 17 also reveals that the strongly temperature-dependent behavior at small bias voltages transposes into a much less temperature-dependent one at higher biases for all samples. In this regime, the electron transport become more field driven. [114, 120] Figure 18 illustrates the transition from the ohmic to the nonlinear power law behavior of the NC films crosslinked with Cu-, Co-, Fe-, Ni-, and Zn4APc at 10 K. As the samples become more insulating, the power law exponent at large bias voltages increases. Simultaneously, the crossover voltage decreases to lower voltages.

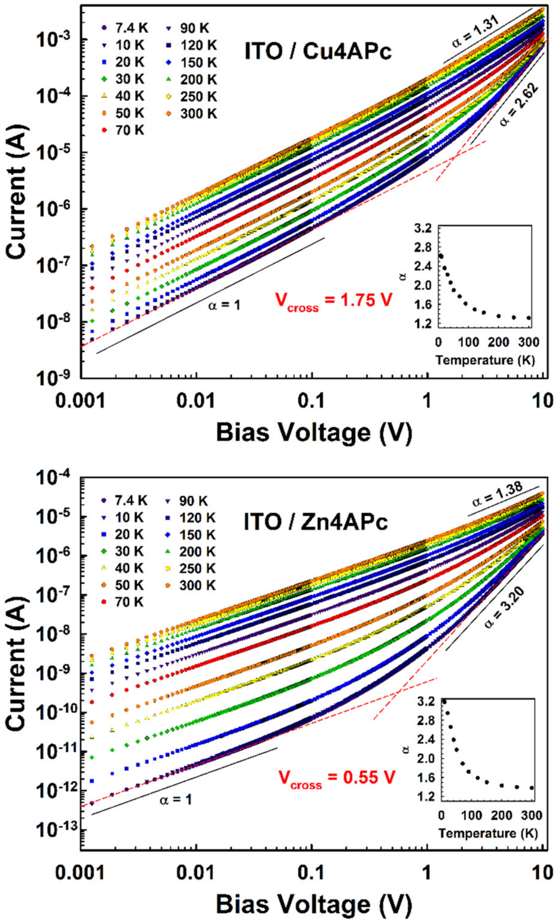

Figure 17. Current–voltage (*I*–*V*) characteristics as a function of temperature for ITO NCs functionalized with Cu- and Zn4APc (the solid lines are guided to the eye corresponding to the power laws with exponents as indicated). The inset graph shows the temperature-dependent change of the power law exponent.

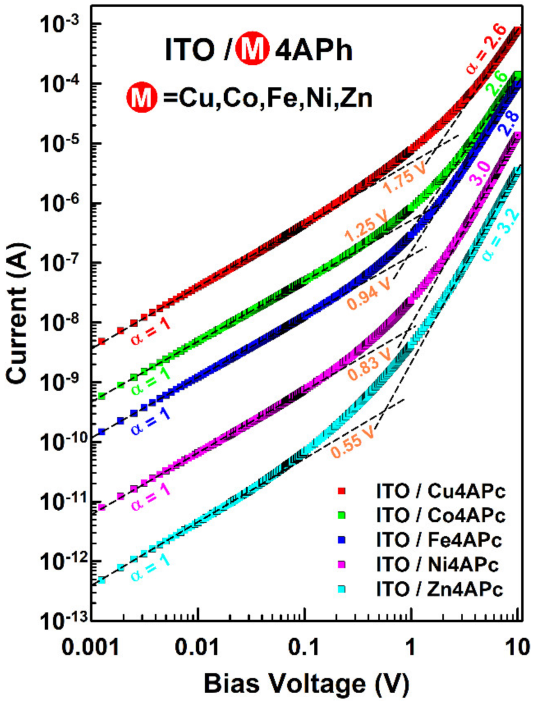

Figure 18. The transition from the ohmic to the nonlinear power law behavior of the NC films crosslinked with Cu-, Co-, Fe-, Ni-, and Zn4APc at 10 K.

Figure 19 shows the zero-voltage conductance, $g(T)$, plotted versus $T^{-1/4}$ and $T^{-1/2}$ for ITO NCs thin films after ligand exchange. We obtained $g(T)$ of each superlattice at specific temperatures by linear fitting of the I–V characteristics at small bias (−50 to 50 mV). The result for the film before ligand exchange is reported in Appendix B (Figure S18). As expected, all the samples show semiconducting behavior in the whole measured temperature range. Evidently, the dependence of $g(T)$ with temperature changes drastically upon exchange with different ligands. At the same time, $g(T)$ increases monotonically with temperature.

As a consistency check, we also provide a plot of the logarithmic derivative $w = d(\log G_{V=0})/d(\log T)$ against temperature on a double logarithmic scale (Appendix B) to verify our choice of exponents for the different temperature regimes. At low temperatures, the zero-voltage conductance for all samples follows $g(T) = g_0\exp[-(T_0/T)^{1/2}]$ which has the same functional form as ES-VRH behavior (Figure 19B). The region for which we observe this functional form is gradually shifted to lower temperatures for more insulating samples. At high temperatures, the zero-voltage conductance for all samples except ITO/Cu4APc follows $g(T) = g_0\exp[-(T_0/T)^{1/4}]$ which has the same functional form as 3D Mott-type behavior (Figure 19A). The array of ITO NCs functionalized with Cu4APc shows the same functional form as the ES-VRH behavior in the whole temperature range. Fits indicated by the dashed lines give the characteristic temperature, T_0, which is summarized in **Error! Reference source not found.**. For more insulating samples, higher values for characteristic temperatures are obtained. For more insulating samples, higher values for characteristic temperatures are obtained. Furthermore, as the samples become more insulating, deviations from Mott-type behavior, i.e., the crossover temperature (T_{cross}) from Mott-type to ES-type behavior, occurs at increasingly lower temperatures (see **Error! Reference source not found.**). The prefactor, g_0, includes the tunneling through the barrier created by the ligand molecule layer capping ITO NCs. It can be considered as the attempt frequency of electrons trying to escape the nanoparticles. This prefactor decreases with the order Cu > Co > Fe > Ni > Zn.

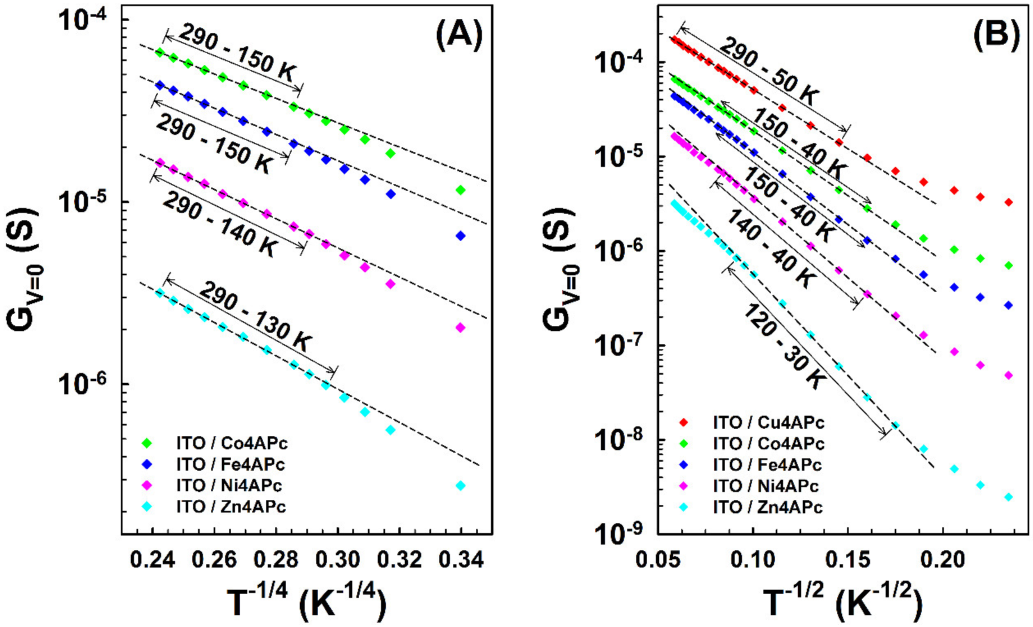

Figure 19. Temperature-dependent zero-voltage conductance of ITO NCs functionalized with Cu-, Co-, Fe-, Ni-, and Zn4APc plotted versus (A) $T^{-1/4}$ and (B) $T^{-1/2}$ (fits indicated by the dashed lines).

As mentioned before, charge transport properties in NC arrays can be significantly affected by the interparticle distance of the nanocrystals (width of the tunnel barrier) as well as the dielectric constant of the environment (height of the tunnel barrier). Therefore, changing one or both of these parameters by an external stimulus (e.g., vapor sorption) can vary the transport properties of the system (e.g., overall resistance of the superlattice). Figure 20A,B shows the typical response of the films upon three exposures of 120 s to 4M2P for ITO/Cu4APc and ITO/Zn4APc as the most conductive and the most insulating superlattice, respectively. The sensor responses are expressed as the relative differential resistance response; that is, the change in the resistance, ΔR, divided by the baseline resistance, R_0. In all cases, a fast (few seconds) and fully reversible, approximately rectangular response is observed. In order to investigate the chemical selectivity of the NC superlattices, the samples were also exposed to toluene, 1-propanol, and water vapor analytes. Figure 20C represents the response of the samples to 3200 ppm of four analytes. For all analytes, ITO/Zn4APc shows less sensitivity in comparison to ITO/Cu4APc. A decreasing sensitivity from Cu^{2+} to Zn^{2+} has also been observed and reported for the liquid sensing properties of a set of phthalocyanines (Pcs). [280] Furthermore, in both cases the sensitivities to toluene, 1-propanol, and water vapors are quite similar and lower than the response of the samples to 4M2P vapor.

Table 4. The characteristic temperatures (T_0), the exponential prefactors (g_0), the Coulomb gap (Δ_{CG}), the crossover temperature (T_{cross}), the ratio of mean hopping distance ($R_{hop,Mott}$) to localization length (ξ), and the mean hopping energy difference between sites ($E_{hop,Mott}$) for MA-capped ITO NC superlattices before and after ligand exchange to Cu-, Co-, Fe-, Ni-, and Zn4APc.

	$g \propto T^{-1/4}$ behavior				**$g \propto T^{-1/2}$ behavior**
Sample	**T_0 (K) / g_0 (S)**	**R_{hop} /ξ**	**E_{hop} (meV)**	**T_{cross} (K)**	**T_0 (K) / g_0 (S)**
ITO / Cu4APc	–	–	–	–	841 / 9.33×10^{-4}
ITO / Co4APc	56228 / 2.76×10^{-3}	1.40	23.3	~150	1004 / 4.46×10^{-4}
ITO / Fe4APc	75498 / 2.43×10^{-3}	1.50	25.1	~150	1243 / 3.76×10^{-4}
ITO / Ni4APc	115730 / 1.42×10^{-3}	1.68	27.9	~140	1566 / 1.96×10^{-4}
ITO / Zn4APc	191823 / 5.04×10^{-4}	1.90	31.7	~125	2433 / 7.86×10^{-5}
ITO / MA	648434 / 3.58×10^{-6}	2.58	42.9	~150	5385 / 4.41×10^{-7}

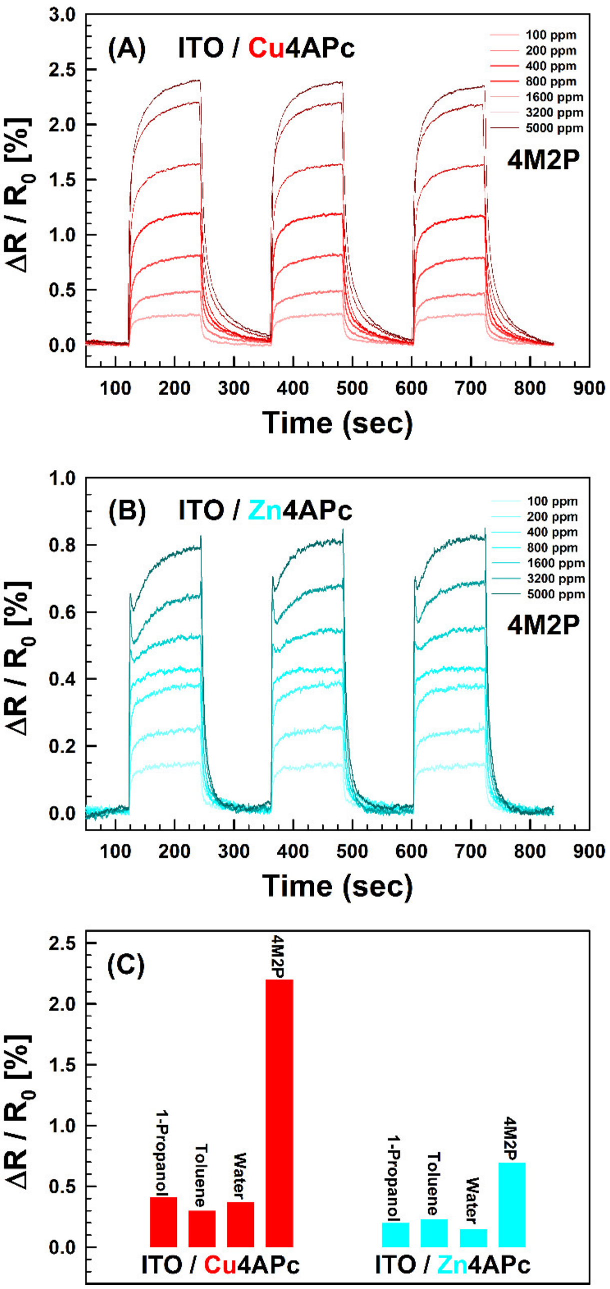

Figure 20. (A and B) Response traces of ITO/Cu4APc and ITO/Zn4APc films toward 100–5000 ppm of 4M2P at 0% relative humidity. (C) Responses traces of ITO/Cu4APc and ITO/Zn4APc films toward 3200 ppm of 4M2P, toluene, 1-propanol, and water vapors.

3.4. Discussion

3.4.1. Characterization of the arrays of ITO NCs before and after ligand exchange

We have shown how the incorporation of Cu4APc into an array of ITO NCs can be achieved by a Langmuir-type assembly at the liquid/air interface in our previous work. [276] Here, the same property is used to introduce tetraaminophthalocyanines containing different metal centers into the arrays of ITO NCs allowing to study the effect of the metal center on the conductance increase of the films. Initially, the nanoparticles are capped by MA. During the ligand exchange process, the incoming M4APc molecules penetrate the floating NC superlattice films, replace the MA molecules, and bind to the NCs. The obtained XPS and UV–vis–NIR results clearly demonstrate that the new incoming ligand molecules are present in the structure of thin-films after ligand exchange (Figure S11 and Figure S12). In agreement with XPS and UV–vis–NIR, our GISAXS results also confirm the successful ligand exchange. The average correlation distance between neighboring NCs (center to center distance) is reduced by ≈0.7 ± 0.1 nm (see Figure S13 and Figure S14 as well as Table S2) upon ligand exchange, matching the difference between the molecular lengths of MA and the new M4APc molecules. As demonstrated by STEM images as well as GISAXS results, ligand exchange does not disturb the structural order of the NC arrays. For all samples after ligand exchange and annealing, we observe a total redshift of 18–62 meV of the localized surface plasmon resonance, depending on the metal center of the ligand (see Table S1). We attribute this bathochromic shift to: (i) decreasing the distance between ITO NCs due to a growing interaction of the surface electrons and (ii) changes in the dielectric environment of the surface electrons. All these evidences as well as the strong increase in conductance demonstrate that M4APc acts not only as a spacer but also as an electronic linker, which greatly facilitates transport between adjacent nanocrystals.

3.4.2. Correlation between dielectric environment and transport properties

The ligand-dependent increase in conductivity of M4APc-capped ITO NC thin films can be understood in terms of a reduction of the tunneling barrier height. At room temperature, transport occurs via sequential tunneling which is dominated by independent electron hops from one ITO nanocrystal to its nearest neighbor along the current path (Figure 21A). In sequential tunneling, the electron–hole pair is separated by one particle. The Coulomb charging energy of a nanoparticle, E_C, which is defined as the energy needed to add an excess electron onto an electronically neutral nanoparticle, is approximated by [104]

$$E_C = \frac{e^2}{4\pi\epsilon\epsilon_0 a} \quad , \qquad (1)$$

where e is the elementary charge, ϵ_0 is the vacuum permittivity, ϵ is the dielectric constant, and a is the particle radius. Different methods and models [97, 121-125] are reported in order to estimate the Coulomb charging energy in the array of nanoparticles but in general it can be affected by (i) the particle core size, (ii) the interparticle distance, (iii) the number of nearest neighbors, and (iv) the dielectric constant of the ligand molecules. [121] Based on our STEM images and GISAXS results, the structural and geometrical properties of ITO/M4APc thin-films are very similar, and thus, the first three parameters should be almost identical for all the samples. Therefore, the sheet resistance in ITO NC networks is expected to be correlated to the dielectric environment, ε. To the best of our knowledge, no values of dielectric constants are reported yet for M4APcs; however, one can find the respective data for metal-phthalocyanines, which can be used as a rough estimation for a qualitative discussion. In this respect, the dielectric constant values of 1.58, 1.7–2.7, 3.1, and 3.6 are reported for Zn-, Ni-, Co-, and Cu-phthalocyanine at room temperature, respectively. [281-285] According to equation 1, smaller ε implies larger E_C and thus a significant suppression of tunneling in arrays of NCs. For NC arrays connected via Cu4APc, due to the higher dielectric constant of the environment, the Coulomb interaction is screened and electrons can propagate more easily. This explanation supports the order of conductance values observed for the array of ITO NCs coupled via M4APc (Cu > Co > Fe > Ni > Zn) and demonstrates that a decrease in resistance is caused by an increase in the average permittivity of the nanocrystals' environment.

3.4.3. Charge transport at high temperatures

In order to fully characterize the mechanisms of transport, we varied the temperature (7–300 K) and the bias voltage (0.001–10 V) over a wide range. The conductance data of the arrays at high temperatures were primarily analyzed using the thermal activation model $g(T) \approx \exp[-E_a/k_B\mathrm{T}]$, where E_a is the activation energy and k_B is the Boltzmann constant. However, the fitting quality was poor indicating that this model is not applicable here. Instead, the transport data fit well to the 3D Mott-VRH mechanism ($g(T) = g_0\exp[-(T_0/T)^{1/4}]$) except for ITO/Cu4APc, which follows $g(T) = g_0\exp[-(T_0/T)^{1/2}]$ within the whole temperature range. For the Mott-VRH theory to be valid, the mean hopping distance, $R_{\mathrm{hop,Mott}}$, must be larger than the localization length, ξ, thus the ratio $R_{\mathrm{hop,Mott}}/\xi = 3/8[T_{\mathrm{Mott}}/T]^{1/4}$ should be larger than unity. ξ characterizes the tunneling probability between nearest sites and longer values represent smaller barrier height between the nanocrystals. In all cases, the calculated $R_{\mathrm{hop,Mott}}/\xi$ values (see **Error! Reference source not found.**) are larger than 1, thus satisfying the criterion of the Mott-VRH model. Knowledge of the Mott characteristic temperature also provides the mean hopping energy difference between sites, $E_{\mathrm{hop,Mott}} = \frac{1}{4}k_BT[T_{\mathrm{Mott}}/T]^{1/4}$, which are on the order of few tens of meV (see **Error! Reference source not found.**). Depending on the ligand metal center, the mean hopping energy difference between sites increases from Co- to Zn4APc capped ITO NCs (Zn > Ni > Fe > Co).

Based on the variable range hopping model prediction, VRH should evolve from the Mott-type regime, $T^{-1/4}$, at higher temperatures to ES-type behavior, $T^{-1/2}$, at thermal energies smaller than the width of the Coulomb gap. [286] The clear crossover from Mott- to ES-VRH-type behavior observed in our samples indicates the opening of a soft Coulomb gap at low temperatures, Δ_{CG}. [268] This crossover has been also observed for bulk indium oxide films [287] as well as CdSe quantum dots films. [113] The transition temperature between these charge transport mechanisms is observed to depend on the metal center of the connecting ligand in this work with the transition taking place at higher temperatures for more conductive samples.

3.4.4. Charge transport at low temperatures

With decreasing the temperature, the *I–V* characteristics become more nonlinear (See Figure S17). The more pronounced nonlinear behavior for more insulating samples at low temperatures can be attributed to the lower dielectric constant of the NCs environment, and thus, higher charging energy between them. Furthermore, consistent with other measurements on nanoparticle arrays, the current starts to be suppressed in the low bias region, which is considered to be the consequence of the Coulomb blockade. When the Coulomb blockade regime dominates, cooperative tunneling of several charges through N_{cot} junctions becomes significant (Figure 21B), and this is known as the multiple inelastic cotunneling mechanism. The current flow in this type of charge transport is given by a Tailor series proposed by Tran et al [116]:

$$I \propto V_{jct} \sum_j \left(\frac{h}{e^2 R_T}\right)^j \left(\frac{k_B^2 T^2 + e^2 V_{jct}^2}{E_C^2}\right)^{j-1} exp\left(-\frac{\frac{E_C}{j} - jeV_{jct}}{k_B T}\right). \qquad (2)$$

Here, T is the temperature, k_B is Boltzman constant, R_T is the resistance of a single junction, and V_{jct} is the voltage drop over a single tunneling junction connecting two neighboring nanocrystals. Based on equation (2), Dayen *et. al.*[120] have found that when the thermal energy becomes smaller than the Coulomb charging energy, the electronic behavior during cotunneling can be split into three regimes depending on different voltage ranges between neighboring nanocrystals:

$$C1: \quad I \propto V \qquad\qquad eV_{jct} < k_B T \qquad (3a)$$

$$C2: \quad I \propto V^{\propto} \qquad\qquad k_B T < eV_{jct} < k_B T ln\left(\frac{e^2}{h} R_T\right) \qquad (3b)$$

$$C3: \quad I \propto exp\left(\sqrt{\frac{V^*}{V}}\right) \qquad\qquad k_B T ln\left(\frac{e^2}{h} R_T\right) < eV_{jct}, \qquad (3c)$$

where V^* is a characteristic voltage. The number of junctions across the gap between the electrodes in our system is ≈300, thus, the global Coulomb blockade threshold $V_t \approx NE_C$ can easily reach several volts. In an ideal case by considering the straight path between the electrodes, the applied bias voltage and the bias per junction are related by $V_{jct} = V/n$, where n is the number of junctions involved in transport. Therefore, based on equation 3a and by considering the number of NCs present across the gap between the electrodes (≈300), at $T = 10$ K we expect a linear behavior at a bias voltage less than ≈0.25 V. This is indeed what we find in Figure 18.

At higher bias voltages (i.e., $k_BT < eV_{jct} < k_BT\ln[e^2h/R_T]$), the data are fitted well by power laws of the form $I \propto V^{\alpha}$, in line with equation 3b. At 10 K, the exponents are ≈3.2, 3, 2.8, 2.6, and 2.6 for ITO NCs array crosslinked by Zn-, Ni-, Fe-, Co-, and Cu4APc, respectively. The greatest power-law exponent of ≈4.3 is obtained for MA-capped ITO NCs thin-films at 10 K (see Appendix B). The cotunneling distance, which is a characteristic length scale, invokes the curvature of the nonlinear I–V characteristics as well as the temperature dependence of the zero-voltage conductance. The number of cotunneling events, N_{cot}, relates as $\alpha = 2N_{cot} - 1$; therefore, the typical number of the junctions participating in the cotunnel events are 2.1, 2, 1.9, 1.8, and 1.8 for the NC films connected via ligand molecules with Zn, Ni, Fe, Co, and Cu metal centers, respectively. For MA-capped ITO NCs thin-films, the number of junctions involved is 2.65. This indicates that at low temperatures, transport across the arrays occurs via a sequence of cotunneling events, each involving ≈3–4 ITO NCs (schematically shown in Figure 21C). The necessity for multiple cotunneling events arises from the fact that the number of NCs participating in one cotunneling event (≈3–4) is much lower than the number of NCs present across the gap between the electrodes (≈300). Inelastic cotunneling takes over inside the Coulomb blockade regime, while at high temperatures and/or at large bias voltage above the global Coulomb blockade threshold, $eV_{jct} \approx E_C$, transport occurs via sequential tunneling. The range of cotunneling hops changes with temperature. As apparent in Figure 17, at higher temperatures the power-law exponent decreases toward unity, which means that the number of hops decreases to one and cotunneling behavior makes way for sequential tunneling.

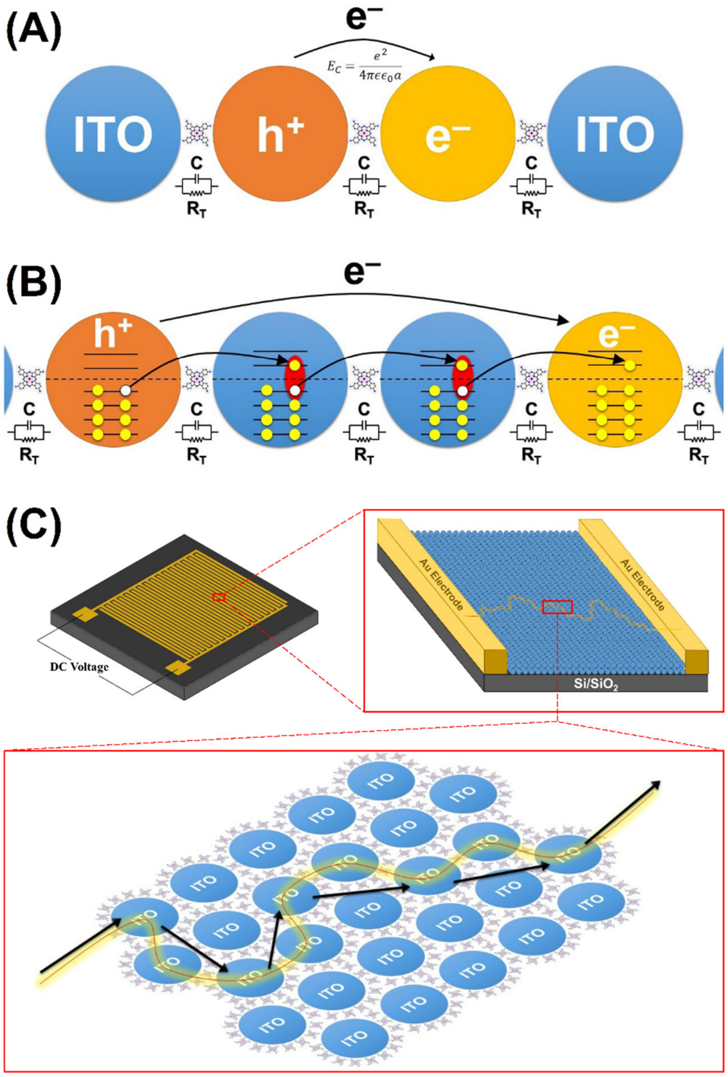

Figure 21. Schematic representation of (A) sequential tunneling, (B) inelastic cotunneling, and (C) electron transport in nanocrystal array via inelastic cotunneling (black arrows) along paths that optimize the overall energy costs.

For further investigation of the transport mechanism in the superlattices, the temperature dependence of the zero-voltage conductance (Figure 19) was studied. The positive temperature coefficient of the zero-voltage conductance is a significant feature of an insulator. For low temperatures above 30 K, a good linear relationship is found in the $\ln[g(T)]$ versus $(1/T)^{1/2}$ plot which arises from multiple inelastic cotunneling. [274] We note that for $T < 30$ K in Figure 19B, the change in slope indicates a slightly altered transport mechanism, which we tentatively attribute to the gradual onset of elastic cotunneling. Within the framework of inelastic cotunneling, the temperature dependence of the conductance follows [116, 271]

$$g = g_0 \exp[-(T_0/T)^{1/2}], \qquad (4)$$

where T_0 is the activation temperature and is linked to the Coulomb charging energy, E_C, through $T_0 = CE_c/(k_B\xi)$. Here, ξ is the localization length and C is a numerical constant ($C \approx 2.8$ for 3D). From the conductance versus temperature behavior, several characteristic parameters describing charge transport in the array of ITO NCs can be extracted. For our experimental data, the fits of the conductance yield T_0 = 841, 1004, 1243, 1566, and 2433 K for ITO NCs array coupled via Cu-, Co-, Fe-, Ni-, and Zn4APc, respectively. Obviously, the increase in the activation temperature is related to the role of the metal center of the connecting ligand molecule, as the geometrical properties of the ITO/M4APc thin-films are very similar in all the samples. The localization length in the inelastic cotunneling regime can be calculated as [112, 116, 271]

$$\xi = \frac{Ce^2}{4\pi\epsilon\epsilon_0 k_B T_0}, \qquad (5)$$

using the measured activation temperature, T_0, and the estimated dielectric constant of the environment. However, it can be also calculated independent of the dielectric constant via the number of cotunneling events, N_{cot} (from the curvature of I–V characteristics) as well as the activation temperature, T_0, through equating N_{cot} to the number of junctions involved in a typical hop: [91, 116, 271, 274, 288]

$$N_{cot} = \frac{r^*}{d} = \left(\frac{e^2\xi}{4\pi\epsilon\epsilon_0 k_B T}\right)^{1/2} \frac{1}{d} = \left(\frac{T_0}{CT}\right)^{1/2} \frac{\xi}{d}. \qquad (6)$$

Here, d is the average interparticle distance (estimated as 8.0 nm by GISAXS). At T = 50 K, we find 2.36 nm < ξ < 4.70 nm depending on the connecting ligand between ITO NCs (see Table 5), which is in the range of observed values for closed-pack arrays of metallic or semiconductor nanoparticles. [114, 271] The localization length calculated for ITO/M4APc thin-films characterizes the overlap of the wave functions between different sites. It is essentially defined as the decay length of an electron in NCs assemblies. In all cases, it is larger than the nanocrystal separation (i.e., edge-to-edge interparticle distance of ≈1.2 nm). The greatest obtained localization length for ITO/Cu4APc reflects the strongest correlation of the electronic wave function in that case. Having the localization length, one can calculate the dielectric constant of the environment using the localization length and the activation temperature from equation 5. [268] At 50 K, the calculated dielectric constant values decrease from 11.83 for ITO NCs connected via Cu4APc to 6.30 for the arrays interlinked by Zn4APc (Cu > Co > Fe > Ni > Zn). The order is in good agreement with that observed in phthalocyanines (see section 4.2 and Refs. [281-285]). This shows that the metal center of the ligand can significantly affect the dielectric constant of the molecule, and thus, the Coulomb charging energy of NCs. We note that the rather large values obtained for the dielectric constants in comparison to those reported for metal Pcs might arise from three reasons: (i) in M4APcs, there are four additional polar amino groups which can significantly alter the dielectric behavior of the molecule; (ii) the model considers the simple self-capacitance of NCs in order to calculate the charging energy which can be improved by including the mutual capacitance arising from nearest-neighbor interactions to the total capacitance; and (iii) the calculations for M4APcs in this work are carried out for T = 50 K; however, the results reported for metal Pcs correspond to room-temperature measurements. The temperature dependence of dielectric constants is well documented for isotropic or cubic inorganic materials, [289] and was also recently reported for CuPc [290] and Pc derivatives. [291] Using the conductivity pre-exponential factor, g_0, we can describe the hopping rate between nanocrystals. This prefactor decreases for M4APc-coupled ITO NCs arrays along the order Cu > Co > Fe > Ni > Zn, demonstrating that the number of hops necessary for charge transport as well as interparticle coupling between NCs decrease in the mentioned order. Therefore, our results demonstrate that arrays of nanocrystals coupled by organic connecting ligands with larger dielectric constants exhibit weaker temperature dependence (see Figure 17) as well as higher conductivity (see Figure 16) in line with previous expectations. [114]

Table 5. The number of cotunneling events (N_{cot}), electron localization length (ξ), dielectric constant of the environment (ε), and the Coulomb charging energy (E_C) for arrays of MA-capped ITO NCs before and after ligand exchange to Cu-, Co-, Fe-, Ni-, and Zn4APc at 50 K.

Sample	**N_{cot}**	**ξ (nm)**	**ε**	**E_C (meV) / K**
ITO / Cu4APc	1.44	4.70	11.83	35.8 / ~415
ITO / Co4APc	1.46	4.36	10.68	39.6 / ~460
ITO / Fe4APc	1.49	4.00	9.40	45.0 / ~522
ITO / Ni4APc	1.53	3.65	8.16	51.9 / ~602
ITO / Zn4APc	1.59	3.05	6.30	67.2 / ~780
ITO / MA	1.83	2.36	3.68	115.0 / ~1335

The occurrence of cotunneling and the ability to fine-tune the number of junctions involved in this process open new opportunities for device applications. [120, 292] Conduction via inelastic cotunneling can increase the sensitivity of the sample to an external stimulus, since the resistance will be proportional to $R_T^{N\mathrm{cot}}$ (where R_T is the resistance of a simple NC–molecule–NC junction). Well-documented examples include spin-dependent resistance in magnetic systems enhanced by cotunneling [292-293] as well as the enhanced tunnel magnetoresistance in spintronic systems. [294-296]

3.4.5. Vapor Sensing Properties

One major aim of this study was to demonstrate the potential applicability of coupled ITO/M4APc structures in sensing applications. The results shown in Figure 20 clearly demonstrate that the ITO NC superlattices connected via both Zn- and Cu4APc respond (with an increase in resistance) to all four analytes with highest sensitivity to 4M2P. The vapors we have used in this study cover different classes of analytes: hydrophilic hydrocarbons (4M2P), hydrophobic hydrocarbons (toluene), H-bonding organic compounds (1-propanol), and polar H-bonding inorganic compounds (water). Furthermore, different dielectric constant of these analytes (water: 80.1, 1-propanol: 20.8, 4M2P: 13.11, and toluene: 2.4 at 20 °C [297]), together with their different classes, render them well suited to study the chemical selectivity of the sensor samples. Considering the nanostructure of our superlattice, one can find four possible binding sites with very different chemical nature: (i) vacant sites on ITO nanocrystals that contain hydroxyl groups or oxygen bridges, [276] (ii) four amino functional groups of each linker molecule which can be unbound or bound to the surface of the nanocrystals, [276] (iii) the metal center (Cu or Zn) of the linker molecules, and (iv) the hydrophobic backbone of the ligands in between the nanocrystals. Figure 22 indicates the response isotherms for the films of ITO/Cu4APc and ITO/Zn4APc superlattices for analyte concentrations from 100 to 5000 ppm. In agreement with the literature, we fitted the data points with a Langmuir adsorption model which has been described previously by Barlett and Ling-Chung according to the following equation (see Figure 22): [298]

$$\frac{\Delta R}{R_0} = \left[\frac{\Delta R}{R_0}\right]_S \frac{K_b C_{vapor}}{1+K_b C_{vapor}}\ , \qquad (7)$$

where $[\Delta R/R_0]_s$ is the relative change of resistance at saturation, K_b is the binding constant, and C_{vapor} is the concentration of the analyte in the gas phase. The data measured for the films of ITO/Cu4APc exposed to 4M2P and ITO/Zn4APc exposed to toluene fit fairly well to the Langmuir adsorption model according to equation 7 (solid lines in Figure 22). Using the first order of Langmuir adsorption model for ITO/Cu4APc exposed to 1-propanol and water and ITO/Zn4APc exposed to 4M2P, 1-propanol, and water, we recognize some deviations in the fittings; therefore, the data were also fitted using the second order Langmuir adsorption model based on the following equation (see Figure 22):

$$\frac{\Delta R}{R_0} = \left[\frac{\Delta R}{R_0}\right]_S \frac{K_b\sqrt{C_{vapor}}}{1+K_b\sqrt{C_{vapor}}}\,. \qquad (8)$$

This model gives even better fits to the measured data. The relative differential resistance response at saturation $[\Delta R/R_0]_s$ and the binding constants K_b obtained from the 1st and 2nd order Langmuir adsorption model are tabulated in Table 6. As seen by the $[\Delta R/R_0]_s$-values, the highest sensitivity is detected for superlattices exposed to 4M2P. The higher response amplitudes of both superlattices to 4M2P might be the result of larger partitioning of analyte in the films. This is in agreement with the nature of the M4APc molecule (partly polar and hydrophobic with a minor ability to form hydrogen bonds), that is expected to be the sorption site for the vaporous analytes. [299] Although the $[\Delta R/R_0]_s$-value is rather low, the high signal-to-noise ratio of the response curves (Figure 20) suggests that the detection limit for this system can well go below 100 ppm. The lower sensitivity values observed for all analytes in the case of ITO/Zn4APc compared to ITO/Cu4APc can be attributed to the weaker interaction capabilities of metal center ions of ligands with analyte molecules. [280] The stronger curvature of the response isotherms for both superlattices exposed to 1-propanol and water (Figure 22B and D) indicates that these analytes bind significantly stronger to the nanostructure than 4M2P and toluene. This can also be deduced from the higher binding constants K_b obtained by fitting (e.g., for ITO/Zn4APc; see Table 6). The ligand molecules, Cu- and Zn4APc, have an aromatic nature with a high delocalization of π-electrons, and thus, the adsorption of toluene probably occurs by weak physisorption involving noncovalent π–π stacking interactions. [300] We argue that hydrophobic 4M2P and toluene adsorb to the nanostructure by swelling in the organic matrix (by adsorption on the hydrophobic backbone of the ligands in between the nanocrystals), and thus, behave more vapor-like. In contrast, 1-propanol and water behave more gaseous-like in their interaction with the metal center of the M4APc linkers, reaching saturation when every metal center is occupied. In line with this argument, it has been shown that water vapor acts as an effective donor on metal phthalocyanine surfaces, [301-302] and simulations have demonstrated that only two water molecules on average may be placed in the neighborhood of the metal center. [303] One might also expect the adsorption of analytes on the possible binding sites present on the nanocrystals surface; however, since most of the surface is covered by ligand molecules, diffusion and adsorption on these sites are quite challenging for analyte molecules due to steric hindrance as well as the limited number of free available sites. It also has to be noted that all measurements were carried out on dry purified air as carrier gas at room temperature. As shown, water sorbs to the material and it can be assumed that measurements under ambient conditions at higher humidity levels will lead to a blockage of the water sorption sites and will influence the sorption of other analytes competing with water for the same sites. However, detailed investigations on this cross sensitivity and also on sensitivity changes due to temperature variations are beyond the scope of this work and should be addressed in the future.

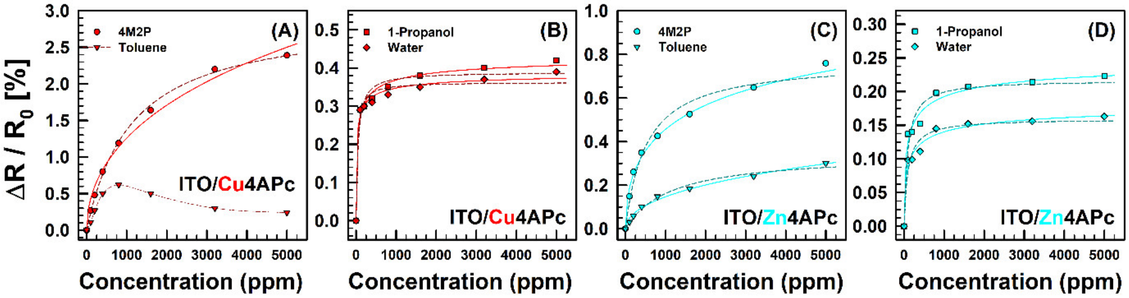

Figure 22. Response isotherms of (A,B) ITO/Cu4APc and (C,D) ITO/Zn4APc superlattices indicating concentration-dependent responses to 100–5000 ppm of analytes. The dashed lines are the Langmuir fits according to a 1st order adsorption model (i.e. equation 7) and the solid lines are the Langmuir fits according to a 2nd order adsorption model (i.e. equation 8). In the case of ITO/Cu4aPc exposed to toluene, the dashed line is a guide to the eye.

Table 6. The relative differential resistance response at saturation *[ΔR/R₀]ₛ* and the binding constants K_b obtained from the 1st and 2nd order Langmuir adsorption model according to equations 7 and 8, respectively. The numbers in parenthesis demonstrate the better fitting results in each case.

		1st order kinetics		**2nd order kinetics**	
NC Film	**Analyte**	**$[\Delta R/R_0]_s$ (%)**	**K_b (M^{-1})**	**$[\Delta R/R_0]_s$ (%)**	**K_b ($M^{-0.5}$)**
ITO/Cu4APc	4M2P	(2.92)	(88.59)	12.35	1.14
	Toluene	-	-	-	-
	1-propanol	0.39	1201.90	(0.44)	(38.34)
	Water	0.36	532.53	(0.39)	(30.29)
ITO/Zn4APc	4M2P	0.77	191.90	(1.52)	(4.30)
	Toluene	(0.35)	(81.27)	1.80	0.85
	1-propanol	0.21	680.87	(0.25)	(23.43)
	Water	0.16	187.90	(0.19)	(11.99)

Considering the positive response (resistance increase) of the films and the charge transport at high temperatures discussed in the previous part, we propose that swelling can be one dominating component of the sensing mechanism in the presented materials. Accordingly, swelling of the superlattice network during vapor sorption leads to an increase in the interparticle tunnel distance, which in turn results in an increased tunneling barrier height and, thus, an increased resistance. [279, 304] Furthermore, one should consider that the response of the superlattices can also be determined by the change in dielectric constant of the environment of the nanocrystals. As shown in previous sections, a change in dielectric constant of the environment can significantly modulate the charge transport properties of the system. Since the mixture of swelling and permittivity changes play major roles in sensing mechanisms, distinguishing the contribution and importance of each factor needs more systematic experiments, which will be subject to a forthcoming publication. In the case of ITO/Cu4APc superlattices exposed to toluene, the Langmuir adsorption model cannot describe the behavior satisfactorily. By increasing the vapor concentration, we first observe an increase in the relative change of resistance followed by a decrease at higher vapor concentrations (see Figure 22A), suggesting the existence of a competition between at least two different parameters in this special system that requires more investigations in future works.

Conclusion

In this work, we expanded the choice of the metal center of M4APc (M = Cu, Co, Fe, Ni, and Zn), incorporated them into an array of ITO NCs by a Langmuir-type assembly at the liquid/air interface and studied the electron transport mechanism in the NC arrays. Two-point probe conductivity measurements revealed that ligand exchange leads to a ligand metal-center-dependent increase in conductance of thin-films by six to nine orders of magnitude. It was shown that the decrease in resistance (in ITO superlattices connected via M4APc with different metal centers) is caused by an increase in the average permittivity of the nanocrystals' environment. The resulting *I–V* characteristics as well as the temperature-dependent conductivity measurements indicated that at low temperatures, transport across the arrays occurs via a sequence of cotunneling events, each involving ≈3–4 ITO NCs. At higher temperatures, the number of hops decreases to one and cotunneling behavior makes way for sequential tunneling. The results presented in this work also demonstrate the potential and functionality of these superlattices as novel transparent vapor sensing materials. Swelling of the NCs network as well as the permittivity changes seem to play major roles in the sensing mechanism. In conclusion, the fast response, high sensitivity, robustness under ambient condition, room-temperature operability, and optical transparency render phthalocyanine-coupled ITO NC superlattices promising materials for novel sensing applications.

Acknowledgements

The authors acknowledge the Deutsche Forschungsgemeinschaft (DFG) for support under Grants SCHE1905/3, SCHE1905/4, and SCHR700/25. The authors also thank Elke Nadler, Institute of Physical and Theoretical Chemistry, University of Tübingen, scanning electron microscopy (SEM) and STEM measurements using a Hitachi SU 8030 SEM which was funded by the DFG under contract INST 37/829–1 FUGG partially. The paper was written through contributions of all authors. All authors have given approval to the final version of the paper.

Corresponding Author:

*email: marcus.scheele@uni.tuebingen.de

Conflict of Interest:

The authors declare no conflict of interest.

Supplementary Material:

The STEM images of the ITO NCs thin-films before and after ligand exchange; histogram for size analysis of nanocrystals; the XPS spectra of N 1s and ligand metal center regions of the ITO NC superlattices prepared by the interface method before and after ligand exchange; the UV–vis–NIR absorption spectra of as-prepared ITO NC films before and after ligand exchange as well as the results before and after annealing stage; GISAXS patterns of the self-assembled ITO NCs arrays before and after ligand exchange as well as the results after annealing stage; and the temperature-dependent I–V characteristics of the NC films cross-linked with Co-, Fe-, and Ni4APc as well as primary myristic acid ligand.

Chapter 4

The Role of the Density of Interface States in Interfacial Energy Level Alignment of PTCDA

Manuscript 3

The Role of the Density of Interface States in Interfacial Energy Level Alignment of PTCDA

Mahdi Samadi Khoshkhoo[†]*, Heiko Peisert*[†]*, Thomas Chassé*[†,§]*, and Marcus Scheele*[†,§,*]

[†] Institute of Physical and Theoretical Chemistry, University of Tübingen, Auf der Morgenstelle 18, 72076 Tübingen, Germany.

[§] Center for Light-Matter Interaction, Sensors & Analytics LISA+, University of Tübingen, Auf der Morgenstelle 15, 72076 Tübingen, Germany

Abstract

We introduce extensions to a recently developed numerical model to understand the origin of universal Fermi level pinning of perylene-3,4,9,10-tetracarboxylic dianhydride (PTCDA) and its underlying mechanism. Our calculations are supported by ultraviolet and X-ray photoelectron spectroscopy to investigate the electronic structure of PTCDA on a wide range of substrates with different work functions and coupling interactions. For 20 nm thick layers of PTCDA, nearly unchanged hole injection barriers on all substrates are observed without any dependence on the type of substrate (unreactive, reactive or passivated metals and polymers). The simulation results demonstrate how the shape of the DOS near the interface has long-range influence on key parameters (e.g. the barrier to charge injection) of the entire organic film.

Keywords: Numerical electrostatic model; Energy level alignment; Fermi level pinning; Density of interface states; PTCDA; Injection barrier

4.1. Introduction

A thorough understanding of the electronic structure at the metal/organic interface is crucial for improving the performance of organic semiconductor (OSC) electronic devices, such as field-effect transistors (OFETs) [305-308], light emitting diodes (OLEDs) [305, 309-311], and photovoltaic cells (OPVCs) [312-315]. Carrier injection and extraction in these devices are strongly dependent on the energy level offsets between the Fermi level of the metal and the highest occupied molecular orbital (HOMO) or lowest unoccupied molecular orbital (LUMO) of the OSC. Amongst other techniques, the energy level alignment at these interfaces has been investigated extensively using ultraviolet and X-ray photoelectron spectroscopy (UPS and XPS) [183, 316-319]. For interfaces characterized by weak interactions one can find a linear relationship between the magnitude of the injection barrier and the substrate's work function accompanied by vacuum level alignment across the interface. This is referred to as the Schottky-Mott limit [320]. However, most organic-metal interfaces deviate from this simple Schottky-Mott behavior and often large interface dipoles are observed [152, 161, 170]. In these examples their origin is attributed to several phenomena including charge transfer, polarization and a modification of the metal work function upon adsorption of molecules (often called push back, Pauli repulsion or pillow effect) [143, 321-323]. Also the presence of molecular quadrupoles may affect the potential change at interfaces [324]. Successful models to explain these effects include integer charge transfer to/from molecular polaronic levels [142, 166-167], charge transfer due to pinning and an induced electric field across the interface [137, 192, 325], tailing of the density of states into the semiconductor gap [326-327], as well as induced density of interface states accompanied by respective interface charge transfer [139, 151, 171, 183].

In order to rationalize the design of metal/organic semiconductor contacts, the development of numerical models capable of quantitative predictions of crucial parameters, such as charge carrier injection barriers, is highly desired. Oehzelt *et al.* have recently introduced an electrostatic model, which made accurate predictions about the injection barriers for pentacene on various substrates [137].

In this work, we examine the applicability of this model for the special organic semiconductor perylene-3,4,9,10-tetracarboxylic dianhydride (PTCDA). This molecule differs greatly from pentacene as it is well-known to show Fermi level pinning behavior on unreactive (e.g. Au) as well as reactive (e.g. Mg) metal substrates [193]. We show how the original model by Oehzelt *et al.* can be extended to make predictions in excellent agreement with UPS data for this molecule. We believe that these modifications have the potential to increase the applicability of the model to a much wider range of organic semiconductors, allowing for accurate quantitative predictions also for molecules with strong Fermi level pinning.

4.2. Methods

4.2.1. Electrostatic Potential Calculations: We carry out electrostatic calculations using the recently developed model by Oehzelt *et al*. [137, 192, 325] Briefly, this model discretizes the organic deposited film into layers of thickness Δx and distance x from the substrate in order to calculate the amount of transferred charges in each layer, therefore it can see the effect of thickness and spatial profile of charge distribution (interfacial dipole and/or band bending). The core formula which specified the charge density, *ρ(x)*, in different thicknesses of deposited organic film is given by:

$$\text{Equation 61} \qquad \rho(V(x)) = e \cdot n \cdot \left\{\int_{-\infty}^{+\infty} dE \cdot f_H(E) \cdot D_H[E + eV(x)] - \int_{-\infty}^{+\infty} dE \cdot f_L(E) \cdot D_L[E + eV(x)]\right\}$$

where *e* is the elementary charge, *n* is the number of molecules per unit area and per discretization interval Δx, $f_H(E)$ and $f_L(E)$ are the Fermi functions for each individual energy levels, *V(x)* is the electrostatic potential at the position *x* from the substrate and finally $D_H[E+eV(x)]$ and $D_L[E+eV(x)]$ are the energy distributions of HOMO- and LUMO-derived levels. Numerical solving of the generalized one dimensional Poisson equation (Equation 62) yields the electrostatic potential across the PTCDA deposited film as a function of thickness, *V(x)*.

$$\text{Equation 62} \qquad \nabla[\varepsilon(x)\nabla V(x)] = -\frac{\rho(V(x))}{\varepsilon_0}$$

where ε_0 is vacuum permittivity and $\varepsilon(x)$ is the static dielectric constant for each discretization interval. The details of these calculations can be found in the Appendix C.

4.2.2. Photoelectron Spectroscopy: The substrates used in this experiment are chosen to span a wide range of work functions: Aluminum with native oxide (Φ_{SUB} = 3.3 eV), titanium with native oxide (Φ_{SUB} = 3.9 eV), indium tin oxide (Φ_{SUB} = 4.1 eV), contaminated Au (Φ_{SUB} = 4.2 eV), contaminated Pt (Φ_{SUB} = 4.4 eV) sputter-cleaned Ag (Φ_{SUB} = 4.4 eV), silicon with native oxide layer (Φ_{SUB} = 4.4 eV), sputter-cleaned platinum (Φ_{SUB} = 4.8 eV), sputter-cleaned Ni (Φ_{SUB} = 5.0 eV), PEDOT:PSS (Φ_{SUB} = 5.2 eV), and sputter-cleaned Au (Φ_{SUB} = 5.3 eV). All substrates are first cleaned in an ultrasonic bath of deionized water, acetone, ethanol, and isopropanol and, where necessary, by additional UV-ozone treatment as well as Ar ion-sputtering (beam voltage of 1 kV).

The main experimental technique used for investigating the electronic structure of the interface in this work is photoelectron spectroscopy (PES). In order to study valence band features, ultra-violet photoemission spectroscopy (UPS) is carried out with a helium discharge lamp using He(I) excitation (hν = 21.22 eV). The position of the HOMO is determined by the low binding energy onset of the UPS spectra, i.e. the intercept between the tangent line of the onset feature and the baseline of the spectrum, is considered. The vacuum level position is obtained via the secondary electron cut-off. Details of the analysis of important parameters such as the substrate work function (Φ_{sub}), interface dipole (Δ), and hole injection barriers (Φ_{HIB}) are extensively described in the literature. More details of experimental procedures can be found in the Appendix C.

4.3. Results and Discussion

It is well-known that a molecular film of PTCDA deposited on reactive and non-reactive metal substrates shows Fermi level pinning, leading to metal independent injection barriers [193]. In line with this, we observe pinning of the Fermi level on all eleven substrates described in the experimental section at 4.5 ± 0.1 eV vs. vacuum level (Figure 23A), which corresponds to approx. 2.0 ± 0.1 eV above the HOMO of PTCDA (Figure 23B). Irrespective of the different substrates used in this work, nearly unchanged hole injection barriers (Φ_{HIB}) on all substrates were observed without any dependence on the initial work function and reactivates. Figure 23B represents the evolution of interface dipole (Δ) versus substrate work function (Φ_{sub}) for a molecular film of PTCDA deposited on different substrates. Within the range of work functions studied here, the magnitude of the interfacial dipole generated at the interface decreases linearly by decreasing the work function of the substrate. Upon deposition of PTCDA, Δ changes in a way that the distance between the Fermi level and HOMO edge remains constant. The behavior is similar to related systems, where a change of the dipole was observed by changing the work function of the metal or, vice-versa, the ionization potential of the organic material [170, 328]. For a detailed discussion on valence band photoelectron spectroscopy and electronic structure of the interface, the reader is referred to the Appendix C.

To understand the origin of this universal Fermi level pinning and underlying mechanism, we carry out electrostatic calculations using the recently developed model by Oehzelt *et al.* [137, 192, 325] The details of these calculations can be found in Appendix C. We examine the model and run the calculations considering three different scenarios based on our experimental observations. Figure 24A shows the magnification of the HOMO region of a 20 nm thick film of PTCDA deposited on a sputtered-cleaned Au surface (topmost spectrum). As can be seen, the HOMO feature can be well fitted by a Gaussian distribution with a HOMO edge about 2.0 eV. Very similar results are observed for a 20 nm thick film of PTCDA deposited on the other substrates as well (see Appendix C). The energy distribution of the HOMO feature of thick film starts to become broader at lowest thicknesses and tails into the fundamental gap of the organic semiconductor. As two examples, the magnified HOMO regions of 2.5 nm thick films of PTCDA deposited on Al/Al_xO_y and Si/SiO_x are shown in Figure 24A. Gap states are experimentally observed within the first 5 nm of PTCDA near the interface and their impact can be included into this model by: (i) introducing a Lorentzian broadening contribution to the

DOS according to our UPS results for Si/SiO$_x$ in order to simulate the tailing of the density of states into the semiconductor gap, or (ii) direct addition of one more peak to the DOS based on our experimental observation for the Al/Al$_x$O$_y$ substrate.

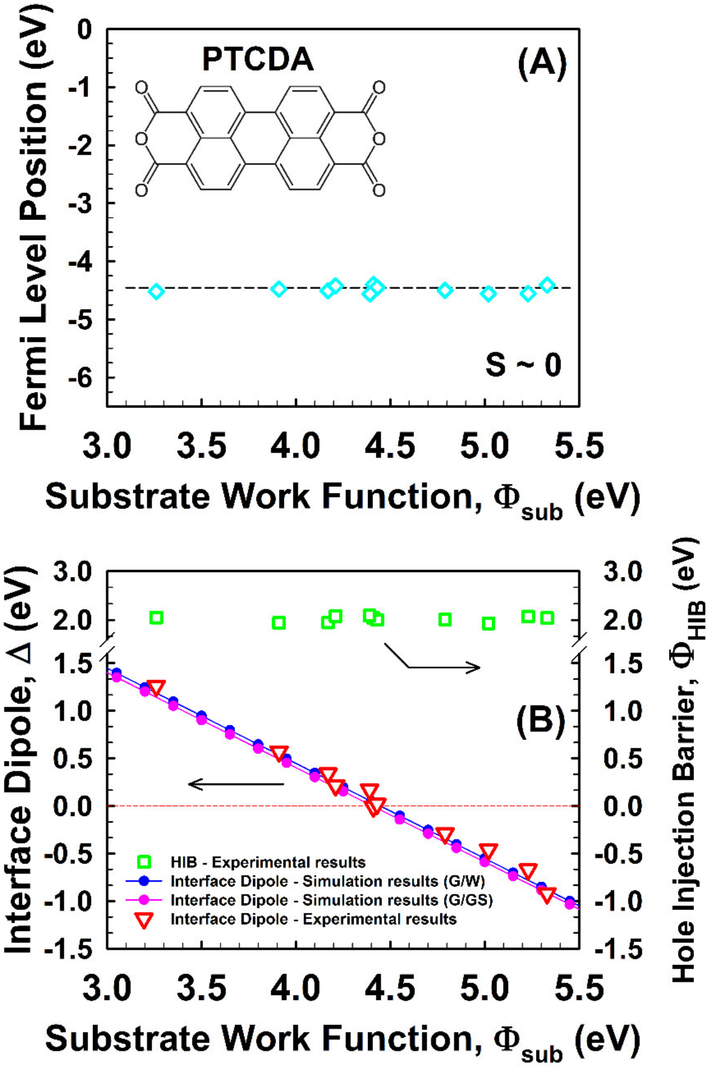

Figure 23. (A) The position of the Fermi level with respect to vacuum level for 20 nm thick PTCDA versus substrate work function (dashed line serves as a guide to the eye – the inset of the figure shows the chemical structure of PTCDA). (B) The evolution of interface dipoles (red triangles) and hole injection barriers, Φ_{HIB} (green squares) of 20 nm thick films of PTCDA with respect to the work function of the substrate. Blue and pink circles represent the simulation results of the interface dipoles with respect to the work function of the substrates. The DOS of the organic layers are approximated by Gaussian/Lorentzian (G/L) and Gaussian/Gap-State (G/GS) peaks, respectively (the connecting line serves as a guide to the eye).

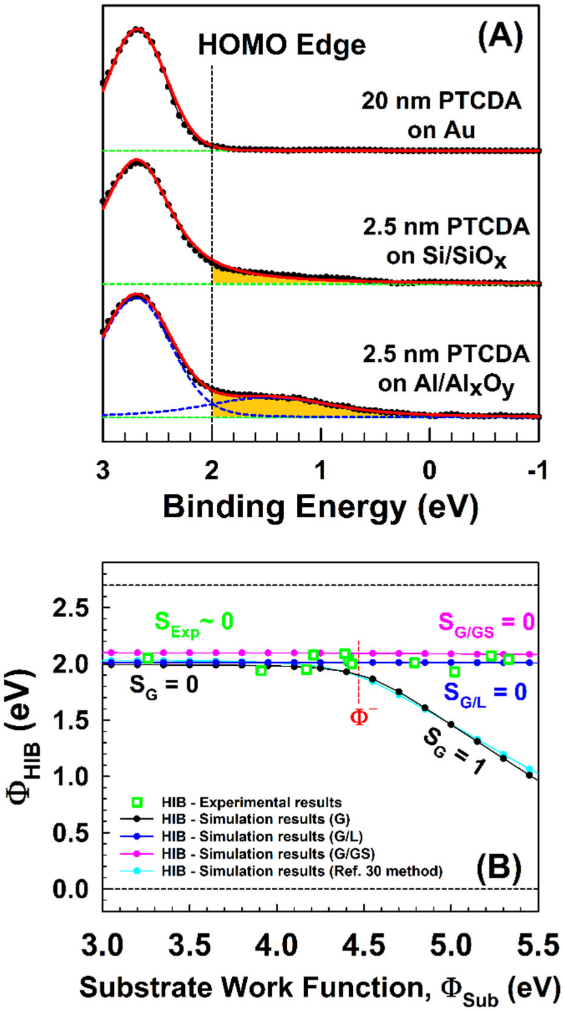

Figure 24. (A) Magnified HOMO regions of PTCDA films. Topmost spectrum represents the HOMO feature of a 20 nm thick film deposited on a sputtered-clean Au substrate. The spectrum is well-fitted by a pure Gaussian distribution. The middle spectrum shows the HOMO feature of a 2.5 nm thick film of PTCDA on Si/SiO$_x$. The density of states tails into the gap of the organic semiconductor, and is approximated by a Lorentzian contribution. The bottom spectrum represents the HOMO feature of a 2.5 nm thick film of PTCDA on Al/Al$_x$O$_y$. The spectrum is fitted by a pure Gaussian (HOMO) and a Voigt (gap-state) distribution. (B) Hole injection barrier (Φ_{HIB}) as a function of the substrate work function (Φ_{sub}) for a 20 nm thick PTCDA film. Black, blue, and pink circles represent the simulation results where the DOS of the organic layers are approximated by Gaussian (G), Gaussian/Lorentzian (G/L), and Gaussian/Gap-State (G/GS) peaks respectively (connecting line serves as a guide to the eye). Cyan circles represent the simulation results where the DOS of the organic layers are approximated by the method described in Ref. 30. Green circles represent the experimental results of the present work.

As a first assumption and for simplicity, the density of states (DOS) of the organic layers are approximated by Gaussian peaks centered at the HOMO and LUMO maxima (in order to define frontier orbital levels). The results for 62 layers (~20 nm) of organic molecules lying flat on substrates with different work functions are shown in Figure 24B. Specifically, the final energy level alignment and the resulting electrostatic potential in thermal equilibrium for a film deposited on a substrate with a work function set at 3.2 eV is depicted in Figure S19A (see Appendix C). The results indicate that with increasing distance from the electrode, the local electron potential energy, *–eV(x)*, shifts the density of states as well as the vacuum level to lower binding energies, leading to a decrease of Φ_{HIB} and an increase of Φ_{EIB}. According to the results depicted in Figure 24B (which represent the dependence of Φ_{HIB} on the substrate work function), the model predicts two different regions in which the slope parameter (S) can be either zero or unity. The value of Φ_{HIB} for the interface between organic molecules and substrates with the work function less than ~4.45 eV is obtained as 1.95 eV which is in good agreement with the experimental results in this work (about 2.0 ± 0.1 eV); however, the overall trend is in obvious contrast with our experimental observation. The model predicts a Fermi level pinning regime characterized by a slope of zero ($S_G = 0$) for substrate work functions lower than $\Phi^- = 4.45$ eV and vacuum level alignment regime with $S_G = 1$ for work functions higher than 4.45 eV. In contrast, our experimental results show Fermi level pinning at 4.5 ± 0.1 eV over the whole range of substrate Fermi energies (Figure 24A). Figure 25A represents the final energy level alignment and the resulting interface dipole for a 20 nm thick film of PTCDA deposited on three representative substrates with work functions set to 3.2, 4.3, and 5.4 eV. As the work function of the substrate increases and falls into the gap of semiconductor, simulation predicts a transition from the Fermi level pinning to vacuum level alignment regime. We argue that this contradiction may originate from the choice to model the density of states for the first layers with simple Gaussian line shape. This type of behavior was only observed for substrate-organic interfaces with weak interaction where the organic molecules were electronically decoupled from the substrate. Considering the electronic coupling of organic semiconductors with the substrate states can lead to fractional slope parameters between 0 and 1 ($S = d\Phi_{HIB}/d\Phi_{sub} = d\Phi_{EIB}/d\Phi_{sub} = d\Phi_{org/sub}/d\Phi_{sub}$) as reported in many other studies [138-139, 151, 161, 170-173].

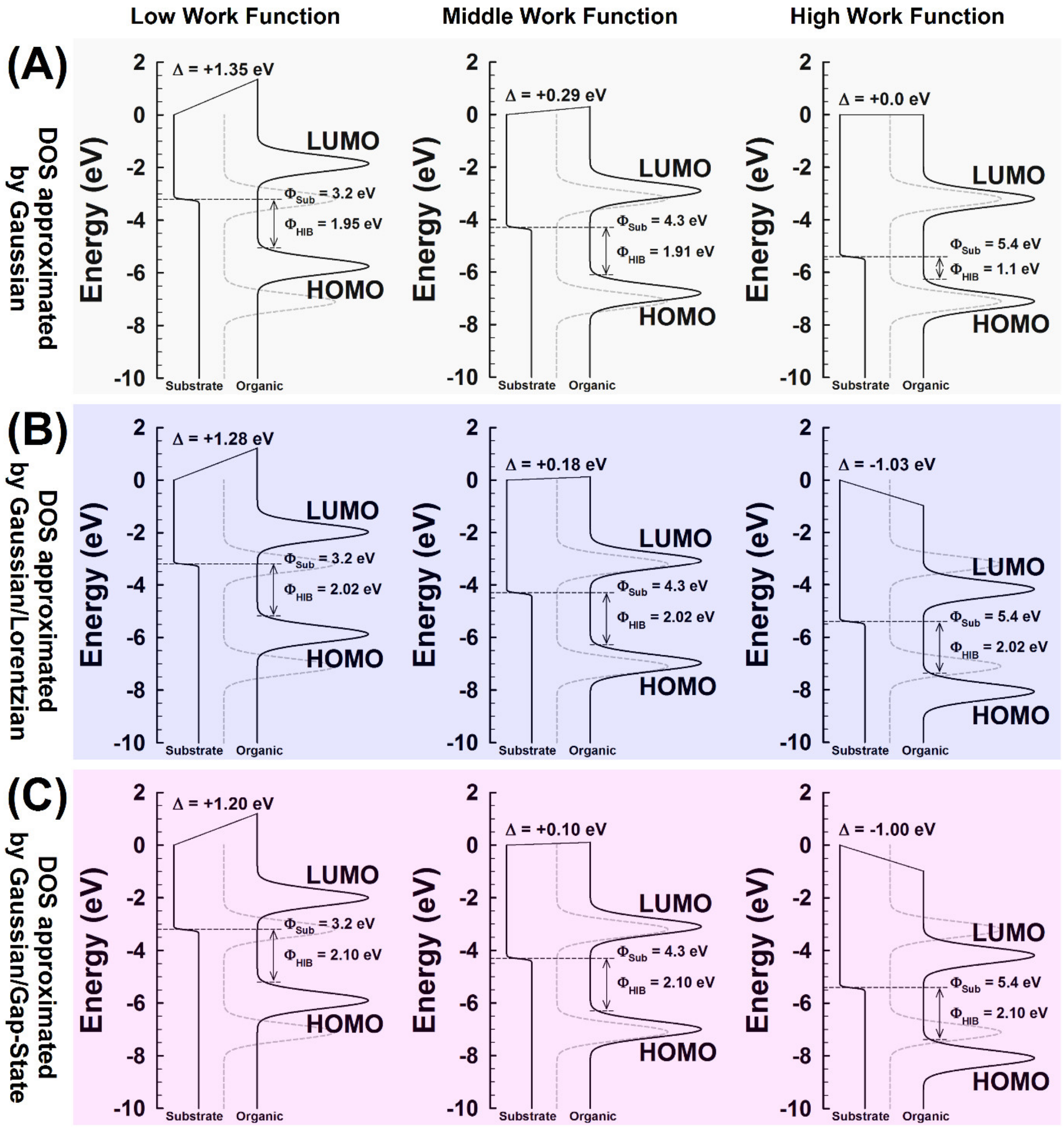

Figure 25. Final energy level alignment as well as the resulting interface dipole in thermal equilibrium for a 20 nm thick PTCDA film deposited on substrates with Φ_{sub} of 3.2, 4.3, and 5.4 eV. (A) The DOS of the organic layers are approximated by Gaussian peaks. (B) The gradual change of DOS line shapes from pure Lorentzian for the first molecular layer to pure Gaussian distribution for layer number 15. (C) The gradual reduction of the contribution of gap-states to the DOS from the first layer to layer number 15. (the gray dashed-line represents the DOS for the final layer of the organic before starting the iteration which is in vacuum level alignment with the substrate)

Through perturbation theory, it is well known that the interaction of semiconductor molecules with a substrate can lead to broadening of molecular energy levels and, thus, creation of induced density of interface states inside the gap of organic molecules [139]. Therefore, direct electronic coupling of the first molecular layers to the substrate may result in a homogeneous life-time broadening that can be considered as a Lorentzian contribution [329-330]. We argue that the much broader HOMO peaks measured by us for the first deposited layers are due to this effect. With reference to previously reported approaches, one can find that in the induced density of interface states (IDIS) model, Vázquez et al [151] only consider a monolayer of organic semiconductor with a pure Lorentzian distribution of DOS. In the electrostatic model, Oehzelt et al. [137] introduce the Lorentzian broadening only to the first monolayer, while retaining pure Gaussians for all subsequent layers. The simulation under this condition, does not really improve the results for this semiconductor (Figure 24B) and similar to the previous section it again predicts a transition from Fermi level pinning to vacuum level alignment regime.

In the second approach, we include the effect of electronic coupling of PTCDA molecules to the substrate on the model by modifying the DOS peak shape for the first 15 discretization intervals beyond a pure Gaussian distribution as discussed in the previous section. Our experimental UPS data shows that the broadening of the HOMO level and energy distribution of electronic states tailing into the fundamental gap can extend up to 5 nm for PTCDA. Therefore, we introduce a successively damped Lorentzian broadening to the first 15 layers (~4.8 nm) at the interface. For the first layer (which is in direct contact with the substrate), we choose a pure Lorentzian (as considered by Vázquez et al [151]) or Voigt peak function (as considered by Oehzelt et al [137]). While progressing from layer 2 to 15, we gradually change the peak shape to a pure Gaussian distribution and retain the pure Gaussian shape for all subsequent layers (layer 16 to 62, Figure S19B). The results for changing from a Voigt peak function to pure Gaussian distribution (through decreasing the weight of Lorentzian contribution) is not presented due to similarity. A comparison with the experimental data in Figure 23B shows excellent agreement, suggesting that tailing of the density of interface states into the gap plays a pivotal role for the observed Fermi level pinning. We obtain Φ_{HIB} = 2.02 eV and $S_{G/L}$ = 0 which are in good agreement with the experimental values, Φ_{HIB} = 2.0 ± 0.1 eV and S_{Exp} ~ 0. Figure 25B represents the energetic alignment as well as the resulting interface dipole for a 20 nm thick film of PTCDA deposited on three representative substrates with Φ_{sub} of 3.2, 4.3, and 5.4 eV. Figure S19B represents the electron potential energy for a 20 nm thick PTCDA film situated on a substrate with Φ_{sub} of 3.2 eV.

In the last approach, we directly introduce a damped peak of gap-state to the DOS of the first layers based on our experimental observation for PTCDA deposited on Al/Al_xO_y. Similar to the second approach, we assume that the first 15 molecular layers are under an electronic coupling effect of the substrate. For the first layer (which is in direct contact with substrate), we choose a Gaussian distribution of the HOMO feature as well as a Voigt profile of gap-state centered 1.3 eV lower than the HOMO maxima. For layers 2 t o15, we gradually reduce the contribution of gap-state and finally retain only the pure Gaussian HOMO distribution for the subsequent layers (layer 16 to 62). Figure S19C schematically represents the gradual reduction of the contribution of gap-state to the DOS (through linear combination). Once again, electrostatic calculations reveals a steep potential change as well as a compression of the band-bending region towards the interface between the first monolayer and the substrate (see Figure 25B). The model predicts the direction and the amount of the shift of the vacuum level at the interface in good accordance with experimental results (Figure 23B). A linear dependence of the injection barriers versus substrate work function, i.e. Fermi level pinning behavior, is predicted for the film of PTCDA. Through this approach, we obtain Φ_{HIB} = 2.10 eV and $S_{G/GS}$ = 0 which are again in a very good agreement with the experimental observations, Φ_{HIB} = 2.0 ± 0.1 eV and $S_{Exp} \sim 0$. The final energy level alignment and the resulting interface dipole for a 20 nm thick film of PTCDA deposited on three representative substrates with Φ_{sub} of 3.2, 4.3, and 5.4 eV are depicted in Figure 25C. The results are in excellent agreement with experimental electronic structures determined by UPS (see Appendix C, Figure S20 and Table S1).

Thus by using both approaches, the electrostatic model by Oehzelt et al. [137] succeeds in a qualitative and a quantitative description of the pivotal role of the induced density of interface states for Fermi level pinning. It demonstrates how the shape of the DOS near the OSC/substrate interface has long-range influence on key parameters (e.g. the barrier to charge injection) of the entire organic film.

4.4. Conclusion

Universal Fermi level pinning of PTCDA on eleven different substrates is found to be the direct result of a high density of interface states for this organic semiconductor. Electrostatic calculations operating with the concept of an induced density of interface states successfully explain these results with quantitative agreement. This is realized by either introducing a gradual change in the DOS shape from Lorentzian or Voigt profile at the interface to Gaussian distribution far away from the surface of the substrate or considering a direct gap-state in the DOS shape for the first layers at the interface. The results of this work should facilitate the application of numerical electrostatic models for the prediction of the interfacial electronic structure of organic semiconductors on metals with strong interactions.

Acknowledgements:

Financial support of MSK and MS has been provided by the Institutional Strategy of the University of Tübingen (Deutsche Forschungsgemeinschaft, ZUK 63) and under grant SCHE1905/3, respectively.

Corresponding Author:

*email: marcus.scheele@uni.tuebingen.de

Author Contributions:

The manuscript was written through contributions of all authors. All authors have given approval to the final version of the manuscript.

Supplementary Material:

Details of the electrostatic potential calculations and the material parameters used for electrostatic potential calculations; energy level alignment as well as the resulting electrostatic potential in thermal equilibrium for a 20 nm thick PTCDA film; details of the experimental procedures; the electronic structure of PTCDA on different eleven substrates; description of the "pillow" or "push-back" effect and its role in the amount work function; estimation of oxide layer thicknesses and the possibility of charge transfer through tunneling; UPS spectra of the secondary electron cut-off and the magnification of the valence band for different substrates coated with PTCDA of various thicknesses.

Chapter 5

Collaborated Manuscripts

5.1. Collaborated Manuscript 1: Toward Conductive Mesocrystalline Assemblies: PbS Nanocrystals Cross-Linked with Tetrathiafulvalene Dicarboxylate

(by Alexander André, Danylo Zherebetskyy, David Hanifi, Bo He, **Mahdi Samadi Khoshkhoo**, Maciej Jankowski, Thomas Chassé, Lin-Wang Wang, Frank Schreiber, Alberto Salleo, Yi Liu, and Marcus Scheele published in *Chem. Mater.* **2015**, 27, 8105-8115, DOI: 10.1021/acs.chemmater.5b03821)

In this manuscript, we report on PbS NC solids cross-linked with the OSC tetrathiafulvalene dicarboxylate (TTFDA). We demonstrate that this molecule invokes a mesocrystalline assembly of PbS NCs into a near-cubic close-packed structure in which the atomic lattices are strictly coaligned with the NC lattices. The mesocrystalline structure is already observed in the first NC monolayer indicating that strong in-plane interactions are responsible for the observed packing. The interparticle distance along the [001] direction of the NC lattice coincides with the length of TTFDA implying that the NCs are separated by one monolayer of the OSC. Our results are supported by optical spectroscopy and density functional theory (DFT). The latter is also used to predict the transport properties of this coupled organic-inorganic nanostructure (COIN), which are found to be dominated by a weak resonance for holes, especially for larger NC diameters. This is confirmed by field-effect transistor (FET) measurements revealing unipolar hole conduction with a 40-fold increase in mobility as the NC diameter is increased from 6.3 to 9.7 nm.

Methods

Synthesis of PbS Nanocrystals. The details on the synthesis of PbS nanocrystals can be found in the original publication.

Synthesis of [TBA]$_2$TTFDA. The details on the synthesis of [TBA]2TTFDA can be found in the original publication.

Ligand Exchange with TTFDA – Solid/Air Exchange. Three milligrams of [TBA]$_2$TTFDA was dissolved with 3 mL of methanol. Substrates for various characterization methods (FET, XPS, PDS, SEM, GIXD, etc.) were cleaned on using soap scrub, rinsed with distilled water, followed by isopropanol and acetone, blow-dried, UV/ozone cleaned for 5 min, and mounted onto a spin-coater. One drop of a filtered hexanes solution of nanoparticles (roughly 1 mg/mL) was drop-cast onto the substrate and spun at 2000 rpm with a 1 s ramp for 15 s. At rest, the substrate was covered with the TTFDA solution (approximately 200 μL) and allowed to dry completely within roughly 10 min. While spinning at 2000 rpm, it was washed with methanol to spin-off excess TTFDA followed by hexanes to wash off the oleate. This procedure was repeated one more time to yield a continuous film.

Ligand Exchange with TTFDA – Liquid/Air Exchange. Three milligrams of $[TBA]_2TTFDA$ was dissolved with 3 mL of methanol in a Teflon well. Two-hundred microliters of a dilute solution of PbS nanocrystals in hexane (~ 0.1 mg/mL) was carefully deposited on top of the methanol solution and allowed to dry under a glass slide cover. The barely visible, floating membrane of NCs that formed on top of the methanolic TTFDA solution was allowed to ligand exchange and assemble overnight.

The TTFDA-exchanged membrane was carefully "stamped" onto a desired support (Si substrate or Cu/C grid) by holding the substrate upside-down and approaching the membrane from the top. The transferred membrane was mildly annealed at 80° C for 20 min and the film carefully rinsed with methanol to remove excess TTFDA.

Photoelectron spectroscopy. Silicon substrates were cleaned, coated with PbS nanoparticles and ligand exchanged with TTFDA as described under "ligand exchange with TTFDA" in the main body of the manuscript. XPS measurements were carried out using a SPECS spectrometer which was equipped with a XR50 X-ray source (Al Kα, working at 12.5 kV and 20 mA, 1486.61 eV) and a PHOIBOS 100 MCD analyzer. The pressure in the analyzer chamber was maintained below 5×10^{-10} mbar during the measurements. All survey spectra, scans of 1000 eV, were taken at analyzer pass energy of 50 eV. High resolution scans were performed at the pass energy of 20 eV and steps of 0.05 eV. The binding energies were corrected for electrical charge effects by referencing to the Au 4f 7/2 peak which was assumed to have a binding energy of 84.0 eV. The photoelectrons were detected at a takeoff angle of $\Phi = 0^o$ with respect to the surface normal. Acquisition and storage of data were accomplished using SpecsLab software version 2.35-r13657. Data were converted to VAMAS format and processed using Unifit2014 software. Each spectrum was also corrected for the satellite peaks (9.8 and 11.8 eV from $K_{\alpha 3}$ and $K_{\alpha 4}$ respectively).

Ligand exchange with $[TBA]_2TTFDA$ is carried out either at the solid/air interface by using orthogonal solvents ("solid/air exchange") or by a Langmuir-type "liquid/air exchange" as detailed in the Methods. The effect of the ligand exchange is monitored in Figure 26. X-ray photoemission spectroscopy (XPS) in the S 2p (Figure 26a) and S 2s (Figure 26b) spectral region of the same PbS NC sample (1) before and (2) after exchange with $[TBA]_2TTFDA$

reveals the occurrence of a second sulfur species at higher binding energy (164 and 228 eV) than the sulfur species in PbS (161 and 226 eV). In accordance with previous XPS results on Poly(3-hexylthiophene) (P3HT) (doublet at 164.5 and 165.5 eV), which provides a similar chemical environment for the S 2p core levels, we attribute this new sulfur species to TTFDA on the surface of PbS NCs. [331] The S 2p core level of the PbS NCs before ligand exchange is also in good agreement with previous results on bulk PbS (S 2p3/2 = 161.0 eV). [332]

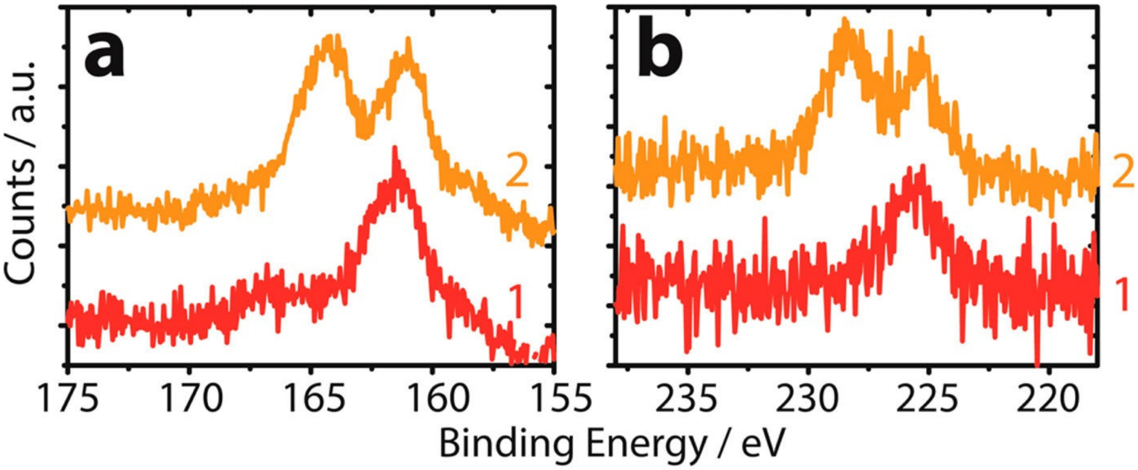

Figure 26. (a) XPS spectra of the S 2p region and (b) of the S 2s region of (1) PbS NCs functionalized with Pb[oleate]$_2$, (2) PbS NCs after ligand exchange with TTFDA.

5.2. Collaborated Manuscript 2: Solution-Processed Two-Dimensional Ultrathin InSe Nanosheets

(by Jannika Lauth, Friederieke E. S. Gorris, **Mahdi Samadi Khoshkhoo**, Thomas Chassé, Wiebke Friedrich, Vera Lebedeva, Andreas Meyer, Christian Klinke, Andreas Kornowski, Marcus Scheele, and Horst Weller published in *Chem. Mater.* **2016**, 28, 1728-1736, DOI: 10.1021/acs.chemmater.5b04646)

In this manuscript, we present a facile solution-processable way for stable colloidal ultrathin InSe nanosheets with lateral dimensions up to ~800 nm by a lamellar ligand templated route. For the first time, the atomic thickness, crystal structure, and chemical composition of the hexagonal phase InSe layers are fully characterized by atomic force microscopy (AFM), electron diffraction (ED), and X-ray photoelectron spectroscopy (XPS). The crystalline inorganic-organic InSe-organic template structure is evaluated by grazing incidence small-angle X-ray scattering (GISAXS). Confocal absorption and photoluminescence measurements on ultrathin InSe layers reveal a strong size quantization in the z-direction, and electrical transport measurements on the sheets emphasize their potential for ultrathin optoelectronics.

EXPERIMENTAL SECTION

Chemicals. The details on chemicals can be found in the original publication.

InSe Nanosheet Synthesis. The details on the synthesis of InSe nanosheets can be found in the original publication.

X-ray Photoelectron Spectroscopy (XPS). XPS measurements were carried out using a SPECS spectrometer equipped with a XR50 X-ray source (Al Kα, working at 12.5 kV and 20 mA, 1486.61 eV) and a PHOIBOS 100 MCD analyzer. The pressure in the analyzer chamber was maintained below 5×10^{-10} mbar during the measurements. All survey spectra, scans of 1000 eV, were taken at analyzer pass energy of 50 eV. High-resolution scans were performed at the pass energy of 20 eV and steps of 0.05 eV. The binding energies were corrected for electrical charge effects by referencing to C 1s sp3 peak, which was assumed to have a binding energy of 284.6 eV. The photoelectrons were detected at a takeoff angle of $\Phi = 0°$ with respect to the surface normal. Acquisition and storage of data were accomplished using SpecsLab software version 2.35-r13657. Data were converted to VAMAS format and processed using Unifit2014 software. Data fitting was performed using Gauss-Lorentz profiles. The background was calculated and subtracted using the Shirley method. Each spectrum was also corrected for the satellite peaks (Δ = 9.8 and 11.8 eV from $K_{\alpha 3}$ and $K_{\alpha 4}$, respectively). The sensitivity factors used for In(3d$_{3/2}$), In(3d$_{5/2}$), In(3d), Se(3d$_{3/2}$), Se(3d$_{5/2}$), and Se(3d) were 9.22, 13.32, 22.54, 0.934, 1.36, and 2.294, respectively.

Stoichiometry of Ultrathin InSe Nanosheets. The chemical composition of the InSe nanosheets is determined by X-ray photoelectron spectroscopy (XPS, Figure 27). To fit the raw data for the In(3d) and Se(3d) spectral regions, we use three constraints: A fixed In 3d 5/2: In 3d 3/2 as well as Se 3d 5/2: Se 3d 3/2 ratio of 3:2, a constant spin-orbit split for the two indium and selenium components and a fixed full-width at half-maximum (fwhm) for each element. We observe two In(3d) species with spin-orbit split doublets (ΔE = 7.6 eV) at 444.8/452.4 eV and 445.8/453.4 eV, respectively (Figure 27a). Similarly, we detect two Se(3d) species at 54.0/54.9 eV and 55.0/55.9 eV (ΔE = 0.9 eV) which are typical values for metal selenides (Figure 27b). We find no signs of any Se–O bonds (~59 eV) in all samples. The O(1s) region exhibits a rather unspecific broad peak with a binding energy maximum at 533.1 eV. Owing to the history of the samples, this feature originates most likely from adsorbed oxygen/moisture and/or from the 2-propanol utilized during purification of the material after synthesis. We note that for (partially) oxidized indium, two O(1s) signals are expected at roughly 530 and 532 eV, and that our O(1s) spectrum does not show a significant shoulder in this region. [333-334] To determine the In:Se ratio from XPS, we use

$$C_{In}/C_{Se} = \frac{I_{In}J_{In}}{F_{In}}/\frac{I_{Se}J_{Se}}{F_{Se}},$$

where C_i is the concentration of the photoelectron emitting atom/ion within the sampled volume, J_i represents the X-ray flux striking the analyzed area, and F_i is the sensitivity factor of element i, given by

$$F_i = \alpha_{pc(i)} k_f \lambda_{IMFP(i)},$$

with $\alpha_{pc(i)}$ the photoelectron cross section of i, k_f the combined instrument factor, and $\lambda_{IMFP\,(i)}$ the inelastic mean free path (IMFP) of the photoelectron emitted by the element i. By keeping $J_{In} = J_{Se}$, the stoichiometric ratio In:Se of a typical nanosheet is directly inferred from the absolute areas of the fitted components. We find an average element In:Se ratio in the nanosheets of 1.1 (±0.1):1. In light of the two different In and Se species, we attempt an analysis by postulating a mixture of two In_XSe_Y species and compare both "low binding energy" as well as "high binding energy" In and Se components with each other. We note that in both cases, the overall 1.1:1 In:Se ratio is exactly obeyed. The component at lower binding energies is by far the most abundant with a relative content of 93.5%. Additionally, the In (3d 5/2) (444.8 eV vs 444.7 eV) and Se (3d 5/2) (54.0 eV vs 54.1 eV) signals are in rather good agreement with previous XPS investigations of InSe thin films. [335] The same authors of this previous work report that freshly cleaved InSe single crystals without any surface-oxygen exhibit high In(3d 5/2) and Se(3d 5/2) binding energies of 445.7 and 55.1 eV, respectively, which are again in excellent agreement with our "high binding energy" component. The differences in binding energy of 1.0 eV between freshly cleaved and thin-film InSe are explained with surface modifications because of the exposure to ambient conditions by the authors, and we hold a similar effect responsible for the almost identical XPS data obtained with the material presented here.

To summarize the XPS experiment, our data suggest a near-stoichiometric indium selenide composition with clear signs of surface modification (e.g., by organic surfactants). A minor portion (6.5%) is consistent with atomically clean InSe (e.g., atoms in the interior of a sheet).

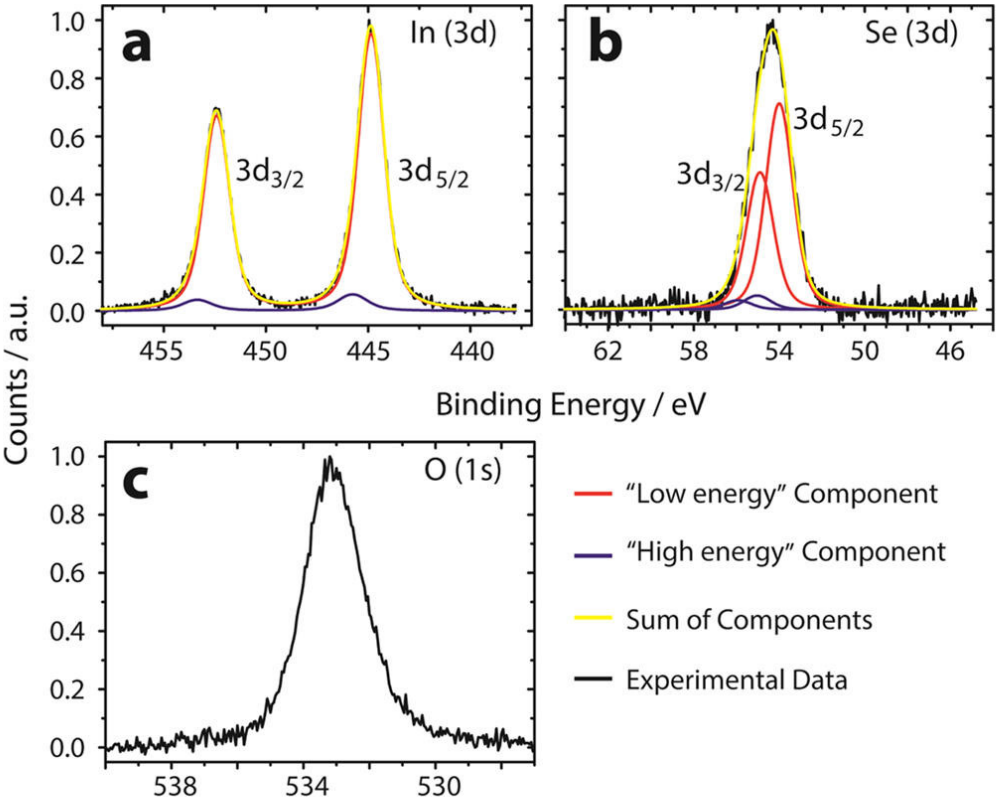

Figure 27. XPS of InSe nanosheets in (a) the In(3d) core level, (b) the Se(3d) core level, and (c) the O(1s) core level region. Two components for In and Se are detected, the attribution and fitting parameters of which are detailed in the main text. The O(1s) signal is not fitted because of a likely contribution from various unspecific contaminants such as surface oxygen, alcohols, etc.

5.3. Collaborated Manuscript 3: Towards Photo-Switchable Transport in Quantum Dot Solids

(by Christine Schedel, Robert Thalwitzer, **Mahdi Samadi Khoshkhoo** and Marcus Scheele published in *Z. Phys. Chem.* **2017**, 231(1), 135–146, DOI 10.1515/zpch-2016-0863)

In this manuscript, we investigate the potential of 1,2-Bis(5′-carboxy-2′-methylthien-3′-yl)-cyclopentene (DTCP) as a photochromic linker to cross-link PbS QDs and yield nanostructured thin films with photoswitchable transport.

Experimental

Materials: The details on the materials can be found in the original publication.

Ligand exchange with DTCP – liquid/air-exchange: Ligand exchange with DTCP and assembly into superlattices of PbS QDs was carried out at the liquid/air interface in a home-built, sealable cell following a modified procedure from Dong et al. as recently described by us. [277, 336] Substrates for the characterization methods (XPS, FET) were cleaned by ultrasonication in distilled water, followed by acetone, ethanol and isopropanol for 5 min each and UV/ozone treatment for 10 min. In a homemade reaction chamber (3 cm diameter) the desired slanted substrate (Si or Au) was covered with acetonitrile. Fifty-five microliter of a dilute solution of PbS nanocrystals in hexane/octane 1:1 (5 μM) was carefully deposited on top of the acetonitrile with a rate of 0.2 mL/min and allowed to dry. Once a barely visible, floating membrane of nanocrystals (NCs) had formed, 1 mL of a dimethylsulfoxide solution of DTCP (roughly 1 mg/mL) was carefully injected into the bottom of the acetonitrile phase. The sample was allowed to ligand exchange and assemble overnight in the sealed chamber. The DTCP-exchanged membrane was carefully lowered onto the substrate by gradually removing the acetonitrile solution. The substrate was mildly annealed at 60 °C for 5 min and washed with methanol to remove excess DTCP.

X-ray photoemission spectroscopy (XPS): XPS measurements were carried out using a SPECS spectrometer equipped with an XR50 X-ray source (Al Kα, working at 12.5 kV and 20 mA, 1486.61 eV) and a PHOIBOS 100 MCD analyzer. Samples were prepared by drop casting of the pure ligand and PbS QDs as well as deposition of PbS QDs film after ligand exchange on gold substrates. The pressure in the analyzer chamber was maintained below 3×10^{-10} mbar during the measurements. No changes in the core level signals of the as-prepared films and the films under X-ray irradiation were observed, underlining the stability of the molecules during data acquisition. The resolution in XPS measurements is determined as 0.8 eV (calculated from the width of Fermi edge on the Au substrate). The binding energies were corrected for electrical charge effects by referencing to the Au4f peak, which was assumed to have a binding energy of 84.0 eV. The photoelectrons were detected at a takeoff angle of Φ = 0° with respect to the surface normal. Data were converted to VAMAS format and processed using Unifit2014 software. Data fitting was performed using Gauss-Lorentz profiles. The background was calculated and subtracted using the Shirley method. Each spectrum was also corrected for satellite peaks (Δ=9.8 and 11.8 eV from $K_{\alpha3}$ and $K_{\alpha4}$, respectively).

To further verify successful functionalization of PbS QDs with DTCP, we perform X-ray photoelectron spectroscopy (XPS) of the S2p and S2s spectral region in Figure 28 of pure DTCP as well as of the QDs before and after ligand exchange. The sulfur atoms of pure DTCP appear at much higher binding energies (164.2 eV for S2p and 228.3 eV for S2s, respectively) than the sulfur in PbS QDs capped with oleic acid (160.9 eV for S2p and 225.5 eV for S2s, respectively), which allows for a facile differentiation. For PbS QDs exchanged with DTCP, we observe the signature of both sulfur species in the XPS spectra, which – within the uncertainty of the fitting procedure – appear to be largely unchanged in terms of their binding energy compared to the pure components.

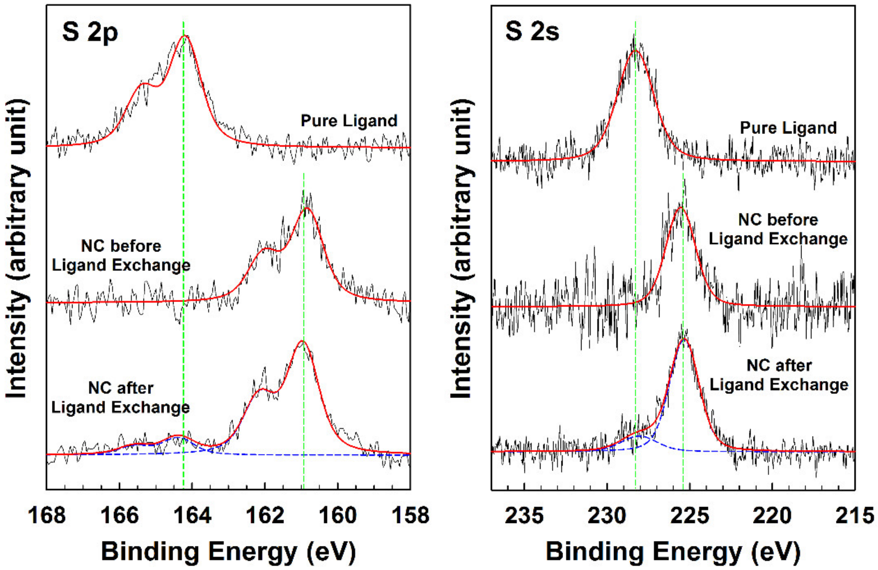

Figure 28. X-ray photoemission spectra (XPS) in the S2p and S2s core level regime of pure DTCP (top), PbS QDs functionalized with oleic acid before (middle) and after treatment with DTCP (bottom).

5.4. Collaborated Manuscript 4: Structure, transport and photoconductance of PbS quantum dot monolayers functionalized with a copper phthalocyanine derivative

(by A. André, C. Theurer, J. Lauth, S. Maiti, M. Hodas, **M. Samadi Khoshkhoo**, S. Kinge, A. J. Meixner, F. Schreiber, L. D. A. Siebbeles, K. Braun and M. Scheele published in *Chem. Commun.*, **2017**, 53, 1700-1703, DOI 10.1039/C6CC07878H)

In this manuscript, we develop a chemical procedure to fabricate ordered monolayers of PbS NCs surface-functionalized with Cu 4,4′,4″,4‴-tetraaminophthalocyanine (Cu-4APc). We monitor the ligand exchange at the NC surface, characterize the structure of the hybrid film, measure important electric transport parameters and assess the potential of this COIN for photodetection. Thin films of oleic acid-capped PbS NCs are assembled at the liquid/air interface and simultaneously ligand-exchanged with Cu-4APc in a closed cell, using acetonitrile as the liquid substrate. The surface-functionalization with Cu-4APc is verified via X-ray photoemission spectroscopy (XPS) and vibrational spectroscopy (FT-IR).

Ligand exchange at the liquid-air interface. The substrate to be coated was put onto a slanted substrate holder in the home-made, sealable reaction chamber filled with 8 ml acetonitrile (Figure 29). The inclined sample position greatly improves the drying procedure of the deposited film. After sealing the chamber, 80 µl of a PbS nanocrystal solution in a 2:1 mixture of octane and hexane were deposited on top of the acetonitrile. The particle deposition rate is one of the most critical parameters and was therefore controlled by using a syringe pump. Low rates around 0.2 ml/min yielded uniform monolayered thin-films, while higher rates (i.e. 1.0 ml/min) yielded thicker and rougher films. The nanoparticle concentration (typically around 3 µM as determined spectroscopically) [337] was chosen so as to have enough particles to completely cover the acetonitrile surface.

The octane/hexane completely evaporated within ~ 2 min and the nanoparticles formed a thin film floating on top of the acetonitrile phase. 200 µl of a solution of 1 mg/ml Cu4APc in dimethylsulfoxide (DMSO) were carefully injected into the sub-phase and the ligand was allowed to diffuse over the duration of 2 hours. We carefully removed the now homogeneously coloured solution to deposit the nanocrystal film on top of the substrate. The substrate was slowly dried, washed with DMSO to remove excess ligand, baked out at 100 °C for 1 min and kept under vacuum overnight.

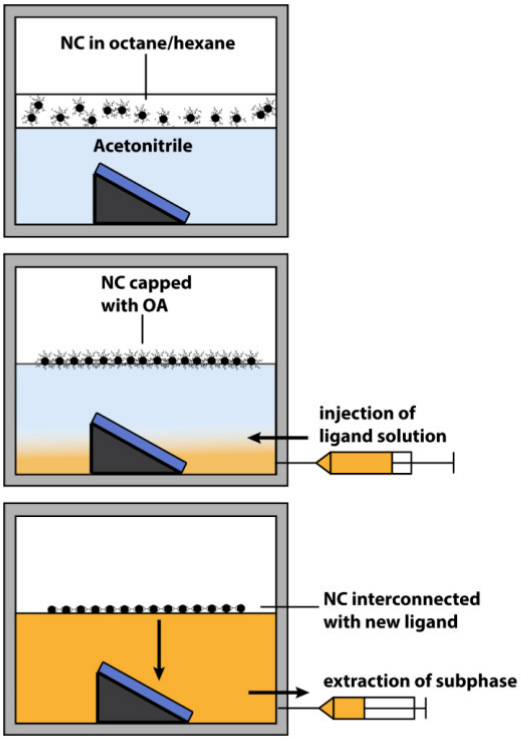

Figure 29. Basic scheme of the thin film preparation procedure in the closed reaction chamber (adapted with permission from original publication, Copyright 2017 The Royal Society of Chemistry).

X -ray photoemission spectroscopy (XPS). XPS measurements were carried out using a SPECS spectrometer equipped with an XR50 X-ray source (Al Kα, working at 12.5 kV and 20 mA, 1486.61 eV) and a PHOIBOS 100 MCD analyzer. Samples were prepared as described under "Ligand Exchange". The pressure in the analyzer chamber was maintained below 3×10^{-10} mbar during the measurements. No changes in the core level signals of the as-prepared films and the films under X-ray irradiation were observed, underlining the stability of the molecules during data acquisition. The resolution in XPS measurements is determined as 0.8 eV (calculated from the width of Fermi edge on the Au substrate). The binding energies were corrected for electrical charge effects by referencing to the Au 4f peak, which was assumed to have a binding energy of 84.0 eV. The photoelectrons were detected at a takeoff angle of $\Phi = 0°$ with respect to the surface normal. Data were converted to VAMAS format and processed using Unifit2014 software. Data fitting was performed using Gauss-Lorentz profiles. The background was calculated and subtracted using the Shirley method. Each spectrum was also corrected for satellite peaks ($\Delta = 9.8$ and 11.8 eV from $K_{\alpha3}$ and $K_{\alpha4}$, respectively).

XPS measurements in the Pb $4f_{5/2}$ and Pb $4f_{7/2}$ spectral region of the same PbS NC sample before (Figure 30a) and after exchange with Cu4APc (Figure 30b) reveal the occurrence of two

Pb species before and three Pb species after ligand exchange. The strong signals at 142.7 eV and 137.8 eV for Pb $4f_{5/2}$ and Pb $4f_{7/2}$, respectively, are consistent with bulk PbS from the interior of the NCs. The weaker signals at 143.8 eV and 138.8 eV can be assigned to surface Pb bound to oleic acid/oleate. After ligand exchange, the latter signal is significantly reduced and a new species at 144.8 eV and 139.8 eV appears, which we attribute to surface Pb, bound to Cu4APc. Moreover, a nitrogen signal appeared in the N 1s spectral region after ligand exchange.

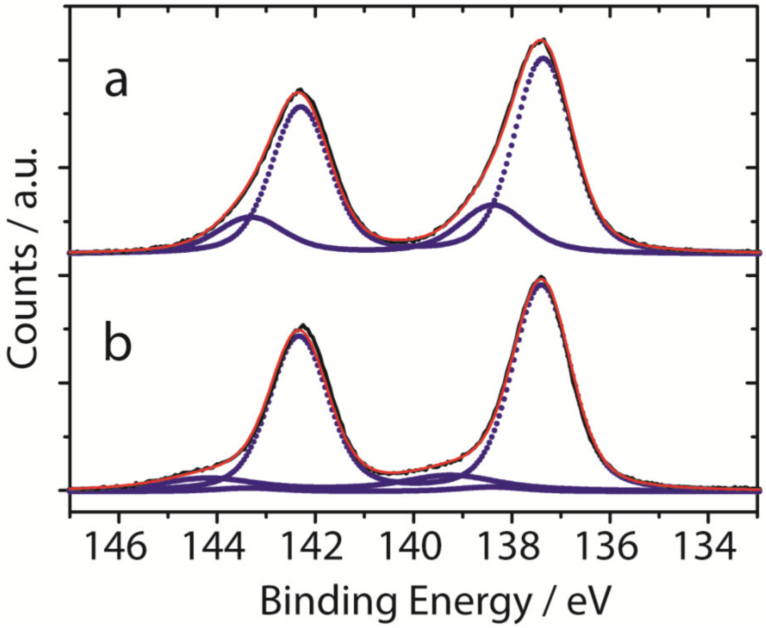

Figure 30. XPS spectra of the Pb 4f region of a) PbS NCs functionalized with $Pb[Oleate]_2$ and b) PbS NCs after ligand exchange with Cu4APc (adapted with permission from original publication, Copyright 2017 The Royal Society of Chemistry).

Appendix A

Supporting information

Surface Functionalization with Cu Tetraaminophthalocyanine Enables Efficient Charge Transport in Indium Tin Oxide Nanocrystal Thin-Films

Mahdi Samadi Khoshkhoo[†], *Santanu Maiti*[‡], *Frank Schreiber*[‡,§], *Thomas Chassé*[†,§], *and Marcus Scheele*[†,§,*]

[†] Institute of Physical and Theoretical Chemistry, University of Tübingen, Auf der Morgenstelle 18, 72076 Tübingen, Germany.

[‡] Institute of Applied Physics, University of Tübingen, Auf der Morgenstelle 10, 72076 Tübingen, Germany

[§] Center for Light-Matter Interaction, Sensors & Analytics LISA+, University of Tübingen, Auf der Morgenstelle 15, 72076 Tübingen, Germany.

S1. Scanning Transmission Electron Microscopy

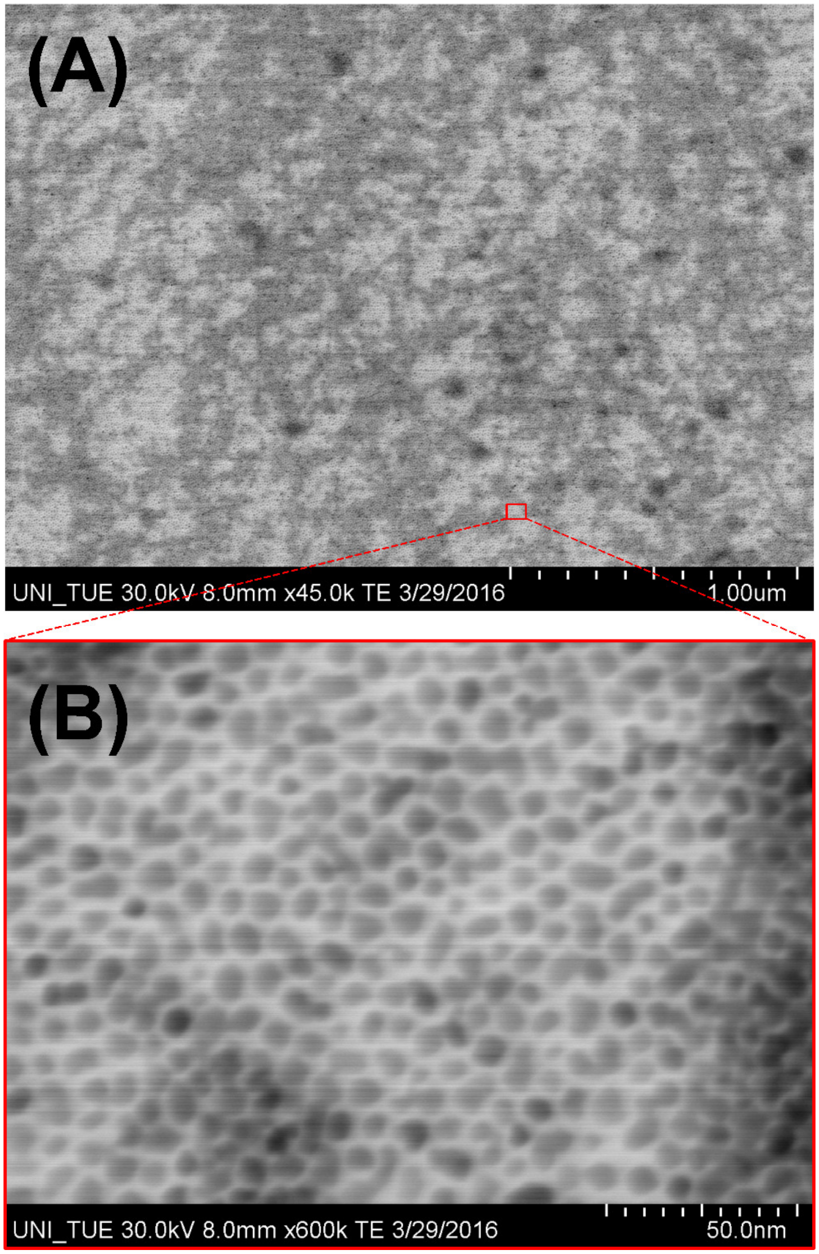

Figure S1. (A) STEM images of a 1-2 monolayer thick film of MA-capped ITO NCs self-assembled into 2D close-packed arrays at the air/liquid interface recorded on a TEM grid. (B) High-magnification STEM image of a selected region.

S2. Histogram for Size Analysis

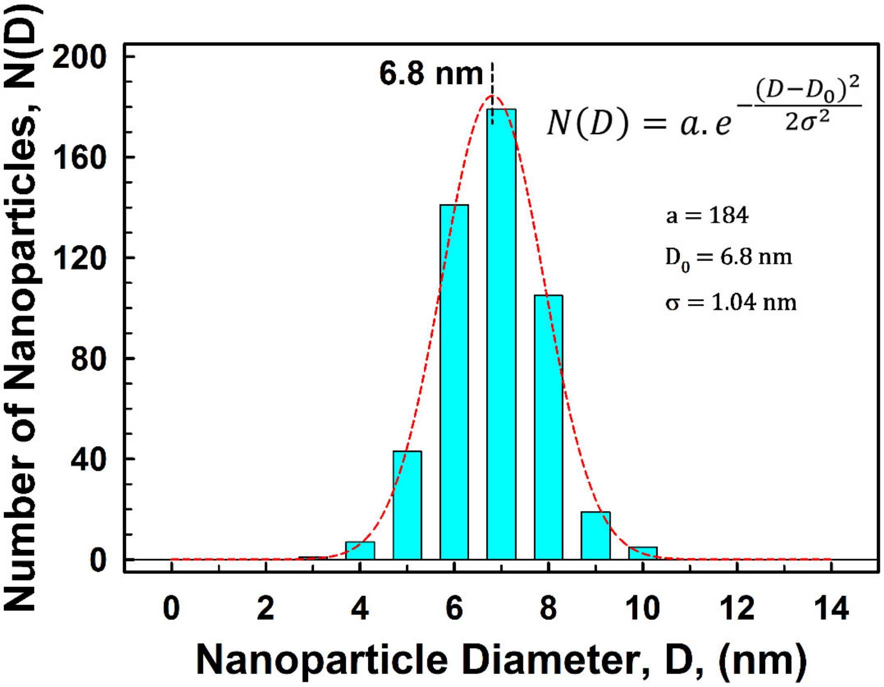

Figure S2. The size distribution of 500 random nanoparticles. Data fitting was performed using Gauss profile. The average particle size (D_0) and the standard deviation (σ) are found to be 6.8 and 1.04 nm, respectively.

S3. Contact Resistance

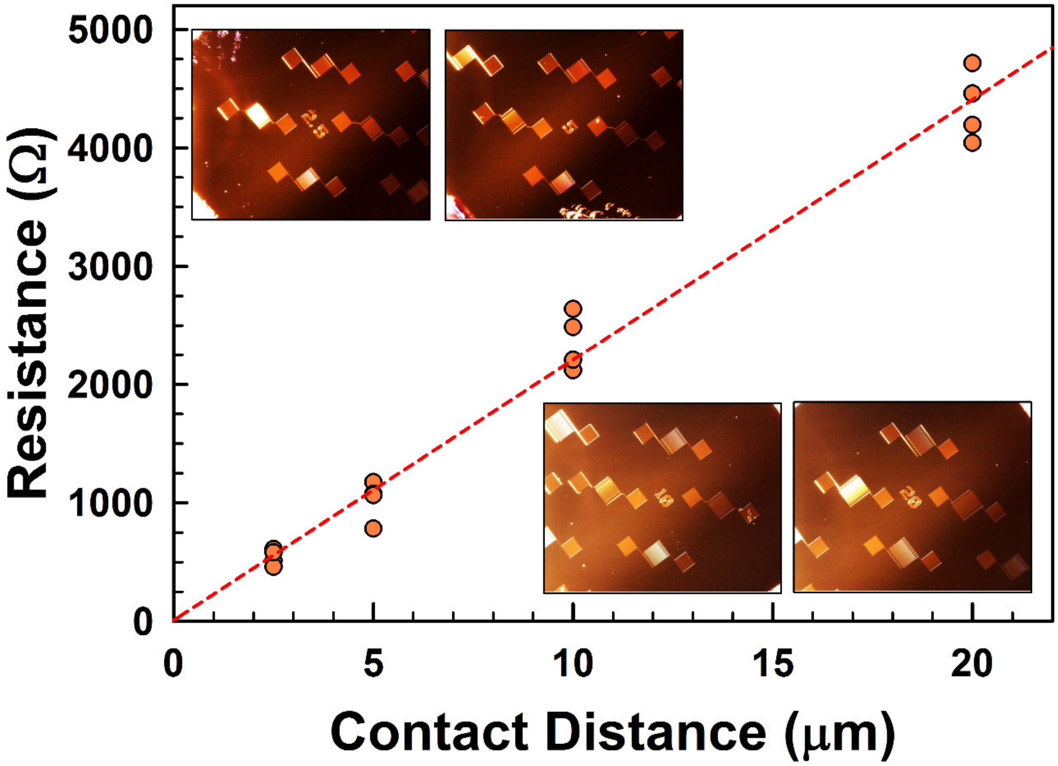

Figure S3. Plot of total resistance *vs.* contact distance for ITO NC film after ligand exchange with Cu4APc. The y-intercept of the fitted line gives the contact resistance and the slop multiply by channel width (*w*) yields the sheet resistance. The inset images show a commercially available pre-patterned substrate with Au contacts of 10 mm width and varying channel lengths (2.5, 5, 10, and 20 μm). The contact resistance is extracted by a linear fit to this data.

Appendix B

Supporting Information

Tunable Charge Transport in ITO Nanocrystal Superlattices – Towards Sensing Applications

Mahdi Samadi Khoshkhoo[†], *Yvonne Joseph*[⊥], *Santanu Maiti*[‡], *Frank Schreiber*[‡,§], *Thomas Chassé*[†,§], *and Marcus Scheele*[†,§,*]

[†] Institute of Physical and Theoretical Chemistry, University of Tübingen, Auf der Morgenstelle 18, 72076 Tübingen, Germany.

[⊥] Institute of Electronic and Sensor Materials, TU Bergakademie Freiberg, Gustav-Zeuner-Straße 3, 09599 Freiberg, Germany.

[‡] Institute of Applied Physics, University of Tübingen, Auf der Morgenstelle 10, 72076 Tübingen, Germany

[§] Center for Light-Matter Interaction, Sensors & Analytics LISA+, University of Tübingen, Auf der Morgenstelle 15, 72076 Tübingen, Germany.

Corresponding Author:

*email: marcus.scheele@uni.tuebingen.de

S1. Scanning Electron Microscopy (SEM)

Figure S4 shows the STEM image of a 2-monolayer thick film of myristic acid (MA)-capped ITO nanocrystals self-assembled into close-packed arrays at the air/liquid interface. Figure S5 to Figure S9 show the same film after ligand exchange to Cu-, Co-, Fe-, Ni-, and Zn4APc respectively.

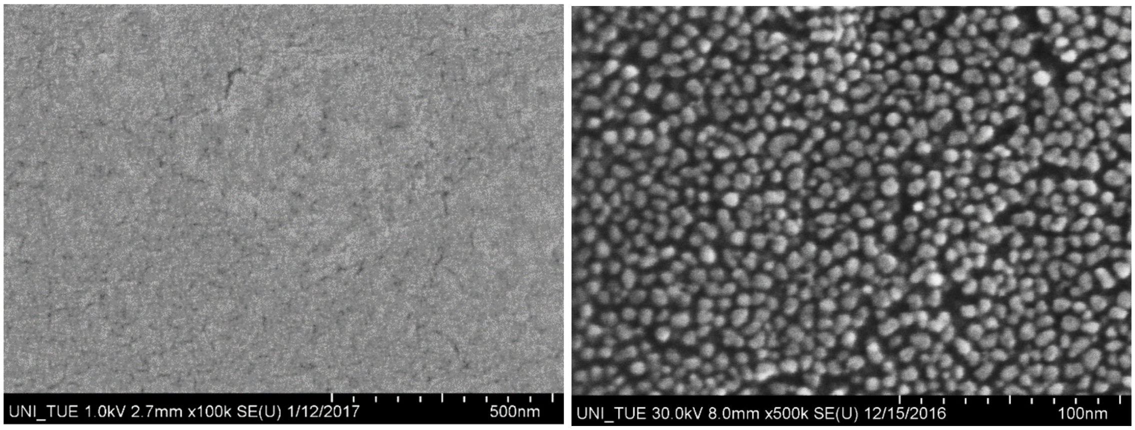

Figure S4. Electron microscopy images of a 2-monolayer thick film of MA / ITO NC prepared at an air/liquid interface

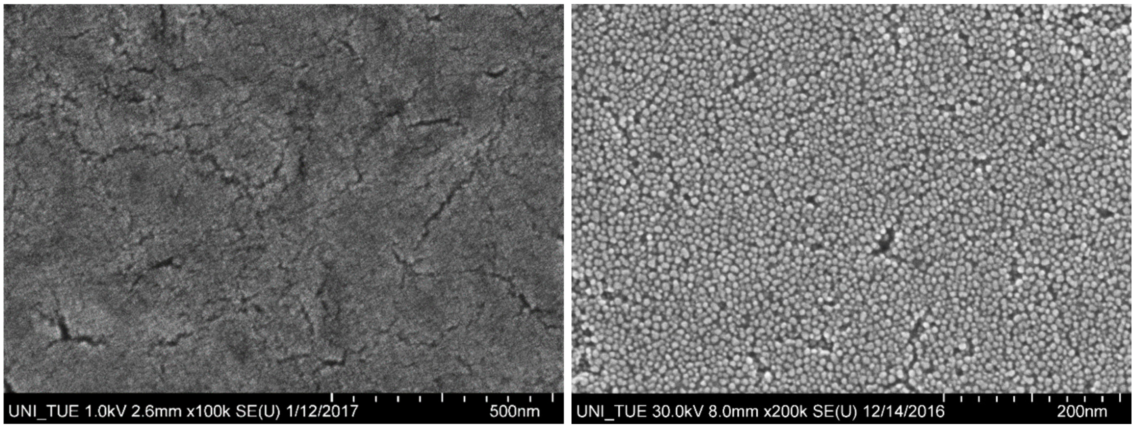

Figure S5. Electron microscopy images of a 2-monolayer thick film of Cu4APc / ITO NC prepared at an air/liquid interface

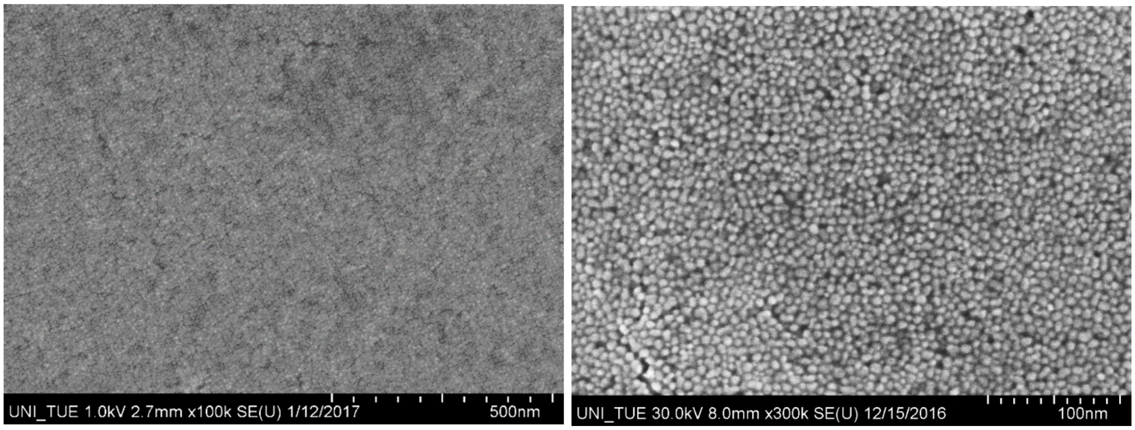

Figure S6. Electron microscopy images of a 2-monolayer thick film of Co4APc / ITO NC prepared at an air/liquid interface

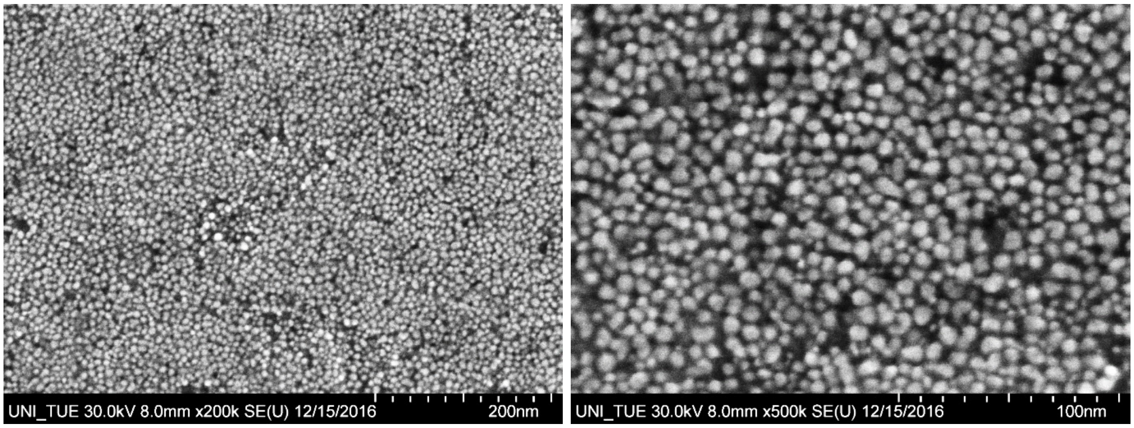

Figure S7. Electron microscopy images of a 2-monolayer thick film of Fe4APc / ITO NC prepared at an air/liquid interface

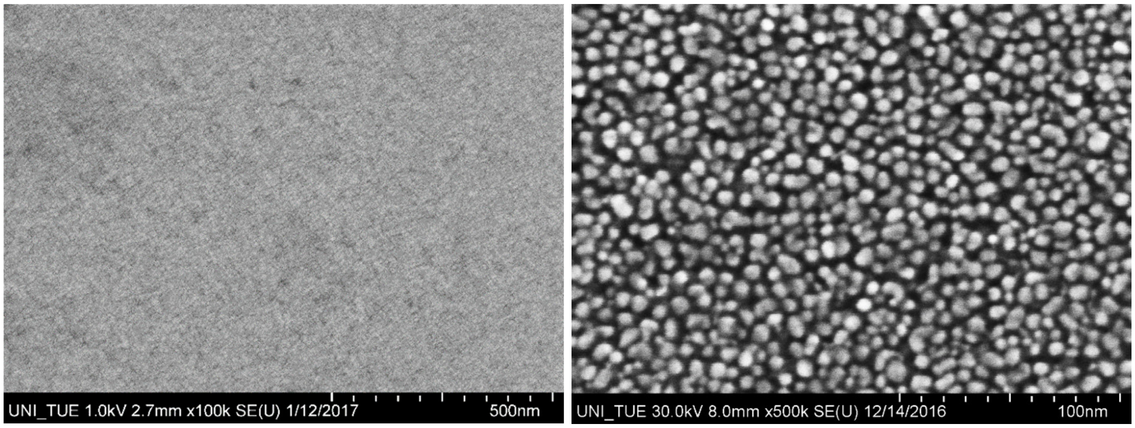

Figure S8. Electron microscopy images of a 2-monolayer thick film of Ni4APc / ITO NC prepared at an air/liquid interface

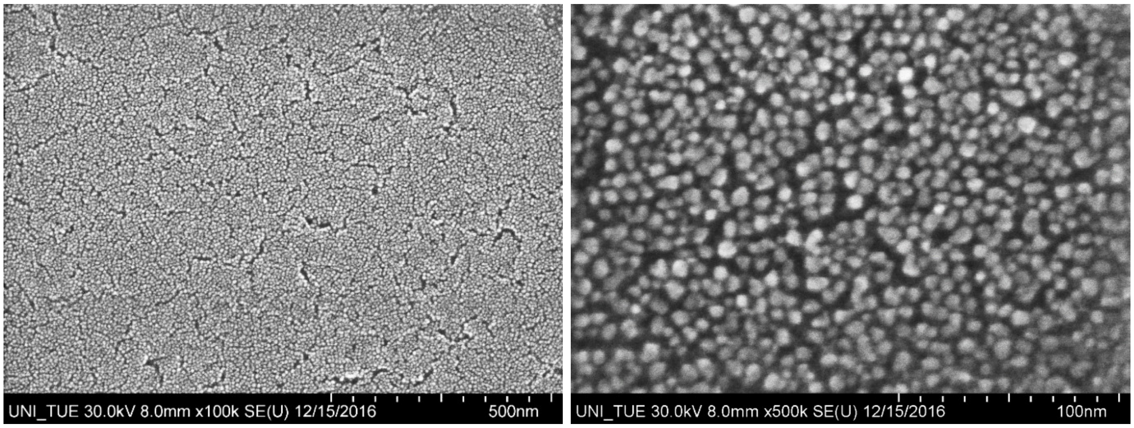

Figure S9. Electron microscopy images of a 2-monolayer thick film of Zn4APc / ITO NC prepared at an air/liquid interface

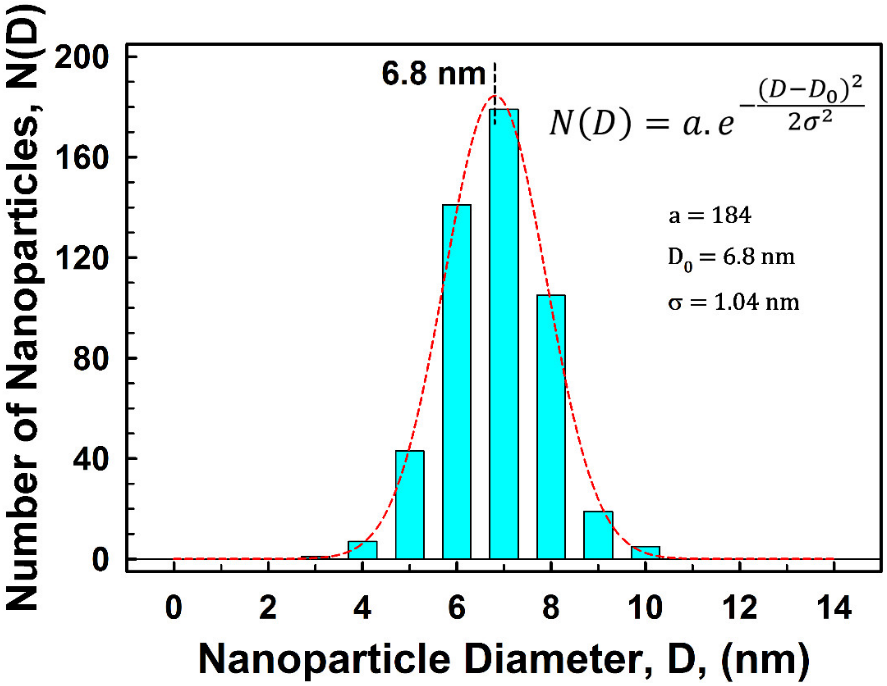

Figure S10. The size distribution of 500 random nanoparticles. Data fitting was performed using a Gaussian profile. The average particle size (D_0) and the standard deviation (σ) are found to be 6.8 and 1.04 nm, respectively. (Reprinted with permission from ref. [276]. Copyright 2017 American Chemical Society)

S2. X-ray Photoelectron Spectroscopy (XPS)

The XPS spectra of the N 1s and ligand metal center regions of the ITO NC superlattices prepared by the interface method before and after ligand exchange are presented in Figure S11. The left column of the figure represents the N1s core-level signal. Before ligand exchange, no nitrogen signal can be detected in the film, but a strong signal appears after exchange. The right column of the figure shows the XPS spectra of Zn 2p, Ni 2p, Fe 2p, Co 2p, and Cu 2p regions for the films after ligand exchange. The relatively weak signals from the metal centers of the ligands are due to the low concentration of metal center atoms (only one atom per ligand molecule) and also strong attenuation of this signal by the surrounding atoms. The detection of these characteristics signals in ITO NC superlattices reveals the presence of the ligand molecules in the structure of thin-films after ligand exchange. The relative tin content is calculated to be ~ 4.9 %, by taking the sensitivity factors of 13.32, 9.22, 14.8, and 10.25 for $In3d_{5/2}$, $In3d_{3/2}$, $Sn3d_{5/2}$, and $Sn3d_{3/2}$, respectively; using the ratio of the Sn3d peak area to the total area of the In3d and Sn3d signals.

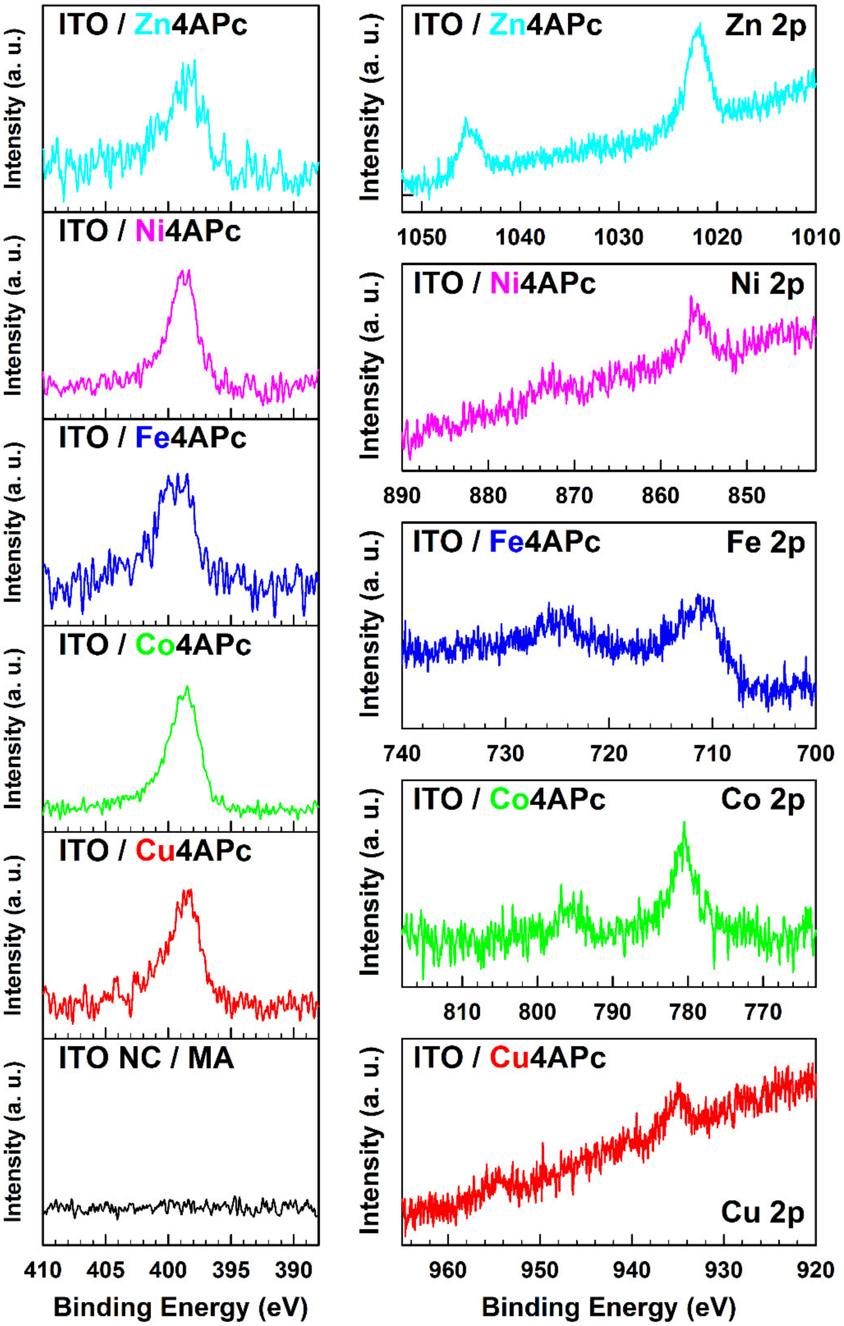

Figure S11. (Left column) XPS spectra of the N1s region of the ITO NC superlattices prepared by the interface method before and after ligand exchange. (Right Column) XPS spectra of the metal center regions of the ITO NC thin-films after ligand exchange to Zn-, Ni-, Fe-, Co-, and Cu4APc.

S3. Ultraviolet-Visible-Near Infrared (UV-vis-NIR) Spectroscopy

The UV–vis–NIR absorption spectra of as-prepared ITO NC films before and after ligand exchange as well as the results before and after annealing stage are displayed in Figure S12. A strong localized surface plasmon resonance (LSPR) peak in the near infrared region is observed in all samples indicating a significant density of free electrons. After ligand exchange, we observe the appearance of a new absorption bands at 600-750 nm which are assigned to ligand molecules. Furthermore, the position of the LSPR peak for all the samples is red-shifted from 2107 nm for MA-capped ITO NCs arrays to 2161, 2133, 2144, 2135, and 2123 nm for the films after ligand exchange to Cu-, Co-, Fe-, Ni-, and Zn4APc, respectively. After annealing at 250 °C for 2 h under nitrogen atmosphere, the LSPR peaks are further shifted to lower energies in all cases (see Table S1 for details).

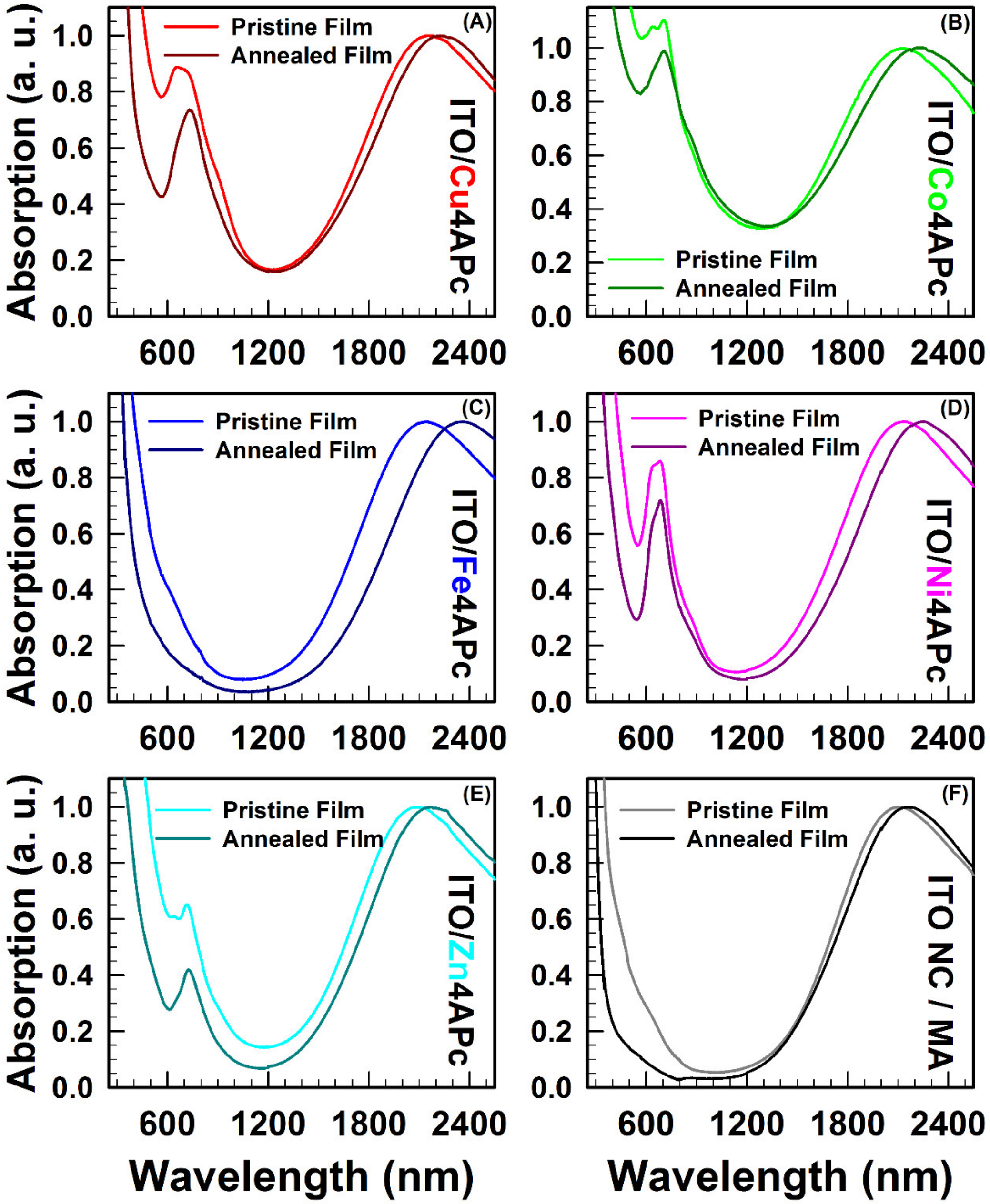

Figure S12. UV–vis–NIR spectra of a 2-monolayer thick film of MA-capped ITO nanocrystals after exchange to (A) Cu4APc, (B) Co4APc, (C) Fe4APc, (D) Ni4APc, and (E) Zn4APc before and after annealing at 250 °C for 2 h under nitrogen atmosphere. (F) The UV–vis–NIR spectra of a pristine 2-monolayer thick film of MA-capped ITO nanocrystals before and after annealing.

Table S1. The position of LSPR maxima for MA-capped ITO nanocrystals before and after exchange to Cu-, Co-, Fe-, Ni-, and Zn4APc and the respective change after annealing at 250 °C for 2 h under nitrogen atmosphere.

Sample	**Pristine Film LSPR maxima (nm / meV)**	**Annealed Film LSPR maxima (nm / meV)**	**Δ_{Exchange} (nm / meV)**	**$\Delta_{\text{Annealing}}$ (nm / meV)**	**Δ_{Total} (nm / meV)**
ITO/Cu4APc	2161 / 573.7	2232 / 555.5	54 / 14.7	71 / 18.2	125 / 32.9
ITO/Co4APc	2133 / 581.3	2229 / 556.2	26 / 7.1	96 / 25.1	122 / 32.2
ITO/Fe4APc	2144 / 578.3	2358 / 525.8	37 / 10.1	214 / 52.5	251 / 62.6
ITO/Ni4APc	2135 / 580.7	2252 / 550.5	28 / 7.7	117 / 30.2	145 / 37.9
ITO/Zn4APc	2123 / 584.0	2176 / 569.8	16 / 4.4	53 / 14.2	69 / 18.6
ITO NC	2107 / 588.4	2163 / 573.2	–	56 / 15.2	56 / 15.2

S4. Grazing-Incidence Small-Angle Scattering (GISAS)

Grazing-incidence small-angle X-ray scattering (GISAXS) [338] is used to probe the ITO NC correlations in the prepared film of hybrid NCs-organic molecule network and to study the effect of ligand exchange and thermal annealing onto the self-assembled hybrid structure. The typical GISAXS patterns of a MA-capped ITO NCs thin-film and the ligand exchanged film of NCs with Cu-, Co-, Fe-, Ni-, and Zn4APc and the corresponding films after thermal annealing at 250^{0}C for 2 hours are shown in 1st and 2nd columns of Figure S13 and Figure S14. A comparative plot of the line profiles along q_y of the films before and after annealing is shown in the 3rd column of the respective row in Figure S13 and Figure S14. The presence of a broad diffraction rod along in-plane scattering direction for each samples indicating a significant in-plane correlation among the ITO NCs. For MA-capped ITO NCs, we find an in-plane correlation 'arc-like rod' scattering spectra at qy = 0.0735 Å which corresponds to the in-plane radial average distance of 8.65 $\pm$ 0.1 nm between the NCs. After ligand exchange, the first-order correlation peak shift to higher q_y values demonstrates a decrease in average in-plane correlation distance between the nanoparticles (a decrease of 0.6-0.7 nm). We attribute this shift to the significantly smaller size of M4APc (~1.1 nm) molecules, acting as a cross-linker between adjacent NCs and establishing the ligand exchange process. [276] Upon annealing the pristine and exchanged films, we observe no significant shifts along q_y which represents the thermal stability and robustness of the structure. The respective in-plane peak positions along q_y, the corresponding correlation lengths, and the relative changes upon ligand exchange and annealing are summarized in Table S2.

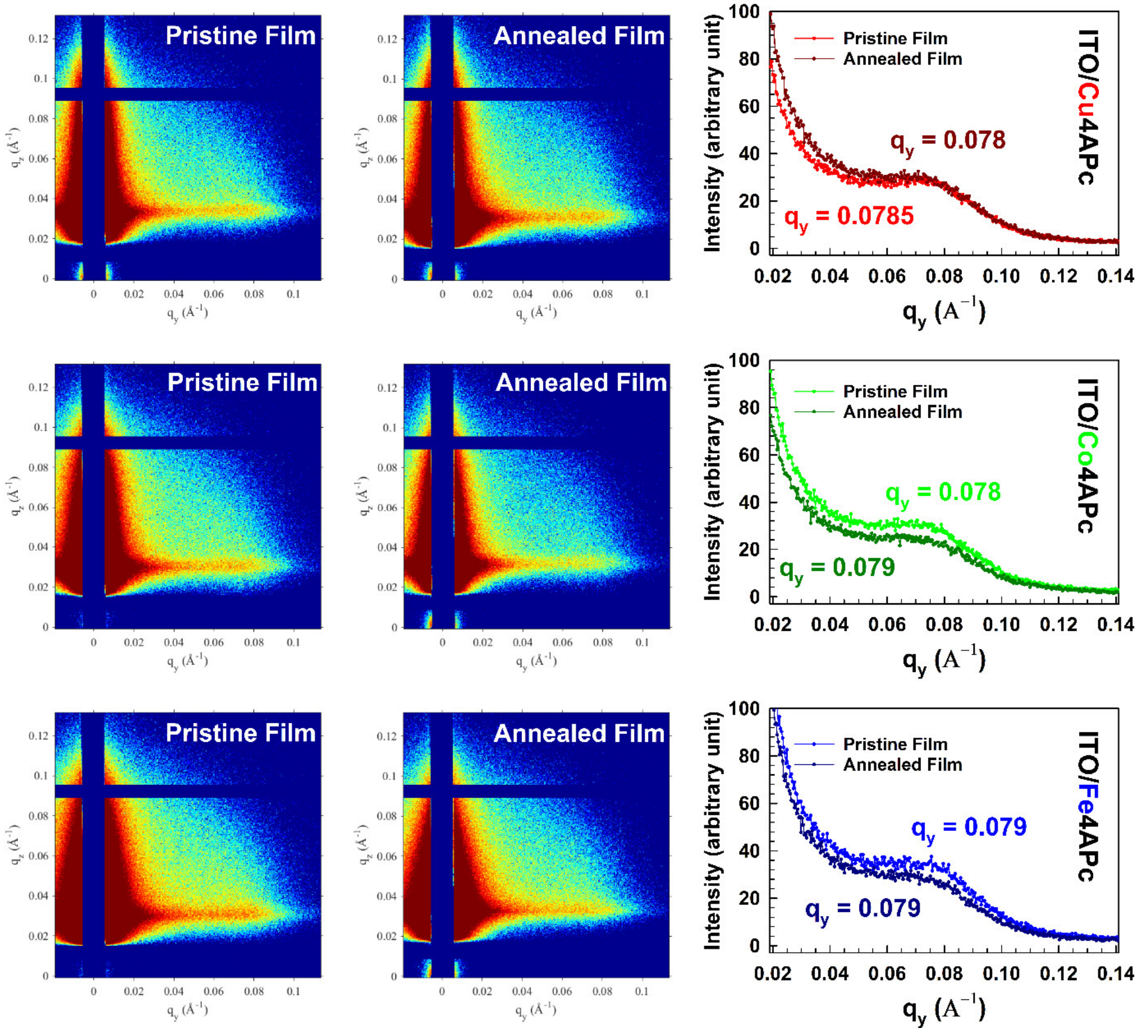

Figure S13. GISAXS patterns of self-assembled ITO NCs arrays after ligand exchange to Cu-, Co-, and Fe4APc for pristine (middle panels) and anealded (right panels) films. Left panels: the extracted line profiles from the corresponding GISAXS images as a function of in-plane scattering vector q_y.

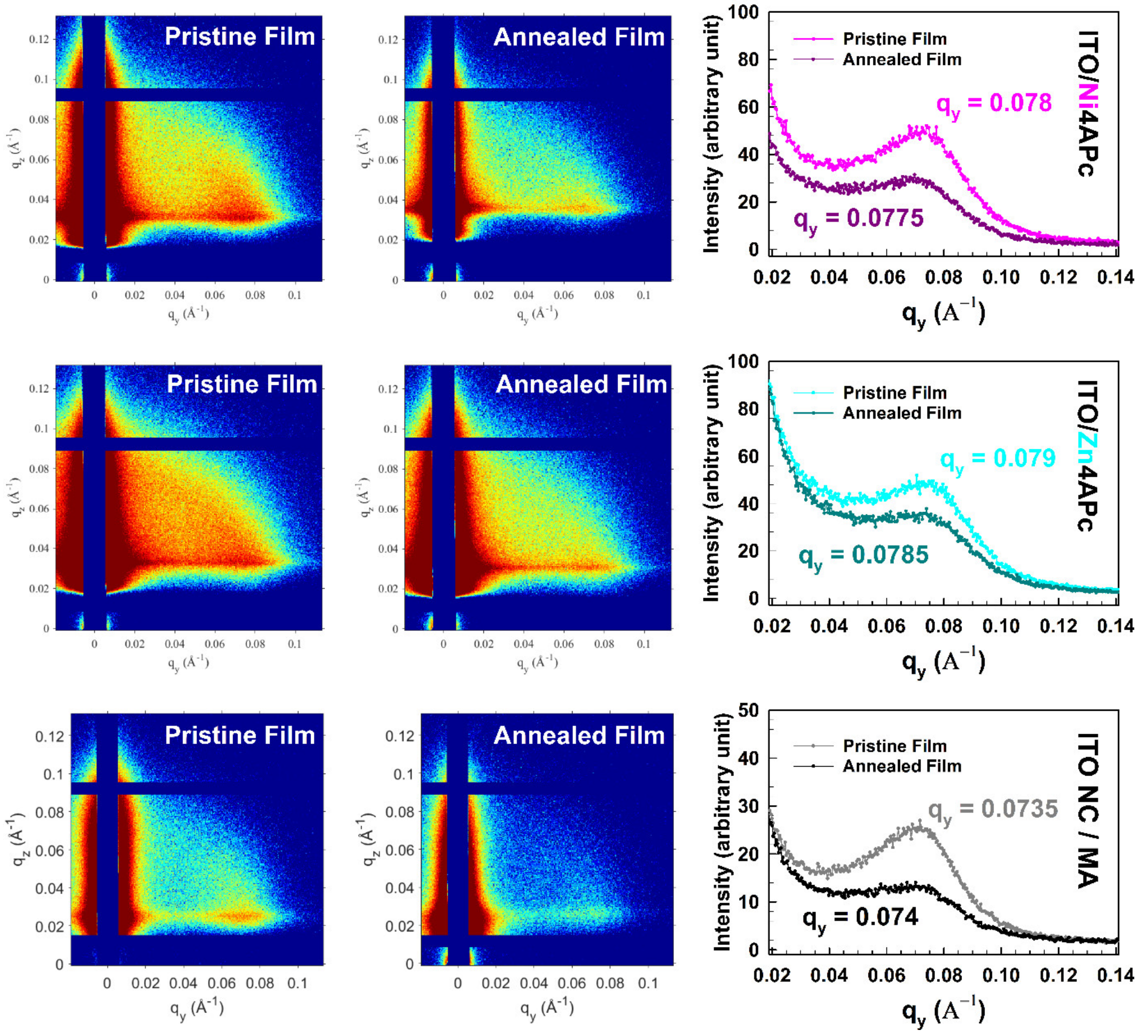

Figure S14. GISAXS patterns of self-assembled ITO NCs arrays before and after ligand exchange to Ni- and Zn4APc for pristine (middle panels) and anealded (right panels) films. Left panels: the extracted line profiles from the corresponding GISAXS images as a function of in-plane scattering vector q_y.

Table S2. The respective in-plane peak positions along q_y, the corresponding correlation lengths, and the relative changes upon ligand exchange and annealing for ITO NC superlattices.

Sample	**Pristine Film** **q_y ($Å^{-1}$) / Correlation Length (nm)**	**Annealed Film** **q_y ($Å^{-1}$) / Correlation Length (nm)**	**$\Delta_{Exchange}$ (nm)**
ITO/Cu4APc	0.0785 / 8.00 ± 0.1 nm	0.078 / 8.05 ± 0.1 nm	0.65
ITO/Co4APc	0.078 / 8.05 ± 0.1 nm	0.079 / 7.95 ± 0.1 nm	0.60
ITO/Fe4APc	0.079 / 7.95 ± 0.1 nm	0.079 / 7.95 ± 0.1 nm	0.70
ITO/Ni4APc	0.078/ 8.05 ± 0.1 nm	0.0775 / 8.10 ± 0.1 nm	0.60
ITO/Zn4APc	0.079 / 7.95 ± 0.1 nm	0.0785 / 8.00 ± 0.1 nm	0.70
ITO NC	0.0735 / 8.65 ± 0.1 nm	0.074 / 8.50 ± 0.1 nm	–

S5. Temperature-Dependent I–V Characterization

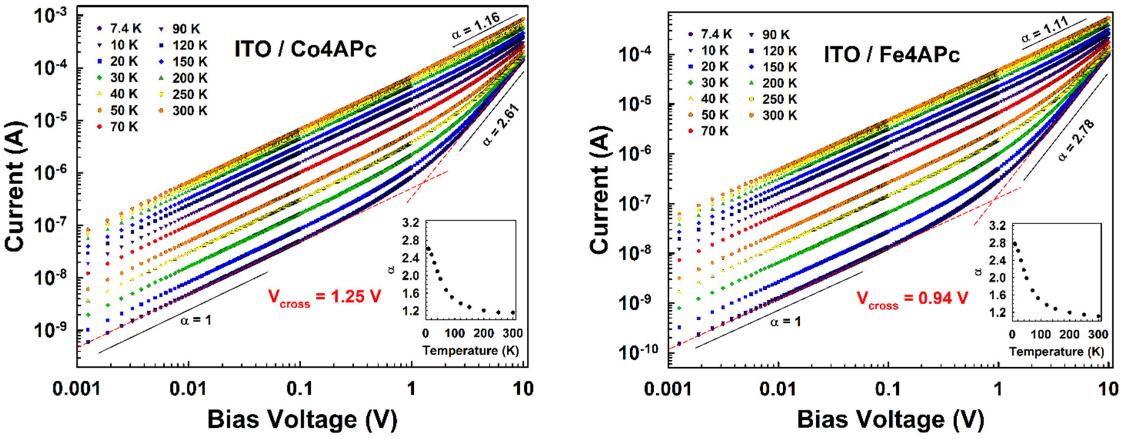

Figure S15. Current–Voltage (I–V) characteristics as a function of temperature for ITO NCs functionalized with Co- and Fe4APc (the solid lines are guided to the eye corresponding to the power laws with exponents as indicated). The inset graph shows the change of power law exponent upon increasing the temperature.

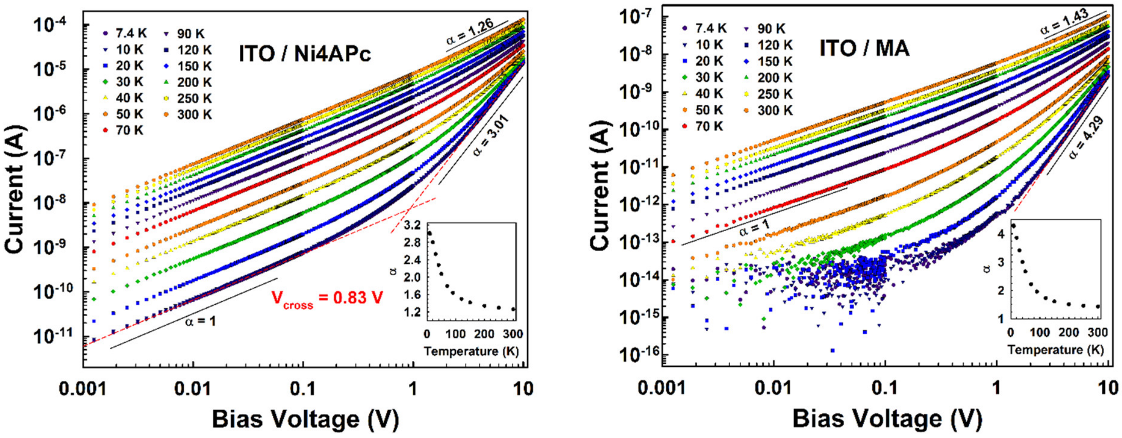

Figure S16. Current–Voltage (I–V) characteristics as a function of temperature for MA-capped ITO NCs before and after ligand exchange to Ni4APc (the solid lines are guided to the eye corresponding to the power laws with exponents as indicated). The inset graph shows the change of power law exponent upon increasing the temperature.

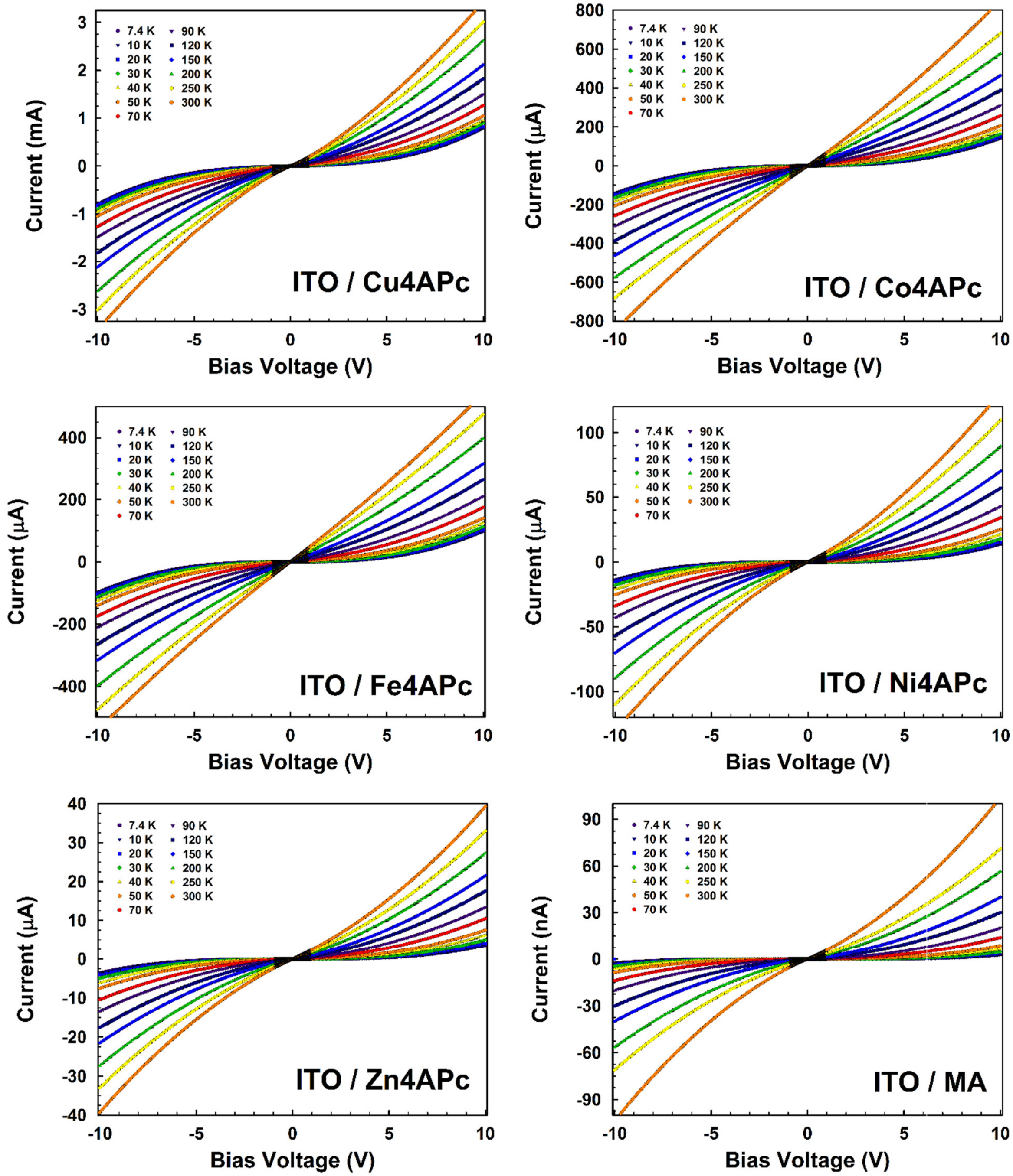

Figure S17 Current-voltage curves of ITO NCs superlattices after ligand exchange to Cu-, Co-, Fe-, Ni-, and Zn-4APc as well as MA-capped ITO NCs thin-film measured at different temperature, ranging from 7.4.K to 300 K.

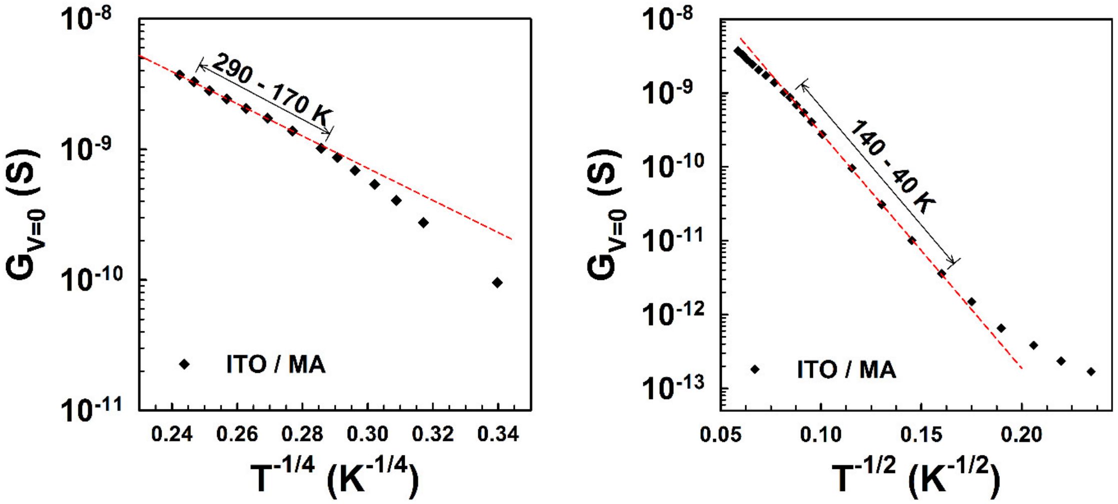

Figure S18. Temperature-dependent zero-voltage conductance of MA-capped ITO NCs plotted versus $T^{-1/4}$ and $T^{-1/2}$ (fits indicated by the dashed lines).

Appendix C

Supporting Information

The Role of the Density of Interface States in Interfacial Energy Level Alignment of PTCDA

Mahdi Samadi Khoshkhoo[†], *Heiko Peisert*[†], *Thomas Chassé*[†,§], *and Marcus Scheele*[†,§,*]

[†] Institute of Physical and Theoretical Chemistry, University of Tübingen, Auf der Morgenstelle 18, 72076 Tübingen, Germany.

[§] Center for Light-Matter Interaction, Sensors & Analytics LISA+, University of Tübingen, Auf der Morgenstelle 15, 72076 Tübingen, Germany

Contents:

S1. Electrostatic Potential Calculations

S2. Experimental Procedures

S3. Electronic Structure of the Interface

S4. Photoelectron Spectroscopy

- **S4.1. Non-Reactive Clean Metal Surfaces**
- **S4.2. Passivated Surfaces and Polymeric Substrate**
- **S4.3. Reactive Clean Surfaces**
- **S4.4. Valence Band Photoelectron Spectroscopy**
- **S4.5. Additional Photoelectron Spectroscopy Results**

S5. “Pillow” or “Push-Back” Effect

S6. Charge Transfer through Tunneling

References

S1. Electrostatic Potential Calculations

This model discretizes the organic deposited film into layers of thickness *Δx* and distance *x* from the substrate in order to calculate the amount of transferred charges in each layer, therefore it can see the effect of thickness and spatial profile of charge distribution (interfacial dipole and/or band bending). The core formula here which specified the charge density, *ρ(x)*, in different thicknesses of deposited organic film is given by:

Equation 63

$$\rho(V(x)) = e \cdot n \cdot \left\{ \int_{-\infty}^{+\infty} dE \cdot f_H(E) \cdot D_H[E + eV(x)] - \int_{-\infty}^{+\infty} dE \cdot f_L(E) \cdot D_L[E + eV(x)] \right\}$$

where *e* is the elementary charge, *n* is the number of molecules per unit area and per discretization interval *Δx*, $f_H(E)$ and $f_L(E)$ are the Fermi functions for each individual energy levels, *V(x)* is the electrostatic potential at the position *x* from the substrate and finally $D_H[E+eV(x)]$ and $D_L[E+eV(x)]$ are the energy distributions of HOMO- and LUMO-derived levels. In fact, Equation 61 shows the density profile of charge carriers in PTCDA according to Fermi statistics and the first and second integral terms correspond to the number of holes and electrons in occupied and unoccupied density of states, respectively. For simplicity, we start with consideration of one Gaussian peak centered at HOMO maximum, E_H, with a standard deviation of σ_H (Equation 64) and one another peak centered at LUMO maximum, E_L, with a standard deviation of σ_L (Equation 65).

Equation 64 $$D_H(E + eV(x)) = G_H(E + eV(x)) = \frac{1}{\sigma_H\sqrt{2\pi}} exp\left[-\frac{(E+eV(x)-E_{HOMO})^2}{2\sigma_H^2}\right]$$

Equation 65 $$D_L(E + eV(x)) = G_L(E + eV(x)) = \frac{1}{\sigma_L\sqrt{2\pi}} exp\left[-\frac{(E+eV(x)-E_{LUMO})^2}{2\sigma_L^2}\right]$$

The standard deviation for PTCDA HOMO and LUMO can be estimated from full width at half maximum (FWHM) of experimental UPS (in this work) and inverse photoemission spectroscopy (IPES) [339] measurements which evaluated to be $\sigma_H = \sigma_L = 0.3$ eV. HOMO and LUMO centers can be found using IE and EA of PTCDA. IE was measured to be 6.5 ± 0.1 eV and EA was calculated to be 3.8 ± 0.1 eV by adding the edge-to-edge transport gap to IE. As the position of IE was recognized through the position of intercept between the tangent line of the HOMO onset feature and the baseline of the spectrum, one should put the centers 2σ away from the onset edges, that is, at $E_H = 7.1 \pm 0.1$ eV and $E_L = 3.2 \pm 0.1$ eV. By considering the layer-by-layer deposition for PTCDA molecules on substrate, *Δx* can be chosen equal to distance between stacking planes, 3.21 Å [340], which corresponds to height of one molecular layer. Based on the area associated with a PTCDA molecule, around 120 Å^2 [183], the number of molecules per unit area and per discretization interval is calculated to be $n = 8.33 \times 10^{17}$ $molecules/(m^2 \cdot \Delta x)$. Assuming a single charging of each PTCDA molecules, the Fermi function for each individual energy level can be obtained through Equation 66 and Equation 67 for HOMO and LUMO, respectively.

Equation 66 $$f_H(E) = \frac{1}{\frac{1}{g_H} e^{-\beta(E-E_F)} + 1}$$

Equation 67 $$f_L(E) = \frac{1}{\frac{1}{g_L} e^{+\beta(E-E_F)} + 1}$$

Finally the numerical solving of generalized one dimensional Poisson equation (Equation 62) can give us the electrostatic potential across the PTCDA deposited film as a function of thickness, $V(x)$.

Equation 68 $$\nabla[\varepsilon(x)\nabla V(x)] = -\frac{\rho(V(x))}{\varepsilon_0}$$

where ε_0 is vacuum permittivity and $\varepsilon(x)$ is static dielectric constant for each discretization interval. The latter quantity was considered to be constant through the thickness and set to be 1.9 as recently reported for PTCDA along stacking direction of the molecules [340]. Iterative solving of Equation 61 simultaneously with Equation 62 considering the electric field equal to zero at the outside surface of the PTCDA provide us the charge density and electron potential energy as a function of PTCDA film thickness. The organic film is assumed to be in thermal equilibrium with the substrate; hence, the Fermi level of PTCDA film is aligned with the Fermi level of substrate that is substrate work function, Φ_{sub}.

The effect of electronic coupling of PTCDA molecules to the substrate is included into this model through modifying the DOS peak shape for the first discretization intervals beyond a pure Gaussian distribution. In the second approached, assuming that the first 15 molecular layers (approximately the first 5 nm) are under electronic coupling effect of substrate, we chose for the first layer (which is in direct contact with substrate) a pure Lorentzian (as considered by Vázquez et al [151], Equation 69) or Voigt peak function (as considered by Oehzelt et al [137], Equation 70), then we gradually and layer-by-layer changed the peak shape to pure Gaussian distribution form the layer number 2 to 15 and finally retained the pure Gaussian shape for the subsequent layers (layer 16 to 62). Figure 3B schematically represents the gradual change of peak shapes from pure Lorentzian to pure Gaussian distribution (through linear combination).

The results for changing from Voigt peak function to pure Gaussian distribution (through decreasing the weight of Lorentzian contribution) is not presented due to similarity.

Equation 69 $$D_H(E + eV(x)) = L_H(E + eV(x)) = \frac{1}{\pi}\frac{\gamma}{(E+eV(x)-E_{HOMO})^2+\gamma^2}$$

Equation 70 $$D_H(E) = \mathrm{V}_H(\mathrm{E}) = \int_{-\infty}^{+\infty} G_H(E')L_H(\mathrm{E}-E')dE'$$

In the last approach, we directly introduce a damped peak of gap-state to the DOS of the first layers based on our experimental observation for PTCDA deposited on Al/Al_xO_y. Similar to the second approach, we assume that the first 15 molecular layers are under an electronic coupling effect of the substrate. For the first layer (which is in direct contact with substrate), we choose a Gaussian distribution of the HOMO feature (Equation 64) as well as a Voigt profile of gap-state centered 1.3 eV lower than the HOMO maxima (Equation 71, Equation 72, and Equation 73). For layers 2 t o15, we gradually reduce the contribution of gap-state and finally retain only the pure Gaussian HOMO distribution for the subsequent layers (layer 16 to 62). Figure 3C schematically represents the gradual reduction of the contribution of gap-state to the DOS (through linear combination).

Equation 71 $$D_G\big(E + eV(x)\big) = G_G\big(E + eV(x)\big) = \frac{1}{\sigma_G\sqrt{2\pi}} exp\left[-\frac{(E+eV(x)-E_{HOMO}-1.3)^2}{2\sigma_G^2}\right]$$

Equation 72 $$D_G\big(E + eV(x)\big) = L_G\big(E + eV(x)\big) = \frac{1}{\pi}\frac{\gamma}{(E+eV(x)-E_{HOMO}-1.3)^2+\gamma^2}$$

Equation 73 $$D_G(E) = \mathrm{V}_G(\mathrm{E}) = \int_{-\infty}^{+\infty} G_G(E')L_G(\mathrm{E}-E')dE'$$

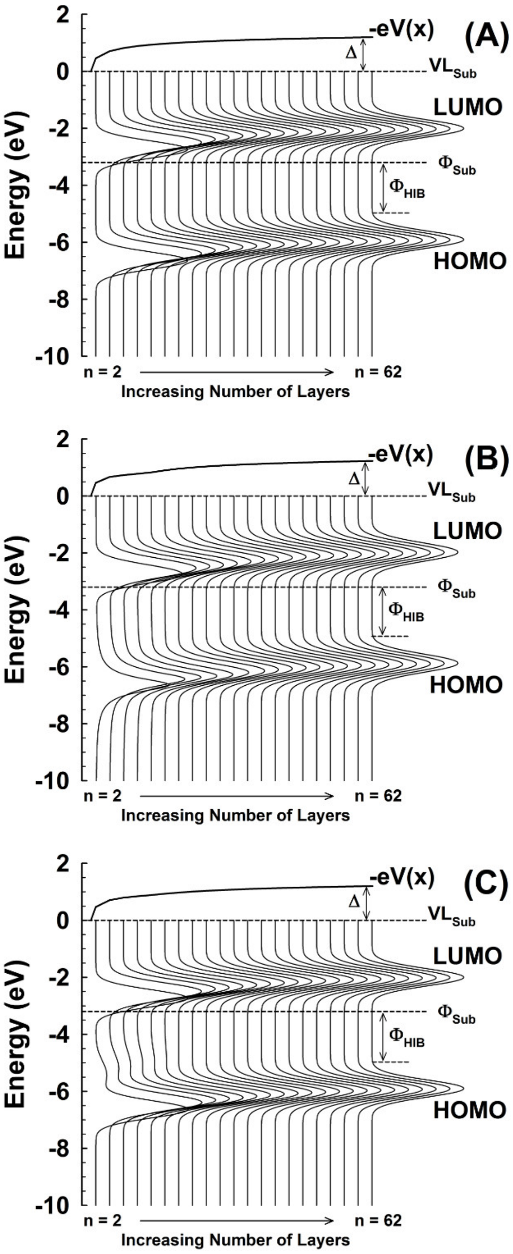

Figure S19. Energy level alignment as well as the resulting electrostatic potential in thermal equilibrium for a 20 nm thick PTCDA film deposited on a substrate with Φ_{sub} of 3.2 eV. With increasing distance from the electrode, the local electron potential energy, *–eV(x)*, shifts the density of states as well as the vacuum level to lower binding energies. (A) The DOS of the organic layers are approximated by Gaussian peaks. (B) The gradual change of DOS line shapes from pure Lorentzian for the first molecular layer to pure Gaussian distribution for layer number 15. (C) The gradual reduction of the contribution of gap-state to the DOS from the first layer to layer number 15.

S2. Experimental Procedures

All experiments are performed in a three chamber ultra-high vacuum (UHV) system, equipped with XPS, UPS, evaporation and ion sputtering source. The base pressure in the analysis chamber is 1×10^{-9} mbar. PTCDA molecules are obtained from Sigma-Aldrich. Before sample preparation, the molecules are heated to the sublimation temperature and outgassed under UHV condition. Samples are prepared by vapor deposition (at a rate of 1-2 Å/min) on various substrates which are kept at room temperature in UHV. During vacuum deposition, the pressure in vacuum chamber is in the low 10^{-9} mbar regime. The thickness of as-deposited films is obtained by monitoring the attenuation of the Si 2p and Au 4f core level spectra. These results are used to calibrate the quartz crystal microbalance in order to determine the evaporation rates and thicknesses of deposited films on other substrates. Metal substrates used in this experiment are prepared by thermal evaporation of the metal on a Si(111) wafer at base pressure in the low 10^{-7} mbar regime and at an evaporation rate of 1 Å/s. The typical composition of the substrates for a metal of choice is: bulk Si(111) wafer/Ti (200 Å)/Metal (1000 Å). Thin film of PEDOT:PSS is spin-coated onto an ITO substrate and heated for 2 h at 120 °C in UHV in order to remove possible water contamination.

XPS and UPS measurements were carried out using a multichamber UHV system which was equipped with an Omicron hemispherical analyzer (EA 125), a conventional X-ray tube (Omicron DAR 400, Al Kα, working at 12.5 kV and 20 mA, 1486.61 eV) and a helium discharge lamp (Leybold-Hereaus UVS10/35, 21.22 eV). UPS spectra were taken at analyzer pass energy of 3 eV and steps of 0.05 eV. All XPS survey spectra, scans of 1000 eV, were taken at analyzer pass energy of 25 eV. High resolution scans were performed at the pass energy of 5-10 eV and steps of 0.05 eV. The binding energies were corrected for electrical charge effects by referencing to the Au $4f_{7/2}$ peak which was assumed to have a binding energy of 84.0 eV. The photoelectrons were detected at a takeoff angle of $\Phi = 0^{\circ}$ with respect to the surface normal. Acquisition and storage of data were accomplished using Croissant Software (v. 1.2.1.7). Data were converted to VAMAS format and processed using Unifit2014 software. Each XPS and UPS spectrum was also corrected for the satellite peaks. Core level XPS is performed using a standard non-monochromatized X-ray source providing Al Kα radiation with an energy of 1486.6 eV. No changes in the core level signals of the as-prepared films and the films under X-ray/UV-irradiation are observed that represent the stability of the molecules during the data acquisition time. Furthermore, no charging effects are observed for the final 20 nm thick films. The resolution in UPS and XPS measurements is determined as 0.1 and 0.8 eV, respectively (calculated from the width of Fermi edge on the Au substrate).

S3. Electronic Structure of the Interface

The interfaces between PTCDA and the present substrates formed by vacuum evaporation are more abrupt in comparison to those prepared by evaporating the metal onto the OSC. This is due to the much lower heat of adsorption of organic molecules and also the higher stability of metal/inorganic semiconductor surfaces. The electronic structure at the interface for 20 nm PTCDA deposited on different substrates is shown in Figure S20. One can clearly see that regardless of the initial work function of the substrate, the position of the HOMO edge with respect to the Fermi level is strongly pinned at 2.0 ± 0.1 eV (Figure 1B). The same pinning behavior is also observed for the Fermi level position of PTCDA/substrate in Figure1A. Irrespective of the initial work function of the substrate and its reactivity, the position of the Fermi level is also observed to be strongly pinned at 4.5 ± 0.1 eV with the slop parameter equal to 0.006 (≈ 0) (Figure 1A). According to previous UPS and IPES measurements, the HOMO-LUMO transport gap of PTCDA is 2.74 ± 0.2 eV [339]. Here, the transport gap is defined as the edge-to-edge distance between the HOMO and LUMO features (HOMO-LUMO peak-to-peak gap was measured and reported to be 4.0 ± 0.2 eV [339, 341]). Therefore, in all substrates the Fermi level is pinned around 0.7 ± 0.1 eV below the LUMO edge of the neutral PTCDA molecule.

Figure 1B also represents the evolution of interface dipole (Δ) versus substrate work function (Φ_{sub}) for a molecular film of PTCDA deposited on different substrates. Within the range of work functions studied here, the magnitude of the interfacial dipole generated at the interface decreases linearly by decreasing the work function of the substrate. Upon deposition of PTCDA, Δ changes in a way that the distance between the Fermi level and HOMO edge remains constant. The behavior is similar to related systems, where a change of the dipole was observed by changing the work function of the metal or, vice-versa, the ionization potential of the organic material. [170, 328] The magnitude of the substrate work function (Φ_{sub}), substrate/organic work function ($\Phi_{sub/org}$), interface dipole (Δ), PTCDA ionization energy (IE), and hole injection barrier (Φ_{HIB}) for PTCDA films deposited on different substrates are summarized in Table S3.

Table S3. The magnitudes of substrate and substrate/PTCDA work function (Φ_{sub} and $\Phi_{sub/org}$), interface dipole (Δ), PTCDA ionization energy (IE), and the binding energy of the HOMO edge of PTCDA with respect to the Fermi level (E_{HOMO-F}) for the films deposited on different substrates.

Substrate	Φ_{sub} (eV)	$\Phi_{sub/org}$ (eV)	Δ (eV)	IE (eV)	E_{HOMO-F} (eV)
Sputter-cleaned Au	5.33	4.41	-0.92	6.44	2.04
Sputter-cleaned Pt	4.79	4.50	-0.29	6.50	2.01
PEDOT:PSS	5.23	4.56	-0.67	6.63	2.07
Contaminated Au	4.21	4.42	+0.21	6.50	2.08
Contaminated Pt	4.39	4.56	+0.17	6.65	2.09
Si/SiO_x	4.43	4.45	+0.02	6.44	2.00
ITO	4.17	4.51	+0.34	6.45	1.95
Al/Al_xO_y	3.26	4.52	+1.26	6.56	2.05
Sputter-cleaned Ni	5.02	4.56	-0.46	6.49	1.93
Sputter-cleaned Ag	4.41	4.40	-0.01	6.44	2.04
Ti/TiO_x	3.91	4.48	+0.57	6.41	1.94

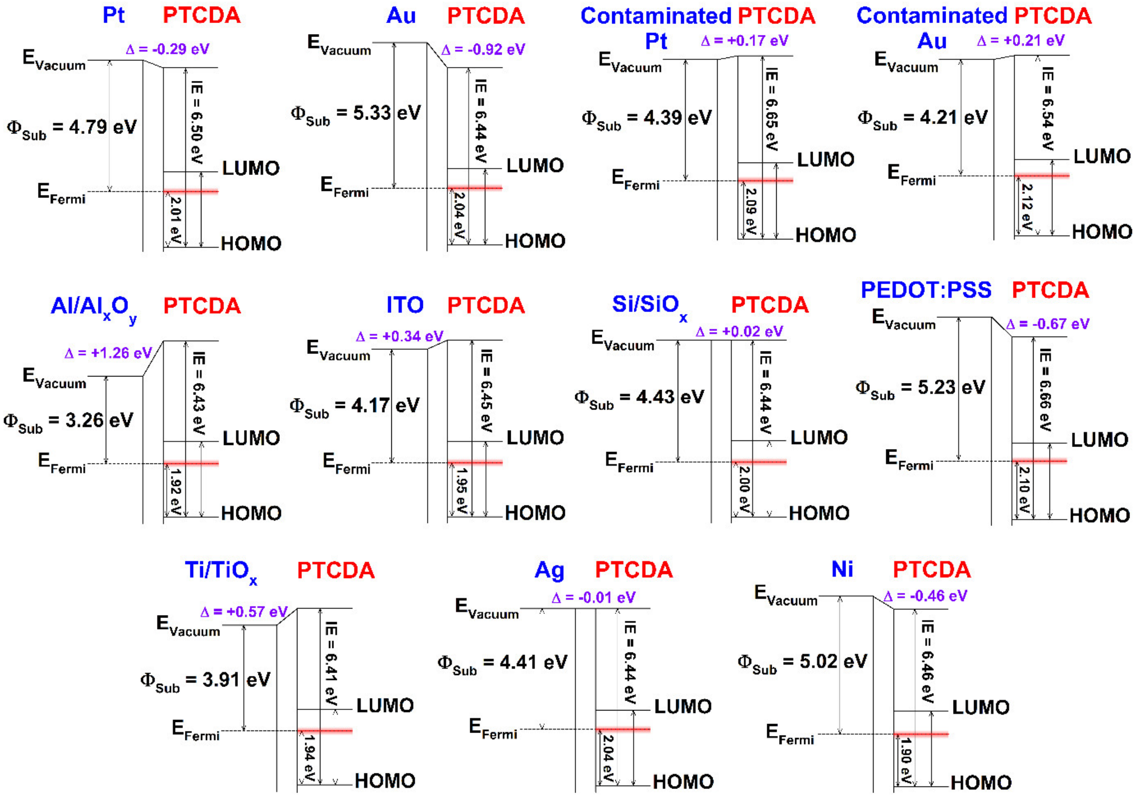

Figure S20. The electronic structure of substrate/PTCDA interfaces. In all cases, independent of the work function of the substrate, one can see that the Fermi level is strongly pinned at 4.5 ± 0.1 eV as measured versus vacuum level (around 2 eV above the PTCDA HOMO).

S4. Photoelectron Spectroscopy

We categorize our substrates into three different groups based on their interaction with PTCDA: (i) metallic surfaces which are atomically clean and have a weak interaction (sputter-cleaned Au and Pt), (ii) substrates with oxide surfaces (Al/Al_xO_y, Si/SiO_x), ITO, metal surfaces passivated by hydrocarbons (contaminated Au and Pt), and polymeric substrate (PEDOT:PSS) which have a negligible interaction, and do not have metallic character at the surface, and (iii) reactive clean metal (sputter-cleaned Ni and Ag) and oxide (Ti/TiO_x) surfaces which form covalent bonding and indicate a strong chemisorption. In the following, we will present and explain one example of each category; the detailed results for the other substrates can be found in Section S4.5.

S4.1. Non-Reactive Clean Metal Surfaces: A typical UPS spectrum of PTCDA on sputter-cleaned Au is presented in Figure S21. Panel (A) shows the secondary electron cut-off of the bare substrate and PTCDA deposited on it with various thicknesses. Panel (B) represents several well-defined density of states related features which are attributed to Au (of the bare substrate) and PTCDA HOMO (at thicker layers). The magnification of the valence band region from -1 to 4 eV is depicted in Figure S21C.

The work function of the clean bare substrate is 5.33 eV, which experiences a sharp decrease to 4.7 eV upon deposition of a PTCDA sub-monolayer. In very good agreement with this result, the work function for Au covered by a monolayer of PTCDA has previously been calculated by density functional theory (DFT, 4.82 eV) [319] and was also obtained experimentally as 4.75 eV [318]. As shown in Fig. 2B, the features of the Au substrate disappear at a coverage of 12 Å. Bearing in mind that the probing depth of UPS is in the order of one nanometer, this confirms the formation of a PTCDA monolayer at the early stages of the evaporation. Upon deposition of a first monolayer, the vacuum level shifts considerably to lower energies (~ 0.6 eV). Figure S21 shows that by increasing the layer thickness, the shape of the HOMO and that of higher binding energy features, the relative intensities and the relative energy positions are practically unchanged corroborating that PTCDA is very weakly bound on Au with (nearly) no chemical interaction with the substrate. The slight shift (~0.1 eV) of all spectra to lower binding energies at the interface can be attributed to better screening of the core hole final state by image charges which is also observed in the C 1s and O 1s core levels (data not shown here). The results show that the Fermi level at the interface is situated relatively close to the PTCDA LUMO. The same result is also obtained for PTCDA on Pt (see Section S4.5).

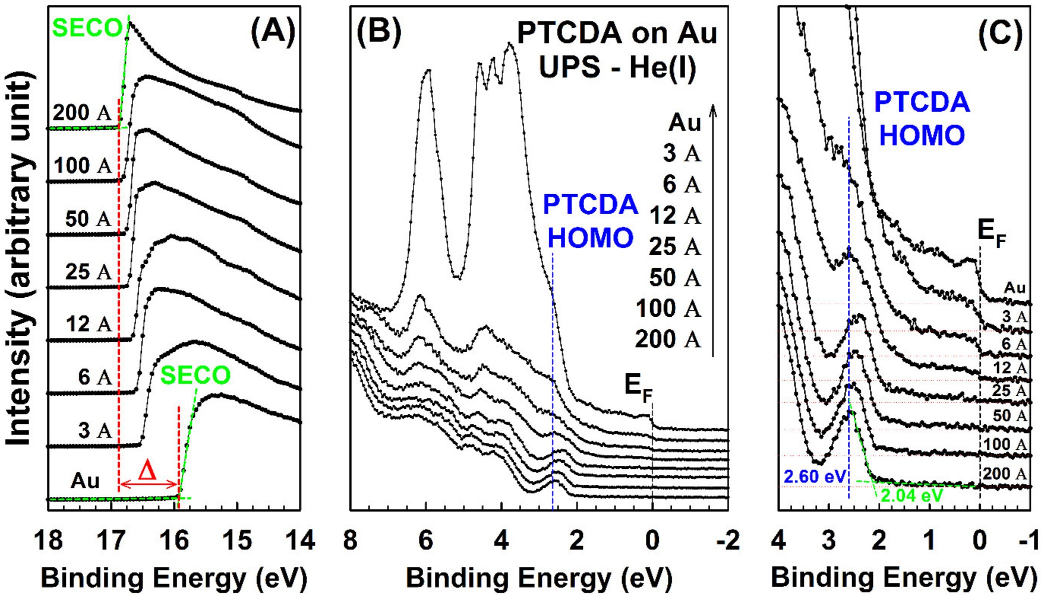

Figure S21. (A) UPS spectra of the secondary electron cut-off for sputter-cleaned Au covered with PTCDA of various thicknesses. (B) He(I) spectra of sputter-cleaned Au and PTCDA/Au interfaces for various PTCDA thicknesses. (C) Magnification of the valence band which represents the Au Fermi level and the PTCDA HOMO edge.

S4.2. Passivated Surfaces and Polymeric Substrate: The surfaces of substrates passivated with oxide layers (Al/Al_xO_y and Si/SiO_x) as well as ITO do not have pure metallic character and therefore the electron density of a typical metal is not present in these substrates. As an example, Figure S22A, B, and C represent the UPS spectra from the interface formed by deposition of PTCDA on Al/Al_xO_y, which do not have any strong features in the energy regime of 0-4 eV. As such, it is suitable for detecting any gap states of significant intensity. In contrast to the Au counterpart, one can see no binding energy shift in the valence band features upon PTCDA deposition which is due to a lack of image charges at the oxide interfaces used in this study (based on the observation of no shift in core-level XPS signals; not shown here). Upon deposition of the molecular sub-monolayer, the work function spontaneously experiences a sharp increase from 3.33 eV to 4.63 eV which corresponds to the formation of a very large interface dipole (1.3 eV), after which it stabilizes around 4.5 ± 0.1 eV.

Similar to surfaces passivated with an oxide layer, surfaces passivated with hydrocarbon monolayers (contaminated Au and Pt) do not have metallic character. These surfaces are prepared by exposure of the sputter-cleaned metals to ambient air. The surface of sputter-cleaned Au has a work function of 5.33 eV. Upon physisorption of a few monolayers of hydrocarbons on the Au surface after exposure to ambient air, the work function substantially drops to 4.2 eV, demonstrating a strong effect of the adsorbed (mono)layers of hydrocarbon on the metal surface. In both cases (Au and Pt), one can see a significant reduction in the interface dipole. Neither a change in the hole nor in the electron injection barrier is detected, and the Fermi level is again pinned within the gap of PTCDA.

PEDOT:PSS is chosen as a polymeric substrate due to its relatively high work function (5.23 eV here); however, the large work function mostly results from the chemical potential of the bulk material. In other words, the contribution of the electrostatic potential across the surface [342] to the total work function is small and the final work function mostly originates from energy levels created by the charge transfer between the sulfonate and ethylene dioxythiophene moieties [161, 343]. The position of the Fermi level for PEDOT:PSS falls in between the HOMO and LUMO level of PTCDA and, based on the non-reactive and non-metallic characteristics of the substrate, one can expect that the PEDOT:PSS/PTCDA interface falls into the vacuum level alignment regime. However, the resulting electronic structure of PEDOT:PSS covered by PTCDA again shows Fermi level pinning within the gap of PTCDA along with the generation of an interface dipole (about 0.7 eV).

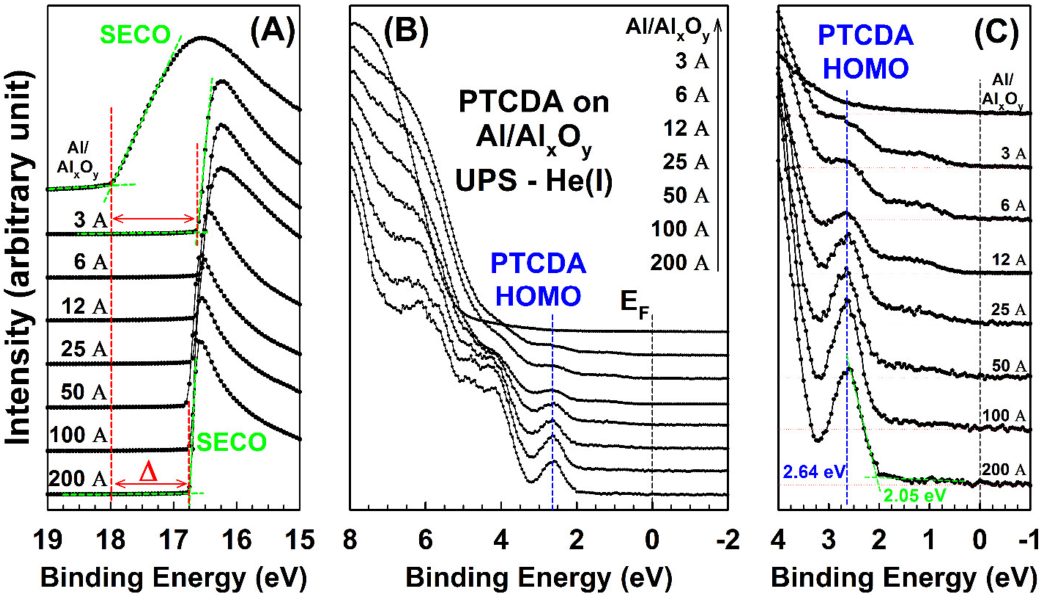

Figure S22. (A) UPS spectra of the secondary electron cut-off for an Al/Al$_x$O$_y$ substrate coated with PTCDA (B). He(I) spectra of Al/Al$_x$O$_y$ and PTCDA-on-Al/Al$_x$O$_y$ interfaces for various PTCDA thicknesses. (C) The magnification of the valence band which shows no valence features for Al/Al$_x$O$_y$ between -1 to 4 eV and PTCDA HOMO edge.

S4.3. Reactive Clean Surfaces: In the case of Ag, Ni, and Ti/TiO$_x$, chemical interactions, involving covalent metal-PTCDA, result in the formation of organometallic complexes. The

UPS data of PTCDA deposited on Ag, Ni, and Ti/TiO_x reveals a drastic change of the shape of the valence band features in comparison to that of the pristine molecule (see Figure S23 and Section S4.5). These newly emerged states can be attributed to induced metal-PTCDA gap-states which are formed by a chemical reaction and correspond to charge transfer between metal atoms and PTCDA molecules. Figure S23A, B, and C represent the UPS spectra of the interface formed by deposition of PTCDA on Ag. Upon deposition of the first monolayer on the Ag surface (3 Å), the vacuum level shifts to lower binding energies (~ 0.2 eV). The direction of the shift corresponds to the formation of a positive dipole at the interface and electron transfer from Ag to PTCDA. For the surface covered by a monolayer of PTCDA, an increase in the work function from 4.41 eV to 4.61 eV is observed. We note that a very similar result was recently calculated by DFT for a monolayer-covered Ag surface (an increase from 4.5 eV to 4.69 eV [319]). In the spectrum of 200 Å PTCDA on Ag, the HOMO related feature of PTCDA at 2.6 eV below the Fermi level is clearly observed. When approaching the interface (lower thicknesses), the position of the HOMO is changed to around 2.2 eV *vs.* the Fermi level at the interface. Furthermore, new features start to appear in the gap between the HOMO and the Fermi level, indicating a change in the shape of the orbitals due to a strong interaction at the interface and a significant hybridization between the substrate and the molecular wave functions.

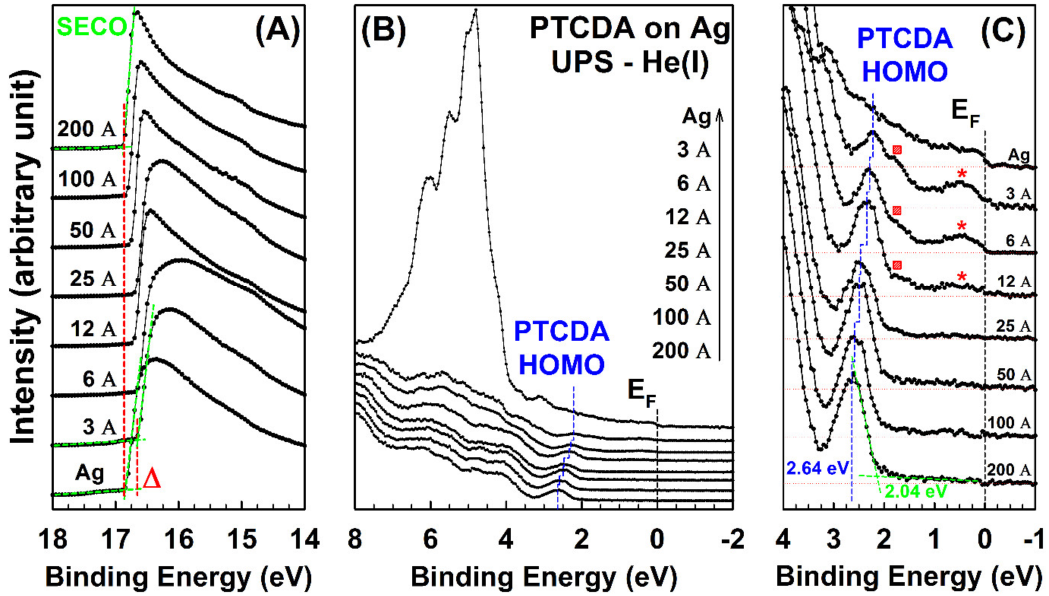

Figure S23. (A) UPS spectra of the secondary electron cut-off for sputter-cleaned Ag covered by PTCDA. (B) He I spectra of sputter-cleaned Ag and PTCDA/Ag interfaces for various PTCDA thicknesses. (C)

Magnification of the valence band which represents the sputter-cleaned Ag Fermi level, gap states, and PTCDA HOMO edge

S4.4. Valence Band Photoelectron Spectroscopy: A significant fraction of the negative interface dipole barrier at the PTCDA/Au interface (and also at PTCDA/Pt) corresponds to a decrease in the work function of the metal due to the deposition of organic material and hence the physisorption on the surface. The magnitude of the work function substantially drops during the deposition of the first monolayer of the organic material. Generally, a lowering of the work function upon adsorption of molecules can be described by the "pillow" or "push-back" effect, which is discussed controversially but often seen to be on the order of ~0.3 eV [171, 328, 344-345] (see Section S5). The large interface dipole of -0.9 eV for PTCDA on Au suggests that an additional mechanism contribute to the dipole formation (see the discussion in the simulation part).

In the case of substrates prepared by exposure of non-reactive sputter-cleaned metals to ambient air (referred to as "contaminated" Au and Pt), the observed reduction in the interface dipole, in comparison to their atomically clean counterparts, is attributed to the effective decrease of the metal work function caused by a significant decrease in the electrostatic potential across the metal surface. [342, 346-347] In the core-level photoemission spectra of these substrates (O 1s and C 1s region, data not shown), no oxygen, but a little trace of carbon was observed which shows that the clean metals were covered by a thin layer of hydrocarbons. One can see the valence band features even after air-contact in the UPS spectra (see Figure S27), which confirms that the thickness of a passivated hydrocarbon layer should be on the order of a few angstroms. The remaining interface dipole for metal/PTCDA interfaces demonstrates that the physisorbed hydrocarbon layer does not completely decouple the two materials, such that charge transfer can still take place between metal and PTCDA through tunneling (see Section 6).

For the surfaces of substrates passivated with oxide layers (Al/Al_xO_y and Si/SiO_x) as well as ITO, a positive interface dipole is found, probably originating from charge transfer based on differences between the organic EA and the work function of the substrates [161]. This dipole barrier shifts the vacuum level of the organic part upward and interface gap states situated above the HOMO and below the Fermi level become partially filled, which are detected by UPS in this work (as apparent in Figure S22C). As the signal from these induced states rapidly disappears by increasing the thickness of the deposited organic film, one can conclude that the localization of transferred charges is at the interface and not through the bulk of PTCDA. The above discussion implies that the oxide band structure does not affect the energy alignment, as the negatively charged molecules become thermodynamically more stable when the Fermi energy of the substrate is smaller than the electron affinity of PTCDA molecules.

For the Ag/PTCDA interface, the change in the work function is likely to be the result of two contributions: (a) the intrinsic dipole moment which has a purely geometrical nature and (b) the bond dipole which is attributed to the change in electron density [317]. The newly emerged features in the gap (one around 0.2-0.3 eV [marked by red-stars] and the other around 1.6-1.7 eV [marked by re-squares] below the Fermi level, see Figure S23C) are attributed to hybrid states of the Ag 4d-bands with the LUMO and HOMO of PTCDA, which are also described in earlier reports [317-318]. The appearance of a peak right below the Fermi level indicates chemical bonding between Ag and PTCDA, probably manifesting in a mixing of the neutral molecules' LUMO with the Ag 5s-states. This is supported by DFT calculations reporting that the LUMO level of PTCDA situated on the Ag surface is largely occupied and the peak maximum is located below the Fermi level [319]. The presence of the peak slightly below the Fermi level indicates the metallic character of the first PTCDA adsorbed layer on Ag. In all the cases for Ag, Ni, and Ti/TiO_x, we can see a step-like increase of the work function upon deposition of the first monolayer of organic molecules on the surface. This jump corresponds to the formation of a positive dipole at the interface (electron transfer from substrate to PTCDA) which is the result of a strong interaction of substrate with the first PTCDA monolayer. This system can now be considered as a new organic-passivated substrate with a new work function. As the amount of work function is now far away from its pinning level, by increasing the thickness of the film, it starts to decrease toward the pinning point and finally stabilize around it.

S4.5. Additional Photoelectron Spectroscopy Results

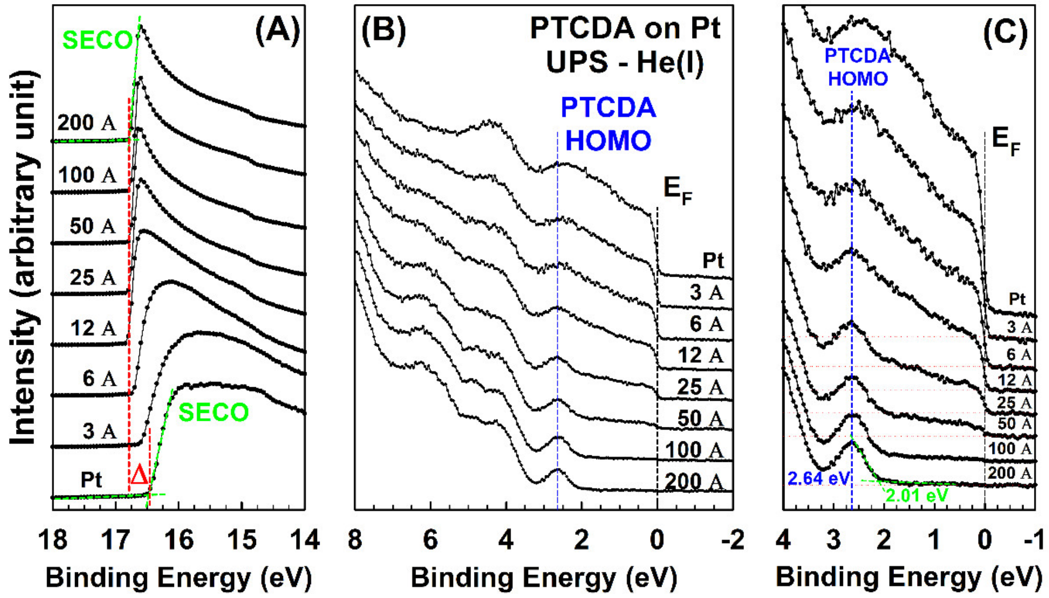

Figure S24. (A) UPS spectra of the secondary electron cut-off for sputter-cleaned Pt coated with PTCDA of various thicknesses. (B) He(I) spectra of sputter-cleaned Pt and PTCDA/Pt interfaces for various PTCDA thicknesses. (C) Magnification of the valence band which represents the Pt Fermi level and the PTCDA HOMO edge.

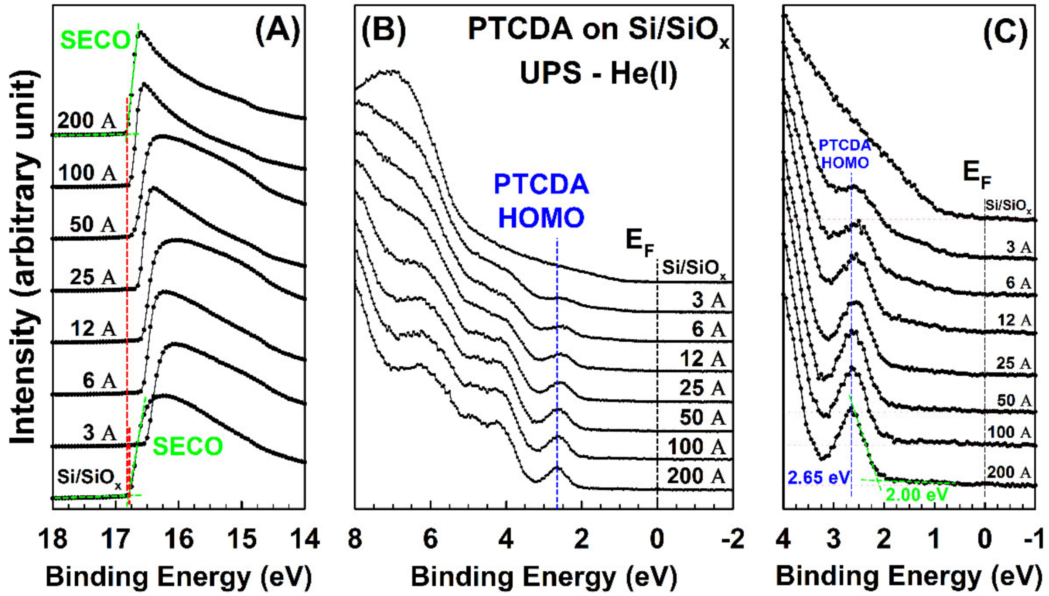

Figure S25. (A) UPS spectra of the secondary electron cut-off for Si/SiO$_x$ and PTCDA-covered substrate (B). He(I) spectra of Si/SiO$_x$ and PTCDA/(Si/SiO$_x$) interfaces for various PTCDA thicknesses. (C) The magnification of the valence band which represents the Si/SiO$_x$ valence region and PTCDA HOMO edge.

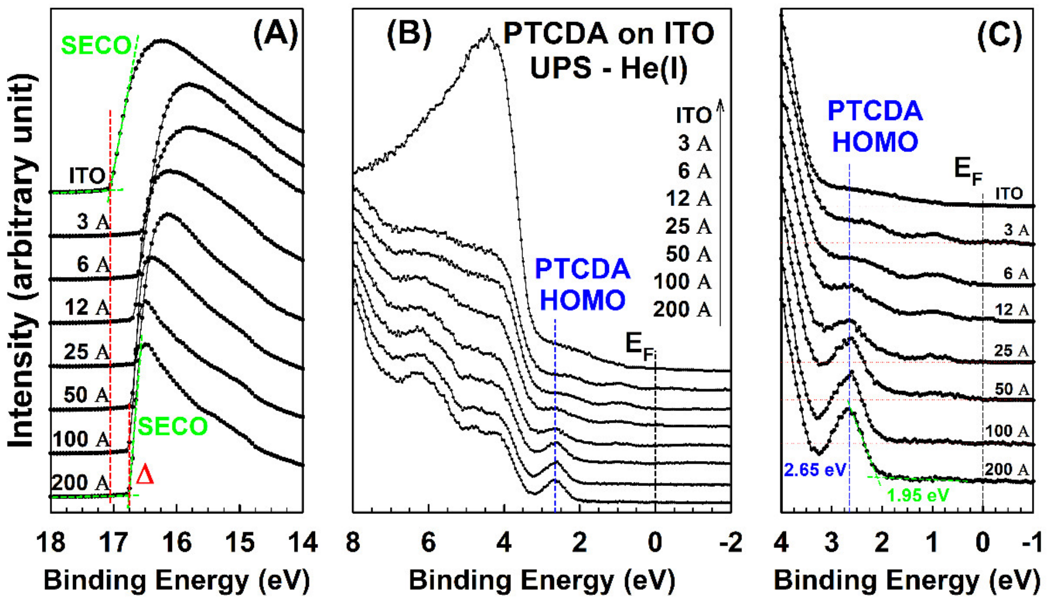

Figure S26. (A) UPS spectra of the secondary electron cut-off for ITO and PTCDA-covered substrate (B). He(I) spectra of ITO and PTCDA/ITO interfaces for various PTCDA thicknesses. (C) The magnification of the valence band which represents the ITO valence band region and PTCDA HOMO edge.

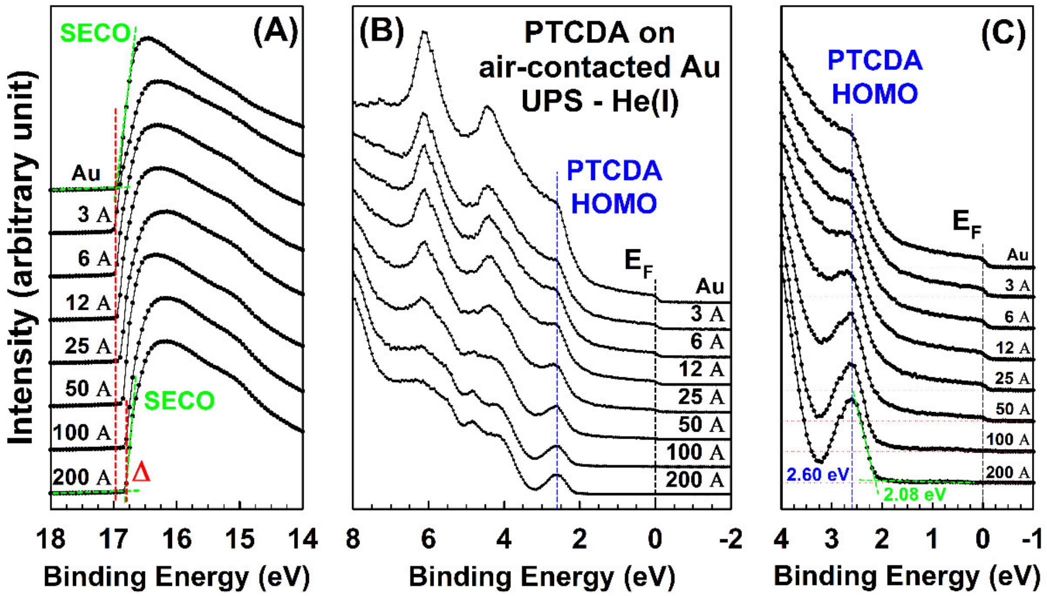

Figure S27. (A) UPS spectra of the secondary electron cut-off for air-contacted Au and PTCDA-covered substrate (B). He(I) spectra of air-contacted Au and PTCDA/(air-contacted) interfaces for various PTCDA thicknesses. (C) The magnification of the valence band which represents the air-contacted Au Fermi level and PTCDA HOMO edge.

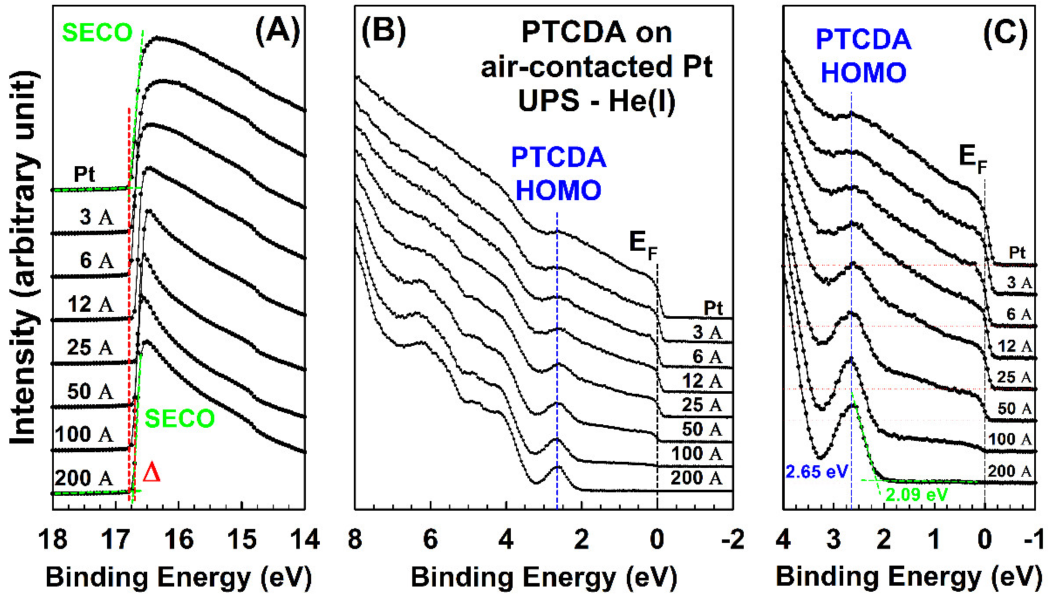

Figure S28. (A) UPS spectra of the secondary electron cut-off for air-contacted Pt and PTCDA-covered substrate (B). He(I) spectra of air-contacted Pt and PTCDA/(air-contacted) interfaces for various PTCDA thicknesses. (C) The magnification of the valence band which represents the air-contacted Pt Fermi level and PTCDA HOMO edge.

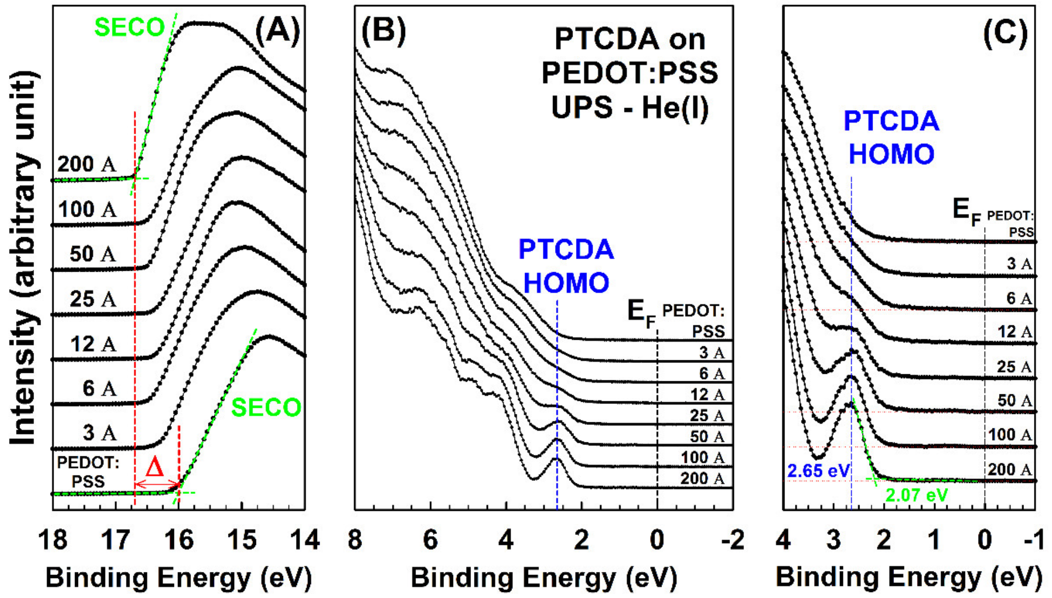

Figure S29. (A) UPS spectra of the secondary electron cut-off for PEDOT:PSS and PTCDA-covered substrate (B). He(I) spectra of PEDOT:PSS and PTCDA/PEDOT:PSS interfaces for various PTCDA thicknesses. (C) The magnification of the valence band which represents the PEDOT:PSS valence region and PTCDA HOMO edge.

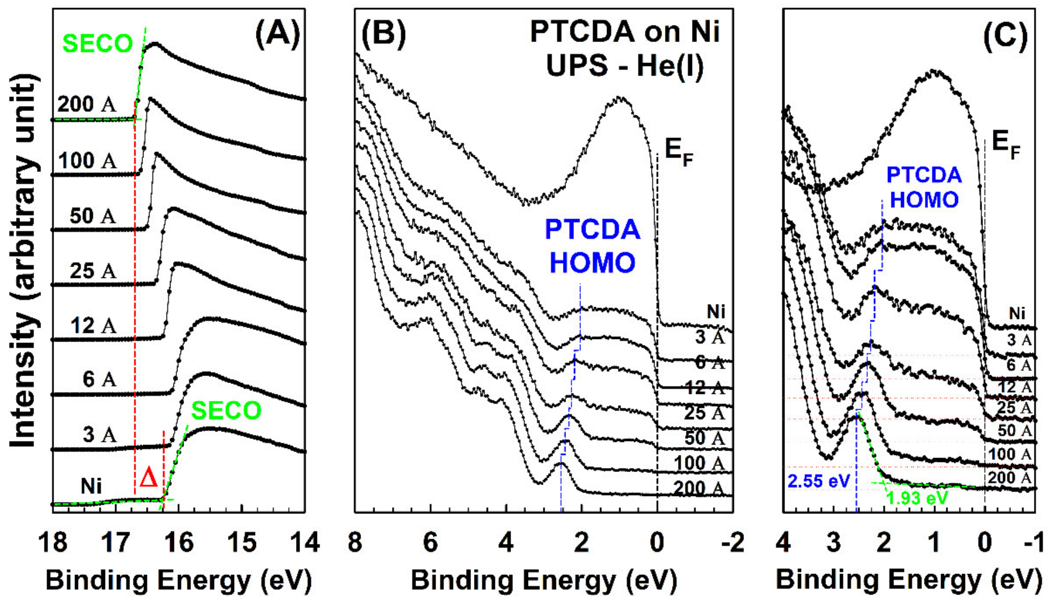

Figure S30. (A) UPS spectra of the secondary electron cut-off for sputter-cleaned Ni and PTCDA-covered substrate (B). He(I) spectra of sputter-cleaned Ni and PTCDA/Ni interfaces for various PTCDA thicknesses. (C) The magnification of the valence band which represents the sputter-cleaned Ni Fermi level and PTCDA HOMO edge.

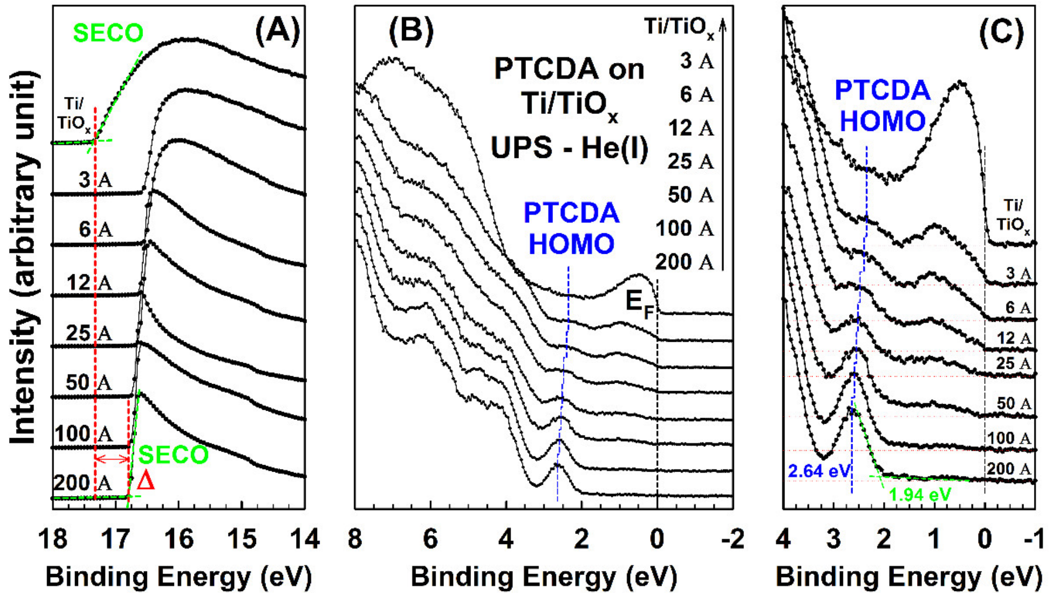

Figure S31. (A) UPS spectra of the secondary electron cut-off for Ti/TiO$_x$ and PTCDA-covered substrate (B). He(I) spectra of Ti/TiO$_x$ and PTCDA/(Ti/TiO$_x$) interfaces for various PTCDA thicknesses. (C) The magnification of the valence band which represents the Ti/TiO$_x$ valence band and PTCDA HOMO edge.

S5. “Pillow” or “Push-Back” Effect

The energy level alignments of PTCDA on contaminated Au and Pt are represented in Figure S20. Comparing the results with the electronic structures of atomically clean Au and Pt surfaces (also presented in Figure S20) provides important information about the interface characteristics and especially the “push-back” effect. In order to understand the mechanism of this effect, it is worth noting that the total work function of the metal originates from two main potentials, namely the chemical potential of the bulk metal and the electrostatic potential across the metal surface [342, 347]. Physisorption of organic molecules at the interface cannot affect the bulk chemical potential of the metal, however, it can have a substantial effect on the electrostatic potential across the surface by modifying the tail of the electron cloud leaking out into the vacuum.

In the case of atomically clean Au, upon deposition of a mono- or sub-monolayer of PTCDA, a considerable part of the observed changes in the work function is caused by the so-called “push-back” effect. In this process, repulsion between the electrons of physisorbed organic molecules and the electrons leaking from the metal surface compresses the electron-density tail which significantly reduces the contribution of electrostatic potential across the surface to the total work function. This, in turn, results in a downward shift of the vacuum level from the substrate to PTCDA at the interface. The eventual interface dipole is the result of several components: (a) an intrinsic dipole exists at the surface of the metal before the deposition of organic molecules, (b) the change in electrostatic potential across the surface after PTCDA physisorption, and (c) a generated dipole due to possible electron transfer at the interface after deposition. The contributions of each of these components to the interface dipole are difficult to distinguish experimentally, but they can be identified computationally.

In the case of Au substrate covered by a thin layer of hydrocarbons, the bare substrate already experiences the “push-back” effect due to adsorption of hydrocarbons on the surface. Thus, there is less inherent dipole at the metal surface due to smaller tail of electron cloud leaking out into the vacuum and the work function is significantly lower than the work function of atomically clean Au. Therefore, upon deposition of PTCDA on hydrocarbon-passivated Au (which is referred also to contaminated Au), the observed changes in the work function mostly originate from the charge transfer at the interface and not from the “push-back” effect. In comparison to atomically clean Au, as the work function of the hydrocarbon-passivated Au is considerably smaller and closer to the final pinning point, the amount of observed changes in the work function upon deposition of PTCDA is also smaller.

S6. Charge Transfer through Tunneling

For the surfaces of substrates passivated with oxide layers (Al/Al_xO_y and Si/SiO_x), a positive interface dipole is found, probably originating from charge transfer based on differences between the organic EA and the work function of the substrates [161]. In such a case, when bringing the organic material in contact with the substrate, electrons will flow spontaneously from the substrate to PTCDA molecules. This electron transfer can take place by tunneling of electrons in the case of substrates with thin oxide layers (Al/Al_xO_y or Si/SiO_x) to a state of PTCDA [142]. The essential reason for this charge transfer is that the cost in energy which is gained by PTCDA at the interface when accepting an electron is higher than the cost in energy of taking off an electron from the substrate. Therefore, upon this charge transfer, the substrates progressively become positively charged and PTCDA becomes negatively charged which develops a potential at the interface [142]. Tunneling implies the transfer of an integer amount of charge into well-defined charged states on the organic molecule. It can happened if the passivating layer is thin enough (also in the case of atomically clean Au and Pt substrates covered by a thin layer of contamination molecules, e. g. hydrocarbons). The thickness of oxide layer for Si/SiO_x can be determined by the following equation [348]:

Equation 74 $$d_{SiO_2} = \lambda_{SiO_2}\sin(\alpha_A)\ln\left[\frac{I_{SiO_2}}{I_{Si}\cdot\beta} + 1\right],\ \beta = \frac{I_{SiO_2,\infty}}{I_{Si,\infty}}$$

where λ_{SiO2} is the photoelectron effective attenuation length in the oxide film, α_A is the photoelectron take-off angle, I_{SiO2} is the Si 2p core level intensity of the oxidized silicon film, I_{Si} is the Si 2p core level intensity of the silicon, and $\beta = I_{SiO2,\infty} / I_{Si,\infty}$ is measure on photoelectron opaque films. The XPS core level spectrum of Si 2p is shown in Figure S32.

One can easily see the contribution of two components in the spectrum. The main signal centered on 99.3 eV is attributed to the bulk silicon atoms and the second one situated around 102.0 eV is attributed to the oxide layer on top. λ_{ox} is equal to 2.96 ± 0.19 *nm* and β is equal to 0.75 [348-349]. The Si 2p core level intensities based on the fitted spectrum give us the thickness of oxide layer equal to 0.87 *nm*.

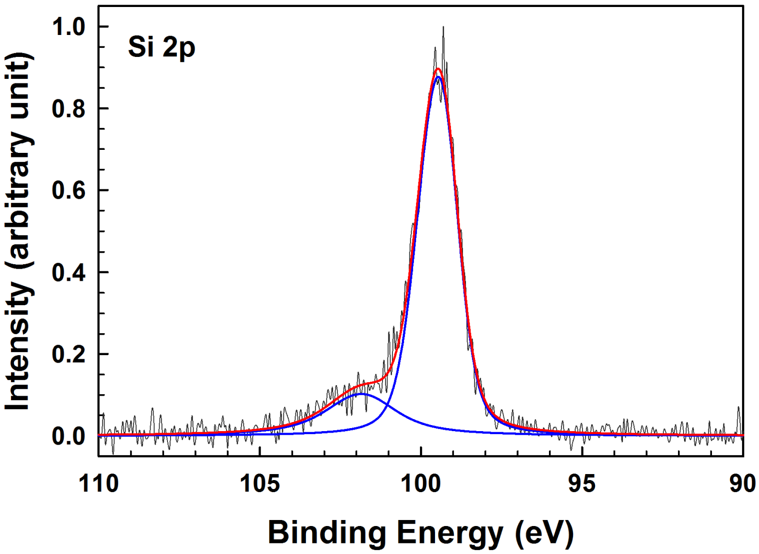

Figure S32. The XPS Si 2p core level spectrum of the Si/SiO$_x$ substrate

For Aluminum with native oxide, the thickness of oxide layer can be determined by the following equation [350]:

$$\frac{I_{Ox}}{I_{Al}} = \frac{n_{Ox} \cdot \lambda_{Ox}}{n_{Al} \cdot \lambda_{Al}} \left[exp\left(\frac{d}{\lambda_{Ox} \cdot cos\theta}\right) - 1 \right] \qquad \text{Equation 75}$$

where I_{ox} is the Al 2p core level intensity of the aluminum oxide layer, I_{Al} is the Al 2p core level intensity of the aluminum sublayer, n is the volume density of electron-emitting atoms in the oxide layer (n_{Ox}) and aluminum sublayer (n_{Al}), λ denotes the inelastic mean free path of the electrons in oxide layer (λ_{Ox}) and aluminum sublayer (λ_{Al}), θ is the electron off-axis angle with respect to the surface normal and d is the thickness of the oxide layer. The amounts of n_{Ox}, n_{Al}, λ_{Ox}, and λ_{Al} are equal to 72.6 $kmol\ m^{-3}$, 100 $kmol\ m^{-3}$, 2.8 nm, and 2.6 nm, respectively [350]. The XPS core level spectrum of Al 2p is shown in Figure S33. The main signal centered about 72.7 eV is attributed to the bulk aluminum atoms and the second one situated around 75.3 eV is attributed to the oxide layer on top. Using the Al 2p core level intensities based on the fitted spectrum results in a thickness of the oxide layer of 1.12 *nm*.

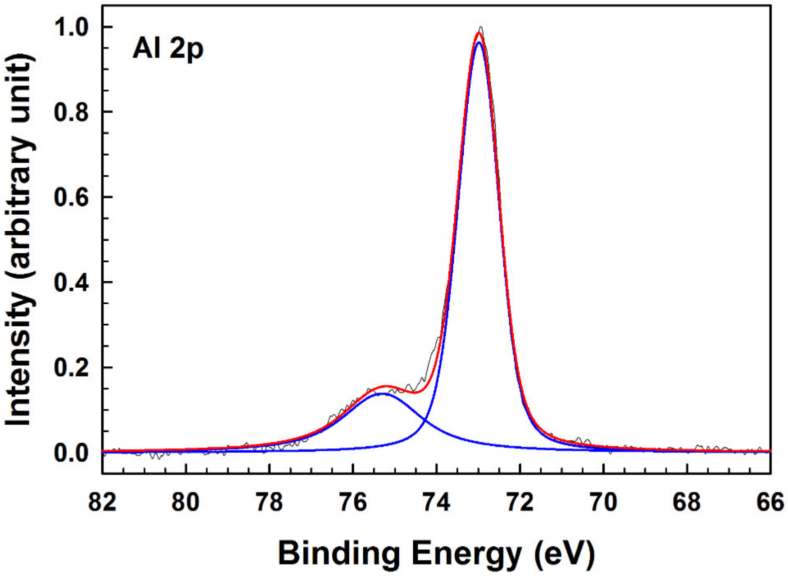

Figure S33. The XPS Al 2p core level spectrum of the Al/Al_xO_y substrate

Therefore, the oxide layer is thin enough and the electron transfer can still occur via tunneling process.

Acknowledgements

First of all, I would like to express my gratitude to Dr. Marcus Scheele for his skillful guidance, stoic patience, open-minded attitudes towards unexplored subjects, and the provided large degree of freedom in this research. During my PhD carrier, I always felt that I have not only a supervisor but more than that i.e. a real friend. His kind supports and helps in every imaginable problems and situations (scientific and non-scientific) provide me a relaxed atmosphere to focus on my research. The door to his office was always open to everyone for discussions and supports and our regular weekly meeting sections greatly help me to find the right way during my doctoral studies. His persistence and financial supports in order to send me to reputable international scientific conferences greatly help me to meet the most famous scientists in the field and build valuable relationships for future collaborations.

I am very grateful to Prof. Dr. Thomas Chassé and Dr. Heiko Peisert who provide me the possibility to work on photoelectron spectrometers which greatly extended my knowledge and skills in surface and interface science as well as ultrahigh vacuum systems. Their scientific advices, as well as countless discussions and comments, add lots of inputs on my aspects treated in this work.

Further, I thank Prof. Dr. Frank Schreiber and Dr. Santanu Maiti for stablishing a truly fruitful collaboration and for providing vital high-quality information on the structure of the samples via grazing-incidence small-angle scattering (GISAS) technique. I would also like to especially thank Prof. Dr. Yvonne Joseph for our productive collaboration without which none of the sensing measurements in this work would have been possible.

A very special thank you goes to Christine Schedel who translate the English abstract of this dissertation to German language and also to Dr. Mathias Glaser, Hilmar Adler, Małgorzata Polek, and Milutin Ivanovic for their technical support for every imaginable problem regarding photoelectron spectrometers. I would like to acknowledge Mrs. Nadler for SEM/STEM measurements and Dr. Liang for assistance with XRD experiments. It was a great pleasure to explore the limits of measurement instruments with you. The great support from the instrument scientists of Center for Light-Matter Interaction, Sensors & Analytics LISA+ of University of Tübingen, Dr. Ronny Löffler and Dr. Markus Turad, are also kindly acknowledged.

I am also grateful to the Management and Head of Institute Administration, Dr. Wolfgang Langer, as well as the institute administration staff: Bettina Kappler, Brigitte Doez, Christine

Stadler, Diana Strauss, and Andrea Teufel for their unfailing support and assistance and the *Deutsche Forschungsgemeinschaft (DFG)* for funding the PhD research.

And finally, last but by no means least, also thanks to all my colleagues in Scheele, Chassé, and Meixner groups. It was great sharing laboratory with all of you during three memorable years.

References

(1) Nasilowski, M.; Mahler, B.; Lhuillier, E.; Ithurria, S.; Dubertret, B. Two-Dimensional Colloidal Nanocrystals. *Chem Rev* **2016,** *116*, 10934-10982.

(2) Boles, M. A.; Ling, D.; Hyeon, T.; Talapin, D. V. The Surface Science of Nanocrystals. *Nat Mater* **2016,** *15*, 141-153.

(3) Boles, M. A.; Engel, M.; Talapin, D. V. Self-Assembly of Colloidal Nanocrystals: From Intricate Structures to Functional Materials. *Chem Rev* **2016,** *116*, 11220-11289.

(4) Grim, J. Q.; Manna, L.; Moreels, I. A Sustainable Future for Photonic Colloidal Nanocrystals. *Chem Soc Rev* **2015,** *44*, 5897-5914.

(5) Carey, G. H.; Abdelhady, A. L.; Ning, Z. J.; Thon, S. M.; Bakr, O. M.; Sargent, E. H. Colloidal Quantum Dot Solar Cells. *Chem Rev* **2015,** *115*, 12732-12763.

(6) Talapin, D. V.; Lee, J. S.; Kovalenko, M. V.; Shevchenko, E. V. Prospects of Colloidal Nanocrystals for Electronic and Optoelectronic Applications. *Chem Rev* **2010,** *110*, 389-458.

(7) Ekimov, A. I.; Onushchenko, A. A. Quantum Size Effect in Three-Dimensional Microscopic Semiconductor Crystals. *JETP Lett* **1981,** *34*, 345-349.

(8) Spanhel, L.; Haase, M.; Weller, H.; Henglein, A. Photochemistry of Colloidal Semiconductors. 20. Surface Modification and Stability of Strong Luminescing CdS Particles. *J Am Chem Soc* **1987,** *109*, 5649-5655.

(9) Weller, H.; Schmidt, H. M.; Koch, U.; Fojtik, A.; Baral, S.; Henglein, A.; Kunath, W.; Weiss, K.; Dieman, E. Photochemistry of Colloidal Semiconductors. Onset of Light Absorption as a Function of Size of Extremely Small CdS Particles. *Chem Phys Lett* **1986,** *124*, 557-560.

(10) Brus, L. Electronic wave functions in semiconductor clusters: experiment and theory. *J Phys Chem* **1986,** *90*, 2555-2560.

(11) Rossetti, R.; Ellison, J. L.; Gibson, J. M.; Brus, L. E. Size Effects in the Excited Electronic States of Small Colloidal Cds Crystallites. *J Chem Phys* **1984,** *80*, 4464-4469.

(12) Chen, Z.; Nadal, B.; Mahler, B.; Aubin, H.; Dubertret, B. Quasi-2D Colloidal Semiconductor Nanoplatelets for Narrow Electroluminescence. *Adv Funct Mater* **2014,** *24*, 295-302.

(13) Ithurria, S.; Dubertret, B. Quasi 2D Colloidal CdSe Platelets with Thicknesses Controlled at the Atomic Level. *J Am Chem Soc* **2008,** *130*, 16504.

(14) Joo, J.; Son, J. S.; Kwon, S. G.; Yu, J. H.; Hyeon, T. Low-Temperature Solution-Phase Synthesis of Quantum Well Structured CdSe Nanoribbons. *J Am Chem Soc* **2006,** *128*, 5632-5633.

(15) Zecchina, A.; Groppo, E.; Bordiga, S. Selective Catalysis and Nanoscience: An Inseparable Pair. *Chem Eur J* **2007,** *13*, 2440-2460.

(16) Narayanan, R.; El-Sayed, M. A. Catalysis with Transition Metal Nanoparticles in Colloidal Solution: Nanoparticle Shape Dependence and Stability. *J Phys Chem B* **2005,** *109*, 12663-12676.

(17) Valden, M.; Lai, X.; Goodman, D. W. Onset of Catalytic Activity of Gold Clusters on Titania with the Appearance of Nonmetallic Properties. *Science* **1998,** *281*, 1647-1650.

(18) Shi, A. C.; Masel, R. I. The Effects of Gas Adsorption on Particle Shapes in Supported Platinum Catalysts. *J Catal* **1989,** *120*, 421-431.

(19) Kelly, K. L.; Coronado, E.; Zhao, L. L.; Schatz, G. C. The optical properties of metal nanoparticles: The influence of size, shape, and dielectric environment. *J Phys Chem B* **2003,** *107*, 668-677.

(20) Jia, G. H.; Sitt, A.; Hitin, G. B.; Hadar, I.; Bekenstein, Y.; Amit, Y.; Popov, I.; Banin, U. Couples of Colloidal Semiconductor Nanorods Formed by Self-Limited Assembly. *Nat Mater* **2014,** *13*, 302-308.

(21) Cassette, E.; Mahler, B.; Guigner, J.-M.; Patriarche, G.; Dubertret, B.; Pons, T. Colloidal CdSe/CdS Dot-in-Plate Nanocrystals with 2D-Polarized Emission. *ACS Nano* **2012,** *6*, 6741-6750.

(22) Ithurria, S.; Tessier, M. D.; Mahler, B.; Lobo, R. P. S. M.; Dubertret, B.; Efros, A. Colloidal Nanoplatelets with Two-Dimensional Electronic Structure. *Nat Mater* **2011,** *10*, 936-941.

(23) Carbone, L.; Nobile, C.; De Giorgi, M.; Sala, F. D.; Morello, G.; Pompa, P.; Hytch, M.; Snoeck, E.; Fiore, A.; Franchini, I. R.; Nadasan, M.; Silvestre, A. F.; Chiodo, L.; Kudera, S.; Cingolani, R.; Krahne, R.; Manna, L. Synthesis and Micrometer-Scale Assembly of Colloidal CdSe/CdS Nanorods Prepared by a Seeded Growth Approach. *Nano Lett* **2007,** *7*, 2942-2950.

(24) Kim, S.; Fisher, B.; Eisler, H.-J.; Bawendi, M. Type-II Quantum Dots: CdTe/CdSe(Core/Shell) and CdSe/ZnTe(Core/Shell) Heterostructures. *J Am Chem Soc* **2003,** *125*, 11466-11467.

(25) Peng, X.; Manna, L.; Yang, W.; Wickham, J.; Scher, E.; Kadavanich, A.; Alivisatos, A. P. Shape Control of CdSe Nanocrystals. *Nature* **2000,** *404*, 59-61.

(26) Hines, M. A.; Guyot-Sionnest, P. Synthesis and Characterization of Strongly Luminescing ZnS-Capped CdSe Nanocrystals. *J Phys Chem* **1996,** *100*, 468-471.

(27) Parak, W. J.; Gerion, D.; Pellegrino, T.; Zanchet, D.; Micheel, C.; Williams, S. C.; Boudreau, R.; Le Gros, M. A.; Larabell, C. A.; Alivisatos, A. P. Biological Applications of Colloidal Nanocrystals. *Nanotechnology* **2003,** *14*, R15-R27.

(28) Lhuillier, E.; Dayen, J. F.; Thomas, D. O.; Robin, A.; Doudin, B.; Dubertret, B. Nanoplatelets Bridging a Nanotrench: A New Architecture for Photodetectors with Increased Sensitivity. *Nano Lett* **2015,** *15*, 1736-1742.

(29) Grim, J. Q.; Christodoulou, S.; Di Stasio, F.; Krahne, R.; Cingolani, R.; Manna, L.; Moreels, I. Continuous-Wave Biexciton Lasing at Room Temperature using Solution-Processed Quantum Wells. *Nat Nanotechnol* **2014,** *9*, 891-895.

(30) Deng, Z. T.; Cao, D.; He, J.; Lin, S.; Lindsay, S. M.; Liu, Y. Solution Synthesis of Ultrathin Single-Crystalline SnS Nanoribbons for Photodetectors via Phase Transition and Surface Processing. *ACS Nano* **2012,** *6*, 6197-6207.

(31) Somorjai, G. A.; Park, J. Y. Colloid Science of Metal Nanoparticle Catalysts in 2D and 3D Structures. Challenges of Nucleation, Growth, Composition, Particle Shape, Size Control and Their Influence on Activity and Selectivity. *Top Catal* **2008,** *49*, 126-135.

(32) Li, J.; Jiang, F.; Yang, B.; Song, X. R.; Liu, Y.; Yang, H. H.; Cao, D. R.; Shi, W. R.; Chen, G. N. Topological Insulator Bismuth Selenide as a Theranostic Platform for Simultaneous Cancer Imaging and Therapy. *Sci Rep* **2013,** *3*, 1998.

(33) Homan, K. A.; Souza, M.; Truby, R.; Luke, G. P.; Green, C.; Vreeland, E.; Emelianov, S. Silver Nanoplate Contrast Agents for in Vivo Molecular Photoacoustic Imaging. *Acs Nano* **2012,** *6*, 641-650.

(34) Gao , C.; Lu , Z.; Liu , Y.; Zhang, Q.; Chi, M.; Cheng, Q.; Yin, Y. Highly Stable Silver Nanoplates for Surface Plasmon Resonance Biosensing. *Angew Chem Inter Ed* **2012,** *51*, 5629-5633.

(35) Chen, Y.; Tan, C.; Zhang, H.; Wang, L. Two-Dimensional Graphene Analogues for Biomedical Applications. *Chem Soc Rev* **2015,** *44*, 2681-2701.

(36) Li, H.; Wu, J.; Yin, Z.; Zhang, H. Preparation and Applications of Mechanically Exfoliated Single-Layer and Multilayer MoS2 and WSe2 Nanosheets. *Accounts Chem Res* **2014,** *47*, 1067-1075.

(37) Jariwala, D.; Sangwan, V. K.; Lauhon, L. J.; Marks, T. J.; Hersam, M. C. Emerging Device Applications for Semiconducting Two-Dimensional Transition Metal Dichalcogenides. *ACS Nano* **2014,** *8*, 1102-1120.

(38) Nicolosi, V.; Chhowalla, M.; Kanatzidis, M. G.; Strano, M. S.; Coleman, J. N. Liquid Exfoliation of Layered Materials. *Science* **2013,** *340*.

(39) Eda, G.; Yamaguchi, H.; Voiry, D.; Fujita, T.; Chen, M.; Chhowalla, M. Photoluminescence from Chemically Exfoliated MoS2. *Nano Lett* **2011,** *11*, 5111-5116.

(40) Novoselov, K. S.; Jiang, D.; Schedin, F.; Booth, T. J.; Khotkevich, V. V.; Morozov, S. V.; Geim, A. K. Two-Dimensional Atomic Crystals. *P Natl Acad Sci USA* **2005,** *102*, 10451-10453.

(41) Shi, Y.; Li, H.; Li, L.-J. Recent Advances in Controlled Synthesis of Two-Dimensional Transition Metal Dichalcogenides via Vapour Deposition Techniques. *Chem Soc Rev* **2015,** *44*, 2744-2756.

(42) Mata, M. d. l.; Zhou, X.; Furtmayr, F.; Teubert, J.; Gradecak, S.; Eickhoff, M.; Fontcuberta i Morral, A.; Arbiol, J. A Review of MBE Grown 0D, 1D and 2D Quantum Structures in a Nanowire. *J Mater Chem C* **2013,** *1*, 4300-4312.

(43) Tabor, C.; Qian, W.; El-Sayed, M. A. Dependence of the Threshold Energy of Femtosecond Laser Ejection of Gold Nanoprisms from Quartz Substrates on the Nanoparticle Environment. *J Phys Chem C* **2007,** *111*, 8934-8941.

(44) Haynes, C. L.; Van Duyne, R. P. Nanosphere Lithography: A Versatile Nanofabrication Tool for Studies of Size-Dependent Nanoparticle Optics. *J Phys Chem B* **2001,** *105*, 5599-5611.

(45) Murray, C. B.; Norris, D. J.; Bawendi, M. G. Synthesis and Characterization of Nearly Monodisperse CdE (E = Sulfur, Selenium, Tellurium) Semiconductor Nanocrystallites. *J Am Chem Soc* **1993,** *115*, 8706-8715.

(46) Tao, A. R.; Habas, S.; Yang, P. Shape Control of Colloidal Metal Nanocrystals. *Small* **2008,** *4*, 310-325.

(47) Kumar, S.; Nann, T. Shape Control of II–VI Semiconductor Nanomaterials. *Small* **2006,** *2*, 316-329.

(48) De Smet, Y.; Deriemaeker, L.; Finsy, R. A Simple Computer Simulation of Ostwald Ripening. *Langmuir* **1997,** *13*, 6884-6888.

(49) Ostwald, W. Über Die Vermeintliche Isomerie Des Roten Und Gelben Quecksilberoxyds Und Die Oberflächenspannung Fester Körper. *Z Phys Chem* **1900,** *34*, 495-503.

(50) Reiss, H. The Growth of Uniform Colloidal Dispersions. *J Chem Phys* **1951,** *19*, 482-487.

(51) Thanh, N. T. K.; Maclean, N.; Mahiddine, S. Mechanisms of Nucleation and Growth of Nanoparticles in Solution. *Chem Rev* **2014,** *114*, 7610-7630.

(52) Park, J.; Joo, J.; Kwon, S. G.; Jang, Y.; Hyeon, T. Synthesis of Monodisperse Spherical Nanocrystals. *Angew Chem Inter Ed* **2007,** *46*, 4630-4660.

(53) Mer, V. K. L. Nucleation in Phase Transitions. *Ind Eng Chem Res* **1952,** *44*, 1270-1277.

(54) Becker, R.; Döring, W. Kinetische Behandlung der Keimbildung in übersättigten Dämpfen. *Ann Phys* **1935,** *416*, 719-752.

(55) Polte, J. Fundamental Growth Principles of Colloidal Metal Nanoparticles - A New Pperspective. *CrystEngComm* **2015,** *17*, 6809-6830.

(56) Kovalenko, M. V.; Manna, L.; Cabot, A.; Hens, Z.; Talapin, D. V.; Kagan, C. R.; Klimov, V. I.; Rogach, A. L.; Reiss, P.; Milliron, D. J.; Guyot-Sionnnest, P.; Konstantatos, G.; Parak, W. J.; Hyeon, T.; Korgel, B. A.; Murray, C. B.; Heiss, W. Prospects of Nanoscience with Nanocrystals. *ACS Nano* **2015,** *9*, 1012-1057.

(57) Xu, L.; Ma, W.; Wang, L.; Xu, C.; Kuang, H.; Kotov, N. A. Nanoparticle Assemblies: Dimensional Transformation of Nanomaterials and Scalability. *Chem Soc Rev* **2013,** *42*, 3114-3126.

(58) Hanrath, T. Colloidal Nanocrystal Quantum Dot Assemblies as Artificial Solids. *J Vac Sci Technol A* **2012,** *30*, 030802.

(59) Gong, J.; Li, G.; Tang, Z. Self-Assembly of Noble metal Nanocrystals: Fabrication, Optical Property, and Application. *Nano Today* **2012,** *7*, 564-585.

(60) Vanmaekelbergh, D. Self-Assembly of Colloidal Nanocrystals as Route to Novel Classes of Nanostructured Materials. *Nano Today* **2011,** *6*, 419-437.

(61) Velev, O. D.; Gupta, S. Materials Fabricated by Micro- and Nanoparticle Assembly – The Challenging Path from Science to Engineering. *Adv Mater* **2009,** *21*, 1897-1905.

(62) Claridge, S. A.; Castleman, A. W.; Khanna, S. N.; Murray, C. B.; Sen, A.; Weiss, P. S. Cluster-Assembled Materials. *ACS Nano* **2009,** *3*, 244-255.

(63) Bishop, K. J. M.; Wilmer, C. E.; Soh, S.; Grzybowski, B. A. Nanoscale Forces and Their Uses in Self-Assembly. *Small* **2009,** *5*, 1600-1630.

(64) Bigioni, T. P.; Lin, X. M.; Nguyen, T. T.; Corwin, E. I.; Witten, T. A.; Jaeger, H. M. Kinetically Driven Self Assembly of Highly Ordered Nanoparticle Monolayers. *Nat Mater* **2006,** *5*, 265-270.

(65) Talapin, D. V.; Murray, C. B. PbSe Nanocrystal Solids for n- and p-Channel Thin Film Field-Effect Transistors. *Science* **2005,** *310*, 86-89.

(66) Bodnarchuk, M. I.; Kovalenko, M. V.; Heiss, W.; Talapin, D. V. Energetic and Entropic Contributions to Self-Assembly of Binary Nanocrystal Superlattices: Temperature as the Structure-Directing Factor. *J Am Chem Soc* **2010,** *132*, 11967-11977.

(67) Dong, A.; Chen, J.; Vora, P. M.; Kikkawa, J. M.; Murray, C. B. Binary Nanocrystal Superlattice Membranes Self-Assembled at the Liquid-Air Interface. *Nature* **2010,** *466*, 474-477.

(68) Diroll, B. T.; Doan-Nguyen, V. V. T.; Cargnello, M.; Gaulding, E. A.; Kagan, C. R.; Murray, C. B. X-ray Mapping of Nanoparticle Superlattice Thin Films. *ACS Nano* **2014,** *8*, 12843-12850.

(69) Rupich, S. M.; Shevchenko, E. V.; Bodnarchuk, M. I.; Lee, B.; Talapin, D. V. Size-Dependent Multiple Twinning in Nanocrystal Superlattices. *J Am Chem Soc* **2010,** *132*, 289-296.

(70) Talapin, D. V.; Shevchenko, E. V.; Kornowski, A.; Gaponik, N.; Haase, M.; Rogach, A. L.; Weller, H. A New Approach to Crystallization of CdSe Nanoparticles into Ordered Three-Dimensional Superlattices. *Adv Mater* **2001,** *13*, 1868.

(71) Murray, C. B.; Kagan, C. R.; Bawendi, M. G. Self-Organization of CdSe Nanocrystallites into Three-Dimensional Quantum Dot Superlattices. *Science* **1995,** *270*, 1335-1338.

(72) Wang, T.; Zhuang, J.; Lynch, J.; Chen, O.; Wang, Z.; Wang, X.; LaMontagne, D.; Wu, H.; Wang, Z.; Cao, Y. C. Self-Assembled Colloidal Superparticles from Nanorods. *Science* **2012,** *338*, 358-363.

(73) Zhuang, J.; Wu, H.; Yang, Y.; Cao, Y. C. Supercrystalline Colloidal Particles from Artificial Atoms. *J Am Chem Soc* **2007,** *129*, 14166-14167.

(74) Haubold, D.; Reichhelm, A.; Weiz, A.; Borchardt, L.; Ziegler, C.; Bahrig, L.; Kaskel, S.; Ruck, M.; Eychmüller, A. The Formation and Morphology of Nanoparticle Supracrystals. *Adv Funct Mater* **2016,** *26*, 4890-4895.

(75) Rabani, E.; Reichman, D. R.; Geissler, P. L.; Brus, L. E. Drying-Mediated Self-Assembly of Nanoparticles. *Nature* **2003,** *426*, 271-274.

(76) Vogel, N.; Retsch, M.; Fustin, C.-A.; del Campo, A.; Jonas, U. Advances in Colloidal Assembly: The Design of Structure and Hierarchy in Two and Three Dimensions. *Chem Rev* **2015,** *115*, 6265-6311.

(77) Scheele, M.; Brutting, W.; Schreiber, F. Coupled organic-inorganic nanostructures (COIN). *Phys Chem Chem Phys* **2015,** *17*, 97-111.

(78) Zhang, J.; Qin, Z.; Zeng, D.; Xie, C. Metal-Oxide-Semiconductor Based Gas Sensors: Screening, Preparation, and Integration. *Phys Chem Chem Phys* **2017,** *19*, 6313-6329.

(79) Potyrailo, R. A. Toward High Value Sensing: Monolayer-Protected Metal Nanoparticles in Multivariable Gas and Vapor Sensors. *Chem Soc Rev* **2017,** *46*, 5311-5346.

(80) Potyrailo, R. A. Multivariable Sensors for Ubiquitous Monitoring of Gases in the Era of Internet of Things and Industrial Internet. *Chem Rev* **2016,** *116*, 11877-11923.

(81) Saha, K.; Agasti, S. S.; Kim, C.; Li, X.; Rotello, V. M. Gold Nanoparticles in Chemical and Biological Sensing. *Chem Rev* **2012,** *112*, 2739-2779.

(82) Wohltjen, H.; Snow, A. W. Colloidal Metal−Insulator−Metal Ensemble Chemiresistor Sensor. *Anal Chem* **1998,** *70*, 2856-2859.

(83) Calderón, M. F.; Zelaya, E.; Benitez, G. A.; Schilardi, P. L.; Creus, A. H.; Orive, A. G.; Salvarezza, R. C.; Ibañez, F. J. New Findings for the Composition and Structure of Ni Nanoparticles Protected with Organomercaptan Molecules. *Langmuir* **2013,** *29*, 4670-4678.

(84) Dalfovo, M. C.; Salvarezza, R. C.; Ibañez, F. J. Improved Vapor Selectivity and Stability of Localized Surface Plasmon Resonance with a Surfactant-Coated Au Nanoparticles Film. *Anal Chem* **2012,** *84*, 4886-4892.

(85) Moreno, M.; Ibañez, F. J.; Jasinski, J. B.; Zamborini, F. P. Hydrogen Reactivity of Palladium Nanoparticles Coated with Mixed Monolayers of Alkyl Thiols and Alkyl Amines for Sensing and Catalysis Applications. *J Am Chem Soc* **2011,** *133*, 4389-4397.

(86) Dovgolevsky, E.; Konvalina, G.; Tisch, U.; Haick, H. Monolayer-Capped Cubic Platinum Nanoparticles for Sensing Nonpolar Analytes in Highly Humid Atmospheres. *J Phys Chem C* **2010,** *114*, 14042-14049.

(87) Zabet-Khosousi, A.; Dhirani, A. A. Charge Transport in Nanoparticle Assemblies. *Chem Rev* **2008,** *108*, 4072-4124.

(88) Drake, C.; Deshpande, S.; Bera, D.; Seal, S. Metallic Nanostructured Materials Based Sensors. *Int Mater Rev* **2007,** *52*, 289-317.

(89) Franke, M. E.; Koplin, T. J.; Simon, U. Metal and Metal Oxide Nanoparticles in Chemiresistors: Does the Nanoscale Matter? *Small* **2006,** *2*, 36-50.

(90) Joseph, Y.; Peić, A.; Chen, X.; Michl, J.; Vossmeyer, T.; Yasuda, A. Vapor Sensitivity of Networked Gold Nanoparticle Chemiresistors: Importance of Flexibility and Resistivity of the Interlinkage. *J Phys Chem C* **2007,** *111*, 12855-12859.

(91) Beloborodov, I. S.; Lopatin, A. V.; Vinokur, V. M.; Efetov, K. B. Granular Electronic Systems. *Rev Mod Phys* **2007,** *79*, 469-518.

(92) Sze, S. M.; Ng, K. K., *Physics of Semiconductor Devices*. Wiley: **2006**.

(93) Glazman, L. I.; Pustilnik, M., *Nanophysics: Coherence and Transport*. Elsevier Science: San Diego, CA, **2005**; Vol. 81, p 640.

(94) Shklovskii, B. I.; Efros, A. L., *Electronic Properties of Doped Semiconductors*. Springer-Verlag Berlin Heidelberg: **1984**; Vol. 45, p 388.

(95) Kane, J.; Ong, J.; Saraf, R. F. Chemistry, Physics, and Engineering of Electrically Percolating Arrays of Nanoparticles: A Mini Review. *J Mater Chem* **2011,** *21*, 16846-16858.

(96) Herrmann, J.; Bray, D. J.; Müller, K. H.; Wei, G.; Lindoy, L. F. Tuning the Coulomb Charging Eenergy in Cross-Llinked Nanoparticle Films. *Phys Rev B* **2007,** *76*, 212201.

(97) Quinn, A. J.; Beecher, P.; Iacopino, D.; Floyd, L.; De Marzi, G.; Shevchenko, E. V.; Weller, H.; Redmond, G. Manipulating the Charging Energy of Nanocrystal Arrays. *Small* **2005,** *1*, 613-618.

(98) Grabert, H.; Devoret, M. H., *Single Charge Tunneling: Coulomb Blockade Phenomena In Nanostructures*. Springer US: Plenum, New York, **1992**; Vol. 294, p 335.

(99) Gorter, C. J. A Possible Explanation of the Increase of the Electrical Resistance of Thin Metal Films at Low Temperatures and Small Field Strengths. *Physica* **1951,** *17*, 777-780.

(100) Tran, T. B.; Beloborodov, I. S.; Lin, X. M.; Bigioni, T. P.; Vinokur, V. M.; Jaeger, H. M. Multiple Cotunneling in Large Quantum Dot Arrays. *Phys Rev Lett* **2005,** *95*, 076806.

(101) Efetov, K. B.; Tschersich, A. Coulomb effects in granular materials at not very low temperatures. *Phys Rev B* **2003,** *67*, 174205.

(102) Beloborodov, I. S.; Efetov, K. B.; Lopatin, A. V.; Vinokur, V. M. Transport Properties of Granular Metals at Low Temperatures. *Phys Rev Lett* **2003,** *91*, 246801.

(103) Efetov, K. B.; Tschersich, A. Transition from Insulating to Non-Insulating Temperature Dependence of the Conductivity in Granular Metals. *Europhys. Lett.* **2002,** *59*, 114-120.

(104) Stansfield, G. L.; Thomas, P. J. Substituent Effects on Charge Transport in Films of Au Nanocrystals. *J Am Chem Soc* **2012,** *134*, 11888-11891.

(105) Middleton, A. A.; Wingreen, N. S. Collective Transport in Arrays of Small Metallic Dots. *Phys Rev Lett* **1993,** *71*, 3198-3201.

(106) Parthasarathy, R.; Lin, X. M.; Jaeger, H. M. Electronic Transport in Metal Nanocrystal Arrays: The Effect of Structural Disorder on Scaling Behavior. *Phys Rev Lett* **2001,** *87*, 186807.

(107) Leroy, Y.; Cordan, A. S.; Goltzene, A. Variance Analysis of the Coulomb Blockade Parameters in Nanometer-Size Disordered Arrays. *J Appl Phys* **2001,** *90*, 953-957.

(108) Ancona, M. G.; Kruppa, W.; Rendell, R. W.; Snow, A. W.; Park, D.; Boos, J. B. Coulomb blockade in single-layer Au nanocluster films. *Phys Rev B* **2001,** *64*, 033408.

(109) Bezryadin, A.; Westervelt, R. M.; Tinkham, M. Self-Assembled Chains of Graphitized Carbon Nanoparticles. *Appl Phys Lett* **1999,** *74*, 2699-2701.

(110) Elteto, K.; Lin, X. M.; Jaeger, H. M. Electronic Transport in Quasi-One-Dimensional Arrays of Gold Nanocrystals. *Phys Rev B* **2005,** *71*, 205412.

(111) Skinner, B.; Chen, T. R.; Shklovskii, B. I. Theory of Hopping Conduction in Arrays of Doped Semiconductor Nanocrystals. *Phys Rev B* **2012,** *85*, 205316.

(112) Kang, M. S.; Sahu, A.; Norris, D. J.; Frisbie, C. D. Size- and Temperature-Dependent Charge Transport in PbSe Nanocrystal Thin Films. *Nano Lett* **2011,** *11*, 3887-3892.

(113) Liu, H.; Pourret, A.; Guyot-Sionnest, P. Mott and Efros-Shklovskii Variable Range Hopping in CdSe Quantum Dots Films. *ACS Nano* **2010,** *4*, 5211-5216.

(114) Yu, D.; Wang, C. J.; Wehrenberg, B. L.; Guyot-Sionnest, P. Variable Range Hopping Conduction in Semiconductor Nanocrystal Solids. *Phys Rev Lett* **2004,** *92*, 216802.

(115) Huth, M. Granular Metals: From Electronic Correlations to Strain-Sensing Applications. *J Appl Phys* **2010,** *107*, 113709.

(116) Tran, T. B.; Beloborodov, I. S.; Hu, J. S.; Lin, X. M.; Rosenbaum, T. F.; Jaeger, H. M. Sequential Tunneling and Inelastic Cotunneling in Nanoparticle Arrays. *Phys Rev B* **2008,** *78*, 075437.

(117) Beloborodov, I. S.; Lopatin, A. V.; Vinokur, V. M. Coulomb Effects and Hopping Transport in Granular Metals. *Phys Rev B* **2005,** *72*, 125121.

(118) Feigel'man, M. V.; Ioselevich, A. S. Variable-Range Cotunneling and Conductivity of a Granular Metal. *JETP Lett* **2005,** *81*, 277-283.

(119) Averin, D. V.; Nazarov, Y. V. Virtual Electron-Diffusion during Quantum Tunneling of the Electric Charge. *Phys Rev Lett* **1990,** *65*, 2446-2449.

(120) Dayen, J. F.; Devid, E.; Kamalakar, M. V.; Golubev, D.; Guedon, C.; Faramarzi, V.; Doudin, B.; van der Molen, S. J. Enhancing the Molecular Signature in Molecule-Nanoparticle Networks Via Inelastic Cotunneling. *Adv Mater* **2013,** *25*, 400-404.

(121) Duan, C.; Wang, Y.; Sun, J. L.; Guan, C. R.; Grunder, S.; Mayor, M.; Peng, L. M.; Liao, J. H. Controllability of the Coulomb Charging Energy in Close-Packed Nanoparticle Arrays. *Nanoscale* **2013,** *5*, 10258-10266.

(122) Abeles, B.; Sheng, P.; Coutts, M. D.; Arie, Y. Structural and Electrical Properties of Granular Metal-Films. *Adv Phys* **1975,** *24*, 407-461.

(123) Laikhtman, B.; Wolf, E. L. Tunneling Time and Effective Capacitance for Single Electron-Tunneling. *Phys Lett A* **1989,** *139*, 257-260.

(124) Beecher, P.; Quinn, A. J.; Shevchenko, E. V.; Weller, H.; Redmond, G. Insulator-to-Metal transition in Nanocrystal Assemblies Driven by In Situ Mild Thermal Annealing. *Nano Lett* **2004,** *4*, 1289-1293.

(125) Black, C. T.; Murray, C. B.; Sandstrom, R. L.; Sun, S. H. Spin-Dependent Tunneling in Self-Assembled Cobalt-Nanocrystal Superlattices. *Science* **2000,** *290*, 1131-1134.

(126) Beecher, P.; Quinn, A. J.; Shevchenko, E. V.; Weller, H.; Redmond, G. Charge Transport in Weakly Coupled CoPt3 Nanocrystal Assemblies. *J Phys Chem B* **2004,** *108*, 9564-9567.

(127) Reich, K. V.; Shklovskii, B. I. Dielectric Constant and Charging Energy in Array of Touching Nanocrystals. *Appl Phys Lett* **2016,** *108*, 113104.

(128) Fu, H.; Reich, K. V.; Shklovskii, B. I. Hopping Conductivity and Insulator-Metal Transition in Films of Touching Semiconductor Nanocrystals. *Phys Rev B* **2016,** *93*, 125430.

(129) Chen, T.; Reich, K. V.; Kramer, N. J.; Fu, H.; Kortshagen, U. R.; Shklovskii, B. I. Metal-Insulator Transition in Films of Doped Semiconductor Nanocrystals. *Nat Mater* **2016,** *15*, 299-303.

(130) Reich, K. V.; Chen, T. R.; Shklovskii, B. I. Theory of a Field-Effect Transistor Based on a Semiconductor Nanocrystal Array. *Phys Rev B* **2014,** *89*, 235303.

(131) Mott, N. F. Introductory Talk; Conduction in Non-Crystalline Materials. *J Non-Cryst Solids* **1972,** *8*, 1-18.

(132) Mott, N. F. Conduction in Glasses Containing Transition Metal Ions. *J Non-Cryst Solids* **1968,** *1*, 1-17.

(133) Efros, A. L.; Shklovskii, B. I. Coulomb Gap and Low-Temperature Conductivity of Disordered Systems. *J Phys C Solid State* **1975,** *8*, L49-L51.

(134) Efros, A. L.; Rosen, M. The Electronic Structure of Semiconductor Nanocrystals. *Annu Rev Mater Sci* **2000,** *30*, 475-521.

(135) Ekimov, A. I.; Kudryavtsev, I. A.; Ivanov, M. G.; Efros, A. L. Spectra and Decay Kinetics of Radiative Recombination in Cds Microcrystals. *J Lumin* **1990,** *46*, 83-95.

(136) Maxwell, J. C., *A Treatise on Electricity and Magnetism*. OUP Oxford: **1998**.

(137) Oehzelt, M.; Koch, N.; Heimel, G. Organic Semiconductor Density of States Controls the Energy Level Alignment at Electrode Interfaces. *Nat Commun* **2014,** *5*, 4174

(138) Hwang, J.; Wan, A.; Kahn, A. Energetics of Metal-Organic Interfaces: New Experiments and Assessment of the Field. *Mat Sci Eng R* **2009,** *64*, 1-31.

(139) Flores, F.; Ortega, J.; Vazquez, H. Modelling Energy Level Alignment at Organic Interfaces and Density Functional Theory. *Phys Chem Chem Phys* **2009,** *11*, 8658-8675.

(140) van der Heide, P., *X-ray Photoelectron Spectroscopy: An Introduction to Principles and Practices*. Wiley: **2011**.

(141) Mönch, W., *Semiconductor Surfaces and Interfaces*. Springer-Verlag: **1993**.

(142) Braun, S.; Salaneck, W. R.; Fahlman, M. Energy-Level Alignment at Organic/Metal and Organic/Organic Interfaces. *Adv Mater* **2009,** *21*, 1450-1472.

(143) Ishii, H.; Sugiyama, K.; Ito, E.; Seki, K. Energy Level Alignment and Interfacial Electronic Structures at Organic/Metal and Organic/Organic Interfaces. *Adv Mater* **1999,** *11*, 605-625.

(144) Siegbahn, K.; Uppsala, K. V.-s. i., *ESCA; Atomic, Molecular and Solid State Structure Studied by Means of Electron Spectroscopy*. Almqvist & Wiksells: **1967**.

(145) Turner, D. W. Molecular Photoelectron Spectroscopy. *Philosophical Transactions of the Royal Society of London. Series A, Mathematical and Physical Sciences* **1970,** *268*, 7-31.

(146) Rhoderick, E. H.; Williams, R. H., *Metal-Semiconductor Contacts*. Clarendon Press: **1988**.

(147) Chen, Y. C.; Cunningham, J. E.; Flynn, C. P. Dependence of Rare-Gas-Adsorbate Dipole Moment on Substrate Work Function. *Phys Rev B* **1984,** *30*, 7317-7319.

(148) Lang, N. D. Interaction between Closed-Shell Systems and Metal Surfaces. *Phys Rev Lett* **1981,** *46*, 842-845.

(149) Fahlman, M.; Crispin, A.; Crispin, X.; Henze, S. K. M.; de Jong, M. P.; Osikowicz, W.; Tengstedt, C.; Salaneck, W. R. Electronic Structure of Hybrid Interfaces for Polymer-based Electronics. *J Phys-Condens Mat* **2007,** *19*, 183202.

(150) Tengstedt, C.; Osikowicz, W.; Salaneck, W. R.; Parker, I. D.; Hsu, C. H.; Fahlman, M. Fermi-Level Pinning at Conjugated Polymer Interfaces. *Appl Phys Lett* **2006,** *88*, 053502.

(151) Vazquez, H.; Flores, F.; Kahn, A. Induced Density of States Model for Weakly-Interacting Organic Semiconductor Interfaces. *Org Electron* **2007,** *8*, 241-248.

(152) Braun, S.; de Jong, M. P.; Osikowicz, W.; Salaneck, W. R. Influence of the Electrode Work Function on the Energy Level Alignment at Organic-Organic Interfaces. *Appl Phys Lett* **2007,** *91*, 202108.

(153) Crispin, X.; Geskin, V.; Crispin, A.; Cornil, J.; Lazzaroni, R.; Salaneck, W. R.; Bredas, J. L. Characterization of the Interface Dipole at Organic/Metal Interfaces. *J Am Chem Soc* **2002,** *124*, 8131-8141.

(154) Heimel, G.; Romaner, L.; Zojer, E.; Bredas, J. L. The Interface Energetics of Self-Assembled Monolayers on Metals. *Accounts Chem Res* **2008,** *41*, 721-729.

(155) Chen, J.; Reed, M. A.; Rawlett, A. M.; Tour, J. M. Large On-Off Ratios and Negative Differential Resistance in a Molecular Electronic Device. *Science* **1999,** *286*, 1550-1552.

(156) Hwang, J.; Kim, E. G.; Liu, J.; Bredas, J. L.; Duggal, A.; Kahn, A. Photoelectron Spectroscopic Study of the Electronic Band Structure of Polyfluorene and Fluorene-Arylamine Copolymers at Interfaces. *J Phys Chem C* **2007,** *111*, 1378-1384.

(157) Wan, A.; Hwang, J.; Amy, F.; Kahn, A. Impact of Electrode Contamination on the α-NPD/Au Hole Injection Barrier. *Org Electron* **2005,** *6*, 47-54.

(158) Salaneck, W. R.; Seki, K.; Kahn, A.; Pireaux, J. J., *Conjugated Polymer And Molecular Interfaces: Science And Technology For Photonic And Optoelectronic Application*. CRC Press: **2001**.

(159) Campbell, I. H.; Ferraris, J. P.; Hagler, T. W.; Joswick, M. D.; Parker, I. D.; Smith, D. L. Measuring Internal Electric Fields in organic Light-Emitting Diodes using Electroabsorption Spectroscopy. *Polym Advan Technol* **1997,** *8*, 417-423.

(160) Samadi Khoshkhoo, M.; Peisert, H.; Chassé, T.; Scheele, M. The Role of the Density of Interface States in Interfacial Energy Level Alignment of PTCDA. *Org Electron* **2017,** *49*, 249-254.

(161) Kahn, A.; Koch, N.; Gao, W. Y. Electronic Structure and Electrical Properties of Interfaces between Metals and π-conjugated Molecular Films. *J Polym Sci Pol Phys* **2003,** *41*, 2529-2548.

(162) Hill, I. G.; Kahn, A. Energy Level Alignment at Interfaces of Organic Semiconductor Heterostructures. *J Appl Phys* **1998,** *84*, 5583-5586.

(163) Cardona, M.; Ley, L., *Photoemission in Solids: General Principles*. Springer-Verlag: **1978**.

(164) Lang, N. D.; Kohn, W. Theory of Metal Surfaces: Work Function. *Phys Rev B* **1971,** *3*, 1215-1223.

(165) Hadziioannou, G.; Malliaras, G. G., *Semiconducting Polymers: Chemistry, Physics and Engineering*. Wiley: **2006**.

(166) Braun, S.; Liu, X.; Salaneck, W. R.; Fahlman, M. Fermi Level Equilibrium at Donor-Acceptor Interfaces in Multi-Layered Thin Film Stack of TTF and TCNQ. *Org Electron* **2010,** *11*, 212-217.

(167) Bao, Q. Y.; Sandberg, O.; Dagnelund, D.; Sanden, S.; Braun, S.; Aarnio, H.; Liu, X. J.; Chen, W. M. M.; Osterbacka, R.; Fahlman, M. Trap-Assisted Recombination via Integer Charge Transfer States in Organic Bulk Heterojunction Photovoltaics. *Adv Funct Mater* **2014,** *24*, 6309-6316.

(168) Braun, S.; Osikowicz, W.; Wang, Y.; Salaneck, W. R. Energy Level Alignment Regimes at Hybrid Organic-Organic and Inorganic-Organic Interfaces. *Org Electron* **2007,** *8*, 14-20.

(169) Braun, S.; Salaneck, W. R. Fermi Level Pinning at Interfaces with Tetrafluorotetracyanoquinodimethane (F4-TCNQ): The Role of Integer Charge Transfer States. *Chem Phys Lett* **2007,** *438*, 259-262.

(170) Hill, I. G.; Rajagopal, A.; Kahn, A.; Hu, Y. Molecular Level Alignment at Organic Semiconductor-Metal Interfaces. *Appl Phys Lett* **1998,** *73*, 662-664.

(171) Vazquez, H.; Dappe, Y. J.; Ortega, J.; Flores, F. Energy Level Alignment at Metal/Organic Semiconductor Interfaces: "Pillow" Effect, Induced Density of Interface States, and Charge Neutrality Level. *J Chem Phys* **2007,** *126*, 144703.

(172) Koch, N.; Vollmer, A. Electrode-Molecular Semiconductor Contacts: Work-Function-Dependent Hole Injection Barriers Versus Fermi-Level Pinning. *Appl Phys Lett* **2006,** *89*, 162107

(173) Salomon, E.; Zhang, Q.; Barlow, S.; Marder, S. R.; Kahn, A. Photoemission Studies of Interfaces between a Tris(thieno)Hexaazatriphenylene Derivative and Metals. *Org Electron* **2008,** *9*, 944-951.

(174) Spicer, W. E.; Lilientalweber, Z.; Weber, E.; Newman, N.; Kendelewicz, T.; Cao, R.; Mccants, C.; Mahowald, P.; Miyano, K.; Lindau, I. The Advanced Unified Defect Model for Schottky-Barrier Formation. *J Vac Sci Technol B* **1988,** *6*, 1245-1251.

(175) Brillson, L. J. The Structure and Properties of Metal-Semiconductor Interfaces. *Surf Sci Rep* **1982,** *2*, 123-326.

(176) Watkins, N. J.; Makinen, A. J.; Gao, Y.; Uchida, M.; Kafafi, Z. H. Direct Observation of the Evolution of Occupied and Unoccupied Energy Levels of Two Silole Derivatives at their Interfaces with Magnesium. *J Appl Phys* **2006,** *100*, 103706.

(177) Mason, M. G.; Tang, C. W.; Hung, L. S.; Raychaudhuri, P.; Madathil, J.; Giesen, D. J.; Yan, L.; Le, Q. T.; Gao, Y.; Lee, S. T.; Liao, L. S.; Cheng, L. F.; Salaneck, W. R.; dos Santos, D. A.; Bredas, J. L. Interfacial Chemistry of Alq(3) and LiF with Reactive Metals. *J Appl Phys* **2001,** *89*, 2756-2765.

(178) Lindell, L.; de Jong, M. P.; Osikowicz, W.; Lazzaroni, R.; Berggren, M.; Salaneck, W. R.; Crispin, X. Characterization of the Interface Dipole at the Paraphenylenediamine-

Nickel Interface: A Joint Theoretical and Experimental Study. *J Chem Phys* **2005,** *122*, 084712.

(179) Parr, R. G.; Pearson, R. G. Absolute Hardness - Companion Parameter to Absolute Electronegativity. *J Am Chem Soc* **1983,** *105*, 7512-7516.

(180) Louie, S. G.; Cohen, M. L. Electronic Structure of a Metal-Semiconductor Interface. *Phys Rev B* **1976,** *13*, 2461-2469.

(181) Heine, V. Theory of Surface States. *Phys Rev* **1965,** *138*, A1689-A1696.

(182) Tejedor, C.; Flores, F.; Louis, E. The Metal-Semiconductor Interface: Si (111) and Zincblende (110) junctions. *J Phys C: Solid State Physics* **1977,** *10*, 2163.

(183) Vazquez, H.; Oszwaldowski, R.; Pou, P.; Ortega, J.; Perez, R.; Flores, F.; Kahn, A. Dipole Formation at Metal/PTCDA Interfaces: Role of the Charge Neutrality Level. *Europhys Lett* **2004,** *65*, 802-808.

(184) Vázquez, H.; Flores, F.; Oszwaldowski, R.; Ortega, J.; Pérez, R.; Kahn, A. Barrier Formation at Metal–Organic Interfaces: Dipole Formation and the Charge Neutrality Level. *Appl Surf Sci* **2004,** *234*, 107-112.

(185) Monch, W. Metal-Semiconductor Contacts - Electronic-Properties. *Surf Sci* **1994,** *299*, 928-944.

(186) Flores, F.; Tejedor, C. On the Formation of Semiconductor Interfaces. *J Phys C Solid State* **1987,** *20*, 145-175.

(187) Tersoff, J. Schottky Barriers and Semiconductor Band Structures. *Phys Rev B* **1985,** *32*, 6968-6971.

(188) Salzmann, I.; Heimel, G.; Oehzelt, M.; Winkler, S.; Koch, N. Molecular Electrical Doping of Organic Semiconductors: Fundamental Mechanisms and Emerging Dopant Design Rules. *Accounts Chem Res* **2016,** *49*, 370-378.

(189) Akaike, K.; Nardi, M. V.; Oehzelt, M.; Frisch, J.; Opitz, A.; Christodoulou, C.; Ligorio, G.; Beyer, P.; Timpel, M.; Pis, I.; Bondino, F.; Moudgil, K.; Barlow, S.; Marder, S. R.; Koch, N. Effective Work Function Reduction of Practical Electrodes Using an Organometallic Dimer. *Adv Funct Mater* **2016,** *26*, 2493-2502.

(190) Oehzelt, M.; Akaike, K.; Koch, N.; Heimel, G. Energy-Level Alignment at Organic Heterointerfaces. *Sci Adv* **2015,** *1*, e1501127.

(191) Amsalem, P.; Heimel, G.; Oehzelt, M.; Koch, N. The Interface Electronic Properties of Organic Photovoltaic Cells. *J Electron Spectrosc* **2015,** *204*, 177-185.

(192) Akaike, K.; Koch, N.; Oehzelt, M. Fermi Level Pinning Induced Electrostatic Fields and Band Bending at Organic Heterojunctions. *Appl Phys Lett* **2014,** *105*, 223303.

(193) Hill, I. G.; Milliron, D.; Schwartz, J.; Kahn, A. Organic Semiconductor Interfaces: Electronic Structure and Transport Properties. *Appl Surf Sci* **2000,** *166*, 354-362.

(194) Aradhya, S. V.; Venkataraman, L. Single-Molecule Junctions beyond Electronic Transport. *Nat Nanotechnol* **2013,** *8*, 399-410.

(195) Kuhn, H.; Mobius, D. Systems of Monomolecular Layers - Assembling and Physico-Chemical Behavior. *Angew Chem Int Edit* **1971,** *10*, 620-637.

(196) Xiang, D.; Wang, X. L.; Jia, C. C.; Lee, T.; Guo, X. F. Molecular-Scale Electronics: From Concept to Function. *Chem Rev* **2016,** *116*, 4318-4440.

(197) Lortscher, E. Wiring Molecules Into Circuits. *Nat Nanotechnol* **2013,** *8*, 381-384.

(198) Frisenda, R.; van der Zant, H. S. J. Transition from Strong to Weak Electronic Coupling in a Single-Molecule Junction. *Phys Rev Lett* **2016,** *117*, 126804.

(199) Guo, X. F.; Whalley, A.; Klare, J. E.; Huang, L. M.; O'Brien, S.; Steigerwald, M.; Nuckolls, C. Single-Molecule Devices as Scaffolding for Multicomponent Nanostructure Assembly. *Nano Lett* **2007,** *7*, 1119-1122.

(200) Malen, J. A.; Doak, P.; Baheti, K.; Tilley, T. D.; Segalman, R. A.; Majumdar, A. Identifying the Length Dependence of Orbital Alignment and Contact Coupling in Molecular Heterojunctions. *Nano Lett* **2009,** *9*, 1164-1169.

(201) Reddy, P.; Jang, S. Y.; Segalman, R. A.; Majumdar, A. Thermoelectricity in Molecular Junctions. *Science* **2007,** *315*, 1568-1571.

(202) Rincon-Garcia, L.; Evangeli, C.; Rubio-Bollinger, G.; Agrait, N. Thermopower Measurements in Molecular Junctions. *Chem Soc Rev* **2016,** *45*, 4285-4306.

(203) Schlicke, H.; Battista, D.; Kunze, S.; Schroter, C. J.; Eich, M.; Vossmeyer, T. Freestanding Membranes of Cross-Linked Gold Nanoparticles: Novel Functional Materials for Electrostatic Actuators. *ACS Appl Mater Inter* **2015,** *7*, 15123-15128.

(204) Dubois, V.; Niklaus, F.; Stemme, G. Crack-Defined Electronic Nanogaps. *Adv Mater* **2016,** *28*, 2178-2182.

(205) Requist, R.; Baruselli, P. P.; Smogunov, A.; Fabrizio, M.; Modesti, S.; Tosatti, E. Metallic, Magnetic and Molecular Nanocontacts. *Nat Nanotechnol* **2016,** *11*, 499-508.

(206) Su, T. A.; Neupane, M.; Steigerwald, M. L.; Venkataraman, L.; Nuckolls, C. Chemical Principles of Single-Molecule Electronics. *Nat Rev Mater* **2016,** *1*, 16002.

(207) Bernard, L.; Kamdzhilov, Y.; Calame, M.; van der Molen, S. J.; Liao, J. H.; Schonenberger, C. Spectroscopy of Molecular Junction Networks Obtained by Place Exchange in 2D Nanoparticle Arrays. *J Phys Chem C* **2007,** *111*, 18445-18450.

(208) Liao, J.; Bernard, L.; Langer, M.; Schonenberger, C.; Calame, M. Reversible Formation of Molecular Junctions in 2D Nanoparticle Arrays. *Adv Mater* **2006,** *18*, 2444-2447.

(209) Liao, J. H.; Blok, S.; van der Molen, S. J.; Diefenbach, S.; Holleitner, A. W.; Schonenberger, C.; Vladyka, A.; Calame, M. Ordered Nanoparticle Arrays Interconnected by Molecular Linkers: Electronic and Optoelectronic Properties. *Chem Soc Rev* **2015,** *44*, 999-1014.

(210) Wessels, J. M.; Nothofer, H. G.; Ford, W. E.; von Wrochem, F.; Scholz, F.; Vossmeyer, T.; Schroedter, A.; Weller, H.; Yasuda, A. Optical and Electrical Properties of Three-

Dimensional Interlinked Gold Nanoparticle Assemblies. *J Am Chem Soc* **2004,** *126*, 3349-3356.

(211) Xia, Y. N.; Xiong, Y. J.; Lim, B.; Skrabalak, S. E. Shape-Controlled Synthesis of Metal Nanocrystals: Simple Chemistry Meets Complex Physics? *Angew Chem Int Edit* **2009,** *48*, 60-103.

(212) Buonsanti, R.; Llordes, A.; Aloni, S.; Helms, B. A.; Milliron, D. J. Tunable Infrared Absorption and Visible Transparency of Colloidal Aluminum-Doped Zinc Oxide Nanocrystals. *Nano Lett* **2011,** *11*, 4706-4710.

(213) Buonsanti, R.; Milliron, D. J. Chemistry of Doped Colloidal Nanocrystals. *Chem Mater* **2013,** *25*, 1305-1317.

(214) Gilstrap, R. A.; Capozzi, C. J.; Carson, C. G.; Gerhardt, R. A.; Summers, C. J. Synthesis of a Nonagglomerated Indium Tin Oxide Nanoparticle Dispersion. *Adv Mater* **2008,** *20*, 4163-4166.

(215) Kanehara, M.; Koike, H.; Yoshinaga, T.; Teranishi, T. Indium Tin Oxide Nanoparticles with Compositionally Tunable Surface Plasmon Resonance Frequencies in the Near-IR Region. *J Am Chem Soc* **2009,** *131*, 17736-17737.

(216) Llordes, A.; Garcia, G.; Gazquez, J.; Milliron, D. J. Tunable Near-Infrared and Visible-Light Transmittance in Nanocrystal-in-Glass Composites. *Nature* **2013,** *500*, 323-326.

(217) Reecht, G.; Scheurer, F.; Speisser, V.; Dappe, Y. J.; Mathevet, F.; Schull, G. Electroluminescence of a Polythiophene Molecular Wire Suspended between a Metallic Surface and the Tip of a Scanning Tunneling Microscope. *Phys Rev Lett* **2014,** *112*, 047403.

(218) Dulic, D.; van der Molen, S. J.; Kudernac, T.; Jonkman, H. T.; de Jong, J. J. D.; Bowden, T. N.; van Esch, J.; Feringa, B. L.; van Wees, B. J. One-way optoelectronic switching of photochromic molecules on gold. *Phys Rev Lett* **2003,** *91*, 207402.

(219) Diroll, B. T.; Gordon, T. R.; Gaulding, E. A.; Klein, D. R.; Paik, T.; Yun, H. J.; Goodwin, E. D.; Damodhar, D.; Kagan, C. R.; Murray, C. B. Synthesis of N-Type Plasmonic Oxide Nanocrystals and the Optical and Electrical Characterization of their Transparent Conducting Films. *Chem Mater* **2014,** *26*, 4579-4588.

(220) Ederth, J.; Johnsson, P.; Niklasson, G. A.; Hoel, A.; Hultaker, A.; Heszler, P.; Granqvist, C. G.; van Doorn, A. R.; Jongerius, M. J.; Burgard, D. Electrical and Optical Properties of Thin Films Consisting of Tin-Doped Indium Oxide Nanoparticles. *Phys Rev B* **2003,** *68*, 155410.

(221) Ephraim, J.; Lanigan, D.; Staller, C.; Milliron, D. J.; Thimsen, E. Transparent Conductive Oxide Nanocrystals Coated with Insulators by Atomic Layer Deposition. *Chem Mater* **2016,** *28*, 5549-5553.

(222) Grisolia, J.; Decorde, N.; Gauvin, M.; Sangeetha, N. M.; Viallet, B.; Ressier, L. Electron Transport within Transparent Assemblies of Tin-Doped Indium Oxide Colloidal Nanocrystals. *Nanotechnology* **2015,** *26*, 335702.

(223) Lee, J.; Lee, S.; Li, G. L.; Petruska, M. A.; Paine, D. C.; Sun, S. H. A Facile Solution-Phase Approach to Transparent and Conducting ITO Nanocrystal Assemblies. *J Am Chem Soc* **2012,** *134*, 13410-13414.

(224) Shanker, G. S.; Tandon, B.; Shibata, T.; Chattopadhyay, S.; Nag, A. Doping Controls Plasmonics, Electrical Conductivity, and Carrier-Mediated Magnetic Coupling in Fe and Sn Codoped In2O3 Nanocrystals: Local Structure Is the Key. *Chem Mater* **2015,** *27*, 892-900.

(225) Hsu, C. H.; Chu, Y. H.; Lu, C. I.; Hsu, P. J.; Chen, S. W.; Hsueh, W. J.; Kaun, C. C.; Lin, M. T. Spin-Polarized Transport through Single Manganese Phthalocyanine Molecules on a Co Nanoisland. *J Phys Chem C* **2015,** *119*, 3374-3378.

(226) Thiele, S.; Balestro, F.; Ballou, R.; Klyatskaya, S.; Ruben, M.; Wernsdorfer, W. Electrically driven nuclear spin resonance in single-molecule magnets. *Science* **2014,** *344*, 1135-1138.

(227) Brede, J.; Atodiresei, N.; Kuck, S.; Lazic, P.; Caciuc, V.; Morikawa, Y.; Hoffmann, G.; Blugel, S.; Wiesendanger, R. Spin- and Energy-Dependent Tunneling through a Single Molecule with Intramolecular Spatial Resolution. *Phys Rev Lett* **2010,** *105*.

(228) Bogani, L.; Wernsdorfer, W. Molecular spintronics using single-molecule magnets. *Nat Mater* **2008,** *7*, 179-186.

(229) Wu, W. Exchange interaction between the triplet exciton and the localized spin in copper-phthalocyanine. *J Chem Phys* **2014,** *140*, 224301.

(230) Jung, S. H.; Choi, J. H.; Yang, S. M.; Cho, W. J.; Ha, C. S. Syntheses and Characterization of Soluble Phthalocyanine Derivatives for Organic Electroluminescent Devices. *Mat Sci Eng B-Solid* **2001,** *85*, 160-164.

(231) Dong, A. G.; Chen, J.; Oh, S. J.; Koh, W. K.; Xiu, F. X.; Ye, X. C.; Ko, D. K.; Wang, K. L.; Kagan, C. R.; Murray, C. B. Multiscale Periodic Assembly of Striped Nanocrystal Super lattice Films on a Liquid Surface. *Nano Lett* **2011,** *11*, 841-846.

(232) Dong, A. G.; Jiao, Y. C.; Milliron, D. J. Electronically Coupled Nanocrystal Superlattice Films by in Situ Ligand Exchange at the Liquid-Air Interface. *ACS Nano* **2013,** *7*, 10978-10984.

(233) Andre, A.; Zherebetskyy, D.; Hanifi, D.; He, B.; Khoshkhoo, M. S.; Jankowski, M.; Chasse, T.; Wang, L. W.; Schreiber, F.; Salleo, A.; Liu, Y.; Scheele, M. Toward Conductive Mesocrystalline Assemblies: PbS Nanocrystals Cross-Linked with Tetrathiafulvalene Dicarboxylate. *Chem Mater* **2015,** *27*, 8105-8115.

(234) Sharma, R.; Sawvel, A. M.; Barton, B.; Dong, A. G.; Buonsanti, R.; Llordes, A.; Schaible, E.; Axnanda, S.; Liu, Z.; Urban, J. J.; Nordlund, D.; Kisielowski, C.; Milliron, D. J. Nanocrystal Superlattice Embedded within an Inorganic Semiconducting Matrix by in Situ Ligand Exchange: Fabrication and Morphology. *Chem Mater* **2015,** *27*, 2755-2758.

(235) Hesse, R.; Chasse, T.; Szargan, R. Unifit 2002 - Universal Analysis Software for Photoelectron Spectra. *Anal Bioanal Chem* **2003,** *375*, 856-863.

(236) Luther, J. M.; Law, M.; Song, Q.; Perkins, C. L.; Beard, M. C.; Nozik, A. J. Structural, Optical and Electrical Properties of Self-Assembled Films of PbSe Nanocrystals Treated with 1,2-Ethanedithiol. *ACS Nano* **2008,** *2*, 271-280.

(237) Choi, S. I.; Nam, K. M.; Park, B. K.; Seo, W. S.; Park, J. T. Preparation and Optical Properties of Colloidal, Monodisperse, and Highly Crystalline ITO Nanoparticles. *Chem Mater* **2008,** *20*, 2609-2611.

(238) Yan, C.; Zharnikov, M.; Golzhauser, A.; Grunze, M. Preparation and Characterization of Self-Assembled Monolayers on Indium Tin Oxide. *Langmuir* **2000,** *16*, 6208-6215.

(239) Kim, J. S.; Ho, P. K. H.; Thomas, D. S.; Friend, R. H.; Cacialli, F.; Bao, G. W.; Li, S. F. Y. X-ray Photoelectron Spectroscopy of Surface-Treated Indium-Tin Oxide Thin Films. *Chem Phys Lett* **1999,** *315*, 307-312.

(240) Karsi, N.; Lang, P.; Chehimi, M.; Delamar, M.; Horowitz, G. Modification of Indium Tin Oxide Films by Alkanethiol and Fatty Acid Self-Assembled Monolayers: A Comparative Study. *Langmuir* **2006,** *22*, 3118-3124.

(241) Renaud, G.; Lazzari, R.; Leroy, F. Probing surface and interface morphology with Grazing Incidence Small Angle X-Ray Scattering. *Surf Sci Rep* **2009,** *64*, 255-380.

(242) Muller-Buschbaum, P. Grazing incidence small-angle X-ray scattering: an advanced scattering technique for the investigation of nanostructured polymer films. *Anal Bioanal Chem* **2003,** *376*, 3-10.

(243) Santanu, M.; Milan, K. S.; Manoj, K. J.; Benjamin, R.; Bridget, M. M.; Kanishka, B.; Rao, C. N. R. Evidence of contact epitaxy in the self-assembly of HgSe nanocrystals formed at a liquid–liquid interface. *J Phys: Condensed Matter* **2017,** *29*, 095101.

(244) Frank, C.; Banerjee, R.; Oettel, M.; Gerlach, A.; Novak, J.; Santoro, G.; Schreiber, F. Analysis of island shape evolution from diffuse x-ray scattering of organic thin films and implications for growth. *Phys Rev B* **2014,** *90*, 205401.

(245) Bera, M. K.; Sanyal, M. K.; Pal, S.; Daillant, J.; Datta, A.; Kulkarni, G. U.; Luzet, D.; Konovalov, O. Reversible buckling in monolayer of gold nanoparticles on water surface. *Epl-Europhys Lett* **2007,** *78*, 56003.

(246) Garcia, G.; Buonsanti, R.; Runnerstrom, E. L.; Mendelsberg, R. J.; Llordes, A.; Anders, A.; Richardson, T. J.; Milliron, D. J. Dynamically Modulating the Surface Plasmon Resonance of Doped Semiconductor Nanocrystals. *Nano Lett* **2011,** *11*, 4415-4420.

(247) Andre, A.; Theurer, C.; Lauth, J.; Maiti, S.; Hodas, M.; Samadi Khoshkhoo, M.; Kinge, S.; Meixner, A. J.; Schreiber, F.; Siebbeles, L. D. A.; Braun, K.; Scheele, M. Structure, Transport and Photoconductance of PbS Quantum Dot Monolayers Functionalized with a Copper Phthalocyanine Derivative. *Chem Commun* **2017,** *53*, 1700-1703.

(248) Zaumseil, J.; Baldwin, K. W.; Rogers, J. A. Contact Resistance in Organic Transistors that use Source and Drain Electrodes Formed by Soft Contact Lamination. *J Appl Phys* **2003,** *93*, 6117-6124.

(249) Havare, A. K.; Can, M.; Demic, S.; Okur, S.; Kus, M.; Aydin, H.; Yagmurcukardes, N.; Tari, S. Modification of ITO Surface using Aromatic Small Molecules with Carboxylic Acid Groups for OLED Applications. *Synthetic Met* **2011,** *161*, 2397-2404.

(250) Brumbach, M.; Veneman, P. A.; Marrikar, F. S.; Schulmeyer, T.; Simmonds, A.; Xia, W.; Lee, P.; Armstrong, N. R. Surface Composition and Electrical and Electrochemical Properties of Freshly Deposited and Acid-Etched Indium Tin Oxide Electrodes. *Langmuir* **2007,** *23*, 11089-11099.

(251) Donley, C.; Dunphy, D.; Paine, D.; Carter, C.; Nebesny, K.; Lee, P.; Alloway, D.; Armstrong, N. R. Characterization of Indium-Tin Oxide Interfaces using X-ray Photoelectron Spectroscopy and Redox Processes of a Chemisorbed Probe Molecule: Effect of Surface Pretreatment Conditions. *Langmuir* **2002,** *18*, 450-457.

(252) Fan, J. C. C.; Goodenough, J. B. X-Ray Photoemission Spectroscopy Studies of Sn-Doped Indium-Oxide Films. *J Appl Phys* **1977,** *48*, 3524-3531.

(253) López, G. P.; Castner, D. G.; Ratner, B. D. XPS O 1s Binding Energies for Polymers Containing Hydroxyl, Ether, Ketone and Ester groups. *Surface and Interface Analysis* **1991,** *17*, 267-272.

(254) Mie, G. Beiträge zur Optik Trüber Medien, Speziell Kolloidaler Metallösungen. *Annal Phys* **1908,** *330*, 377-445.

(255) Sheng, P. Electronic Transport in Granular Metal-Films. *Philos Mag B* **1992,** *65*, 357-384.

(256) Sheng, P.; Abeles, B.; Arie, Y. Hopping Conductivity in Granular Metals. *Phys Rev Lett* **1973,** *31*, 44-47.

(257) Zabet-Khosousi, A.; Trudeau, P. E.; Suganuma, Y.; Dhirani, A. A.; Statt, B. Metal to Insulator Transition in Films of Molecularly Linked Gold Nanoparticles. *Phys Rev Lett* **2006,** *96*, 156403.

(258) Guyot-Sionnest, P. Electrical Transport in Colloidal Quantum Dot Films. *J Phys Chem Lett* **2012,** *3*, 1169-1175.

(259) Yun, J.; Park, Y. H.; Bae, T. S.; Lee, S.; Lee, G. H. Fabrication of a Completely Transparent and Highly Flexible ITO Nanoparticle Electrode at Room Temperature. *ACS Appl Mater Inter* **2013,** *5*, 164-172.

(260) Love, J. C.; Estroff, L. A.; Kriebel, J. K.; Nuzzo, R. G.; Whitesides, G. M. Self-Assembled Monolayers of Thiolates on Metals as a Form of Nanotechnology. *Chem Rev* **2005,** *105*, 1103-1169.

(261) Schreiber, F. Structure and Growth of Self-Assembling Monolayers. *Prog Surf Sci* **2000,** *65*, 151-256.

(262) Vogel, N.; Retsch, M.; Fustin, C. A.; del Campo, A.; Jonas, U. Advances in Colloidal Assembly: The Design of Structure and Hierarchy in Two and Three Dimensions. *Chem Rev* **2015,** *115*, 6265-6311.

(263) Gilroy, K. D.; Ruditskiy, A.; Peng, H. C.; Qin, D.; Xia, Y. N. Bimetallic Nanocrystals: Syntheses, Properties, and Applications. *Chem Rev* **2016,** *116*, 10414-10472.

(264) Potyrailo, R. A. Toward High Value Sensing: Monolayer-Protected Metal Nanoparticles in Multivariable Gas and Vapor Sensors. *Chem Soc Rev* **2017,** *46*, 5311-5346.

(265) Saha, K.; Agasti, S. S.; Kim, C.; Li, X. N.; Rotello, V. M. Gold Nanoparticles in Chemical and Biological Sensing. *Chem Rev* **2012,** *112*, 2739-2779.

(266) Zhang, J.; Qin, Z. Y.; Zeng, D. W.; Xie, C. S. Metal-Oxide-Semiconductor Based Gas Sensors: Screening, Preparation, and Integration. *Phys Chem Chem Phys* **2017,** *19*, 6313-6329.

(267) Skinner, B.; Chen, T. R.; Shklovskii, B. I. Theory of hopping conduction in arrays of doped semiconductor nanocrystals. *Phys Rev B* **2012,** *85*.

(268) Shklovskii, B. I.; Efros, A. L., *Electronic Properties of Doped Semiconductors*. Springer Berlin Heidelberg: Berlin, **1984**.

(269) Beverly, K. C.; Sampaio, J. F.; Heath, J. R. Effects of Size Dispersion Disorder on the Charge Transport in Self-Assembled 2-D Ag Nanoparticle Arrays. *J Phys Chem B* **2002,** *106*, 2131-2135.

(270) Bazargan, S.; Heinig, N. F.; Rios, J. F.; Leung, K. T. Electronic Transport in Tin(IV) Oxide Nanocrystalline Films: Two-Medium Transport with Three-Dimensional Variable-Range Hopping Mechanism for the Ultrasmall Nanocrystallite Size Regime. *J Phys Chem C* **2012,** *116*, 4979-4985.

(271) Tran, T. B.; Beloborodov, I. S.; Lin, X. M.; Bigioni, T. P.; Vinokur, V. M.; Jaeger, H. M. Multiple Cotunneling in Large Quantum Dot Arrays. *Phys Rev Lett* **2005,** *95*.

(272) Blok, S.; Mojarro, R. R. A.; Maduro, L. A.; Blaauboer, M.; Van Der Molen, S. J. Inelastic Cotunneling with Energy-Dependent Contact Transmission. *J Chem Phys* **2017,** *146*, 092325.

(273) Beloborodov, I. S.; Glatz, A.; Vinokur, V. M. Transport Properties of Semiconducting Nanocrystal Arrays at Low Temperatures. *Phys Rev B* **2007,** *75*, 052302.

(274) Dugay, J.; Tan, R. P.; Ibrahim, M.; Garcia, C.; Carrey, J.; Lacroix, L. M.; Fazzini, P. F.; Viau, G.; Respaud, M. Charge Transport and Interdot Coupling Tuned by the Tunnel Barrier Length in Assemblies of Nanoparticles Surrounded by Organic Ligands. *Phys Rev B* **2014,** *89*.

(275) Moreira, H.; Yu, Q.; Nadal, B.; Bresson, B.; Rosticher, M.; Lequeux, N.; Zimmers, A.; Aubin, H. Electron Cotunneling Transport in Gold Nanocrystal Arrays. *Phys Rev Lett* **2011,** *107*, 176803.

(276) Samadi Khoshkhoo, M.; Maiti, S.; Schreiber, F.; Chassé, T.; Scheele, M. Surface Functionalization with Copper Tetraaminophthalocyanine Enables Efficient Charge Transport in Indium Tin Oxide Nanocrystal Thin Films. *ACS Appl Mater Inter* **2017,** *9*, 14197-14206.

(277) Dong, A.; Jiao, Y.; Milliron, D. J. Electronically Coupled Nanocrystal Superlattice Films by in Situ Ligand Exchange at the Liquid–Air Interface. *ACS Nano* **2013,** *7*, 10978-10984.

(278) Joseph, Y.; Besnard, I.; Rosenberger, M.; Guse, B.; Nothofer, H. G.; Wessels, J. M.; Wild, U.; Knop-Gericke, A.; Su, D. S.; Schlogl, R.; Yasuda, A.; Vossmeyer, T. Self-Assembled Gold Nanoparticle/Alkanedithiol Films: Preparation, Electron Microscopy, XPS-Analysis, Charge Transport, and Vapor-Sensing Properties. *J Phys Chem B* **2003,** *107*, 7406-7413.

(279) Joseph, Y.; Peic, A.; Chen, X. D.; Michl, J.; Vossmeyer, T.; Yasuda, A. Vapor Sensitivity of Networked Gold Nanoparticle Chemiresistors: Importance of Flexibility and Resistivity of the Interlinkage. *J Phys Chem C* **2007,** *111*, 12855-12859.

(280) Harbeck, M.; Erbahar, D. D.; Gurol, I.; Musluoglu, E.; Ahsen, V.; Ozturk, Z. Z. Phthalocyanines as Sensitive Coatings for QCM Sensors: Comparison of Gas and Liquid Sensing Properties. *Sensor Actuat B-Chem* **2011,** *155*, 298-303.

(281) Saleh, A. M.; Hraibat, S. M.; Kitaneh, R. M. L.; Abu-Samreh, M. M.; Musameh, S. M. Dielectric Response and Electric Properties of Organic Semiconducting Phthalocyanine Thin Films. *J Semicond* **2012,** *33*, 082002.

(282) Samanta, S.; Aswal, D. K.; Singh, A.; Debnath, A. K.; Kumar, M. S.; Hayakawa, Y.; Gupta, S. K.; Yakhmi, J. V. Bias and Temperature Dependent Charge Transport in High Mobility Cobalt-Phthalocyanine Thin Films. *Appl Phys Lett* **2010,** *96*, 013305.

(283) Anthopoulos, T. D.; Shafai, T. S. SCLC Measurements in Nickel Phthalocyanine Thin Films. *Phys Status Solidi A* **2000,** *181*, 569-574.

(284) Gould, R. D.; Blyth, R. I. R. Conductivity and Absorption-Measurements in Nickel Phthalocyanine Thin-Films. *Phys Status Solidi A* **1990,** *120*, K57-K61.

(285) Gould, R. D. Dependence of the Mobility and Trap Concentration in Evaporated Copper Phthalocyanine Thin-Films on Background Pressure and Evaporation Rate. *J Phys D Appl Phys* **1986,** *19*, 1785-1790.

(286) Zhang, J. S.; Shklovskii, B. I. Density of States and Conductivity of a Granular Metal or an Array of Quantum Dots. *Phys Rev B* **2004,** *70*, 115317.

(287) Rosenbaum, R. Crossover from Mott to Efros-Shklovskii Variable-Range-Hopping Conductivity in Inxoy Films. *Phys Rev B* **1991,** *44*, 3599-3603.

(288) Beloborodov, I. S.; Lopatin, A. V.; Vinokur, V. M. Coulomb Effects and Hopping Transport in Granular Metals. *Phys Rev B* **2005,** *72*.

(289) Havinga, E. E. The Temperature Dependence of Dielectric Constants. *J Phys Chem Solids* **1961,** *18*, 253-255.

(290) Bobnar, V.; Levstik, A.; Huang, C.; Zhang, Q. M. Intrinsic Dielectric Properties and Charge Transport in Oligomers of Organic Semiconductor Copper Phthalocyanine. *Phys Rev B* **2005,** *71*, 041202(R).

(291) Yazici, A.; Unus, N.; Altindal, A.; Salih, B.; Bekaroglu, O. Phthalocyanine with a Giant Dielectric Constant. *Dalton T* **2012,** *41*, 3773-3779.

(292) Pauly, M.; Dayen, J. F.; Golubev, D.; Beaufrand, J. B.; Pichon, B. P.; Doudin, B.; Begin-Colin, S. Co-tunneling Enhancement of the Electrical Response of Nanoparticle Networks. *Small* **2012,** *8*, 108-115.

(293) Yakushiji, K.; Mitani, S.; Ernult, F.; Takanashi, K.; Fujimori, H. Spin-dependent Tunneling and Coulomb Blockade in Ferromagnetic Nanoparticles. *Phys Rep* **2007,** *451*, 1-35.

(294) Mitani, S.; Takahashi, S.; Takanashi, K.; Yakushiji, K.; Maekawa, S.; Fujimori, H. Enhanced Magnetoresistance in Insulating Granular Systems: Evidence for Higher-Order Tunneling. *Phys Rev Lett* **1998,** *81*, 2799-2802.

(295) Sukegawa, H.; Nakamura, S.; Hirohata, A.; Tezuka, N.; Inomata, K. Significant Magnetoresistance Enhancement due to a Cotunneling Process in a Double Tunnel Junction with Single Discontinuous Ferromagnetic Layer Insertion. *Phys Rev Lett* **2005,** *94*.

(296) Hirohata, A.; Takanashi, K. Future Perspectives for Spintronic Devices. *J Phys D Appl Phys* **2014,** *47*.

(297) Turner, G. L. E. CRC Handbook of Chemistry and Physics - a Ready-Reference Book of Chemical and Physical Data, 70th Edition - Weast,Rc, Lide,Dr. *Ann Sci* **1991,** *48*, 496-497.

(298) Bartlett, P. N.; Ling-Chung, S. K. Conducting Polymer Gas Sensors Part II: Response of Polypyrrole to Methanol Vapour. *Sensor Actuat* **1989,** *19*, 141-150.

(299) Joseph, Y.; Guse, B.; Yasuda, A.; Vossmeyer, T. Chemiresistor Coatings from Pt- and Au-Nanoparticle/Nonanedithiol Films: Sensitivity to Gases and Solvent Vapors. *Sensor Actuat B-Chem* **2004,** *98*, 188-195.

(300) Kumar, A.; Brunet, J.; Varenne, C.; Ndiaye, A.; Pauly, A.; Penza, M.; Alvisi, M. Tetra-tert-butyl Copper Phthalocyanine-Based QCM Sensor for Toluene Detection in Air at Room Temperature. *Sensor Actuat B-Chem* **2015,** *210*, 398-407.

(301) Belghachi, A.; Collins, R. A. The Effects of Humidity on Phthalocyanine NO2 and NH3 Sensors. *J Phys D Appl Phys* **1990,** *23*, 223-227.

(302) Belghachi, A.; Collins, R. A. Humidity Response of Phthalocyanine Gas Sensors. *J Phys D Appl Phys* **1988,** *21*, 1647-1651.

(303) Martin, E. I.; Martinez, J. M.; Marcos, E. S. Modeling the Interactions of Phthalocyanines in Water: From the Cu(II)-tetrasulphonate to the Metal-Free Phthalocyanine. *J Chem Phys* **2011,** *134*.

(304) Joseph, Y.; Guse, B.; Vossmeyer, T.; Yasuda, A. Gold nanoparticle/organic networks as chemiresistor coatings: The effect of film morphology on vapor sensitivity. *J Phys Chem C* **2008,** *112*, 12507-12514.

(305) Gao, Y. L. Surface Analytical Studies of Interfaces in Organic Semiconductor Devices. *Mat Sci Eng R* **2010,** *68*, 39-87.

(306) Gelinck, G.; Heremans, P.; Nomoto, K.; Anthopoulos, T. D. Organic Transistors in Optical Displays and Microelectronic Applications. *Adv Mater* **2010,** *22*, 3778-3798.

(307) Guo, Y. L.; Yu, G.; Liu, Y. Q. Functional Organic Field-Effect Transistors. *Adv Mater* **2010,** *22*, 4427-4447.

(308) Di, C. A.; Zhang, F. J.; Zhu, D. B. Multi-Functional Integration of Organic Field-Effect Transistors (OFETs): Advances and Perspectives. *Adv Mater* **2013,** *25*, 313-330.

(309) Chen, S. F.; Deng, L. L.; Xie, J.; Peng, L.; Xie, L. H.; Fan, Q. L.; Huang, W. Recent Developments in Top-Emitting Organic Light-Emitting Diodes. *Adv Mater* **2010,** *22*, 5227-5239.

(310) Reineke, S.; Thomschke, M.; Lussem, B.; Leo, K. White Organic Light-Emitting Diodes: Status and Perspective. *Rev Mod Phys* **2013,** *85*, 1245-1293.

(311) Jou, J. H.; Kumar, S.; Agrawal, A.; Li, T. H.; Sahoo, S. Approaches for Fabricating High Efficiency Organic Light Emitting Diodes. *J Mater Chem C* **2015,** *3*, 3500-3500.

(312) Hains, A. W.; Liang, Z. Q.; Woodhouse, M. A.; Gregg, B. A. Molecular Semiconductors in Organic Photovoltaic Cells. *Chem Rev* **2010,** *110*, 6689-6735.

(313) Weickert, J.; Dunbar, R. B.; Hesse, H. C.; Wiedemann, W.; Schmidt-Mende, L. Nanostructured Organic and Hybrid Solar Cells. *Adv Mater* **2011,** *23*, 1810-1828.

(314) Kumar, P.; Chand, S. Recent Progress and Future Aspects of Organic Solar Cells. *Prog Photovoltaics* **2012,** *20*, 377-415.

(315) Ameri, T.; Khoram, P.; Min, J.; Brabec, C. J. Organic Ternary Solar Cells: A Review. *Adv Mater* **2013,** *25*, 4245-4266.

(316) Krause, B.; Schreiber, F.; Dosch, H.; Pimpinelli, A.; Seeck, O. H. Temperature Dependence of the 2D-3D Transition in the Growth of PTCDA on Ag(111): A Real-Time X-ray and Kinetic Monte Carlo Study. *Europhys Lett* **2004,** *65*, 372-378.

(317) Zou, Y.; Kilian, L.; Scholl, A.; Schmidt, T.; Fink, R.; Umbach, E. Chemical Bonding of PTCDA on Ag Surfaces and the Formation of Interface States. *Surf Sci* **2006,** *600*, 1240-1251.

(318) Duhm, S.; Gerlach, A.; Salzmann, I.; Broker, B.; Johnson, R. L.; Schreiber, F.; Koch, N. PTCDA on Au(111), Ag(111) and Cu(111): Correlation of Interface Charge Transfer to Bonding Distance. *Org Electron* **2008,** *9*, 111-118.

(319) Romaner, L.; Nabok, D.; Puschnig, P.; Zojer, E.; Ambrosch-Draxl, C. Theoretical Study of PTCDA Adsorbed on the Coinage Metal Surfaces, Ag(111), Au(111) and Cu(111). *New J Phys* **2009,** *11*, 053010.

(320) Zhong, S.; Zhong, J. Q.; Mao, H. Y.; Zhang, J. L.; Lin, J. D.; Chen, W. The Role of Gap States in the Energy Level Alignment at the Organic-Organic Heterojunction Interfaces. *Phys Chem Chem Phys* **2012,** *14*, 14127-14141.

(321) Knupfer, M.; Peisert, H. Electronic properties of interfaces between model organic semiconductors and metals. *Phys Status Solidi A* **2004,** *201*, 1055-1074.

(322) Peisert, H.; Petershans, A.; Chasse, T. Charge transfer and polarization screening at organic/metal interfaces: Distinguishing between the first layer and thin films. *J Phys Chem C* **2008,** *112*, 5703-5706.

(323) Peisert, H.; Kolacyak, D.; Chasse, T. Site-Specific Charge-Transfer Screening at Organic/Metal Interfaces. *J Phys Chem C* **2009,** *113*, 19244-19250.

(324) Verlaak, S.; Beljonne, D.; Cheyns, D.; Rolin, C.; Linares, M.; Castet, F.; Cornil, J.; Heremans, P. Electronic Structure and Geminate Pair Energetics at Organic-Organic Interfaces: The Case of Pentacene/C-60 Heterojunctions. *Adv Funct Mater* **2009,** *19*, 3809-3814.

(325) Akaike, K.; Koch, N.; Heimel, G.; Oehzelt, M. The Impact of Disorder on the Energy Level Alignment at Molecular Donor–Acceptor Interfaces. *Adv Mater Interfaces* **2015,** *2*, 1500232.

(326) Mao, H. Y.; Bussolotti, F.; Qi, D. C.; Wang, R.; Kera, S.; Ueno, N.; Wee, A. T. S.; Chen, W. Mechanism of the Fermi Level Pinning at Organic Donor-Acceptor Heterojunction Interfaces. *Org Electron* **2011,** *12*, 534-540.

(327) Paasch, G.; Peisert, H.; Knupfer, M.; Fink, J.; Scheinert, S. Mixing of interface dipole and band bending at organic/metal interfaces in the case of exponentially distributed transport states. *J Appl Phys* **2003,** *93*, 6084-6089.

(328) Peisert, H.; Knupfer, M.; Fink, J. Energy Level Alignment at Organic/Metal Interfaces: Dipole and Ionization Potential. *Appl Phys Lett* **2002,** *81*, 2400-2402.

(329) Bussolotti, F.; Kera, S.; Kudo, K.; Kahn, A.; Ueno, N. Gap states in Pentacene Thin Film Induced by Inert Gas Exposure. *Phys Rev Lett* **2013,** *110*, 267602.

(330) Vazquez, H.; Flores, F.; Oszwaldowski, R.; Ortega, J.; Perez, R.; Kahn, A. Barrier formation at metal-organic interfaces: dipole formation and the charge neutrality level. *Appl Surf Sci* **2004,** *234*, 107-112.

(331) Hintz, H.; Peisert, H.; Egelhaaf, H. J.; Chassé, T. Reversible and Irreversible Light-Induced p-Doping of P3HT by Oxygen Studied by Photoelectron Spectroscopy (XPS/UPS). *J Phys Chem C* **2011,** *115*, 13373-13376.

(332) Preobrajenski, A. B.; Chassé, T. Epitaxial Growth and Interface Structure of PbS on InP(110). *Appl Sur Sci* **1999,** *142*, 394-399.

(333) Faur, M.; Faur, M.; Jayne, D. T.; Goradia, M.; Goradia, C. XPS Investigation of Anodic Oxides Grown on p-type InP. *Surf Interface Anal* **1990,** *15*, 641-650.

(334) Ho, C.-H.; Lin, C.-H.; Wang, Y.-P.; Chen, Y.-C.; Chen, S.-H.; Huang, Y.-S. Surface Oxide Effect on Optical Sensing and Photoelectric Conversion of α-In2Se3 Hexagonal Microplates. *ACS Appl Mater Interfaces* **2013,** *5*, 2269-2277.

(335) Brojerdi, G.; Tyuliev, G.; Fargues, D.; Eddrief, M.; Balkanski, M. Ion Beam Modification of InSe Surfaces. *Surf Interface Anal* **1997,** *25*, 111-118.

(336) André, A.; Zherebetskyy, D.; Hanifi, D.; He, B.; Samadi Khoshkhoo, M.; Jankowski, M.; Chassé, T.; Wang, L.-W.; Schreiber, F.; Salleo, A.; Liu, Y.; Scheele, M. Toward Conductive Mesocrystalline Assemblies: PbS Nanocrystals Cross-Linked with Tetrathiafulvalene Dicarboxylate. *Chem Mater* **2015,** *27*, 8105-8115.

(337) Moreels, I.; Lambert, K.; Smeets, D.; De Muynck, D.; Nollet, T.; Martins, J. C.; Vanhaecke, F.; Vantomme, A.; Delerue, C.; Allan, G.; Hens, Z. Size-Dependent Optical Properties of Colloidal PbS Quantum Dots. *ACS Nano* **2009,** *3*, 3023-3030.

(338) Maiti, S.; Sanyal, M. K.; Jana, M. K.; Runge, B.; Murphy, B. M.; Biswas, K.; Rao, C. N. R. Evidence of Contact Epitaxy in the Self-Assembly of HgSe Nanocrystals Formed at a Liquid-Liquid Interface. *J Phys-Condens Mat* **2017,** *29*.

(339) Zahn, D. R. T.; Gavrila, G. N.; Gorgoi, M. The Transport Gap of Organic Semiconductors Studied using the Combination of Direct and Inverse Photoemission. *Chem Phys* **2006,** *325*, 99-112.

(340) Shen, Z. L.; Forrest, S. R. Quantum Size Effects of Charge-Transfer Excitons in Nonpolar Molecular Organic Thin Films. *Phys Rev B* **1997,** *55*, 10578-10592.

(341) Hill, I. G.; Kahn, A.; Soos, Z. G.; Pascal, R. A. Charge-Separation Energy in Films of π-conjugated Organic Molecules. *Chem Phys Lett* **2000,** *327*, 181-188.

(342) Cardona, M.; Ley, L., *Topics in Applied Physics, Photoemission in Solids I*. Springer: Berlin, **1978**; Vol. 26.

(343) Xing, K. Z.; Fahlman, M.; Chen, X. W.; Inganas, O.; Salaneck, W. R. The Electronic Structure of Poly(3,4-ethylene-dioxythiophene): Studied by XPS and UPS. *Synthetic Met* **1997,** *89*, 161-165.

(344) Yamane, H.; Yoshimura, D.; Kawabe, E.; Sumii, R.; Kanai, K.; Ouchi, Y.; Ueno, N.; Seki, K. Electronic Structure at Highly Ordered Organic/Metal Interfaces: Pentacene on Cu(110). *Phys Rev B* **2007,** *76*, 165436.

(345) Betti, M. G.; Kanjilal, A.; Mariani, C.; Vazquez, H.; Dappe, Y. J.; Ortega, J.; Flores, F. Barrier Formation at Organic Interfaces in a Cu(100)-benzenethiolate-Pentacene Heterostructure. *Phys Rev Lett* **2008,** *100*, 027601.

(346) Grobosch, M.; Knupfer, M. Charge-Injection Barriers at Realistic Metal/Organic Interfaces: Metals Become Faceless. *Adv Mater* **2007,** *19*, 754–756.

(347) Lang, N. D.; Kohn, W. Theory of Metal Surfaces - Work Function. *Phys Rev B* **1971,** *3*, 1215-1223.

(348) Lu, Z. H.; McCaffrey, J. P.; Brar, B.; Wilk, G. D.; Wallace, R. M.; Feldman, L. C.; Tay, S. P. SiO2 Film Thickness Metrology by X-ray Photoelectron Spectroscopy. *Appl Phys Lett* **1997,** *71*, 2764-2766.

(349) Hochella, M. F.; Carim, A. H. A Reassessment of Electron-Escape Depths in Silicon and Thermally Grown Silicon Dioxide Thin-Films. *Surf Sci* **1988,** *197*, L260-L268.

(350) Gunter, P. L. J.; Dejong, A. M.; Niemantsverdriet, J. W.; Rheiter, H. J. H. Evaluation of Take-Off-Angle-Dependent Xps for Determining the Thickness of Passivation Layers on Aluminum and Silicon. *Surf Interface Anal* **1992,** *19*, 161-164.